University of Pretoria

In vitro signal transduction mechanism exerted by 2-ethyl-3-O-sulphamoyl-estra-1,3,5(10),15-tetraen-3-ol-17-one in combination with dichloroacetic acid on breast adenocarcinoma (MCF-7) and breast non-tumorigenic (MCF-12A) cells

by

Xiao Xing Stander

Submitted in partial fulfilment of the requirements for the degree

Philosophiae Doctor **(Ph.D) in Human Physiology**

Department of Physiology
School of Medicine
Faculty of Health Sciences
University of Pretoria

Promotor: Professor Annie Joubert

2014

Ph.D candidate:

Mrs X. X. Stander

Student number: 25068530

Department of Physiology
University of Pretoria
Tel : +27 12 420 2864
Mobile: +27 76 690 9680
E-mail address: xiaoxing.stander@up.ac.za

Project promotor:

Professor A. M. Joubert

Department of Physiology
University of Pretoria
Tel: +27 12 319 2246
Fax: +27 12 321 1679
E-mail address: annie.joubert@up.ac.za

Acknowledgements

I would like to express sincere gratitude to my project promotor, Professor Annie Joubert, for accepting me as her student and the opportunity to conduct research in her lab. Her immense knowledge in the anticancer field has been a source of guidance in the past four years. I would also like to thank Professor Van Papendorp as the head of the physiology department for the job opportunity as senior technical assistant and making it financially viable to pursue this degree.

My sincere thanks also go to Dr Sanushka Naidoo and Professor Dave Berger from the Forestry and Agricultural Biotechnology Institute (FABI) for seeing the potential in me and encouraged me to become a scientist. I thank my fellow lab mates and colleagues, previous and present, from the University of Pretoria, Ronishree, Kalien, Brenda, André, Nobantu, Thandi and Alet many of whom taught me valuable skills.

Special thanks to my colleagues at the Hatfield Campus, Professor Peet du Toit, Maryna, Michael and Vangi, for their words of encouragement and all the coffee breaks. They created such a pleasant environment at the work place.

My greatest appreciation goes to my close friends from the Pretoria Evangelical Chinese Christian Church (PECCC). My Reverent Douglas Wu, his wife Whitney, and his children Sharon, Helen and Clearance always welcomed and loved me as one of their own family members. Thanks also go to Alex, Nichole and Samuel for taking excellent care of Andrew, my baby son. Also, I truly enjoy and appreciate two of my best friends, Janis and Bianca, who I met from undergraduate study for their generous friendship and love.

I thank my new family, Pa Johan, Ma Adri, Dalton and Christian for their love and support. My God mother Rosemarie has always been there for me and I am grateful for her.

Children have only one future and that would be the one his/her parents provide. My mother was a single mother. I remember those days that she earned 12 dollar per month, cold drinks and ice lollies were treats. She gave up the opportunity to study medicine so that she could take care of me. Still today I remember her words:

‘Education is the only way to change your life!’ My mother is an inspiration, role model and a teacher. She taught me the most invaluable principles of life including: integrity, loyalty, honesty, trust, diligence, perseverance, self-control and, most importantly, to love.

Lastly, but most importantly, to my husband André and son Andrew - thank you for your love and patience! To our son Andrew: thank you for putting up with all the late nights and weekends.

My husband is a man with few words, but he reserved nothing and taught me everything. We met in the lab during my honours year and ever since then he has guided me every step of the way. He demonstrates ways of love are “patient and kind, … … bears all things, believes all things, hopes all things, endures all things. Love never ends.” André taught me that ‘giving’ is the most powerful communication.

I am incredibly fortunate to have the support of all these loving people, making this thesis possible.

Summary

Most cancer cells rely on aerobic glycolysis to support the mitochondrial oxidative phosphorylation system (OXPHOS). The persistent oxic-anoxic cycle exerts selection pressures which lead to constitutive activation of glycolysis even in the presence of abundant oxygen. Expression of hypoxia-inducible factor 1 (HIF1) increases following hypoxia in neoplastic cells. This leads to the induction of pyruvate dehydrogenase kinase 1 (PDK1). The latter inactivates pyruvate dehydrogenase (PDH) that converts pyruvate to acetyl-coenzyme A for delivery to the tricarboxylic acid cycle (TAC). Dichloroacetic acid (DCA) is an inhibitor of PDK that forces cells into oxidative phosphorylation thereby suppressing cancer growth.

2-Ethyl-3-*O*-sulphamoyl-estra-1,3,5(10),15-tetraen-3-ol-17-one (C9), along with a few other 17β-estradiol analogs, are a novel class of *in silico*-designed inhibitors of microtubule dynamics. These newly designed and synthesized antimitotic compounds induce G_2/M arrest and apoptosis by docking to colchicine binding site between α- and β-tubulin. These compounds are 5 to 20 times more potent than their source molecule, 2-methoxyestradiol (2ME). To improve bioavailability C9 has been *in silico*-modified at carbon positions C2, C3 and C17 compared to 2ME.

The approach to investigate the anticancer potential of the *in silico*-designed antimitotic C9 in combination with the glycolytic inhibitor DCA *in vitro* is novel. Human breast carcinoma cell line MCF-7 and non-tumorigenic breast cells MCF-12A were used as an experimental model system.

The present study demonstrated that DCA (7.5 mM) in combination with C9 (130 nM) selectively inhibited half of MCF-7 cells' population (50.8%). Under the same treatment conditions, MCF-12A cells displayed high number of cell survival (70% cell growth). Qualitative morphological studies revealed decreased cell density in both cell lines, as well as hallmarks of apoptosis and autophagic processes including formation of apoptotic bodies, DNA fragmentation and autophagic vacuoles. Cell cycle- and apoptosis quantification analyses revealed C9+DCA treatment induced apoptosis in both cell lines and exhibited selectivity towards tumorigenic cells. Presence of autophagosome was observed and microtubule-associated protein 1 light chain 3 (II) (LC3-II) expression was elevated. Reduction of mitochondrial membrane potential depolarization in tumorigenic MCF-7 cells was demonstrated,

but not in MCF-12A cells. Oxidative stress tests suggested the combination treatment C9+DCA is able to induce lysosomal rupture and/or mitochondrial damage in tumorigenic MCF-7 cells. Kinase inhibition studies revealed that transient activation of *c*-Jun N-terminal kinase (JNK) plays an important role in cell proliferation. However, C9+DCA stimulated prolonged JNK activation and, in turn, promoted Bcl-2 phosphorylation, thereby facilitating autophagic and apoptotic cell death.

C9+DCA induced expression of a number of genes related to stress in MCF-7 treated cells including *TP53BP1*, *MDM2* and *BBC3/PUMA*. Genes related to cell motility and maintenance of the cytoskeleton such as *ACTG1*, *MAP7*, *TUBA1*, *TUBA6*, *TUBA8* and *TUBB2A* genes were down-regulated. In MCF-12A cells, treatment of C9+DCA induced expression of multidrug resistance gene *ABCB1*. Moreover, genes involved in reactive oxygen species metabolism *FTH1*, *GSTA2*, *NOS2A*, *SMOX*, *SOD1* and *SOD2* were also up-regulated.

In conclusion, the novel 17β-estradiol derivative, C9, in combination with DCA is a potent antiproliferative treatment. This study addressed the mechanisms of combination treatment at the basis of molecular and cellular level, warranting further research projects to develop viable and functional combination treatment as clinically useable anticancer agents.

Keywords: Cell cycle, dichloroacetic acid, glycolytic inhibitor, C9, antimitotic, combination therapy, apoptosis, autophagy, JNK and Bcl-2

Table of contents

List of figures

List of tables

Schematic presentations

Figures presented in this thesis were created in Microsoft PowerPoint or otherwise credited with appropriate citations. Many schematic presentation ideas were inspired from SABiosciens Pathway Centrals, Cell Signalling Technology®, as well as Berridge, M. (2012) Cell signalling biology. Chemical structures were created in ACD/ChemSketch 12.0 (1).

List of abbreviations

$^{\bullet}OH$	Hydroxyperoxyl radical
2DG	2-deoxy-D-glucose
4E-BP	Eif-4E binding protein
53BP1	P53-binding protein 1
A	Adenosine
ABCB1	ATP-binding cassette, sub-family B (MDR/TAP) member 1
ABCC5	ATP-binding cassette, sub-family C (CFTR/MRP), member 5
ACGT	African Centre of Gene Technology
ACTG1	Actin
AIC	Apoptosis inhibitory complex
AIF	Apoptosis inducing factor
ALDA,C	Aldolase A, -C
AMP	Adenosine monophosphate
AMPK	Adenosine monophosphate-activated protein kinase
APAF-1	Apoptotic protease activating factor 1
APC	Anaphase-promoting complex
ASK	Activator of S phase kinase
ASK1	Apoptosis signal-regulating kinase 1
ASK1–Trx	Apoptosis signal-regulating kinase 1-Trx signalling complex
ATF2	Activating transcription factor 2
Atg	Autophagy related genes
ATM	Ataxia-telangiectasia mutated
ATP	Adenosine triphosphate
ATR	Ataxia-telangiectasia and Rad3-related
AUG	Start codon
Bax	Bcl2-associated X protein
BBC3/PUMA	Bcl2 binding component 3/p53 up-regulated modulator of apoptosis
BCR	Btb-cul-3-rbx1
Bid	BH3-interacting domain death agonist
Bim	Bcl2-interacting mediator of cell death
BIR	Baculovirus IAP repeat
BNip3	Bcl-2/adenovirus EIB 19kd-interacting protein 3
BRCA1 namely	Breast cancer 1
BSA	Bovine serum albumin
BTG1	B-cell translocation gene 1
Bub1	Benzimidazoles 1

C	Cytidine
CA	Carbonic anhydrase
CAD	Caspase-activated DNAse
CAK	Cyclin-dependent kinase-activating kinase
CAMP	3', 5'-Cyclic adenosine monophosphate (AMP)
CAPK	Ceramide-activated protein kinases
CAPP	Ceramide-activated protein phosphatases
CARD	Caspase recruitment domain
CBP/p300	Cyclin AMP response element-binding protein (CREB)-binding protein
CCND1	Cyclin D1
Cdc2	Cell division cycle protein 2
Cdc25A	Cell division cycle 25A
Cdc45	Cell division cycle protein 45
Cdc6-ORC	Cell division cycle protein - Origin of replication protein
Cdc7	Cell division cycle protein 7
CDK	Cyclin-dependent kinase
CDK4	Cyclin dependent kinase 4
CDKI	CDK inhibitors
c-FLIP	Cellular FADD-like IL-1β-converting enzyme (FLICE)-inhibitory protein
Chk	Check-point kinase
CI	Cell index
Cip/Kip	CDK interacting protein/Kinase inhibitory protein
CITED4	Cbp/p300-interacting transactivator
CMA	Chaperone-mediated autophagy
$CO_3^{\bullet-}$	Carbonate radical
CoA	Acetyl coenzyme A
CPTP	Cytoplasmic protein tyrosine phosphatase
CREB	Cyclic AMP response element-binding protein
Crm1	Chromosome region maintenance 1
CRNA	Complimentary ribonucleic acid
CRS	Cytoplasmic retention signal
CTP	Deoxycytosine triphosphate
Cu/Zn-SOD	Copper-zinc superoxide dismutase
CV	Crystal violet
cyclin E/CDK2	Cyclin-dependent kinase 2
DAPI	4',6-diamidino-2-phenylindole
dATP	Deoxyadenosine triphosphate

DCA	Dichloroacetic acid
DCF	2', 7'-dichlorofluorescein
dCTP	Deoxycytosine triphosphate
DDIT3	DNA-damage-inducible transcript 3
DDIT4/REDD1/RTP801	DNA-damage-inducible transcript 4
DFF45	DNA fragmentation factor subunit 45
DFO	Deferoxamine mesylate salt
DGTP	Deoxyguanosine triphosphate
DISC	Death-inducing signalling complex
DMEM	Dulbecco's modified eagle's medium
DMSO	Dimethylsulfoxide
DNA	Deoxyribonucleic acid
DNA–PK	DNA-dependent protein kinase
DNTP	Deoxyribonucleotide triphosphate
DR2, Apo-1 or CD95	Fas
DR5	Trailr2
DRAM	Damage-regulated autophagy modulator
DTT	Dithiothreitol
DTTP	Deoxythymidine triphosphate
DUSP13	Dual-specificity phosphatase 13
E2F	Elongation factor 2
E2F1	E2F transcription factor 1
E-box	Enhancer box
EDTA	Ethylenediamine tetraacetic acid
EGF	Epidermal growth factor
EGFR	Epidermal growth factor receptor
EG-VEGF	Endocrine-gland-derived VEGF
EIF	Eukaryotic initiation factor
EIF1	Eukaryotic translation initiation factor 1
EIF4E	Eukaryotic translation initiation factor 4E
ELISA	Enzyme-linked immunosorbent assay
Emi1	Early mitotic inhibitor
Endo G	Endonuclease G
ENO1	Enolase-1
ER	Endoplasmic reticulum
ERK	Extracellular-signal-regulated kinase
ETC	Electron transport chain

FACS	Fluorescence activated cell sorting
FADH2	Reduced flavin adenine dinucleotide
FBS	Fetal bovine serum
Fbw7	F-box and WD40 domain protein 7
FCS	Fetal calf serum
Fe^{2+}	Ferrous ions
Fe^{3+}	Ferric iron
FIP200	Focal adhesion kinase family interacting protein
FITC	Fluorescein isothiocyanate
FOS	Proto-oncogene *c*-Fos
FOXO1	Forkhead box O1
FTH1	Ferritin heavy polypeptide 1
FTH1 and FTL	Ferritin both heavy and light polypeptide genes
G	Guanine
G_0	Quiescent cell
G_1	First cell cycle growth phase
G_2	Second cell cycle growth phase
GADD45	Growth Arrest and DNA-damage-inducible
GADD45A	DNA-damage-inducible 45A
GAPDH	Glyceraldehyde phosphate dehydrogenase
GDP	Guanine diphosphate
GEF	Guanine nucleotide exchange factor
GENECODIS	Gene Annotation Co-occurrence Discovery
GI_{50}	Concentration for 50% of maximal inhibition of cell proliferation
GLU1,3	Glucose transporter-1,3
GO	Gene ontology
GPCR	G protein-coupled receptors
GPx	Glutathione peroxidase
GR	Glutathione reductase
Grb2	Growth factor receptor-bound protein 2
Grx	Glutaredoxins
GSH	Glutathione
GSK3	Glycogen synthase kinase-3
GSSG	Glutathione disulfide
GST	Glutathione S-transferase
GSTA2	Glutathione S-transferase A2
GTP	Guanine triphosphate

H&E	Haematoxylin and eosin
H_2DCF-DA	2′, 7′-Dichlorodihydrofluorescein diacetate
H_2O_2	Hydrogen peroxide
HAT	Histone acetyltransferase
HDAC	Histone deacetylases
HIF-1	Hypoxia-inducible factor-1
Hip	Hsc70-interacting protein
HK1,2	Hexokinase 1,2
HLH	Helix–loop–helix
Hop	Hsc70-hsp90 organizing protein
HR	Homologous recombination
HRE	Hypoxia response element
hROS	Highly reactive oxygen species
Hsp70	Heat shock cognate protein of 70 kDa
Hsp90	Heat shock cognate protein of 90 kDa
HtrA2	High temperature requirement protein A2
IAP	Inhibitor of apoptosis
IC_{50}	Inhibitory concentration 50
ICAD	Inhibitor of caspase-activated DNAse
IF	Intermediate filaments
IGF2	Insulin-like growth factor-2
IKIP	IKK interacting protein
INK4/ARF	Inhibitor of kinase 4/alternative reading frame
IP3Rs	Inositol 1,4,5-trisphosphate receptors
IR	Ionizing radiation
JAK	Janus kinase
JNK	c-Jun N-terminal kinase
JUN	Jun proto-oncogene
KSR1	Protein kinase suppressor of Ras 1
LAMP-2	Lysosomal associated membrane protein type 2
LC3	Microtubule-associated protein 1 light chain 3
LDH	Lactate dehydrogenase
LDHA	Lactate dehydrogenase-A
LWM	Lysosomal wrapping mechanism
MAC	Mitochondrial apoptosis-induced channel
Mad	MAX dimerization protein 1
MAD1/2	Mitotic arrest deficient 1/2

MAM	Mitochondria-associated ER membrane
MAP7	Microtubule-associated protein 7
MAPK	Mitogen-activated protein kinase
MAPK14	Mitogen-activated protein kinase 14
MAPKK	MAPK kinase
MAPKKK	MAPK kinase kinase
Max	Myc-associated factor X
MCM	Minichromosome maintenance
MDM2	Mouse double minute 2
MEK	MAPK ERK kinase
MEKK	mitogen-activated ERK kinase kinase
MELAS	Mitochondrial encephalomyopathy, lactic acidosis, and stroke-like episodes syndrome
MMLV-RT	Moloney murine leukemia virus reverse transcriptase
MnSOD	Manganese superoxide dismutase
Mnt	Max-binding protein
MOPS	3(N-morpholino)propanesulfonic acid
MP1	MAPK scaffold protein 1
MPF	Named mitosis promoting factor
MPS1	Monopolar spindle 1
MPT	Mitochondrial permeability transition
MRE 11	Meiotic recombination protein 11
MRN complex	Meiotic recombination protein 11 (MRE 11), RAD50 and Nijmegen breakage syndrome protin-1 (Nbs1)
mRNA	Messenger RNA
MTOC	Microtubule organizing center
mTOR	Mammalian target of rapamycin
mTORC1	MTOR complex 1
mTORC2	MTOR complex 2
MTPs	Mitochondrial transition pores
Myc	Myelocytomatosis transforming virus
Myt1	Myelin transcription factor 1
NAC	*N*-Acetyl-*L*-cysteine
NADH	Reduced nicotinamide adenine dinucleotide (NAD+)
Nbs1	Nijmegen breakage syndrome protin-1
NEB	Nuclear envelope breakdown
NES	Nuclear export signal
NF-κB	Nuclear factor kappa B

NOS2A	Nitric oxide synthase 2A
NPAT	Mediated nuclear protein mapped to the ataxia telangiectasia locus
NPM	Nucleophosmin
$O_2^{\bullet-}$	Superoxide radical
OD	Optical density
OMM	Outer mitochondria membrane
OR	Origins of replication
ORC	Origin recognition complex
OXPHOS	Mitochondrial oxidative phosphorylation system
p15/INK4B/CDKN2B	Cyclin-dependent kinase 4 inhibitor B
p16/INK4A/CDKN2A/ARF	Cyclin-dependent kinase inhibitor 2A
p18INK4C/CDKN2C	Cyclin-dependent kinase 4 inhibitor C
p19INK4D/CDKN2D	Cyclin-dependent kinase 4 inhibitor D
p21/CIP1/WAF1	Cyclin-dependent kinase inhibitor 1
p27/KIP1	Cyclin-dependent kinase inhibitor 1B
p38	Mitogen-activated protein kinase 14
p57kip2	Cyclin-dependent kinase inhibitor 1C
PAK2	P21 protein (Cdc42/Rac)-activated kinase 2
PARP	Poly ADP ribose polymerase
PAS	Pre-autophagosomal structure
PBS	Phosphate buffered saline
PDH	Pyruvate dehydrogenase
PDK1	3-phosphoinositide-dependent protein kinase 1
PDK1,2	Pyruvate dehydrogenase kinase 1,2
PE	Phosphatidylethanolamine
PEG	Polyethylene glycol
PERK	RNA-activated protein kinase-like ER kinase
PEX	peroxisomal biogenesis factors
PFKFB3	Phosphofructo-2-kinase/gructose-2,6-bisphosphate-3
PFKL	Phosphofructokinase L
PGK1	Phosphoglycerate kinase 1
PH	Pleckstrin homology
PHD	Prolyl hydroxylase domain
PI	Propidium iodide
PI3K	Phosphoinositide 3-kinase
PIK3R1	Phosphoinositide-3-kinase regulatory subunit 1
PIKK	PI3K-related protein kinase

PIP2	Phosphatidylinositol 3,4-bisphosphate
PIP3	Phosphatidylinositol 3,4,5-trisphosphate
PKA	Protein kinase A
PKB	Akt/protein kinase B
PKM	Pyruvate kinase M
PlasDIC	Polarization-optical differential interference contrast
Plks	Polo like kinase
PMCA	Plasma membrane Ca^{2+} ATPase
PPAR-γ	Peroxysome proliferator-activated receptor
PRDX3	Peroxiredoxin 3
Prx	Peroxiredoxin
PS	Phosphatidylserine
PTEN	Phosphatidylinositol-3,4,5-trisphosphate 3-phosphatase and dual- specificity protein phosphatase
PTKRs	Protein tyrosine kinase-linked receptors
PTP	Permeability transition pore
PTPN6	Protein tyrosine phosphatase non-receptor type 6
R	Restriction point of cell cycle
RAD50	DNA repair protein RAD50
Raf	Rapidly accelerated fibrosarcoma
RAPTOR	Regulatory-associated protein of mTOR
Ras	Rat sarcoma-related
RasGEF	Ras guanine nucleotide exchange factor
Rb	Retinoblastoma
Rheb	Ras homologue enriched in brain
RICTOR	Rapamycin-insensitive companion of mTOR
RING	Really Interesting New Gene
RNA	Ribonucleic acid
RNAi	Interfering RNA
$RO_2^{\bullet -}$	Peroxyl radical
ROS	Reactive oxygen species
RPA	Replication protein A
RPTP	Receptor protein tyrosine phosphatases
rRNA	Ribosomal RNA
RTCA	Real-time cell analyzer
RTCA SP®	Real-time cell analyzer single plate
RTKs	Receptor tyrosine kinases

RZZ	Rod-Zw10-Zwilch complex
S	Synthesis phase
S6K1	S6 Kinase 1
SAC	Spindle assembly checkpoint
SAPK	Stress-activated protein kinases
SCF	Skp1-Cullin1-F-Box protein
SDS	Sodium dodecyl sulfate
SEK1	Stress-activated protein kinase/extracellular signal regulated kinase kinase 1
Ser^{70}	Serine 70 position
SERCA	Sarcoplasmic/endoplasmic reticulum Ca^{2+} ATPases
Shc	Src homology 2 domain containing protein
SIN3	Switch independent
SMAC	Second mitochondria-derived activator of caspase
Smad	Mothers against decapentaplegic homolog
SMOX	Spermine oxidase
$-SO_2H$	Sulfinic acid
$-SO_3H$	Sulfonic acid
SOC	Store-operated calcium channels
SOD1	Superoxide dismutase 1
SOD2	Superoxide dismutase 2 mitochondrial
-SOH	Sulfenic acid
SoS	Son-of-sevenless
Src	*v*-src sarcoma (Schmidt-Ruppin A-2) viral oncogene homolog
SREBP	Sterol regulatory element binding proteins
-S-S-	Disulfide bonds
T	Thymidine
TAC	Tricarboxylic acid cycle
TEM	Transmission electron microscopy
TF	Transcription factor
TGF-α,	Transforming growth factor-α
TP53BP1	Tumor protein p53 binding protein 1
TRADD	TNFR1-associated death domain
TRAF2	TNF receptor associated factor 2
tRNA	Transfer RNA
Trx	Thioredoxin
TrxR	Thioredoxin reductase
TSC	Tuberous sclerosis complex

TSC 1/2	Tuberous sclerosis complex
TUBA1, TUBA6, TUBA8 and TUBB2A	Tubulin alpha 1, 6 and 8, as well as tubulin beta 2A
TXNL4A	Thioredoxin-like 4A
TXNL4B	Thioredoxin-like 4B
Ublc	Atg7-dependent ubiquitin-like conjugation
ULK1, ULK2, UKL3	UNC-51-like kinase -1, -2, and -3
UPR	Unfolded protein response
UPS	Ubiquitin-proteasome system
UTR	5'Untranslated region
UV	Ultraviolet
UVRAG	Ultraviolet irradiation resistance-associated gene
VEGF	Vascular endothelial growth factor
VHL	Von Hippel–Lindau protein
Vps34	Vesicular protein sorting 34
Wee1	Wee1-like protein kinase
WT1	Wilms' tumor suppressor
YWHAE	Tyrosine 3-monooxygenase/tryptophan 5-monooxygenase activation protein

1. Chapter 1: Introduction

1.1 Cell signalling and signal transduction

Cell signalling events control and orchestrate vital cell biological processes such as proliferation, differentiation, autophagy and apoptosis (2). Extracellular signals are transmitted to intracellular targets either directly or through receptor-mediated signal transduction pathways (3). The lipid bilayer structure of biomembranes provide a barrier for external signal molecules to communicate with the inside world of a cell. The exception to this rule is hydrophobic molecules which are capable of crossing this barrier to gain access by diffusion. Hydrophilic molecules that cannot cross the biomembranes need assistance from signal transducing receptors to communicate with the cell (2). Steroid hormones, thyroid hormone, vitamin D_3 and retinoic acid are able to diffuse across the plasma membrane owning to their hydrophobic nature (4). These molecules are able to directly influence the gene expression of genes by their interaction with nuclear hormone receptor and the interaction may cause three outcomes: repression, anti-repression and transcription activation (5).

Signalling communication mechanisms require ligand-receptor interactions at the cell surface. The signalling molecule acts as a ligand which in turn binds to a structurally complementary site on the extracellular- or membrane-spanning domains of the receptor. Binding of a ligand to its receptor causes a conformational change in the cytosolic domain or domains of the receptor that ultimately induces specific cellular responses (Figure 1.1). G protein-coupled receptors (GPCR), cytokine receptors and tyrosine kinase receptors are examples of receptors that are involved in conducting cell surface communication (2). The GPCRs function as transducers to receive messages from a ligand/stimulus and forward the message to an appropriate second messenger (6). GPCR is a multidomain membrane spanning receptor (7). The tyrosine kinase-linked receptor and the serine/threonine kinase receptor are single membrane spanning receptors (4). An example of the tyrosine kinase-linked receptor is the epidermal growth factor receptor (EGFR) and the detailed signalling pathway is illustrated in section 1.2.1.

There are two types of G proteins, namely the trimeric G proteins and monomeric G proteins (8). The former receives information from stimulus and acts as guanine

nucleotide exchange factors (GEF) that exchanges guanine diphosphate (GDP) for guanine triphosphate (GTP) on G protein α subunit (6). GTP bounded Gα not only stimulates Gα activity, but also assists with dissociation of the Gβγ subunit from Gα (6). Differences between Gα or Gβγ lie in the various lipid tails which assist them to be inserted into the cell membrane (2,9). Activated Gα or Gβγ have their distinguished downstream targets. 3', 5'-Cyclic adenosine monophosphate (AMP) is a low molecular weight short-lived second messenger signalling molecule which can relay information and also responds to G protein (10,11). Cyclic AMP (cAMP) is a highly versatile second messenger which is capable of activating many downstream effectors. Cyclic AMP-dependent protein kinase A (PKA) is a unique effector that responds to cAMP, resulting in the phosphorylation of a large variety of downstream target proteins (12). During stress and starvation, liver cells prevent formation of glycogen and initiate the process of gluconeogenesis (2,13). Liver cells increase the gene expression of rate limiting enzymes eg. glucose-6-phosphatase by activating its transcription factor, cyclic AMP response element-binding protein (CREB) via PKA-mediated signalling pathways (14,15).

Cascade signalling is eventually passed on and is received by effectors which are responsible for the actions on change certain gene expression (16).

1.2 Cell cycle signalling

Most cells in an adult human are quiescent, however specialized cells such as the hematopoietic system, skin and gastrointestinal mucosa maintain proliferation (17). Cell fate is determined by either inherited intrinsic factors (i.e. cell type) or extrinsic factors such as environmental factors (i.e. stress). Large numbers of signalling systems work in conjunction with each other to control whether or not a cell enters the cell cycle, differentiates into different cell types, or undergoes autophagy or apoptosis (Figure 1.1).

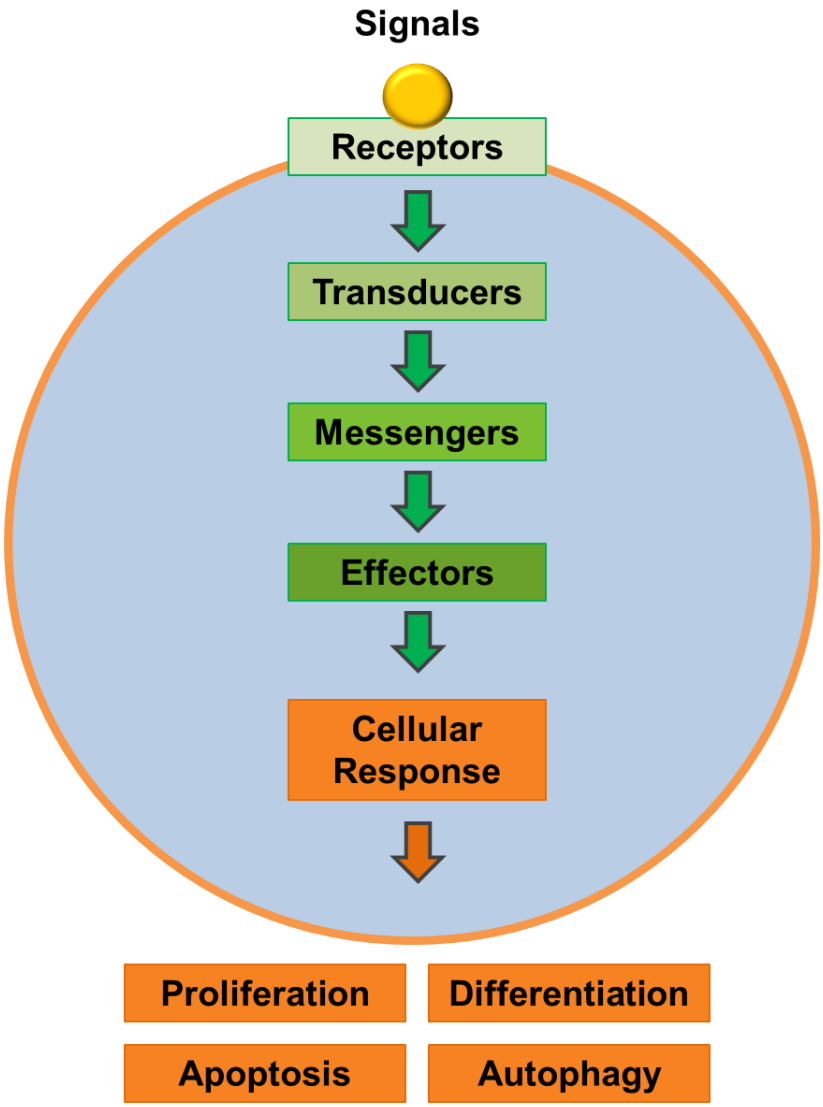

Figure 1.1: The basic principle of cellular signalling. Extracellular signal/stimuli (e.g. hormones, neurotransmitters or growth factors) acting on cell surface receptors relay information through intracellular signalling pathways that can have a number of cellular responses.

The continuity of life depends on punctual and accurate cell proliferation. Cell division results in genetically identical daughter cells (18). The mitotic (M) phase is a rapid cellular process in comparison to the interphase. If a typical human cell undergoes one division in 24 hours, the M phase would take one hour at the most (18). Interphase accounts for approximately 90% of the whole cell cycle process and is subdivided into the gap one (G_1) phase, the synthesis (S) phase and the gap two (G_2) phase (18). G_1 phase is a stage after mitosis when cells get ready for successful deoxyribonucleic acid synthesis and G_2 is a phase after DNA synthesis when the cell plans for successful mitosis (Figure 1.2) (17). The most important outcome for

proliferating cells is to copy three billion bases of DNA accurately during S phase and to separate the duplicated chromosomes evenly into two daughter cells during mitosis (Figure 1.2) (17). A specific, precise and stringent cell cycle regulation system is essential for the normal and healthy development of multicellular organisms. However, loss of function of any cell cycle control point may lead to the production of aneuploid and/or tumor cells (19).

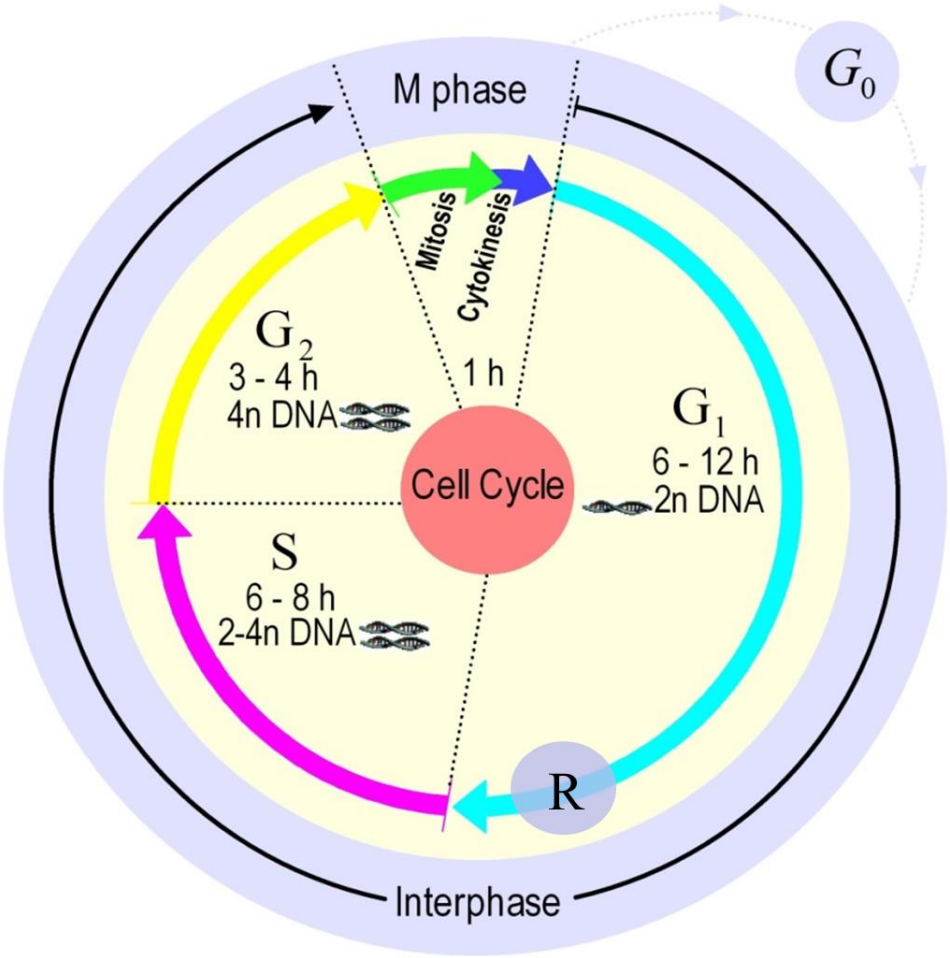

Figure 1.2: Cell cycle progression. Quiescent cell (G_0) enter the first growth phase (G_1) upon growth factor stimulation. When the G_1 surveillance system restriction point (R) and G_1 checkpoint permit a cell to proliferate, it gains entry to synthesis phase (S). If a cell reaches its second growth phase (G_2) and passes the G_2 checkpoint, then the cell is committed to divide into two daughter cells through mitosis followed by cytokinesis (figure adapted from http://users.minet.uni-jena.de/csb/prj/cellcycle/).

The key to unlocking the cell cycle process is the increased expression of cyclin D protein in the cytosol. However, cyclins lack enzymatic activities, and thus activation

of a cyclin requires binding to a specific kinase subunit, cyclin-dependent kinase (CDK) (17). Each cyclin is assigned to a specific CDK to form a complex and carry out their enzymatic functions as serine/threonine kinases. The CDK family gene is highly conserved across a broad spectrum of phylogeny and its activity is stimulated by cyclin-dependent kinase-activating kinases (CAK) and constrained by CDK inhibitors (CDKI) (20). Cyclin/CDK complexes are the central cell cycle regulators with each complex controlling a specific cell cycle transition. Extracellular mitogenic stimuli such as hormones and growth factors promote the intracellular levels of cyclins (D-type) which binds to corresponding CDKs (CDKs 4 and 6) and in turn activate quiescent cells to proliferate (17,20).

Non-dividing cells have zero growth (G_0) and they only enter the cell cycle after receiving mitogenic stimulation such as growth factors (21). There is a complex network that cross references numerous signalling pathway systems and stringently regulates whether or not a cell enters the cell cycle. The signalling pathways can be divided into pro-proliferative, anti-proliferative and surveillance signalling pathways. Pro-proliferative pathways such as extracellular-signal-regulated kinase (ERK) 1/2 (22), *Drosophila wingless* gene and vertebrate homolog, *integrated* or *int-1* (Wnt)/β-catenin (23) and phosphoinositide 3-kinase (PI3K) (24) respond to stimulants and help cells gain entry to cell cycle by activating genes that control cell proliferation. A key event of cell proliferative signalling pathway involves engagement of cyclin D which in turn phosphorylates retinoblastoma protein (Rb). The latter leads to activation of elongation factor 2 transcription factor (E2F) transcriptional system that permits G_1/S transition (25,26) (Figure 1.3). Cell cycle progression and G_1/S transition is facilitated by expression of cyclin E and cyclin A and both of them are regulated by E2F (27). Other antiproliferative pathways such as transforming growth factor-β (TGF-β) and its downstream effectors mothers against decapentaplegic homolog (Smad) transcription factors are able to induce growth arrest at various stages of the G_1 phase of the cell cycle (28,29) (Figure 1.3). Mitogen-activated protein kinase 14 (p38) (22) also prevents cells from entering the cell cycle.

In tumor cells, many genes that are constitutively activated and promote cell cycle progression are termed oncogenes. These same genes in normal somatic cells function as promoters of the cell cycle, however, they are labelled as proto-oncogenes since they are not constitutively active and merely has the potential to become oncogenes. In contrast, several negative cell cycle elements called the

tumor suppressors, which function as down regulators of proliferative genes, are often dysfunctional in tumor cells (2). p53 tumor suppressor protects mammals from neoplasia by inducing DNA repair, cell cycle arrest and in severe cases, apoptosis in response to stress (30). p53 is able to block cell cycle in G_1 phase through p21-mediated pathway. It is also able to block the cell cycle at the G_2/M phase by inhibiting cell division cycle protein 2 (Cdc2) (30,31). G_2/M cell cycle phase inhibition is meditated by three transcriptional targets of p53, GADD45, p21, and 14-3-3 (30) (Figure 1.3).

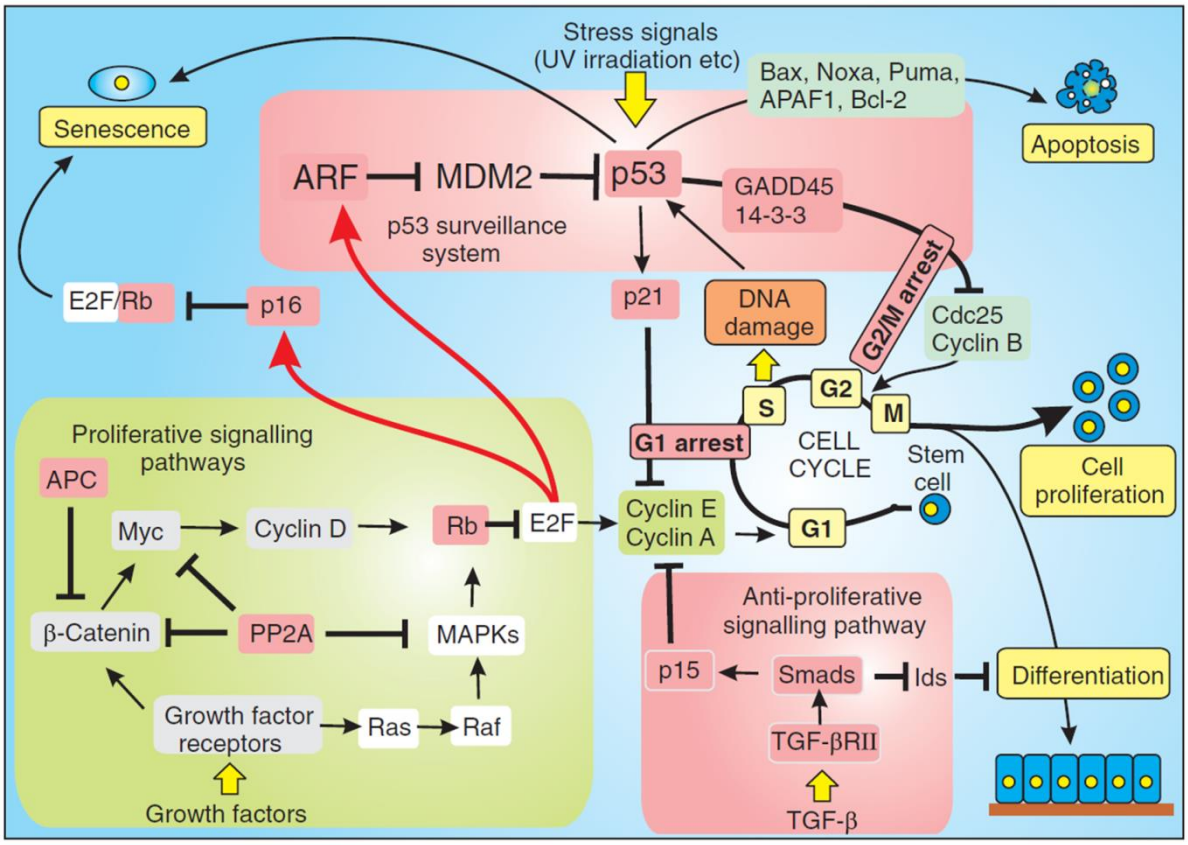

Figure 1.3: Cell proliferation signalling network. The signalling pathways can be divided into pro-proliferative, anti-proliferative and surveillance signalling pathways. Wnt/β-catenin and mitogen-activated protein kinases (MAPK) pro-proliferative pathways have the ability to phosphorylate Rb and transcription factor E2F permits the expression of cyclin E/A thus activates cell cycle G_1/S transition. In contrast, the anti-proliferative signalling pathway such as TGF-β and its downstream effectors Smad are able to induces growth arrest at various stages of the G_1 phase. p53 tumor suppressor protects mammals from neoplasia by inducing DNA repair, cell cycle arrest and in severe cases, apoptosis in response to stress. (Figure adapted from Cell Signalling Biology by M. J. Berridge, Module 9)

1.2.1 Mitogen-activated protein kinase-mediated cyclin D activation signalling

A specific cellular response is determined by the types of signal/stimuli information collected by the cell. Sensors will receive the signal and relay it to the effector for gene and/or protein activation. Several genes will respond to the relayed information and gene expression will occur. Gene transcription is initiated by RNA polymerase binding to the gene promoter region. Transcription factors and co-factors facilitate the binding of the promoter region by sensitizing RNA polymerase towards the gene of interest (25).

"The central dogma of molecular biology deals with detailed residue-by-residue transfer of sequential information" (32). This information has been simplified to "Deoxyribonucleic acid (DNA) -----> ribonucleic acid (RNA) -----> Protein". *Homo sapiens* contain 3 x 10^9 nucleotides in their whole genomic DNA, however, the number of genes estimated in the human genomes is 22 333 (33). Only a small fraction of DNA in complex organisms such as humans is transcribed to give a RNA product. Many of the non-coding regions of a gene serve as regulatory elements. For example, *cis*-acting regulatory elements (resident on DNA that is being transcribed) TATA box is acting as the main initiator for the recognition of the gene. Moreover, further upstream from the TATA box, the promoter proximal elements such as CAAT box and GC box assist with the recognition process. Subsequently, the *trans*-acting elements (mobile regulatory elements) such as transcription factors (TF) recognize the *cis*-acting sequence on DNA thus guiding and activating the RNA polymerase to begin transcription (34). The RNA product from transcription is not the final product that is used to make polypeptides. The RNA transcript undergoes a series of processing modifications such as RNA splicing, 5' capping by 7-methylguanosine triphosphate and 3' tailing by polyadenylation prior to translational process. The mature messenger RNA (mRNA) moves to the cytoplasm where ribosomes bind and assemble a primary protein chain from the mRNA template (11).

The activation of cyclin D gene via MAPK pathway upon growth factor stimulation is explained by emphasizing only the essential points on the pathway. Details of cyclin D gene activation may serve as an example to illustrate the complexity of cascade information relay (Figure 1.4).

Non-dividing cells in G_0 phase can enter the G_1 cell cycle phase when extracellular mitogens are present and bind to a suitable receptor. Many mitogens are well known and epidermal growth factor (EGF) will be discussed below as an example. Epidermal growth factor binds to the extracellular domain of epidermal growth factor receptor (EGFR) which is a transmembrane protein (35). The epidermal growth factor receptor belongs to the EGF factor family of receptor tyrosine kinases (RTKs) family or EGFR family of protein tyrosine kinase-linked receptors (PTKRs) (36). The stimulant-receptor interaction promotes both homo- and heterodimerization of the EGF receptor subunits in the cytosol. Dimerization and activation of EGFR are mechanistically indistinguishable events (37).

Ligand binding results in receptor dimerization, *trans*-phosphorylation and subsequent activation of downstream signalling (38). Tyrosine autophosphorylation is triggered by ligand-induced non-covalent oligomerization of monomeric receptors (i.e. dimerization of receptors). Autophosphorylation of tyrosine residue enhances the catalytic activity by recruiting downstream signalling proteins such as *v*-src avian sarcoma (Schmidt-Ruppin A-2) viral oncogene homolog (Src) homology 3 (SH3)-containing adaptor growth factor receptor-bound protein 2 (Grb2) (39). Grb2 adaptor protein provides a critical link between cell surface growth factor receptors and the rat sarcoma-related (Ras) signalling pathway with its SH2 and SH3 domains respectively (40). Grb2 SH2 domain binds to the region of the EGFR containing the phosphorylated tyrosines and its SH3 domain is used to recruit Son-of-sevenless (SoS) (41) (Figure 1.4).

Ras is a GTPase which belongs to a large family of monomeric G proteins which plays an important role in GTP-dependent cell signalling (42). Ras is inactive when bound to GDP. SoS and Ras guanine nucleotide exchange factor (RasGEF) function as facilitators for the exchange of GDP for GTP. Once it is associated with the EGF receptor, SoS comes into contact with Ras and can begin to facilitate the exchange of GDP for GTP (42). Subsequently, the Ras/GTP complex may stimulate various signalling pathways such as the MAPK signalling pathway and the PI3K pathway (43).

In the case of the MAPK signalling pathway, Ras has the ability to activate the rapidly accelerated fibrosarcoma (Raf) protein kinase which is part of a multi protein complex in the MAPK pathway. Raf is the main MAPK kinase kinase (MAPKKK)

which phosphorylates two serine residues on the MAPK kinase (MAPKK) MAPK ERK kinase (MEK) (43). The latter will relay the information on by phosphorylating the tyrosine and threonine residues of MAPK components of ERK (43). The cascade component of MAPKKK, MAPKK and MAPK (Raf-MEK-ERK) are held together by membrane surface scaffolding protein kinase suppressor of Ras 1 (KSR1) (44) (Figure 1.4). After phosphorylation of the ERK at the cell membrane, it diffuses into the nucleus where it activates numerous transcription factor genes by phosphorylation. Myelocytomatosis transforming virus (Myc) gene is one of the downstream targets and it is regarded as the master gene which controls about 15% of all gene regulations in the cell, both positive and negative (45).

One of the most striking findings over the recent years has been the discovery that the expression of Myc protein contributes to almost every aspect of tumor cell biology (46-48). Myc belongs to the family of helix–loop–helix (HLH) leucine zipper proteins which does not exist in monometric form *in vivo* (47). Instead, it forms a heterodimer with Max which exists in excess to Myc stoichiometrically (47). Furthermore, Max also binds to Mad, Mxi1 and Mnt. All the different combinations of heterodimers will bind to the same enhancer box (E-box) DNA sequence 5'-CACA/GTG-3' to exert their regulatory function. The Myc-Max protein complex promotes the activation of the cell cycle genes by activating the expression of cyclin D and cyclin dependent kinase 4 (CDK4) expression. Meanwhile it represses CDK inhibitors p27, p21 and p15 gene expression (47). The Mad-Max or Mnt-Max heterodimers, however, inhibit cell proliferation by placing Myc-Max on an E-box sequence in resting or differentiated cells (49). The gene's repression effects are accomplished by Mad/Mnt-Max dimeric complex recruiting the switch independent co-repressor 3 (SIN3) (47,50). The SIN3 adaptor protein hosts a complex which contains histone deacetylases (HDAC) which prevents chromatin exposure, thus inhibiting gene transcription (50) (Figure 1.4).

When Myc expression is increased by MAPK mediated RasGTPase activation, the "on" mechanism Myc-Max heterodimers replaces the "off" Mad/Mnt-Max complex (51). Binding of Myc-Max to the E-box provides a platform for various co-activators to bind and ultimately to open up coiled chromatin (47). The accessibility of certain genes depends on chromatin remodelling by acetylation and the enzyme that acetylates histone is called the histone acetyltransferases (HAT). CREB-binding protein (CBP)/p300 are examples of HAT (52). The stability of Myc protein is post-

transcriptionally regulated via the Ras-dependent signalling pathway. The phosphorylation status of Thr^{58} (53) and Ser^{62} (54) determines the fate of the protein. Phosphorylation at Ser^{62} stabilizes Myc protein, however, at Thr^{58} destabilizes it. Ras phosphorylates Myc Ser^{62} through the MAPK/ERK pathway (47). Glycogen synthase kinase-3 (GSK3) destabilizes Myc by phosphorylating it at Thr^{58} (47) Ras also indirectly stabilizes Myc by inhibition of GSK3 through PI3K signalling (47). Subsequently, the degradation of Myc protein is accomplished by the ubiquitin-proteasome system (UPS) (48) (Figure 1.4).

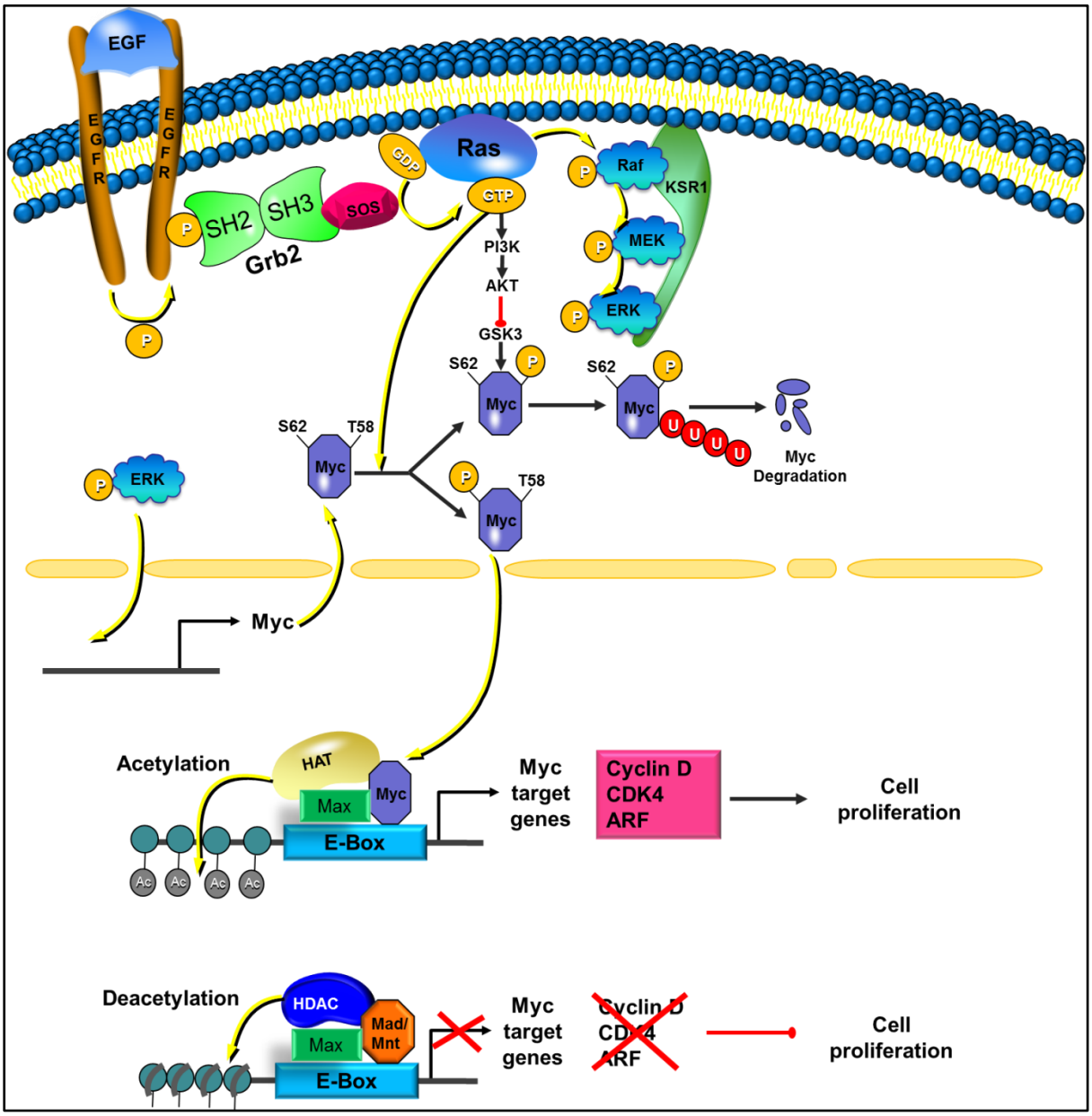

Figure 1.4: Mitogen-activated protein kinase mediated activation of the cell proliferation gene expression. Epidermal growth factor receptor (EGFR) is autophosphorylated in the cytoplasm when epidermal growth factor (EGF) ligand binding occurs at the extracellular matrix. EGFR autophosphorylation recruits adaptor protein Grb2 which in turn attracts SOS. Subsequently, SOS exchanges Ras GDP to GTP, thereby activating the MAPKKK (Raf), MAPKK (MEK) and MAPK (ERK) pathway. As a result, Myc protein is produced and it exchanges Mad/Mnt and binds to Max to form a complex which acetylates the chromatin to facilitate chromatin remodelling. Several Myc target genes such as Cyclin D, CDK4 that are vital for cell proliferation, are activated by this pathway.

1.2.2 Gap one phase, Synthesis phase, Gap two phase and their checkpoints

The central components of the cell cycle signalling are the series of cyclins and CDKs in various combinations with each other. Each cyclin/CDK combination controls a different stage of cell cycle and driving the cycle forward. In early G_1 phase, cyclin D protein expression increases and it interacts with CDK4/6 to form a complex in the cytoplasm (55). The cyclin D/CDK4/6 then moves into the nucleus where CAK phosphorylates and activates the cyclin D/CDK4/6 complex (56). The activated cyclin D/CDK4/6 complex has the ability to phosphorylate Rb which inhibits the transcription of cell cycle related genes under G_0 status (Figure 1.5). Rb is one of the vital gate-keepers repressing the transcription of cell cycle related genes (26). A key event at the restriction point (R) is the phosphorylation of Rb which stimulates its dissociation from elongation factor 2 (E2F) transcription factor 1 (E2F1) and HDACs, thus promoting chromatin remodelling and transcription of downstream genes (2,26) (Figure 1.5). Cyclin E, cyclin A, E2F and cell division cycle 25A (Cdc25A) are of vital importance to propel cell cycle forward and the expression of these genes are activated by the Rb/E2F signalling mediated pathway (27). Furthermore, cyclin D/CDK4/6 also phosphorylates p107 and p130, which deactivate the repression activity of E2F4/5 for cyclin E gene transcription (57).

Subsequent cell cycle progression from G_1 to S phase depends on the level of Rb hyper-phosphorylation. Cyclin E/CDK2 maintains the phosphorylation status of Rb in G_1 and ensures G_1 progression towards the commitment step of DNA replication (58). In return, this process sets up a positive feedback cycle whereby phosphorylated Rb activates cyclin E expression itself, as well as transcription factors E2F1, 2 and 3. Furthermore, cyclin E/CDK2 plays an important role with regards to assisting the cell in making critical decisions about their fate throughout the G_1 phase. Cyclin E/CDK2 phosphorylates one type of histone acetyl transferase CREB-binding protein CBP/p300, so that it helps to open up chromatin for transcription of many genes that are essential for DNA synthesis in the S phase (59) (Figure 1.5). In addition to its function of chromatin remodelling, it also increase gene transcription of histones which are essential components of eukaryotic chromosomes and play a crucial role in the maintenance of chromosomal integrity.

The stimulation of histone gene transcription is achieved by cyclin E/CDK2 mediated nuclear protein mapped to the ataxia telangiectasia locus (NPAT) transcription factor

activation (60). Furthermore, cyclin E/CDK2 contributes to centrosome duplication by phosphorylating nucleophosmin (NPM) which is associated with unduplicated centrosomes (61). Cyclin E/CDK2 activity has also been demonstrated to inhibit the pro-apoptotic function of forkhead box O1 (FOXO1) by phosphorylating Ser^{249} of FOXO1 (59). Cyclin A plays a major role in the control of DNA replication in mammalian cells and assists with the onset of S phase entry (62).

The regulation of cyclin E/CDK2 activity is complex and performed via three different systems. Cdc25A, a dual-specific phosphatase, activates CDK2 by dephosphorylation (63,64). There are two ubiquitin-proteasome pathways that are involved in abrogation of cyclin E/CDK2 activity. The BTB-Cul-3-Rbx1 (BCR) ubiquitin ligase labels the monomeric unbounded cyclin E (59,65), meanwhile the F-box and WD40 domain protein 7 (Fbw7) component of a Skp1-Cullin1-F-Box protein (SCF)-type E3 ligase complex (SCF^{Fbw7}) is responsible for the degradation of phosphorylated cyclin E which is part of the cyclin E/CDK2 complex (66,67) (Figure 1.5). In addition to previously described regulatory mechanisms, cyclin E/CDK2 catalytic activity can be inhibited by CDK interacting protein/Kinase inhibitory protein (Cip/Kip) inhibitors $p27^{kip1}$ (68) and $p21^{Cip1}$ (69).

There are two main categories of CDK inhibitor, namely the inhibitor of kinase 4/alternative reading frame (INK4/ARF) inhibitors and the Cip/Kip inhibitors that positively and negatively regulate the CDK activity (20) (Figure 1.5). Four members of the INK4 family $p16^{INK4A}$ (70), $p15^{INK4B}$ (71), $p18^{INK4C}$ (72), $p19^{INK4D}$ (73), as well as three members of the Cip/Kip family $p27^{kip1}$ (56), $p21^{Cip1}$ (74) and $p57^{kip2}$ (75) have been discovered (20). Members of the INK4 family specifically inhibit the activity of CDK4 and CDK6 in G_1 phase, whereas Cip/Kip members inhibit a broader spectrum of cyclin/CDK complexes throughout the cell cycle (73,76,77).

Surprisingly, the same locus *INK4a* that produced the INK4 family proteins contains an overlapping gene named the *ARF* gene. The *INK4a/ARF* locus contains two separate promoters, each produces a different transcript. RNAs from exon 1 (*INK4a/ARF* gene) are alternatively spliced to either 1α or 1β, followed by the common exon 2 and 3 (78,79). ARF transcription factor encodes $p19^{ARF}$ in mouse or $p14^{ARF}$ in humans (79,80). The main function of mouse $p19^{ARF}$or human $p14^{ARF}$ is to act upstream of p53 tumor suppressor protein, releasing it by inhibition of mouse double minute 2 (MDM2) which is associated with p53 (78). The ARF promoter is

activated when cells experience sustained proliferative signalling and these signals may be induced by overexpression of oncogenes such as the *Myc*, *Ras* and adenovirus *E1A*. Thus, ARF has ability to sense hyperproliferative signals and relay the information to activate p53 to protect the integrity of the genome (78).

The p53 protein is one of the mostly studied cell surveillance systems and its level is kept low in non-stressed cells by Mdm2 (81). Mdm2 protein binds to p53 and interferes with p53's ability to *trans*-activate target genes (82). Mad2 also contributes to p53 degradation because it demonstrates intrinsic ubiquitin ligase activity (83). When cells encounter stress, one of the coping mechanisms is to activate the p53 surveillance system. If DNA is damaged, either by exogenous agents such as chemicals, ultraviolet (UV) and ionizing radiation (IR) or endogenous agents such as reactive oxygen species (ROS), cell cycle progression is arrested (Figure 1.5). Special protein complexes are able to sense the DNA damage. For example, Ku70-Ku80, MRN complex (meiotic recombination protein 11 (MRE 11), RAD50 and Nijmegen breakage syndrome protein-1 (Nbs1)) are utilized to sense double-stranded DNA damage (84) and replication protein A (RPA) for single-stranded DNA lesions or unreplicated DNA (85). These "sensors" relay information directly or indirectly to p53 protein. In the case of indirect information transduction, a transducer such as ataxia-telangiectasia mutated (ATM) or ataxia-telangiectasia and Rad3-related (ATR) is activated in response to double- and single-stranded damage respectively (86). Subsequently, check-point kinase 1 (Chk1) and/or check-point kinase 2 (Chk2) are activated through ATM and/or ATR phosphorylation respectively (87). In response to genotoxic stress, p53 accumulates in the cell and induces the $p21^{Cip1}$-mediated inhibition of Cyclin D/CDK4/6 (20,88). If the Cyclin-D/CDK complex is inhibited, Rb protein is hypo-phosphorylated and is tightly bound to the transcription factor E2F, inhibiting its activity.

During normal cell division, cyclin E/CDK2 and Cyclin A/CDK2 peak in G_1-S and S phase respectively, thus illustrating their pivotal role in initiation of DNA replication. The initiation of DNA replication during S phase takes place at the origins of replication (OR) and there are multiple sites of OR that occur on the chromosomes simultaneously (89). Eukaryotic DNA replication is a complex multistep process whereby prereplicative complexes first recognize the initiation site for DNA replication licensing, followed by the assembly of multiple protein attachment such as RPA and DNA polymerases (89). OR contain consensus sequences for origin

recognition complexes (ORC) to bind. Subsequently, DNA-bound ORC attract and associate with Cdc6, Cdt1 and members of the minichromosome maintenance (MCM) family for the formation of prereplicative complex (licensing stage) (58,90).

The licensing stage begins with recruiting of Cdc6 to the ORC and the Cdc6 is synthesized during G_1 under the transcription control of E2F. Afterwards, Cdt1 binds to the Cdc6-ORC complex on chromatin and is essential for MCM protein loading. In turn, MCMs 2-7 are loaded onto the prereplicative complex and interact with each other to form a hexameric multiprotein complex which functions as a replicative helicase. DNA replication prereplicative complex installation is completed and the specific chromatin where the complex is situated is considered licensed. Shortly after the replication process begins, cyclin A/CDK2 complex phosphorylates Cdc6 for the prevention of re-replication (58,89,90).

Cdc45 is an essential regulatory factor for replication as it bridges between prereplicative complexes and recruits essential replication proteins such as DNA polymerase and RPA. The loading of Cdc45 onto the origin depends on the activities of activator of S phase kinase (ASK)/DBF4, Cdc7, cyclin E/CDK2 and cyclin A/CDK2 proteins (91). DNA begins to unwind at the origin of replication after Cdc45 loading and is stabilized by RPA at each separated strand (92).

For cells that are past the restriction point and near S phase, the key target for the G_1/S checkpoint signalling is the cyclin E/CDK2 complex. As previously mentioned, the ATM/ATR transducer mediate the pathway between the genotoxic stress signal to the Chk2 or Chk1 effector protein by phosphorylation. The downstream effects of the Chk2/Chk1 pathway are phosphorylation of Cdc25A and reduce its level by degradation through the UPS. Cdc25A is a phosphatase used to remove inhibitory phosphates on substrate CDK2 for its activation. Furthermore, CDK2-dependent Cdc45 loading is also interrupted by G_1/S transition signalling.

Once S phase is completed, the cell transits through the G_2 phase and prepares for mitosis. After duplication of the genome in S phase, the cell enters into G_2 phase where cyclin B/CDK1 complexes form and are kept inactive. Wee1-like protein kinase (Wee1) and myelin transcription factor 1 (Myt1) kinases exert inhibitory effect on cyclin B/CDK1 complex throughout the G_2 phase by phosphorylation (93,94) (Figure 1.5). Wee1 phosphorylates CDK1 of the complex at Tyr15 inside the nucleus

meanwhile Myt1 phosphorylates it at both Tyr14 and Tyr15 in the cytosol (95,96). In addition, cyclin B/CDK1 complexes are kept in the cytosol during the G_2 phase with the assistance of cytoplasmic retention signal (CRS) that has a nuclear export signal (NES) responsible for chromosome region maintenance 1 (Crm1) (97,98).

As the cell cycle progresses towards the G_2 – M transition stage, Cdc25B/C phosphatases remove the phosphates on cyclin B/CDK1 thus activating it (99). Removing phosphate on cyclin B/CDK1 is a complex process which initially involves the activation by Cdc25B (100). A second phosphatase Cdc25C is activated by CDK1, as well as Polo like kinase (Plks) phosphorylation (101). Activated Cdc25C is then able to remove a phosphate on the primed cyclin B/CDK1 complex. The dephosphorylated (active form) cyclin B/CDK1 complex, alternatively named mitosis promoting factor (MPF), is capable of entering the nucleus, where it activates chromosome condensation, nuclear envelope breakdown (NEB) and spindle assembly for mitosis (95,102).

DNA lesions must be repaired to prevent loss or incorrect transmission of genetic information to daughter cells. During S and G_2 phases, the double-strand DNA break is readily repaired by homologous recombination (HR) using the intact sister chromatid. As cell cycle progresses into G_2/M phase, homology search becomes increasingly difficult because chromosomes are condensed (103). The coordination of the DNA-repair pathway and the cell cycle is controlled through different cell-cycle activities, such as DNA-dependent protein kinase (DNA–PK), ATM, and ATR kinases that lead to the activation of p53, Chk1 and Chk2 (104). The downstream target of Chk1/2 is the Cdc25C, which is required to activate cyclin B/CDK1 complexes in G_2/M phase. Chk1/2 mediated phosphorylation of Cdc25C creates a binding site for 14-3-3 rho protein, thus facilitating the inhibition of Cdc25C by sequestering it in the cytoplasm (Figure 1.5).

Phosphorylation of p53 by the ART pathway dissociates it from MDM2 and activates its DNA binding activity. Several genes which are involved in G_2/M checkpoint are expressed by p53 transcription factor. These genes include 14-3-3 rho, GADD45 and p21. 14-3-3 binds to the phosphorylated cyclin B/CDK1 and exports it from the nucleus. GADD45 acts together with the Wilms' tumor suppressor (WT1) to dissociate the cyclin B/CDK1 complex by binding to the CDK1 portion. As previously

mentioned, p21 is an inhibitor of cyclin-dependent kinases including CDK4/6 and CDK1 (105).

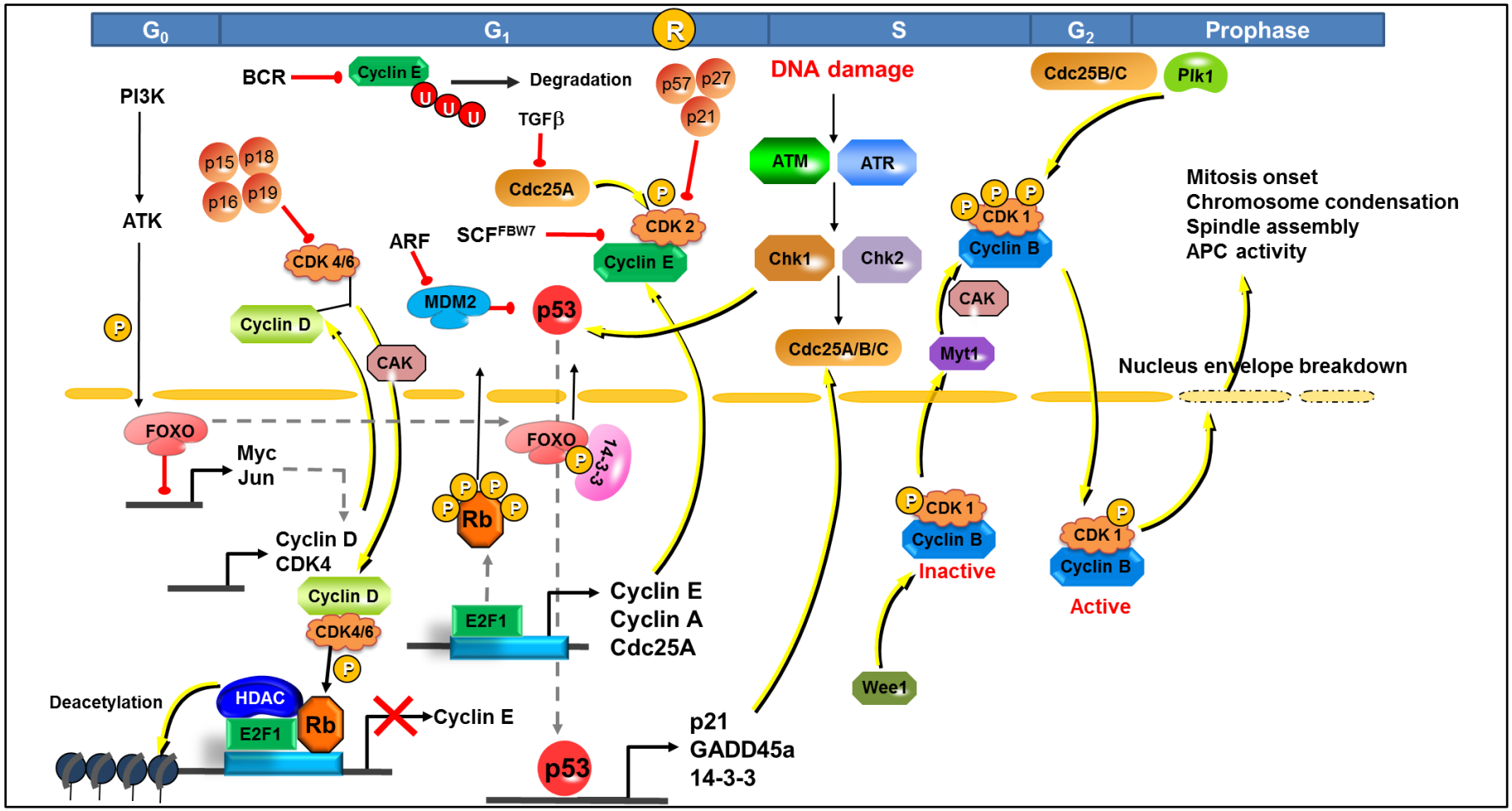

Figure 1.5: Cell cycle signalling gap one phase, DNA synthesis phase, gap two phase and their checkpoints. In G_1, a key event at the restriction point is the phosphorylation of Rb which stimulates its dissociation from elongation factor 2 (E2F) transcription factor 1 (E2F1) and HDACs, thus promoting chromatin remodelling and transcription of downstream genes: cyclin E, cyclin A and Cdc25A. The initiation of DNA replication during S phase takes place at the origins of replication. If DNA is damaged, cell cycle progression is arrested and this information is relayed to p53 or ataxia-telangiectasia mutated (ATM)/ ataxia-telangiectasia and Rad3-related (ATR) pathways. In response to genotoxic stress, p53 accumulates in the cell and induces the $p21^{Cip1}$-mediated inhibition of Cyclin D/CDK4/6. Once S phase is completed without error, the cell enters into G_2 phase. In G_2, cyclin B/CDK 1 is dephosphorylated by Wee1, Myt1 and Cdc25B/C for its activation and gain mitosis entry. Cdc25B/C phosphatases remove the phosphates on cyclin B/CDK1 thus activating it.

1.2.3 Mitosis and spindle assembly checkpoint

The final phase of the cell cycle begins when cells leave the G_2 phase and enter the M phase. Successful cell division is largely dependent on the signalling between the MPF, mitotic spindle checkpoint signalling and anaphase-promoting complex (APC) (95). The active cyclin B/CDK1 complex contributes toward prophase, pro-metaphase and metaphase by playing an important role in chromosome condensation, nuclear envelope breakdown and spindle assembly respectively (106). Anaphase sister chromatids separation, spindle disassembly, as well as telophase cytokinesis are processes regulated by the APC. Before the sister chromatids separate in anaphase, the cell has to ensure all its chromosomes are aligned properly on the metaphase plate and are attached to the spindle via kinetochores (107). The unattached spindles of the cell in M phase sends out a signal by means of the mitotic spindle checkpoint signalling to the APC to inhibit APC's activity until all spindles are attached (107). Cyclin B/CDK1 kinase activity must be reduced towards the end of mitosis and the reduction relies on cyclin B destruction. When all the chromosomes are attached to kinetochores, the mitotic spindle assembly checkpoint (SAC) complex is removed by dynein, thus removing its inhibition activity on APC (108). Subsequently, APC degrade cyclin B and securin to activate chromosome separation. The detailed molecular mechanisms of the mitosis entry, exit and spindle checkpoint signalling are discussed below and illustrated in Figure 1.6.

Previously, the different cyclins and their corresponding CDKs function and regulation have been illustrated throughout the cell cycle progression. One of the key events which determine the success of the eukaryotic cell signalling is protein phosphorylation status. Protein phosphorylation changes its functional status and it is rapid as well as energetically inexpensive. Even though protein phosphorylation is advantageous, cells also require a more robust mechanism for altering the protein landscape to remove unwanted proteins in sequential manner. The UPS is such a system where it labels proteins via its three subunits E1, E2 and E3 for degradation at the 26S proteasome complex. The tagging of a substrate by the UPS is a concerted effort between the ubiquitin activating E1 subunit, ubiquitin conjugating E2 subunit and the E3 ligases which facilitate the transfer of ubiquitin from E2 to the substrate. The Really Interesting New Gene (RING) E3 ligase acts as a scaffold protein that holds E2 with its RING-finger domain and transfers the ubiquitin to lysine residue on the substrate (109).

There are two RING-E3 ligases that control the cell cycle: SCF and APC (alternatively cyclosome). The SCF E3 ligase control the transition from G_1/S and G_2/M (110), meanwhile the APC is primarily required for mitotic exit (109,111). Anaphase-promoting complex is an ubiquitin ligase responsible for the destruction of cyclin B at the end of mitosis. The APC ubiquitin E3 ligase complex is comprised of at least 15 subunits and two co-activators, Cdc20 and Cdh1 (109). Unlike the SCF E3 ligase complex which contains F-box subunit for substrate recognition, the APC complex demonstrates no such a modular control, therefore associates with co-activators for substrate recognition (112). Furthermore, the activation of APC by Cdc20 must be controlled stringently to prevent premature initiation of anaphase because errors in chromosome segregation can lead to the formation of aneuploid daughter cells (113). The precise assembly and activation of the APC complex (with its co-activator) is regulated by phosphorylation. The binding of co-activator Cdc20 to APC is achieved by cyclin B/CDK1 (alternatively MPF) phosphorylation of APC subunits Apc3/Cdc27, Apc6/Cdc16, and Apc8/Cdc23 (114). At the same time, cyclin B/CDK1 or MPF phosphorylates the other co-activator Cdh1 to prevent its function (96).

The successful binding of co-activator Cdc20 to APC by cyclin B/CDK1 (MPF) mediated phosphorylation does not necessarily mean that this complex is active (115,116). The spindle assembly checkpoint is a dynamic surveillance system known to inhibit APC function until all the chromatid pairs are correctly aligned on the mitotic spindle (117). The spindle assembly checkpoint signalling is activated by Aurora kinase B which senses tension from the kinetochores that are incompletely attached to spindles (107). In turn, Aurora kinase B recruits budding uninhibited by benzimidazoles 1 (Bub1), monopolar spindle 1 (MPS1) and the Rod-Zw10-Zwilch complex (RZZ) complex to the active site (118). Bub1, MPS1 and RZZ together recruit mitotic arrest deficient (MAD) 1 to the kinetochore site. Mad1 attached to a kinetochore attracts Mad2 in a closed enzymatic conformation (118). This Mad1 bounded Mad2 (closed) catalyzes an important reaction which converts the Mad2 open conformation to the Mad2 closed conformation (119). The purpose of Mad2 in a closed conformation is that it is able to form a complex with BubR1/Mad3/Bub3 which phosphorylates and inhibits the activity of Cdc20 on APC (118). The inhibition effect of the mitotic spindle assembly checkpoint complex is removed upon complete spindle attachment to the kinetochore.

Various other mechanisms also exist to control the catalytic activity of APC. Stegmeier and co-workers (2007) demonstrated that before Cdc20 can be activated, it must be polyubiquitinated by a combined effort from UbcH10 (E2) and APC itself (E3) (120). Hansen *et al.* (2004) showed the Plk1 regulates activation of the APC by phosphorylating and triggering SCF-dependent destruction of the APC inhibitor early mitotic inhibitor (Emi1) (121). When APC is fully activated it ubiquitinates cyclin B for UPS degradation, consequently releasing CDK1. The unbounded CDK1 no longer exert the inhibition effect on the Cdh1, thus allowing co-activator Cdh1 to bind to APC (113). Subsequently, securin can be labelled by APC^{Cdc20} and APC^{Cdh1} for UPS degradation (122). Sister chromatids are held together at the centromere by cohesin that is part of the kinetochore. Securin is an enzyme which binds to separase that is responsible for hydrolysing cohesin molecules (117). This separation of the chromosome is the hallmark of anaphase and the final process of mitosis is cytokinesis, which cleaves the mitotic cell into two daughter cells.

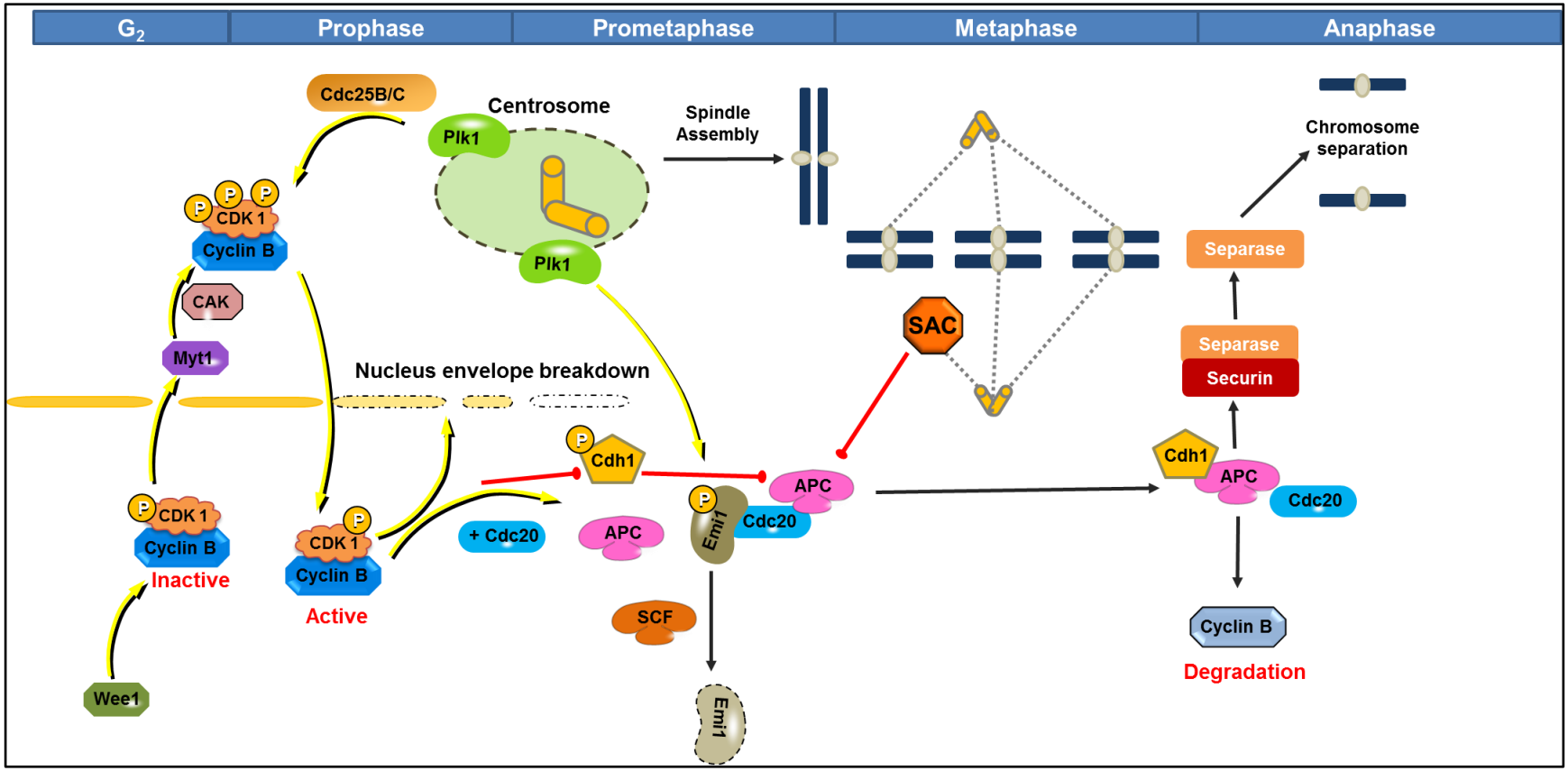

Figure 1.6: Mitosis and spindle assembly checkpoint. Wee1 and Myt1 kinases exert inhibitory effect on cyclin B/CDK1 complex throughout the G_2 phase by phosphorylation. The binding of co-activator Cdc20 to APC is achieved by cyclin B/CDK1 (MPF) phosphorylation of APC subunits. However, cyclin B/CDK1 (MPF) phosphorylates the other co-activator Cdh1 to prevent its function. The sister chromatids separation in anaphase, spindle disassembly, as well as telophase cytokinesis are regulated by APC. Before the sister chromatids separate, the cell has to ensure all its chromosomes are aligned on metaphase plate and are attached to the spindle via kinetochores. The unattached spindle of the cell in M phase sends out a signal by means of the mitotic spindle checkpoint signalling to the APC to inhibit APC's activity until all spindles are attached. Cyclin B/CDK1 kinase activity must be reduced towards the end of mitosis and the reduction relies on cyclin B destruction. When all the chromosomes are attached to kinetochores, the mitotic spindle assembly checkpoint (SAC) complex is removed by dynein, thus removing its inhibition activity on APC. Subsequently, APC degrade cyclin B and securin to activate chromosome separation.

1.3 Programmed cell death

Cells enter programmed cell death when all the surveillance systems failed to protect its genome integrity (123). Programmed cell death is the last option to protect the cell's genome integrity and stability. Many cells became cancerous because their programmed cell death pathway signalling is impaired (124). In a multicellular organism, regulated programmed cell death such as apoptosis and autophagy are vital to the organism's development. Necrosis, however, is one type of uncontrolled non-programmed cell death which is usually accompanied by swelling and may cause serious health issues (123,125).

Since De Duve and his collaborators discovered peroxisomes and lysosomes in the 1960s (126,127), a number of publications emerged in the 1970s related to programmed cell death to lysosomal activity and autophagy (128). The term 'apoptosis' was coined first in 1972 in a paper published by Kerr, Wyllie, and Currie (129). A breakthrough in the field of apoptosis came in 1977 when *Caenorhabditis elegans* was developed as a model organism to study the genetic basis of cell death by Sulston and Horvitz (130).

Programmed cell death, therefore, may be defined as a strictly regulated energy-dependent process that regularly requires gene activation, often shares a certain degree of morphological similarities, and the process plays a unique role in homeostasis, development and neoplasia (125). Besides apoptotic, autophagic and necrotic cell death, other forms of programmed cell death also exist. Aponecrosis (131), paraptosis (132) and ferroptosis (133) are examples of nonapoptotic cell death discovered in recent years.

1.3.1 Apoptosis

Morphological and biochemical features of apoptosis

Apoptotic cells undergo a series of distinctive morphological changes and begin with cell shrinkage and clumping of the chromosomes (pyknosis) (125). An apoptotic cell will begin to reduce its size followed by cytoplasm condensation and the appearance of asymmetry of the plasma membrane become visible (129,134). Eventually small

pieces of cell membrane will bud off to form apoptotic bodies (129,134). A simple histological examination with light microscopy and haematoxylin and eosin staining can demonstrate the morphological changes mentioned above (135). Haematoxylin stains nucleic acids with a deep blue-purple colour and the rest of the cells can be contrasted and visualized with a pink eosin stain which binds non-specifically to protein (135). The apoptotic cell appears shrunken with a more condensed cytoplasm when compared to surrounding healthy cells. Furthermore, the dark purple condensed nuclear chromatin stain, as well as dark pink eosinophilic cytoplasmic stain could be observed (125). Transmission electron microscopy (TEM) is able to detect the ultra-structural changes within the cell. Irregular cell outlines, extrusion of membrane-bound cytoplasm containing organelles, fragmented nuclei and increased density of microvilli are typical morphological observations from TEM micrographs of apoptotic cells (125,136).

Most of the morphological characteristics of apoptosis mentioned above are caused by a class of aspartate-specific cysteine proteases in active apoptotic cells (137). Proteases of this class of are homologous to each other and they form part of the caspase family which are catalytically-dormant proenzymes in nonapoptotic cells (137). Caspases-mediated apoptotic cell death is initiated by the formation of death-inducing signalling complex (DISC) which is followed by stimulation of the extrinsic death receptor pathway (138,139). Alternatively, the intrinsic/mitochondrial caspases-mediated apoptosis pathway may be triggered by the formation of the apoptosome which is composed of cytochrome *c*, apoptotic protease activating factor 1 (Apaf-1) and procaspase 9 (140). Thereafter, these complexes recruit effectors to activate the initiator caspases 2, 4, 8, 9 and 10. Subsequently, a sub-class of caspases namely the executioner caspases (3, 6 and 7) are activated via cleavage and ready to exert their proteolytic action on variety of targets which results in the apoptotic phenotype (139). A key regulator which controls the intrinsic/mitochondrial apoptotic pathway is the B cell leukaemia-2 (Bcl-2) family anti- and pro-apoptotic proteins. This family regulates the release of apoptogenic elements from the mitochondria such as inhibitor of apoptosis (IAPs), caspase-activated DNase (CAD) and cytochrome *c* (137,139). Mitochondria are not the only organelles involved in the intrinsic activation of apoptosis. The endoplasmic reticulum stress pathway can result in the activation of caspase-12 (141) and the lysosomes may secrete cathepsins to exert direct damage on mitochondria or interact with Bcl-2 family proteins (142). In addition, apoptosis may occur at caspase-

independent manner, which includes perforin/granzyme pathway, endonuclease G and apoptosis inducing factor (AIF) (125).

Caspases

Much of the attention related to apoptotic cell death is focused on the central executioners: caspases (138,139). This family of protein is highly conserved across phylogenies through evolution which illustrates their important function in apoptosis (143). In 1993, two caspase related genes *ced-3* from *C. elegans* and mammalian caspase-1 gene from humans were independently identified (144). There are 11 human caspase genes discovered up to date, caspase 1, -2, -3, -4, -5, -6, -7, -8, -9, -10 and -14. Caspases can be classified into two subfamilies: pro-apoptotic caspases (caspase 2, -3, -6, -7, -8, -9 and -10) and pro-inflammatory caspases (caspase 1, -4, -5, -11 and -12) (144). Furthermore, those caspases that are mainly involved in mediating cell death signalling can be subdivided again into the initiator caspases (caspase 2, -8, -9 and -10) and executioner caspases (caspase 3, -6 and -7) (144). Regardless of origins and subfamilies, all known caspases possess a cysteine at the catalytic active-site which recognizes at least four contiguous amino acids in their substrate including an aspartic acid residue at the C-terminal (137,144). A number of substrates containing aspartic acid residues such as nuclear lamins, fodrin, p21 protein (Cdc42/Rac)-activated kinase 2 (PAK2) and DNA fragmentation factor subunit 45 (DFF45) are cleaved by caspases (145). Caspase-activities can be negatively regulated by the inhibitor of apoptosis (IAP) family. IAP proteins contain baculovirus IAP repeat(s) (BIRs) which allow them to bind and exert inhibition activities on caspases (146). At the end point of either intrinsic or extrinsic signalling pathways, the apoptotic process continues toward the execution phase. The ultimate goal of apoptosis is the activation of endonuclease or proteases that will degrade nuclear material and cytoskeletal proteins respectively (125,147).

Caspase-independent inducers of apoptosis

Cathepsins, calpains, granzymes, endonucleases and AIF are non-caspase hydrolases that are effectors of apoptosis (148). AIF and endonuclease G are proteins released from the mitochondria during apoptosis which act on DNA directly (DNA fragmentation) in a caspase-independent manner (149,150) (Figure 1.8). Pro-apoptotic factors such as AIF and Endo G released from the mitochondria are part of the caspase independent pathway and are directly involved in nuclear DNA degradation. These factors are only active once the cell is already committed to die. The 'stage I' nuclear condensation occurs when AIF translocates to the nucleus and fragments DNA into approximately 50 – 300 kb pieces (125,151). Endo G is another caspase-independent mitochondrion-specific nuclease that translocates to the nucleus during apoptosis and functions to cleave chromatin DNA (152).

Cathepsins, including cathepsin B, D and cathepsin L, are proteases that are linked to apoptosis and are associated with mitochondrial membrane permeability, chromatin condensation, the degradation of the intracellular matrix, the processing of procaspases, and the externalization of PS on the plasma membrane of apoptotic cells (153). Under normal physiological conditions, cathepsins are located intralysosomally. Under stressful conditions, cathepsins are released from lysosomes where they participate in pro-apoptotic processes (153).

Calpains are cysteine proteases that reside in the cytosol and are activated by increases in free intracellular Ca^{2+} (154). The M-calpain is able to activate caspase-dependent apoptotic pathways by activating caspase 12 which in turn activates downstream apoptotic pathways (155). Caspase-independent DNA fragmentation is also induced by granzyme B by directly cleaving inhibitor of caspase-activated DNAse CAD (ICAD), allowing caspase-activated DNAse CAD (CAD) to trigger nucleosomal DNA fragmentation (156). Pro-apoptotic Bcl-2 family members BH3-interacting domain death agonist (Bid) and Bcl2-associated X protein (Bax) can be cleaved and activated by granzyme B, causing mitochondrial membrane permeabilization and caspase-dependent apoptosis (157).

Extrinsic apoptotic pathway

The extrinsic apoptotic pathway is initiated via ligands and specific receptor binding interactions. These transmembrane receptors are called death receptors and they typically contain an extracellular ligand binding domain and a cytoplasmic “death domain” which interacts with associated proteins and together cause downstream death signal transduction effects (125). The most well-known death receptor families are Fas (DR2, Apo-1 or CD95), tumor necrosis factor receptor 1 (TNFR1, also known as DR1, CD120a, p55 or p60), DR3 (Apo-3), TNF-related apoptosis-inducing ligand receptor 1 (TRAILR1, also known as DR4 or Apo-2) and TRAILR2 (DR5) and DR6 (125,158-160). TNF-α/TNFR1 is one the best characterized models that scientists use to illustrate the sequence of events of the extrinsic pathway of apoptosis.

Upon ligand binding, the homologous trimeric ligand TNF-α causes clustering of TNFR1 death receptors (125) (Figure 1.7, step 1). Subsequently, the cytosolic portion of clustered TNFR1 receptors are able to attract the adapter protein TNFR1-associated death domain (TRADD) and thereafter recruit FADD (161,162) (Figure 1.7, step 2). Stimulation of Fas/CD95 and TRAIL receptors will also result in the recruitment of FADD (144). Consequently, FADD associates with procaspase-8 via dimerization of the death domain. This type of association between FADD and procaspase-8 is linked by means of homophilic interface with their N-terminal death effector domains (DEDs) (163) (Figure 1.7, step 3). At this point, the formation of the DISC is completed and results in auto-catalytic activation of procaspase-8 (Figure 1.7, step 4) which ultimately initiates apoptosis either by directly interacting with caspase-3/7 or indirectly through the pro-apoptotic family members of Bcl-2 protein (164). Cellular FADD-like IL-1β-converting enzyme (FLICE)-inhibitory protein (c-FLIP) is an anti-apoptotic regulator that suppresses TNF-α, Fas-L, and TRAIL-induced apoptosis (165). *c*-FLIP binds to FADD and/or caspase 8 or -10 and forms an apoptosis inhibitory complex (AIC) which in turn prevents DISC formation (165) (Figure 1.7, step 5).

Thus, two types of cells, type I and type II were identified by Scaffidi *et al.* (1998) based on the whether or not mitochondria are needed for caspase 8 to activate downstream caspases (166). In Type I cells, DISC-mediated caspase 8 activation is sufficient to induce the activation of downstream caspases 3/7, and is able to

complete the execution of apoptosis (144,166) (Figure 1.7, step 6). In contrast, type II cells do not express high level of caspase 8 and the involvement of mitochondrial signalling is essential to complete the apoptotic pathway (144,167). This type of cell death involves the downstream caspases through the activation of BH3-only protein Bid which indirectly leads to the intrinsic apoptotic pathway (163) (Figure 1.7, step 7). Furthermore, death ligand and receptor interaction can also interact with other signalling pathways such as nuclear factor kappa B (NF-κB), *c*-Jun N-terminal kinase (JNK), sphingomyelin signalling pathway (168-170) (Figure 1.7).

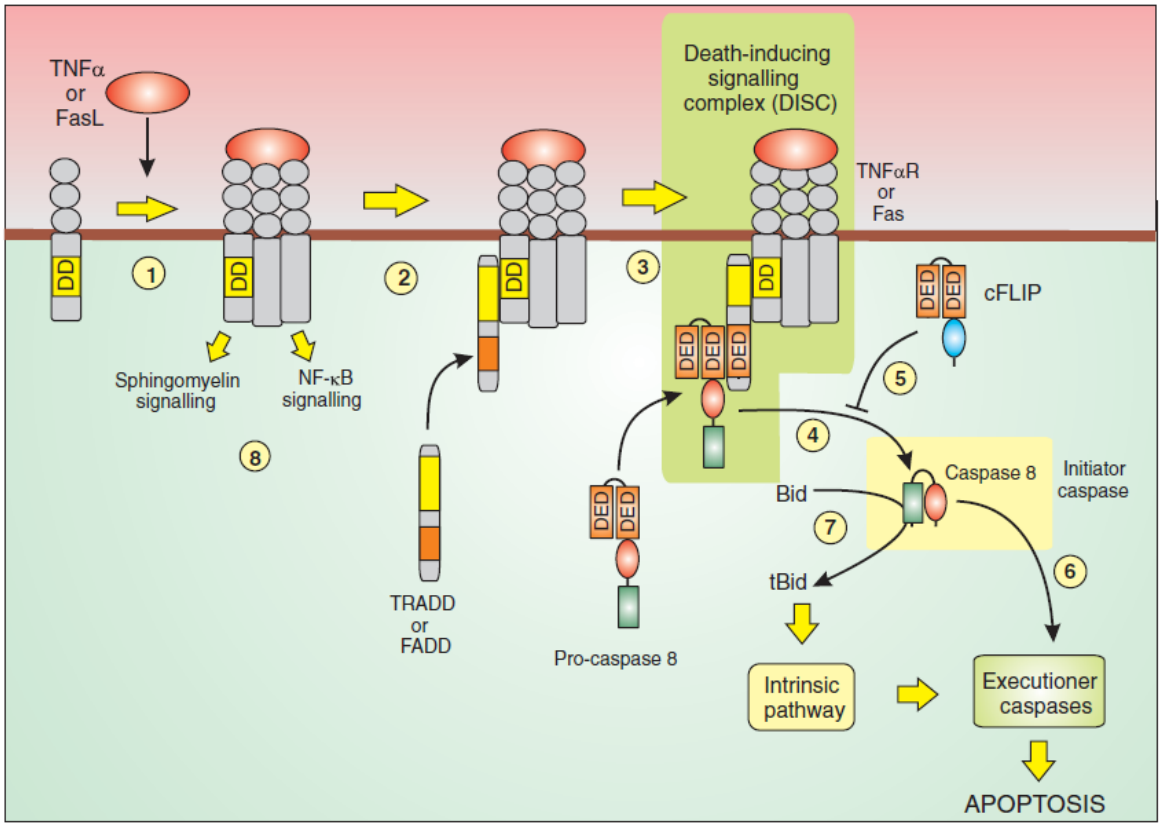

Figure 1.7: Death receptor-mediated extrinsic apoptotic pathway activation. Death ligands such as TNFα or FasL bind to the death receptor stimulated fast-track signalling cascade by recruiting procaspases 8 to the site to form DISC. Subsequently, caspase 8-mediated cell death may occur via two types of methods based on the involvement of Bcl-2 protein from the mitochondria. (Figure from Berridge (2012) Module 11).

Intrinsic apoptotic pathway: caspase-dependent

Mitochondria are dynamic organelles that exist as networks and implemented as an essential component of the intrinsic apoptotic pathway. Various stimuli, including withdrawal of hormones and growth factors, UV, toxins, hypoxia, chemotherapeutics and redox stress induce mitochondrial-mediated apoptosis (125). As previously mentioned, mitochondria have two different membranes, an inner and an outer membrane, and are quite distinct in appearance and function. The intermembrane space contains cytochrome *c*, procaspases, endonuclease G (Endo G), AIF and second mitochondria-derived activator of caspase (SMAC) (171).

The intrinsic signalling pathway engages in intracellular signals that act on targets within the cells which causes mitochondrial-initiated events. The intrinsic pathways may or may not involve caspases. Up-stream of the caspase-dependent pathway signal molecules are able to cause changes in the mitochondrial membrane potential and this results in the formation of mitochondrial permeability transition (MPT) pore. This pore formation results in the release of key apoptotic proteins such as cytochrome *c*, SMAC (also known as DIABLO in mice), or high temperature requirement protein A2 (HtrA2) (125,172). Subsequently, these proteins activate apoptosis in a caspases-dependent manner. Cytochrome *c* release from the mitochondria triggers the activation of caspase 9 through Apaf-1 protein. Apaf-1 functions as an important apoptosis activator which consists of a *C. elegans* Ced-4 homology domain flanked by a caspase recruitment domain (CARD) (145). In the presence of cytochrome *c*, Apaf-1 binds to it and oligomerizes to form a multimeric wheel-shaped complex apoptosome and facilitate the activation of procaspase-9 (145,173). SMAC/DIABLO and HtrA2 (also known as Omi) are factors which positively regulate apoptosis. SMAC/DIABLO and HtrA2/Omi interact with IAPs and prevents caspase inhibition (125).

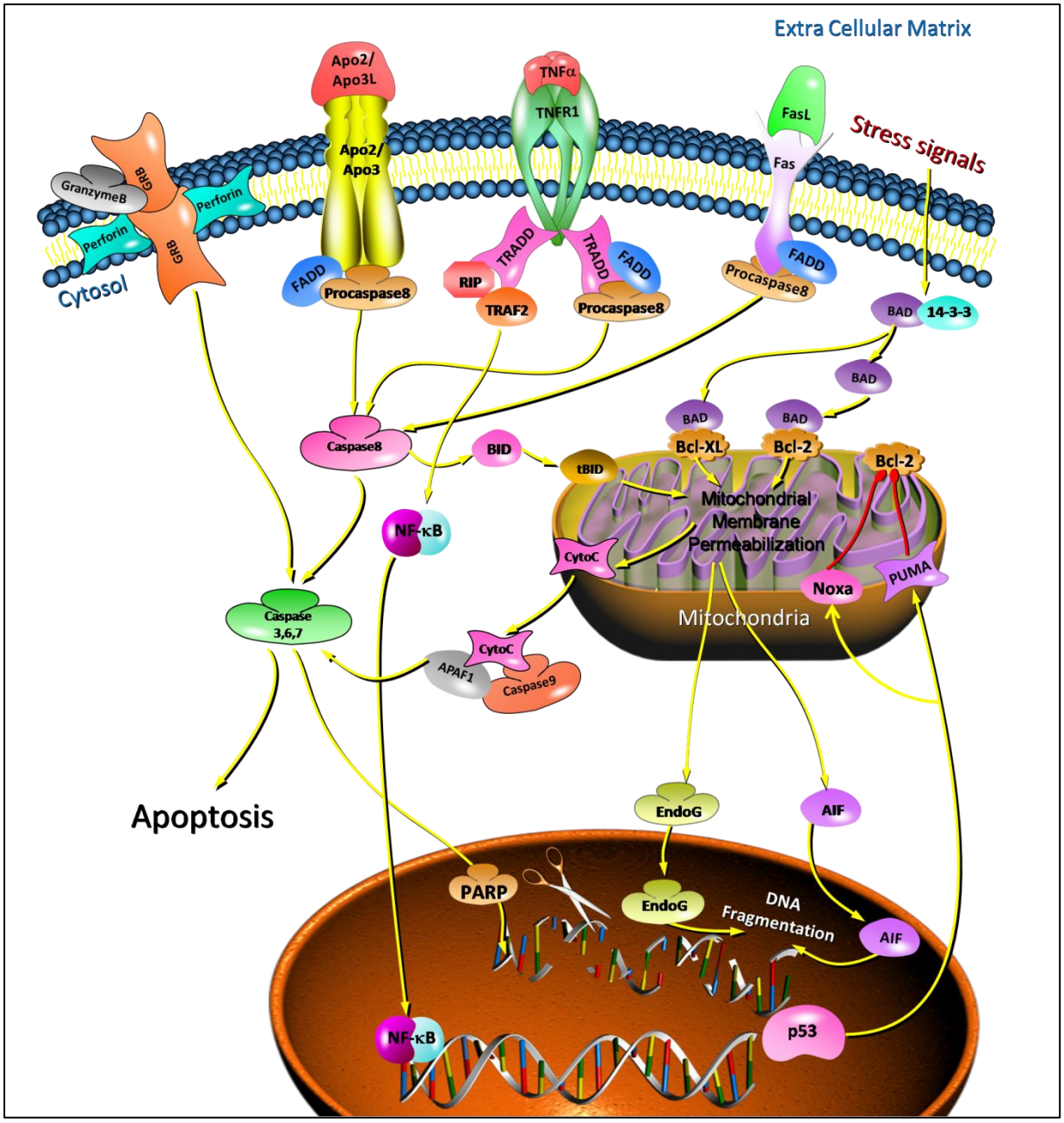

Figure 1.8: Schematic biochemical representation of apoptotic events. The main pathways of apoptosis are extrinsic, intrinsic and perforin/granzyme pathways. Extrinsic pathway involves death receptor (TNF, Fas and Apo 2) ligand binding and the activation of caspase 8. The intrinsic pathway involves the mitochondria and the Bcl-2 family protein. In the absence of apoptotic signals, 14-3-3 protein is coupled with phosphorylated Bad protein. Apoptotic stimuli assisted dephosphorylation of Bad and subsequent translocation of this protein to mitochondria forms complex with either Bcl-XL or Bcl-2, neutralizing their anti-apoptotic effect and facilitate the release of cytochrome *c*.

More than 30 proteins are classified within the Bcl-2 superfamily and they can be categorized into three subgroups: Bcl-2-like survival factors, Bax-like death factors and BH3-only death factors. Bcl-2 family proteins are essential for regulation of apoptosis and autophagy (174). The intrinsic apoptotic pathway is primarily regulated by Bcl-2 superfamily of proteins (2). Bcl-2-like survival factors Bcl-2, Bcl-XL, Bcl-w and Mcl-1 promote cell survival, whereas Bax and Bak provoke mitochondria-mediated intrinsic cell death. The activation of apoptosis depends on balances and interactions between BH3-only, Bax-like proteins and Bcl-2-like survival factors (175). The pro- and anti-apoptotic subgroups of the superfamily dynamically interact with each other through their conserved Bcl-2 homology (BH) domains. The BH-3 only subgroup (with only BH3 domain) is able to collect information and pass it on to multi-domain (BH) members (Bax-like and Bcl-2 like) of the family which will carry out downstream effect (2). Bcl-2 is a product of proto-oncogene *bcl-2* and functions as a prominent apoptosis suppressor (176). In response to a variety of extracellular stimuli, Bcl-2 releases pro-apoptotic factors such as Bax, thereby diminishing its inhibitory action and enables Bax oligomerazation on the mitochondrial membrane (2). Bcl-2/Bax heterodimerization is not sufficient for full Bcl-2 anti-apoptotic function. Phosphorylation of Bcl-2 serine 70 (Ser^{70}) is a crucial requirement which completes its death suppressor signalling activity (176).

In addition to the role that Bcl-2 family proteins play in the mitochondria-mediated apoptosis, Bcl-2 proteins also have been shown to localize to other cellular compartments such as endoplasmic reticulum (ER) to mediated calcium signals. ER is the main storage organelle of calcium, and Bcl-2 family proteins regulate the flux of calcium from ER by interaction with inositol 1,4,5-trisphosphate receptors (IP3Rs) opening (177). Cytosolic calcium entry and exit are controlled by store-operated calcium channels (SOC) and plasma membrane Ca^{2+} ATPase (PMCA) channels on the plasma membrane (177). Calcium is transported into the ER lumen by sarcoplasmic/endoplasmic reticulum Ca^{2+} ATPases (SERCA) and release through type I and III IP3Rs. Type 1 IP3Rs and type III IP3Rs are both located on ER membrane for calcium efflux facing either the cytosol or mitochondria (177). The type III IP3Rs reside at the connection point between the ER and the mitochondria namely, mitochondria-associated ER membrane (MAM) (178). Mitochondrial calcium concentration plays an important role in both healthy and apoptotic cells. Mitochondrial calcium can drive pyruvate into the tricarboxylic acid cycle (TAC) cycle

to facilitate ATP production in normal cells and it can also control the opening of permeability transition pore in apoptotic cells.

The mechanism of how Bcl-2 family proteins control the Ca^{2+} signalling is not fully understood. The evidence suggests the Bcl-2 family protein coordinate Ca^{2+} signalling in a multi-organelle manner, the exact mechanism explained by many studies, however, are contradicting. Preservation of ER luminal Ca^{2+} was observed with Bcl-2 over expression and this increase in ER calcium uptake was attributed to increased SERCA activity (179). In contrast, some research findings showed that Bcl-2 over expression decreases SERCA activity, thereby reducing ER luminal Ca^{2+} level (180). Pro-apoptotic ER-specific Bax/Bak may function to increase the ER luminal Ca^{2+} level, and BH3-only Bcl-2 proteins such as Bik and Nix have been observed to decrease ER Ca^{2+} (177).

As previously mentioned, the first step of oxidative phosphorylation requires the intake of pyruvate into the mitochondria via the enzyme complex pyruvate dehydrogenase. Subsequently numerous enzymes are involved in the production of ATP through the TAC and electron transport chain system. Many enzymes involved in this bioenergetic process including pyruvate dehydrogenase, isocitrate dehydrogenase, α-ketoglutarate dehydrogenase and ATP synthase depend on the cofactor Ca^{2+} (178). Furthermore, a recent study by Giorgio *et al.* (2013) suggests that the permeability transition pore (PTP) formation is composed of ATP synthase, cyclophilin D and Ca^{2+} (181). Thus, the concentration of calcium plays an important role in regulating PTP opening. Prolonged increase in mitochondrial Ca^{2+} concentration can force high-conductive PTP opening which is directly linked to apoptosis. The cytochrome *c* leaked from mitochondrial apoptosis-induced channel (MAC) formed on the outer mitochondria membrane (OMM) during early apoptosis works in conjunction with PTP to initiate apoptotic process (177).

Molecular markers for apoptosis

During early apoptotic process the cell membrane composition changes and leads to exposure of phosphatidylserine (PS) from inner layer of the plasma membrane to the outer layer (182). The PS flip is thought to be important for macrophage recognition of cells undergoing apoptosis, thus allowing the cells to be rapidly phagocytosed (125). Once exposed to the extracellular environment, binding sites on PS become available for Annexin V, therefore PS externalization may be used as marker for apoptosis (183,184). Annexin V, which belong to annexin family proteins that bind to PS in calcium-dependent manner, has been widely used to detect PS expression in apoptotic cells by flow cytometry and microscopy (125). Annexin V is a 35kDa phospholipid-binding protein which has a high affinity for PS in the presence of physiological levels of calcium ions (1.2 mM) (182,185).

Cytochrome *c* leakage from outer mitochondria membrane during early apoptosis may also be used to confirm the initiation of the apoptotic process (177). The release of cytochrome *c* is an important key event, which represents an irreversible hallmark within the apoptotic pathway (172). Furthermore, caspase cleaved substrates such as poly ADP ribose polymerase (PARP) may be detected and illustrate the occurrence of apoptotic events (125). During apoptosis, the mitochondrial membrane potential or electrochemical gradient across the OMM collapses, which results in mitochondrial membrane potential depolarization, which can be detected by using a cation dye (186).

The Bcl-2 family proteins such as Bcl-2, Bax and Bid can also be detected either quantitatively or qualitatively (125,187). As previous mentioned in ‘Intrinsic apoptotic pathway: caspase-dependent’ section, Bcl-2 protein promotes cell survival, whereas Bax provokes the mitochondria-mediate intrinsic cell death (175). Pro-apoptotic Bcl-2 family members Bid and Bax can be cleaved and activated by granzyme B, causing mitochondrial membrane permeabilization and caspase-dependent apoptosis (157).

1.3.2 Autophagy

The degradation of cytosolic components at the lysosome via proteolytic processes is defined as macroautophagy, micro-autophagy, and chaperone-mediated autophagy (188). Autophagy represents another important type of cellular physiological response to stresses such as nutrient deficiency (189). The major route for the turnover of cytoplasmic organelles and proteins is the macroautophagy system and is commonly referred to as autophagy (188). Autophagy processes display a housekeeping role in protein degradation, organelle turnover, such as removing damaged mitochondria, endoplasmic reticulum and peroxisomes, as well as the removal of intracellular pathogens (188,190). Autophagy related genes (Atg) are found to be conserved across phylogeny, emphasizing the vital importance of the autophagic process in responses to starvation (188). Nutrient starvation induced autophagy is achieved through inhibition of mammalian target of rapamycin (mTOR), a key regulatory protein that coordinates the balance between growth and autophagy in response to cellular and environmental stress (191). All autophagic processes, macro-, micro- and chaperone-mediated autophagy, promote proteolytic degradation of cytosolic components at the lysosome (188).

Autophagy is a complex process which is orchestrated by numerous enzymes from many signalling pathways that begins with the formation of a phagophore, an isolated piece of lipid bilayer (188). The location of the isolated membrane formation is controversial, but it is believed the initiation of phagophore formation is primarily from the ER (188). In the yeast model, starvation stimulates the inhibition of TOR, causes dephosphorylation of Atg 13, and promotes the formation of a multi-subunit Atg complex (Atg 1, Atg13, Atg17, Atg29 and Atg31) to “switch on” autophagy (191) (Figure 1.9). It is noteworthy to mention an important element in the nutrient-signalling pathway upstream of mTOR complex 1 (mTORC1), the class III PI3K protein or also known as vesicular protein sorting 34 (Vps34).

PI3K/Vsp34 interacts with Beclin1, a tumor suppressor, for the generation of phosphatidyl inositol triphosphate (PI3P), which is essential for recruitment of Atg proteins and phagophore elongation (188,191). Bcl-2, an anti-apoptotic protein as previously mentioned, has the ability to bind with Beclin1 and causes the dissociation of Beclin1 from the Vsp34 complex and ultimately inhibiting autophagy (192). The dual role of Bcl-2 protein showcased the crosstalk between autophagy and apoptosis;

however, this crosstalk is not restricted on this level and extends beyond the regulation of Beclin1 and Bcl-2 (188) (Figure 1.9).

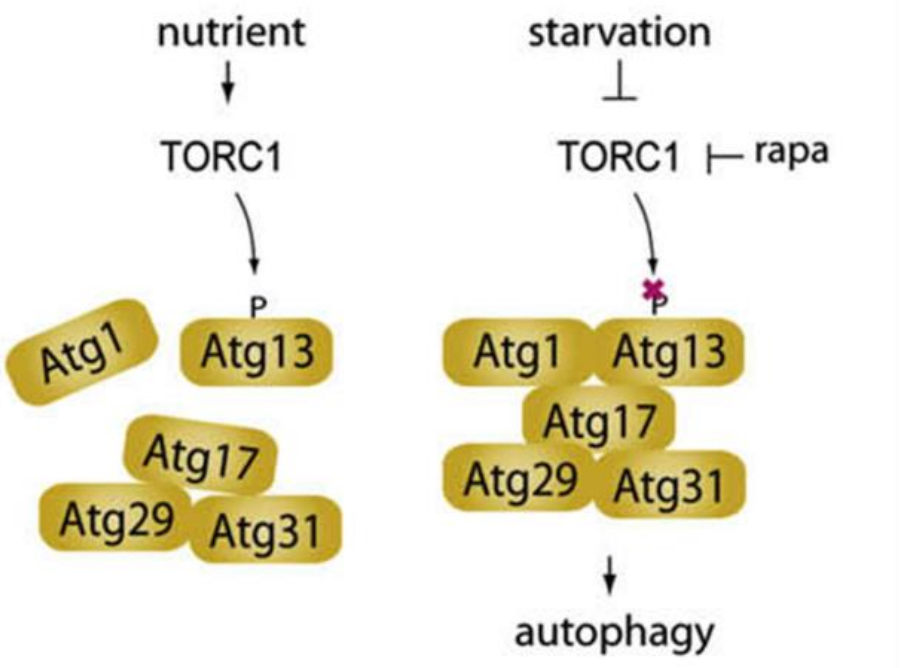

Figure 1.9: Yeast model for the mechanism by which target of rapamycin regulates the Atg1 complex. Starvation stimulates the inhibition of TOR, causes dephosphorylation of Atg 13, therefore promote the formation of multi-subunit Atg complex (Atg 1, Atg13, Atg17, Atg29 and Atg31) to "switch on" autophagy (191). (Figure adapted from Jung *et al.* (2010))

Morphological and biochemical features of autophagy

The morphological characteristics of cells going through autophagy are distinctively different from previously described apoptotic cells (141). One of the most prominent features of autophagy is the appearance of autophagic vacuoles when nuclear and cell shape still look normal (141). Organelles such as mitochondria, endoplasmic reticulum and the Golgi apparatus are often dilated (193). The ribosome free rough endoplasmic reticulum provides the double membrane for initiation of the 'self-eating' process and the piece of membrane is named phagophore (194). This membrane elongates and wraps around and engulfs a portion of cytoplasm forming the unique double membrane bound autophagosome. The maturation of autophagosomes involve acidification by fusion with late endosomes and receiving lysosomal constituents from it. After fusion with endosomes, autophagosomes lose their double

membrane morphology due to hydrolases' degradation of the inner membrane. At this stages the autophagosomes become amphisomes. Autophagosomes can also fuse with lysosomes, forming autolysosomes (194) (Figure 1.10).

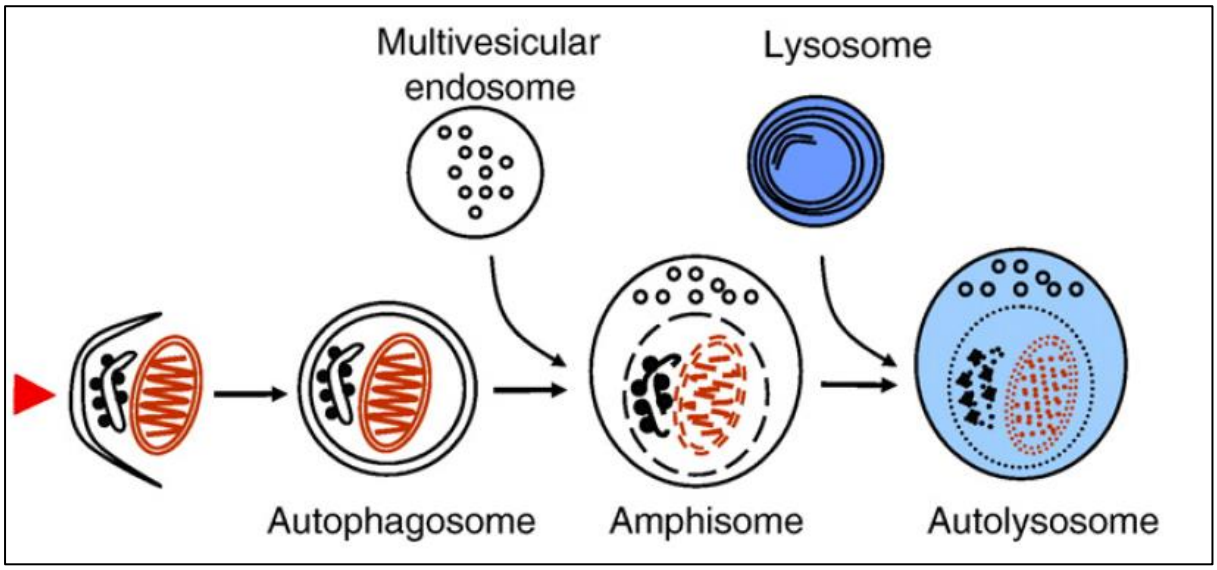

Figure 1.10: Schematic presentation of autophagosome formation and maturation. Phagophore (red arrow) wraps around and engulfs a portion of cytoplasm forming the unique double membrane bound autophagosome. After fusion with endosome, autophagosome loses its double membrane morphology owning to hydrolases degradation of inner membrane and becomes amphisome. Autophagosome can also fuse with lysosome forming autolysosome (194). (Adapted from Eskelinen and Saftig (2009))

Mammalian target of rapamycin signalling pathway

Cells avoid energy imbalance and death by relying on a complex set of programs to cope with environmental stress and nutrient starvation. Various biochemical pathways are switched on to suppress catabolic pathways or biosynthesis and the target of rapamycin is at the center of this network (Figure 1.11). The mTOR belongs to the PI3K-related protein kinases (PIKK) family and it is the catalytic subunit of two distinct complexes: the mTOR complex 1 (mTORC1) and mTOR complex 2 (mTORC2) (195). mTORC1 and mTORC2 are distinguished by their unique scaffolding protein namely, regulatory-associated protein of mTOR (RAPTOR) (196) and rapamycin-insensitive companion of mTOR (RICTOR) (197). Extracellular signalling factors such as growth factors, cytokines and hormones (e.g. insulin)

signal to mTORC1 via Akt/protein kinase B (PKB) which inactivates tuberous sclerosis complex (TSC) tumor suppressors TSC1 and TSC2 to prevent inhibition of mTORC1 which in turn inhibits autophagy (198) (Figure 1.11).

The mTOR signal integration occurs at the level of the TSC1-TSC2 complex. For example, growth factors can activate ERK1/2 signalling pathway through Ras-Raf-MEK pathway (ERK activation is described in section cell cycle signalling and Figure 1.4) and inhibits TSC2 by phosphorylation (195,199). Alternatively, TSC2 can be inhibited by the PI3K-mTORC2-AKT pathway (191,195) (Figure 1.11). PI3K is a group of enzymes that have been classified into class I, II and III PI3Ks. The primary function of the class I PI3K is to phosphorylate phosphatidylinositol 3,4-bisphosphate (PIP2) to form phosphatidylinositol 3,4,5-trisphosphate (PIP3) which in turn activates the mTORC2-AKT pathway (200), meanwhile the class III PI3K functions as a generator of PI3P which controls autophagosome formation (201). Membrane anchored PIP3 binds to the pleckstrin homology (PH) domain of several proteins including AKT/PDK and 3-phosphoinositide-dependent protein kinase 1 (PDK1) facilitates their movement and recruitment towards the plasma membrane (202,203). At the membrane, PDK1 phosphorylates AKT/PDK at Thr^{308} within the AKT kinase domain (204). Phosphatidylinositol-3,4,5-trisphosphate 3-phosphatase and dual-specificity protein phosphatase (PTEN) is a tumor suppressor phosphatase which converts PIP3 back to PIP2, thus inhibiting AKT/PDK signalling (203) (Figure 1.11). Moreover, the activation of AKT/PDK also requires the phosphorylation at its Ser^{473} position within the C-terminal regulatory domain by mTORC2 complex (204). Furthermore, phosphorylation at the AKT Thr^{450} turn motif necessitates the complete activation of this enzyme and it may be facilitated by both mTORC2 and JNK (205). The phosphorylation of TSC2 by ERK1/2 and AKT inhibits its GTPase activating activity towards Ras homologue enriched in brain (Rheb) (195).

Quite the opposite, phosphorylation of TSC-2 can also activate this enzyme instead of suppressing it and the activation can be achieved by upstream regulators AMP-activated protein kinase (AMPK) and hypoxia-ROS signalling (195) (Figure 1.11). AMPK has the ability to sense AMP to ATP ratio by allosteric regulation. When glucose metabolism is decreased, so does the production of ATP (via mitochondria oxidative phosphorylation) and causes an increased AMP:ATP ratio. AMPK is active under nutrient-poor conditions and inactive under nutrient-rich conditions. Subsequently, conditions of low intracellular ATP energy status activate AMPK which

in turn facilitate phosphorylation of TSC1/2, stimulating its GTPase activity toward Rheb/mTORC1 (206). Gwinn *et al.* (2008) showed an additional AMPK phosphorylation substrate besides TSC1/2 and it is the mTORC1 binding partner RAPTOR (207). This AMPK-mediated RAPTOR phosphorylation induces binding of 14-3-3 and thereby suppresses mTORC1 activity (207). Furthermore, impaired mitochondrial respiration caused by hypoxia may also lead to deprived ATP levels and activation of AMPK. This activation is mediated by DNA-damage-inducible transcript 4 (DDIT4, also known as REDD1) (208) (Figure 1.11).

Increasing evidence suggest that a second level of mTOR signalling integration occurs at the lysosome membrane. The lysosome membrane hosts a few important molecular enzymes for mTORC1 activation including the Rag GTPases and the trimeric regulatory protein complex. The trimeric complex, namely Regulator, which consists of p18, p14 and MAPK scaffold protein 1 (MP1) interact with Rag GTPase for the recruitment of mTORC1 to the lysosomal surface in response to amino acids (195). In turn, mTORC1 lysosomal relocation enables it to interact with activated Rheb (GTP-bound). Thus, amino acids may direct growth factor-derived signals by bringing mTORC1 to the location where it can bind to GTP-Rheb (209) (Figure 1.11). Autophagic degradation is promoted by fusion of autophagosome with lysosome, therefore the physical presence of mTORC1 at the lysosome serves as 'on site' surveillance barrier to inhibit macroautophagic process from occurring (210).

Alexander *et al.* reported in 2010 that TSC functions downstream of ataxia telangiectasia mutated (ATM) signal in order to repress mTORC1 activity in response to ROS and regulate autophagy (211,212). A recent publication by Zhang *et al.* (2013) described intimate relationship between the TSC signalling and the peroxisome (213). The authors described the TSC1 and TSC2 localized to peroxisomes and were bound by peroxisomal biogenesis factors 19 (PEX19) and 5 (PEX5), respectively (213). The peroxisome-localized TSC resides on the exterior of the peroxisomal membranes where it suppresses mTORC1 activity and induces autophagy by targeting Rheb (213). TSC2 contained an ARL motif $_{1739}$'KWI**ARL**RHIKR'$_{1749}$ and mutations within this sequence are pathogenic (213,214), where the mutant TSC2 loses its ability to suppress mTORC1.

Following the full activation of mTORC1, protein synthesis is activated by phosphorylation downstream targets S6 Kinase 1 (S6K1) and eIF-4E binding protein

1 (4E-BP1) (215). mTORC1 can also increase lipid accumulation by increasing peroxisome proliferator-activated receptor (PPAR)-γ activity, as well as PPAR-γ transcription factor sterol regulatory element binding protein (SREBP) gene expression (216). Furthermore, formation of autophagosome is inhibited by mTORC1-mediated phosphorylation of ATG13 and UNC-51-like kinase 1 (ULK1) (191,217) (Figure 1.11).

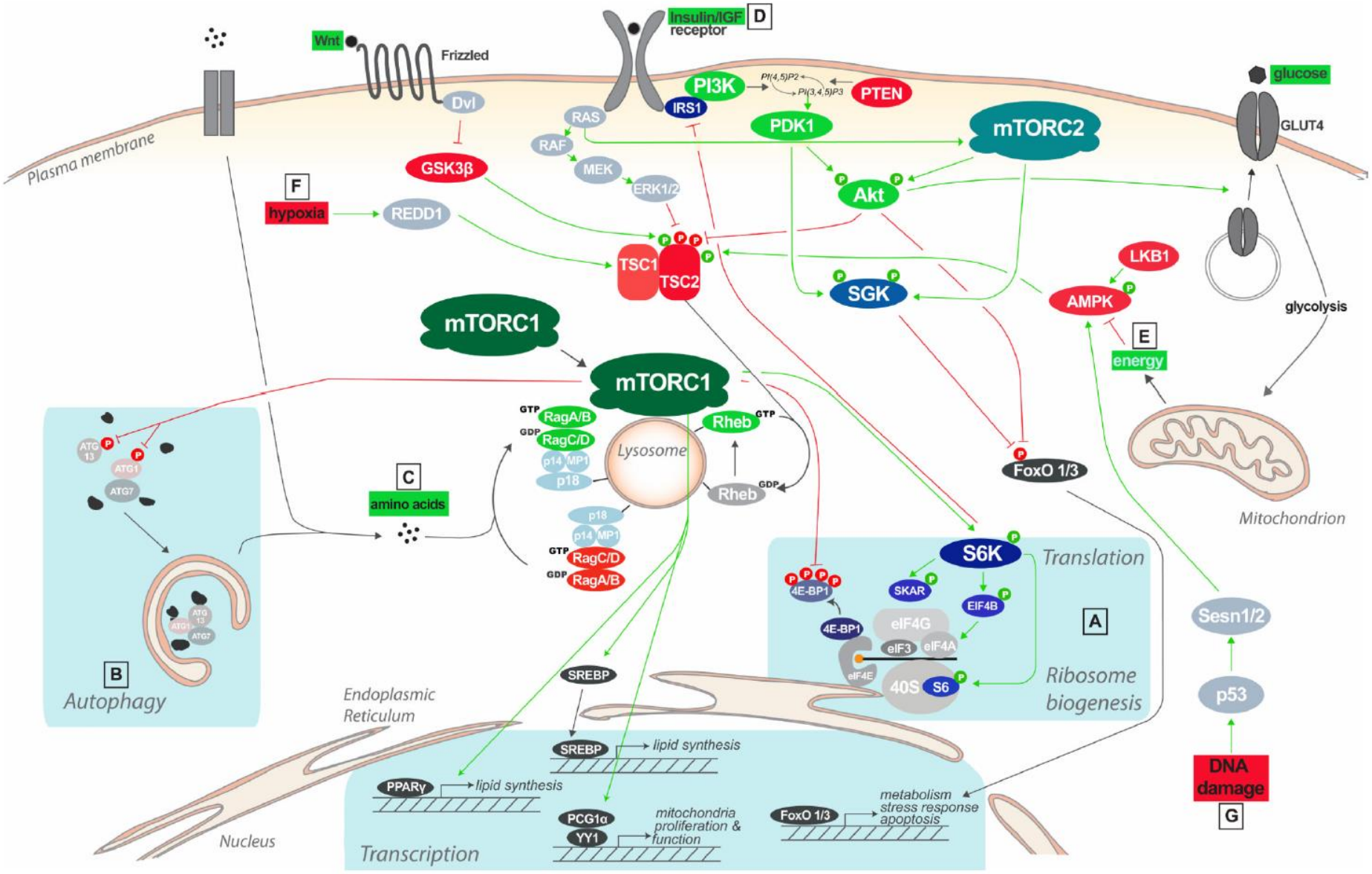
Wnt
Frizzled
Dvl
Insulin/IGF receptor
D
PI3K
IRS1
PTEN
PI(4,5)P2
PI(3,4,5)P3
RAS
RAF
MEK
ERK1/2
PDK1
mTORC2
glucose
GLUT4
Plasma membrane
GSK3β
F
hypoxia
REDD1
Akt
TSC1
TSC2
SGK
LKB1
AMPK
glycolysis
E
energy
mTORC1
mTORC1
GTP
RagA/B
GDP
RagC/D
p14 MP1
p18
Lysosome
Rheb
GTP
GDP
Rheb
FoxO 1/3
Mitochondrion
C
amino acids
ATG 13
ATG1
ATG7
B
Autophagy
S6K
Translation
4E-BP1
SKAR
EIF4B
eIF4G
eIF3
eIF4A
eIF4E
40S
S6
A
Ribosome biogenesis
Sesn1/2
p53
DNA damage
G
SREBP
Endoplasmic Reticulum
SREBP
lipid synthesis
PPARγ
lipid synthesis
PCG1α
YY1
mitochondria proliferation & function
FoxO 1/3
metabolism stress response apoptosis
Transcription
Nucleus

Figure 1.11: Mammalian target of rapamycin signalling pathway. Growth factor receptors activate AKT and ERK via PI3K-mTORC2 and MAPK pathways respectively. ERK and AKT inhibit GTPase activating protein TSC2 activity by phosphorylation; in turn, facilitate Rheb exchange bonded GDP to GTP. Amino acids stimulate the Rag GTPase Regulator recruitment. Docking mTORC1 to the lysosome enables it to interact with the Rheb-GTP. Following the full activation of mTORC1, protein synthesis is activated by phosphorylation of downstream targets S6K1 and 4E-BP1. Formation of autophagosome is inhibited by mTORC1-mediated phosphorylation of ATG13 and ULK1. Conditions of low intracellular ATP energy status activate AMPK which in turn facilitates phosphorylation of TSC1/2, stimulating its GTPase activity toward Rheb/mTORC1 (195). (Adapted from Zoncu *et al.* (2011))

Macroautophagy machinery

In yeast, phagophore membrane formation is originated at a cytosolic structure known as the pre-autophagosomal structure (PAS) (194). However, no data suggest that PAS occurs in mammals. The initiation of yeast autophagy is through Atg-mediated autophagic pathways where TOR regulates the Atg1 complex (Figure 1.9). Mammalian phagophore formation is originated at the ER (188,218). Similar to the yeast model, starvation inhibits mTORC1 and causes dephosphorylation of ULK and Atg13 (191). There are three related serine/threonine kinases in the mammalian system that play a similar role as the yeast Atg1, namely UNC-51-like kinase -1, -2, and -3 (ULK1, ULK2, UKL3) (191). Focal adhesion kinase family interacting protein (FIP200) scaffold protein, an ortholog of yeast Atg17, hold the ULK1/2 together with the mammalian Atg13 for autophagy activation (219) (Figure 1.12). Class III PI3K protein complex containing Vps34 interacts with Beclin1 (a mammalian homolog of yeast Atg6), p150 (a mammalian homolog of yeast Vps15), and ultraviolet irradiation resistance-associated gene (UVRAG) (UVRAG-Beclin1-Vps34-p150) or Atg14 (Atg14-Beclin1-Vps34-p150) for phagophore elongation and recruitment of Atg proteins (220) (Figure 1.12). Endosome/lysosome associated protein Rubicon may negatively regulate the maturation of autophagosome by interacting with the UVRAG-Beclin1-Vps34-p150 complex (221). The exact mechanism of how ULK1 regulates Vps34 is unclear. Lines of evidence suggest activated ULK1 phosphorylates Beclin1 on Ser^{14}, thereby enhancing the activity of the Atg14-containing Vps34 complexes (222).

Elongation of the phagophore depend on two ubiquitin-like systems namely the Atg5-Atg12 conjugation and microtubule-associated protein light chain 3 (LC3) processing (188). The conjugation of Atg12 to Atg5 requires two ubiquitin activating enzymes Atg7 and Atg10 (Figure 1.12). The activation of Atg12 is made possible by E1-like Atg7 enzyme (ATP-dependent). Subsequently, activated Atg12 binds to an E2-like ubiquitin carrier protein which facilitates the linage of Atg12 to Atg5. Conjugated Atg12–Atg5 then interacts with Atg16L in a non-covalent fashion to form a large complex: Atg12-Atg5-Atg16L (188,223). This newly formed complex induces phagophore elongation through recruitment of LC3.

LC3, which is encoded by the mammalian homology Atg8 gene, is universally expressed in most cell types and exist in the cytosol in its inactive form. Cellular

stress or starvation induces the proteolytic cleavage of full length LC3 to LC3-I by cysteine protease Atg4(188). Subsequently, LC3-I is conjugated to phosphatidylethanolamine (PE) also in an ubiquitin-like reaction that requires Atg7 and Atg3 for the formation of LC3-II. Furthermore, the bond between LC3-I and PE is also dependent Atg12-Atg5-Atg16L (223). The LC3-II appears both on the inner and outer surfaces of the autophagosome and can thus be used as specific markers for autophagy (224). Fusion of an autophagosome with lysosomes is necessary for the complete degradation of sequestered materials and several proteins including lysosomal associated membrane protein type 2 (LAMP-2) facilitate the fusion (194) (Figure 1.12).

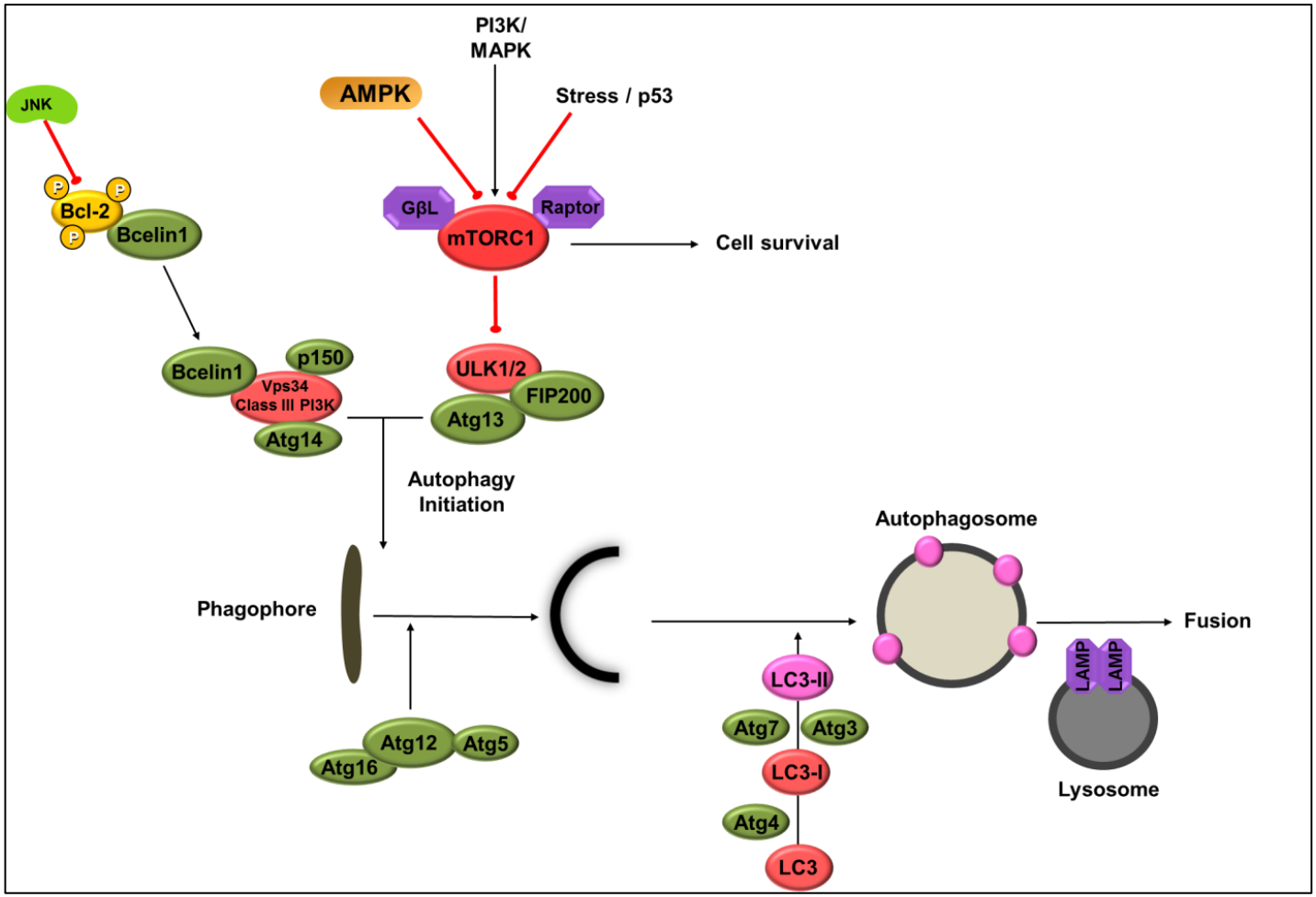

Figure 1.12: Biochemical features of autophagosome formation. JNK promotes autophagy by phosphorylating Bcl-2, thereby releasing Beclin1. The interactions of Beclin1 with Class III PI3K Vps34 at the ER promote formation of phagophore. Autophagy initiation also depends on mTOR signalling as it lies upstream of the autophagic pathway and suppresses it. Stress or starvation inhibits the mTORC1 activity, and leads to dephosphorylation of ULK and Atg13. Elongation of phagophore and autophagosome formation requires the activities of Atg12-Atg5-Atg16L complex and LC3-II respectively. Subsequent fusion with lysosome is directed by lysosomal membrane associated protein LAMP.

Microautophagy

Microautophagy is a non-selective lysosomal degradative process (in mammalian system) where the lysosome itself engulfs small components of the cytoplasm by inward invagination of its own membrane (Figure 1.13) (225). In the yeast model, both non-selective and selective microautophagy exist (226). Several studies conducted with mammalian cells have demonstrated the presence of non-selective microautophagic process within the mammalian system. De Waal *et al.* (1986) showed changes in the lysosomal structure upon nutrient starvation as lysosomes engulfed small portions of cytoplasm in rat hepatocytes (227). Sakai *et al.* (1989) demonstrated another type of microautophagy which exhibits a lysosomal wrapping mechanism (LWM) morphology (228).

Recent research suggest micro-, macro- and chaperon-mediated autophagic processes are coordinated to maintain membrane homeostasis (225). Lysosome size is increased during fusion with autophagosomes, but microautophagic invagination and budding control are able to reduce the size of the fused autophagosomes (229). Nutritional status is a factor that determines the frequency of invagination of lysosomes. Starvation induces the initiation of microautophagic invagination through dynamin-related GTPase Vps1p in *Saccharomyces cerevisiae* (225,230). The engulfed membrane elongates to a characteristic tubular shape termed an ‘‘autophagic tube’’ and Atg7-dependent ubiquitin-like conjugation (Ublc) systems participate in starvation-induced, non-selective microautophagy (225,231).

Following membrane invagination and autophagic tubes formation, the lipid-rich and low density integral protein portion at the tip of the autophagic tube facilitates vesicle formation (225,231). Subsequently, the newly formed vesicle expands and pinches off into the lumen from the tube. Rapamycin inhibits vesicle scission, suggesting that both microautophagy and macroautophagy processes are influenced by the TOR kinase and Atg1 signalling (225,232). Starvation of a particular amino acid glutamine leads to TOR activation and microautophagy (225).

Selective microautophagy is frequently induced in yeasts where specific organelles are sequestered with arm-like protrusions by one of these processes: micropexophagy (degradation of peroxisomes), micromitophagy or piecemeal microautophagy of the nucleus (225). Non-selective microautophagy is usually

observed in mammalian cells where non-exclusive materials would be digested (225). The exact mechanism of action for microautophagic process in mammalian systems remains to be elucidated and is an active area of research at present.

Chaperone-mediated autophagy

The third type of autophagy, chaperone-mediated autophagy (CMA), is an ubiquitin-proteasome system only involved in the digestion of soluble proteins, not organelles. In 1981, CMA was discovered by microinjecting protein into IMR-90 human diploid fibroblasts (233). Unlike macroautophagy whereby cytoplasmic organelles are degraded, CMA is responsible for breaking a very select subset of proteins (234). Also, when compared to macro- and microautophagy that are switched on immediate in response to nutrient starvation, CMA only increases after ten hours post starvation (235). CMA is activated under nutrient-starved conditions in order to break down proteins for energy use (234). Conditions of stress that leads to increased protein misfolding (e.g. increased ROS production) also lead to increased CMA activity (234).

CMA targets short lived or abnormally folded single proteins without the involvement of membrane re-organization (223). CMA targets proteins with a specific motif consensus pentapeptide sequence KFERQ (or KFERQ-like) and VDKFQ (234). This sequence substrate is recognized in the cytosol by a chaperone protein, heat shock cognate protein of 70 kDa (hsc70), and works together with other co-chaperone proteins to unfold the targeted protein and translocate it to the lysosomal membrane (234). Other co-chaperone proteins include the heat shock protein of 90 kDa (hsp90), hsc70-interacting protein (hip) and the hsc70-hsp90 organizing protein (hop) (236). Hsc70 facilitates recognition, as well as unfolding of proteins that are targeted for degradation (Figure 1.13) (234). After protein unfolding and translocation to lysosomes, the protein is recognized by the LAMP-2A receptor and pulled into the lysosomal lumen with the help of lys-hsc70 where the protein is then digested (223).

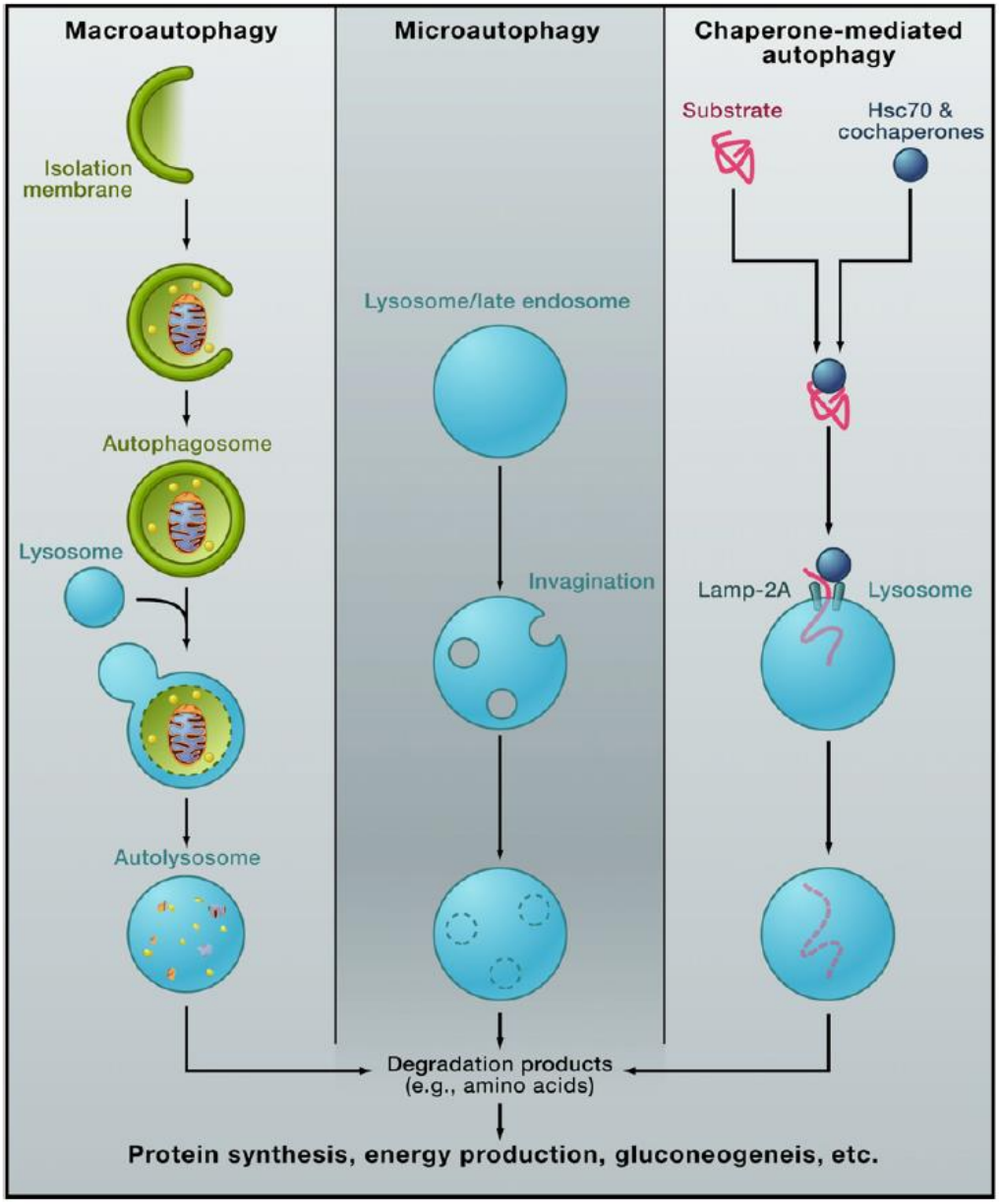

Figure 1.13: Macro-, micro- and chaperone-mediated autophagy. Macroautophagy involves formation of autophagosome and subsequent fusion with lysosome. Microautophagy is a process which involves lysosomal self-invagination. Chaperone-mediated autophagy removes misfolded single protein/substrate (Adapted from Mizushima and Komatsu (2011) (223)).

1.3.3 Apoptosis and autophagy crosstalk

Apoptosis and autophagy are both degradation pathways essential for cellular homeostasis (237). Even though apoptotic pathways are biochemically distinct from the autophagic pathway, they are interconnected on many levels. Sometime, these two processes seem independent from each other (238), often autophagy occurs upstream of apoptosis (238) or inhibits apoptosis (239). During starvation, autophagy functions as a pro-survival mechanism to support cells with essential nutrients. Excessive autophagy, however, may lead to autophagic cell death (240). Previously mentioned pro-apoptotic signals, such as TNF (241), TRAIL (242), and FADD (243), also have the ability to induce autophagy.

The roles of the anti-apoptotic protein Bcl-2 in apoptosis, as well as its anti-autophagy properties have been discussed in previous sections. Bcl-2 binds to Bax/Bak in the absence of apoptotic signalling. The presence of apoptotic stimuli activate BH3-only proteins and facilitate their binding to Bcl-2 protein and free the pro-apoptotic proteins Bax/Bak. Downstream effects of Bax/Bak dimerization are the release of cytochrome *c* via the MTPs and subsequent activation of caspases (237). Also, Bcl-2 exhibits anti-autophagic property by binding to essential autophagic effector Beclin 1 via its BH3 domain in the ER (192).

The first node of crosstalk between apoptosis and autophagy is tied between the interactions of Bcl-2 and Beclin 1 (237). Silencing of Bcl-2 expression by small interfering RNA (RNAi) elevated levels of autophagic cell death in breast carcinoma (MCF-7) cells (244). Moreover, Sun *et al.* (2010) showed Beclin 1 overexpression up-regulated chemosensitivity of cervix cancer cells to anticancer compounds by increased apoptotic cell death (245). These experiments demonstrated the importance of intracellular Bcl-2 and Beclin 1 protein concentrations and their effect on both autophagy and apoptosis. Reduced Bcl-2 expression may result in elevated levels of Beclin 1-mediated autophagy; Beclin 1 overexpression may promote apoptosis by releasing Bak/Bax (237). Furthermore, a compound such as ABT-737 which inhibits Bcl-2 activity has ability to up-regulate autophagy and apoptosis (237). ABT-737 is a pharmacological BH3 only analogue which competes with Beclin 1 binding to proteins such as Bcl-2 and Bcl-XL (246,247).

Two papers authored by Wei *et al.* from the Levine lab revealed an interesting hypothetical regulatory model of JNK-mediated Bcl-2 phosphorylation links to autophagy and apoptosis (248,249). According to their model, starvation induces phosphorylation of Bcl-2 at residues Thr^{69}, Ser^{70} and Ser^{87} of the non-structural loop at the early onset of autophagic signalling, causing the dissociation of Bcl-2 from Beclin 1 (249). This short-lived transit signalling pathway mediated by JNK1 promotes autophagy in an attempt to protect the cell from apoptosis (248). Prolonged cell stress provides stimuli for sustained activation of JNK1, thus accumulation of multi-site phosphorylated Bcl-2. The pro-apoptotic BH3 only protein such as Bax/Bak which exhibit higher affinity interactions with Bcl-2 can be released for the apoptotic cascade (248) (Figure 1.14). An earlier study conducted by Ventura *et al.* in 2006 also revealed signal transduction by early transient JNK activation promoting normal cell survival, whereas prolonged JNK activation can mediate apoptosis (250,251). JNK-mediated Bcl-2 multi-site phosphorylation of the non-structured loop at residues Thr^{69}, Ser^{70} and Ser^{87} was shown to interfere with its binding to pro-apoptotic as well as pro-autophagic BH3 domain-containing proteins (248,252). A recent study by He *et al.* (2012) showed Bcl-2 multi-site phosphorylation has essential roles in the *in vivo* regulation of stimulus-induced autophagy, as well as glucose metabolism (253).

It is well recognized that excessive ROS act as signals for the activation of stress related JNK and/or p38 pathways through the apoptosis signal-regulating kinase 1 (ASK1)-Thioredoxin (Trx) signalsome (169,254). ASK1 is one type of MAPKKK where it functions as part of the MAPK cascade toolkit for the activation of the JNK/p38 pathway (2,254). Under normal conditions, ASK1 is inhibited by direct binding of its N-terminal region with the reduced form of thioredoxin Trx-$(SH)_2$. When ROS formation is increased, it oxidizes Trx-$(SH)_2$ to Trx-S_2 and this facilitates the release of ASK1 into the cytosol. Tobiume *et al.* (169) showed ASK1 is required for sustained activations of JNK/p38 MAP kinases and apoptosis. Several other types of MAPKKKs such as, mitogen-activated ERK kinase kinase (MEKK) group (MEKK1-4), MLK1-3, TAK1 and TPL2 have been reported to activate the JNK signalling pathway (254). Yujiri *et al.* (1998 and 2000) demonstrated MEKK1 (type of MAPKKK) was required for JNK activation in response to microtubule disruption and cold shock (255,256).

Upstream activation of JNK pathway can also be achieved by TNFα and Fas cell death receptor signalling. Activation of TNFα-JNK pathway requires the recruitment of TNF receptor associated factor 2 (TRAF2) adaptor protein (257). Binding of TRAF2 adaptor protein to either MEKK1 (258) or ASK1 (259) is important for TRAF2-mediate MAPKKK activation. The TNFα cytokine-mediated JNK activation requires assistance of TRAF2 (257) and subsequently activates the MAPKKK ASK1 (169). This cascade activation process cannot be completed without TNF-stimulated production of ROS (250,260). The JNK pathway may also act as apoptotic antagonist by NF-κB and Akt signalling pathways induced by AP-1 activity. This interpretation suggests that cell fate is orchestrated by the interaction between NF-κB, TNF-stimulated ROS production and the type of JNK activation (sustained or transient) (261,262).

JNK1 can be activated by p53 within the nucleus and mediate subsequent Bcl-2 phosphorylation of Bcl-2 at Thr^{56}, Ser^{70}, Thr^{74} and Ser^{87} (237). This JNK-mediated Bcl-2 multi-site phosphorylation allow dissociation of Bcl-2 from Beclin 1, thus promote autophagy (263). In addition, nucleic p53 target and increase the expression of damage-regulated autophagy modulator (DRAM) which is localized in the lysosomal membrane, leading to the induction of autophagy in a DRAM-dependent manner (264). The action of cytoplasmic p53, however, inhibits autophagy through inhibition of AMPK-mTORC1 signalling (265). On the other hand, p53 is a master regulator of apoptosis in response to genome instability, cell cycle arrest, as well as other stress signals (266). Nuclear p53 targets gene expression of several death receptors such as Fas (267) and TRAIL (268), as well as pro-apoptotic proteins p53 up-regulated modulator of apoptosis (PUMA), Noxa, Bax and Bid (237,269). Meanwhile, cytoplasmic p53 facilitates the liberation of pro-apoptotic proteins Bax/Bak by forming complex with Bcl-2/Bcl-XL at the mitochondrial outer membrane (270). Interestingly, not only JNK1 can be activated by p53, but vice versa. JNK was reported to phosphorylate and stabilize p53 by inhibiting ubiquitin-mediated degradation (254,271).

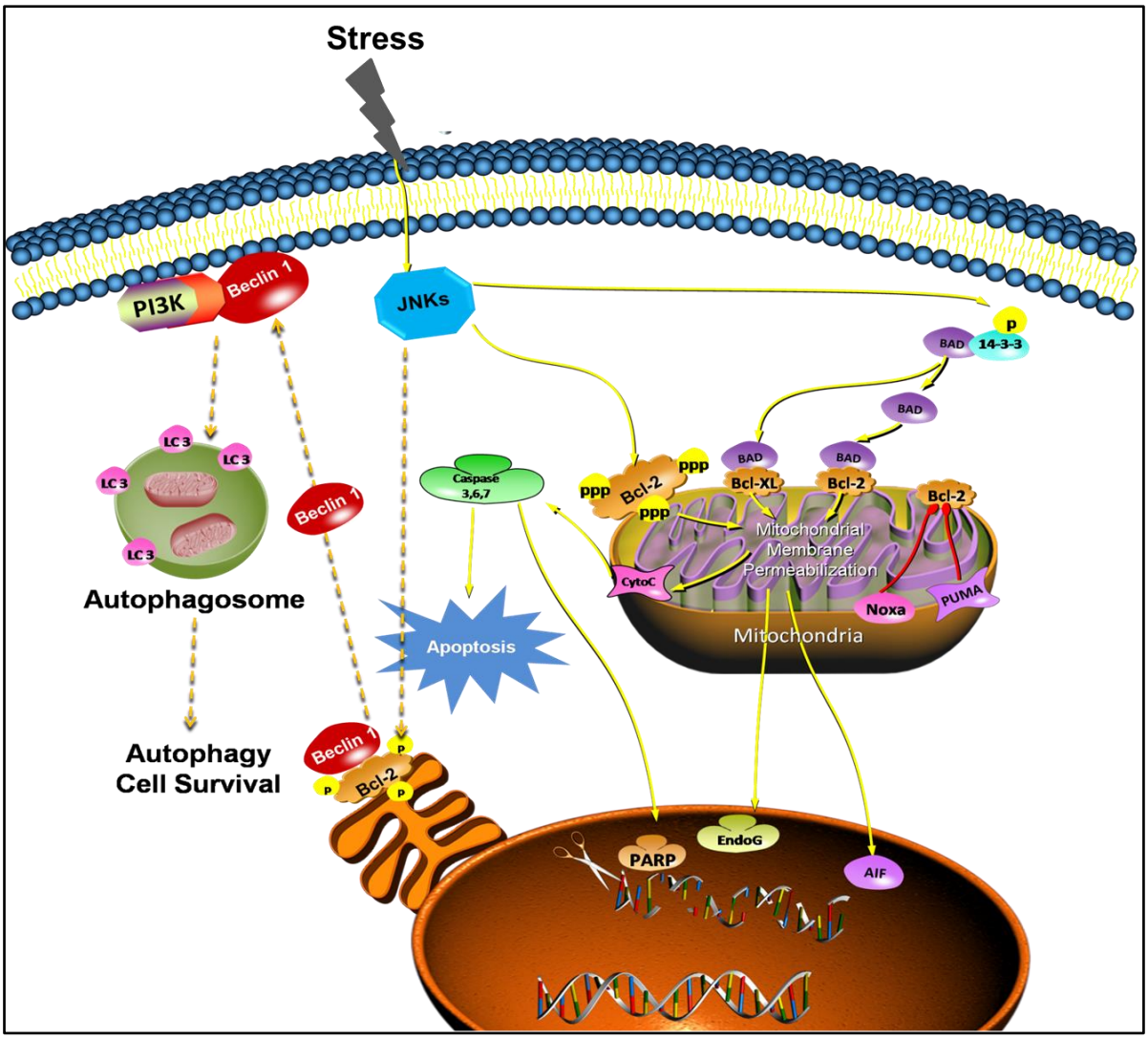

Figure 1.14: *c*-Jun-N-terminal kinase mediated programmed cell death. Initially the cell switches on the autophagic pathway for survival. When cell experience prolonged autophagic process, it switches on the apoptotic pathway for self-destruction; providing protection of integrity of the genome.

1.4 Reactive oxygen species signalling

Reactive oxygen species are defined as oxygen-containing compounds that are more reactive than oxygen itself (272). These include superoxide- ($O_2^{\bullet -}$), hydroxyperoxyl- ($^{\bullet}OH$), carbonate- ($CO_3^{\bullet -}$), peroxyl- ($RO_2^{\bullet -}$) and alkoxyl radicals. Superoxide is unstable and either undergoes a dismutation, resulting in the formation of hydrogen peroxide (H_2O_2) or forms peroxyl radical, a conjugate acid of superoxide, by reacting with hydrogen ions. The dismutation reaction is catalyzed by manganese superoxide dismutase (MnSOD) within the mitochondrial matrix and intracellular superoxide is catalyzed by copper-zinc superoxide dismutase (Cu/Zn-SOD) (273). Superoxide dismutation results in the formation of H_2O_2. Neither superoxide nor H_2O_2 are highly reactive oxygen species (hROS) but are the major sources for the downstream formation of hROS (274). The electron transport chain (ETC) is believed to be one of the major contributors of superoxide generation in mitochondria and mitochondria are considered to be a major source of ROS. It is estimated that between 0.15% - 3% of total oxygen consumption is reduced to superoxide during mitochondrial oxidative phosphorylation system (OXPHOS) (275,276).

Hydrogen peroxide and other ROS and hROS function as important signalling agents in cells (272,277). It does so by regulating redox-reactive cysteine residues on proteins and this in turn results in a change in the structure and function of various proteins that play important roles in cell signalling (278). These include pro-growth, pro-survival and proliferative proteins that signal through the Ras-Raf-ERK1/2, Akt/PKB and NF-κB pathways (279-281) and also stress-activated pathways through the ASK1–Trx signalling complex (282,283).

Cysteine residues of these proteins can undergo oxidation to form reactive sulfenic acid (-SOH). Sulfenic acid can react with nearby cysteine residues to form disulfide bonds (-S-S-) or they can undergo further oxidation to form sulfinic ($-SO_2H$) or sulfonic acid ($-SO_3H$) (278). Hydroxyl radicals are one of the major causes for these oxidant-related cysteine changes (284). H_2O_2 is the major source of hydroxyl radicals generated *in vivo* as a result of the Fenton reaction and contributes to the pro-oxidant balance within cells. The Fenton reaction is when ferrous ions (Fe^{2+}) react with hydrogen peroxide to form the highly reactive hydroxyperoxyl radicals ($H_2O_2 + Fe^{2+} \rightarrow Fe^{3+} + {}^{\bullet}OH + OH^-$) (285). Ferrous iron can be formed when ferric iron (Fe^{3+}) reacts with superoxide (generated in mitochondria for example) to form oxygen (Fe^{3+}

$+O_2^{\bullet-} \rightarrow Fe^{2+} + O_2$) (285). Together these two process combine in a reaction called the Haber-Weiss reaction ($O_2^{\bullet-} + H_2O_2 \rightarrow O_2 + {}^{\bullet}OH + OH^-$) (285).

The disulfide bonds, sulfenic acid and sulfinic acid that are formed due to oxidation by hydroxyl radicals can be enzymatically reversed by glutaredoxins (Grx) or glutathione S-transferases (GST) and non-enzymatically by glutathione (GSH) and Trx (279,286,287). Oxidation of cysteine residues can be prevented by inactivating H_2O_2. Catalase enzymatically promotes the conversion and detoxification of H_2O_2 to water and oxygen (285). Glutathione peroxidase (GPx) reduces H_2O_2 to water and lipid hydroxyperoxides to their corresponding alcohols (288). This reduction process is achieved with the aid of GSH and also results in the formation of glutathione disulfide (GSSG) (288). Peroxiredoxins (Prx) in both the cytosol and mitochondrial matrix reduce hydrogen peroxide to water and oxygen with GSH) and Trx as substrates respectively (279,286,287). These reactions result in GSSG and oxidized Trx. Glutathione reductase (GR) and thioredoxin reductase (TrxR) are able to regenerate GSSG and oxidized Trx respectively at the cost of one NADPH molecule (279,286,287).

The levels of ROS and hROS determine the nature and extent of pro-survival and pro-cell death pathways. Elevated ROS levels can increase the activity of the pro-survival Ras-Raf-ERK1/2 pathway by several means. For example, ROS can inactivate cytoplasmic protein tyrosine phosphatases (cPTPs), receptor protein tyrosine phosphatases (RPTP) which in turn will result in increased activity of increased tyrosine kinase signalling of cytoplasmic and receptor tyrosine kinases (CPTKs and RPTKs respectively) (Figure 1.15) (289). This has the effect of increasing the activity of several downstream pro-growth and pro-survival pathways. ROS, CPTKs and RPTKs can activate Src which in turn activates the pro-survival Ras-Raf-ERK1/2 pathway (290). ROS, CPTKs and RPTKs can also activate Src homology 2 domain containing protein (Shc) that too activate the pro-survival Ras-Raf-ERK1/2 pathway (290). ROS can also indirectly increase the activity of another mitogenic and proliferative kinase, Akt/PKB, by inhibiting the activity of PTEN through the reversible formation of disulfide bonds on crucial cysteine residues (289). Low, transient levels of ROS can also induce the activity of Stress-activated protein kinases (SAPKs) such as JNK and p38 MAPK which in turn induce pro-survival transcription factors including Elk-1 and *c*-jun (283,291,292). The altered redox

status of cancer cells is usually associated with a pro-oxidant status, resulting in the continued activation of these pro-growth signalling through ROS signalling (293).

Excessive and prolonged ROS production can result in pro-cell death signalling. The ASK1–Trx signalling complex plays a role in inducing cell death via ROS. An activated ASK1–Trx signalling complex that is induced by excessive ROS activates SAPKS JNK and p38 (Figure 1.15) (291,292). This in turn results in the activating of pro-apoptotic genes including Bcl2-interacting mediator of cell death (Bim), BH3-interacting domain death agonist (Bid), activating transcription factor 2 (ATF2), p53, and *c*-jun (291,292). Since cancer cells already have elevated ROS levels, compounds that can selectively induce ROS in cancer cells would be advantageous as it may selectively kill cancer cells via ROS signalling (293).

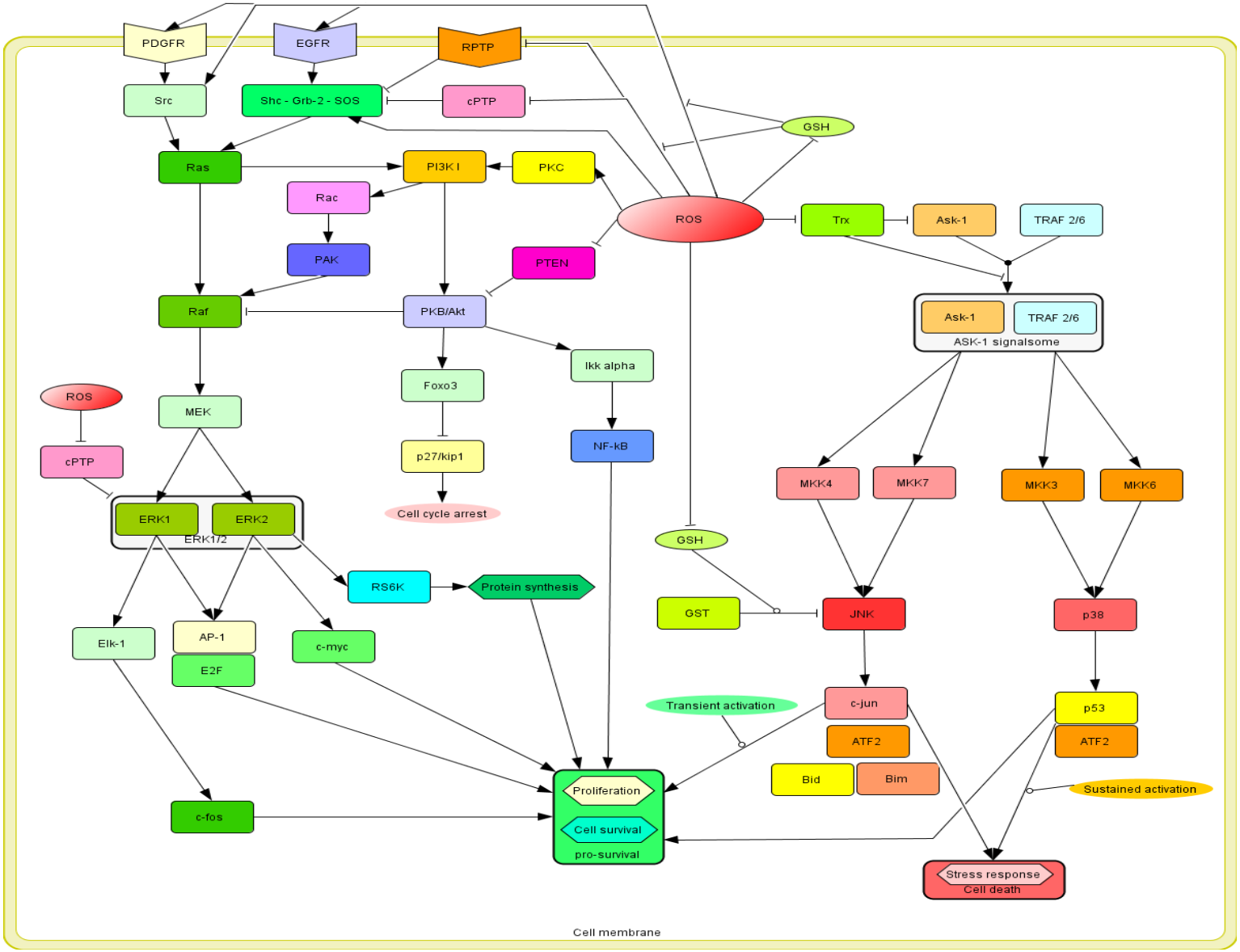

Figure 1.15: Reactive oxygen species signalling pathways. ROS are capable of both pro-survival and pro-death signalling. The outcome of ROS signalling depends on strength and duration of the ROS signal and the redox status of cells (From doctoral thesis of BA Stander (294)).

1.5 Hypoxia signalling

Cells respond to low oxygen levels in a controlled manner by altering gene and protein expression with the intent to restore oxygen homeostasis. Control of mRNA translation and hypoxia-inducible factor-1 (HIF-1) activity are important mediators of the cellular response to hypoxia. Hypoxia, both severe and moderate (1-5% oxygen), has a negative effect on mRNA translation (drops 20-70% during oxygen deprivation) and protein synthesis (295). Initiation of mRNA translation is tightly controlled by the eukaryotic initiation factors (eIFs) and the majority of mRNA translation is cap-dependent (296). An assembled eIF-4F complex located at the 5' end of mRNA is required for initiation and consists of a scaffold protein (eIF-4G) and an ATP-dependent helicase (eIF-4A). Assembly of the eIF-4F complex allows the formation of the 43S-pre-initiation complex which consists of the 40S ribosomal subunit and the ternary complex, with ternary complex consisting of eIF-2, GTP and methionine-transfer RNA. Once the initiation complex is assembled, it scans the 5'untranslated region (UTR) of the mRNA until a methionine start codon (AUG) is reached. Encounter with an AUG codon results in the hydrolysis of the GTP bound to eIF-2 and delivers the methionine amino acid to the start site of translation, resulting in the release of the initiating complex and recruitment of the 60S elongation ribosomal subunit. Termination of translation occurs in response to the presence of a stop codon in the ribosomal A site (296).

Hypoxia signalling controls mRNA translation initiation in two ways through the mTOR and the ER stress and the unfolded protein response (UPS) pathway (295). mTOR is a Ser/Thr kinase that phosphorylates eIF-4E-binding proteins (4E-BPs) thus reduces their affinity for eIF-4E, thus enabling eIF-4E initiation of mRNA translation to proceed. mTOR also phosphorylates S6K, which stimulates translation via the ribosomal protein S6 (295). During hypoxia, mTOR is inhibited, resulting in decreased general mRNA translation. Hypoxia inhibits mTOR by affecting the activity of AMPK. AMPK phosphorylates and activates the TSC1/2, which down-regulates mTOR activity (295). Hypoxia can activate AMPK in two ways. In the first scenario, hypoxia might lead to inhibition of energy production through oxidative phosphorylation and in doing so increases intracellular AMP levels and causes activation of AMPK. In the second scenario, hypoxia results in the increased production of ROS. ROS have been shown to activate both AMPK and JNK pathways. Janus kinase 2 (JAK2) kinase has been implicated as upstream activators

of AMPK through ROS signalling (297). Another upstream activator of the TSC that is responsive to hypoxia is DDIT4 (REDD1 or RTP801) (208). REDD1/DDIT4 is induced following hypoxia also in a ROS-dependent manner through the activation of ERK1/2 (298).

The ER stress and the UPS pathway is also activated in response to hypoxia and is mediated through the double-stranded RNA-activated protein kinase-like ER kinase (PERK) (299). ER is one of the largest protein producers within the cell and up to one third of cellular proteins are synthesized there (300). Protein folding is achieved through chaperone machinery which is energy dependent. Unfolded or misfolded protein could burden ER since the accumulation of inappropriately folded protein depletes energy and reducing agents (300). The UPS is aimed to eliminate inappropriately folded proteins within the ER by reducing the quantities of mRNA templates (300). Hypoxia increases ER-stress, possibly as a consequence of oxidative stress through ROS generation. ROS increases the leakage of Ca^{2+} from the ER lumen which in turn can stimulate further mitochondrial ROS production through multiple mechanisms (301). Excessive ROS contributes to ER-stress and the UPR, resulting in the phosphorylation and activation of PERK(302). PERK phosphorylation causes phosphorylation of the translation initiation factor eIF-2α, resulting in the inhibition of eIF-2α and ultimately leading to the inhibition of eIF-2α-mediated mRNA translation (302).

The second and probably more important mediator of the cellular response to hypoxia is HIF-1. HIF-1 is a transcription factor that activates the hypoxic expression of target genes involved in angiogenesis, oxygen transport, iron metabolism, glycolysis, glucose uptake, growth factor signalling, apoptosis, invasion and metastasis (303,304). During normoxia, HIF-1 is hydoxylated by prolyl hydroxylase domain (PHD) enzymes, resulting in the binding to the von Hippel–Lindau protein (VHL) (303,305). VHL is an E3 ligase, which targets the HIF-1α protein for rapid degradation via the ubiquitin proteasome pathway. PHD enzymes require oxygen, 2-oxoglutarate and Fe^{2+} to function and thus connects hypoxia and ROS signalling to the control of HIF-1α (304,305). Hypoxia itself results in the increased formation of ROS and the Q_o site of complex III of the electron transport chain is responsible for ROS production during hypoxia (306). Excessive ROS (hypoxia-induced or otherwise) results in a pro-oxidative intracellular redox status and this in turn results in ferrous iron depletion that is as a result of the Fenton reaction (Figure 1.16).

Depletion of intracellular ferrous iron as a result of excessive ROS in turn diminishes the activity of the PHD and in turn results in HIF-1α stabilization and activity (303,304).

ROS are also able to activate AMPK, which in turn stabilizes HIF-1α in a PHD-independent manner (307). Paradoxically, hypoxia and ROS signalling that lead to the stabilization and activation of HIF-1α also result in decreased translation of the protein, because of capped-mRNA translation inhibition. However, translation is not fully inhibited (drops 20-70% during hypoxic signalling), and hypoxic and ROS-signalling are sufficient to stabilize and activate appreciable levels of HIF-1α in order to mediate the cellular response to hypoxia (Figure 1.16) (308).

Upon stabilization and activation of HIF, a myriad of genes are activated that are involved in angiogenesis (vascular endothelial growth factor (VEGF), endocrine-gland-derived VEGF (EG-VEGF)), glucose metabolism (hexokinase 1,2 (HK1,2), aldolase-A,C (ALDA,C), CAIX, enolase-1 (ENO1), glucose transporter-1,3 (GLU1,3), glyceraldehyde phosphate dehydrogenase (GAPDH), lactate dehydrogenase-A (LDHA), pyruvate kinase M (PKM), phosphofructokinase L (PFKL), phosphoglycerate kinase 1 (PGK1), phosphofructo-2-kinase/fructose-2,6-bisphosphate-3 (PFKFB3)), deactivated genes such as OXPHOS (pyruvate dehydrogenase kinase 1,2 (PDK1,2)), cell proliferation and survival (insulin-like growth factor-2 (IGF2), transforming growth factor-α (TGF-α), *c*-myc and also apoptosis (Bcl-2/adenovirus EIB 19kD-interacting protein 3 (BNip3) (303).

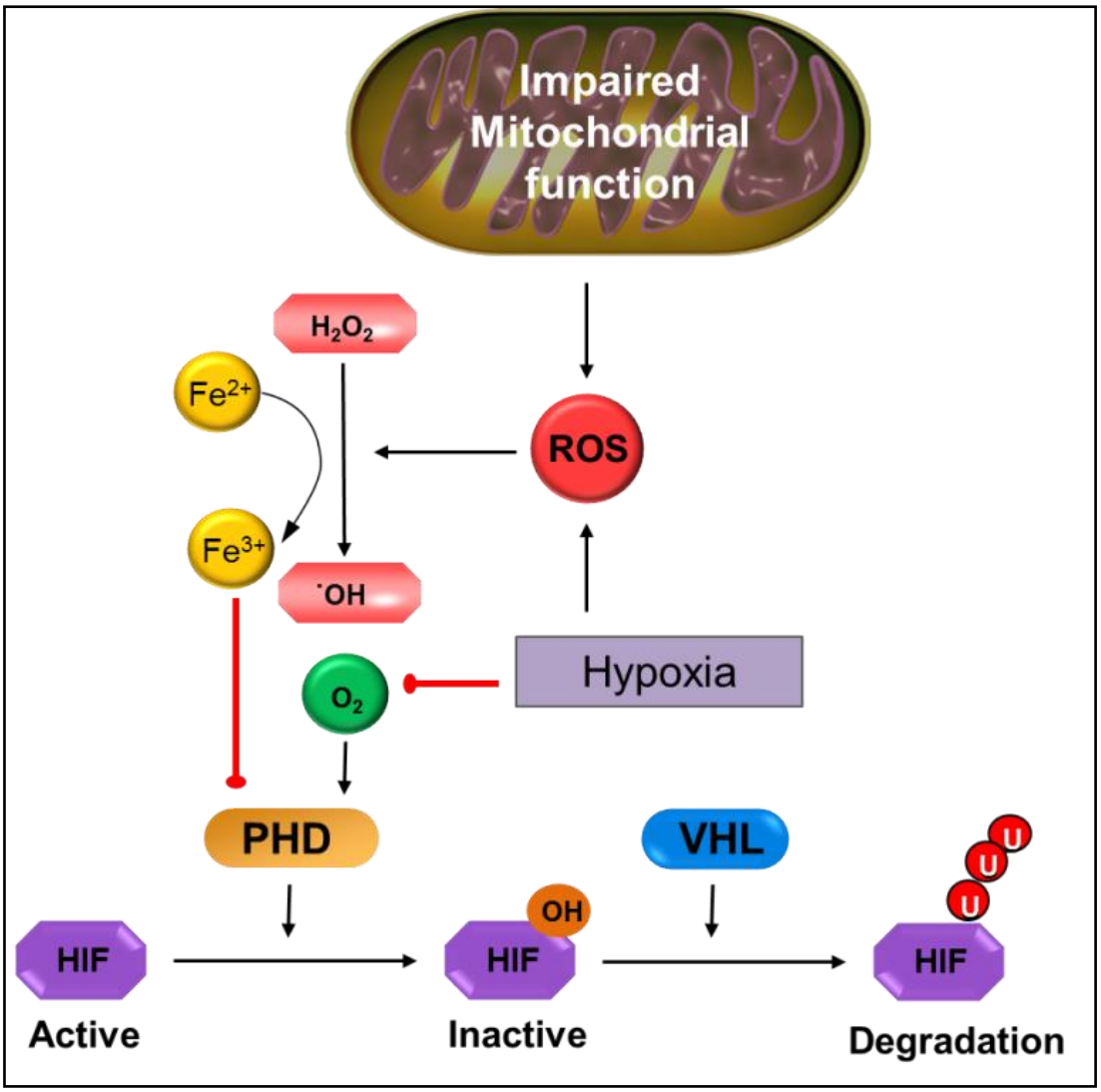

Figure 1.16: Hypoxia and reactive oxygen species-mediated signalling results in the stabilization and activation hypoxia inducible factor-1α.

1.6 Cancer cell metabolism

Most cancer cells rely on aerobic glycolysis even under conditions of sufficient oxygen supply to support OXPHOS (309). A series of papers authored by Gatenby and Gillies (2004, 2007 and 2008) (310-312) reviewed in depth the knowledge of their understanding towards aerobic glycolysis and proposed that it is a crucial evolutionary consequence in the development of invasive cancer. Oxygen is the first substrate that becomes limited during neoplastic growth. The persistent oxic-anoxic cycle subsequently exerts selection pressures which lead to the constitutive activation of glycolysis even in the presence of abundant oxygen. This phenotype might occur as a result of genotype instability through somatic cell mutation and/or epigenetic alterations (310).

Tumor microenvironmental changes such as increased hypoxia, limited substrate availability and an acidotic environment, however, are the main drivers of carcinogenesis that result in fitness differences in populations of cells that ultimately result in bioenergetic changes associated with malignant neoplastic growths (310). As hypoxia increases, so does the hypoxic signal and ROS formation (313). Together, ROS and hypoxia result in the activation of a hypoxic signal, causing increased glycolysis, angiogenesis, cell proliferation, as well as increased insensitivity to apoptosis (303,304). Increased glycolysis and decreased dependence on mitochondrial OXPHOS system due to hypoxia signalling leads to formation of excess lactic acid. In turn, lactic acid accumulation affects pH in the immediate environment of the hyperproliferative neoplastic cells. Following hypoxia in neoplastic cells, the up-regulated HIF1 heterodimers bind and activate genes involved in pH regulation, glycolysis, lactic acid formation, glucose transport, pro-angiogenic pathways and inhibit mitochondrial respiration (314-316).

In neoplastic cells, HIF1 induces a key enzyme PDK1, which inactivates the TAC cycle enzyme pyruvate dehydrogenase (PDH) E1α subunit within the pyruvate dehydrogenase complex, by *trans*-activating the *PDK1* gene directly (Figure 1.17). Consequently, HIF1-mediated *PDK1* expression prevents excessive mitochondrial ROS production, shunt pyruvate toward lactate and NAD^+ generation and facilitates ATP production via glycolysis (317). Dichloroacetic acid (DCA) and Nov3r-class agents are well-characterized inhibitors of PDK (318). Recent studies suggest that forcing cells into oxidative phosphorylation suppresses cancer growth (319-321).

Plas and Thompson (2002) proposed that metabolic and apoptotic pathways are not independent from each other and the glycolytic phenotype is indeed associated with apoptosis resistance (322). Genetic analysis of microarray data from several studies indicate that the glycolytic phenotype is accompanied by gene expression changes that are closely related to tumorigenic processes, such as resistance to apoptosis and increased metastatic potential (323,324). Consequently, cancer cells rely more on glycolysis for energy production (325). This opens the opportunity to selectively killing cancer cells by targeting the glycolytic pathway.

The ideal antitumor therapeutics should easily gain entry into the tumorigenic cells and exhibit characteristics of low dosage, low drug resistance, together with antimitotic, anti-angiogenic ability. It should be able to be administered regularly, have high solubility and high oral bioavailability (326,327).

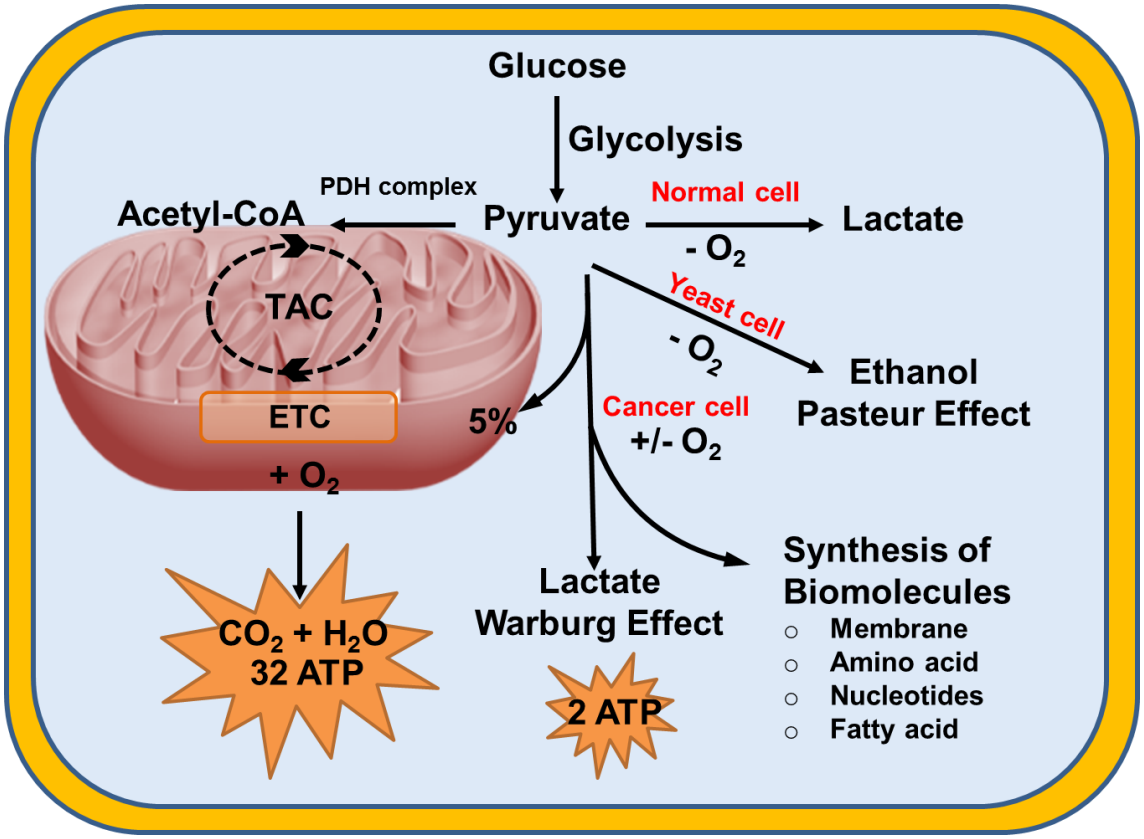

Figure 1.17: Glucose metabolism in normal and cancer cells. Non-proliferating cells first metabolize glucose to pyruvate via glycolysis. In the present of oxygen, pyruvate is converted to acetyl-CoA by pyruvate dehydrogenase complex (PDH complex) for subsequent ETC oxidative phosphorylation process. In the absence of oxygen, normal cells complete the glycolysis process in the cytosol to produce lactate (lactic acid). Pasteur noticed yeast cells produce alcohol via anaerobic glycolysis (the Pasteur Effect). Warburg observed that cancer cells tend to convert most glucose to lactate regardless of the presence of oxygen (the Warburg Effect).

1.7 Dichloroacetate targets the bioenergetic properties of cancer cells

Bioenergetic alterations in cancers including a pro-oxidant status, increased glycolysis and inhibited OXPHOS, aid in increased proliferation and insensitivity to pro-apoptotic signals (328,329). These characteristics separate cancer cells from normal functioning cells and can be seen as a weak point and a target for selective growth inhibition (330). A pro-oxidant intracellular status causes both a survival response, partly through ERK1/2 and PKB/Akt activation, and sensitizes cells to cell death partly through ASK1-Trx signalosome signalling and by causing irrepairable oxidative damage to DNA, lipids and proteins. However, the cell-death sensitizing action of the pro-oxidant status is blunted by the fact that the Trx/TrxR-system is up-regulated in a variety of cancer cells and is also could be linked to resistance to chemotherapies (331,332). Thus, the pro-oxidant status is tolerated in cancer cells as a result of impaired ROS-cell death signalling as well as abrogated programmed cell death normally associated with cancer cells. However, cells have an upper limit of in their ability to handle oxidative stress before becoming susceptible to the damaging effects that oxidation has on DNA, lipids and proteins (333).

DCA and Nov3r-class agents are well-characterized inhibitors of PDK (318). DCA is a small molecule (contains two carbon molecules) and it is an unpatentable by-product of drinking water chlorination (318). DCA binds to PDK and attenuates inhibition of PDH activity. The increased PDH activity shifts metabolism from glycolysis to glucose oxidation and decreases $\Delta\Psi m$ hyperpolarization, which opens mitochondrial transition pores. This allows for the translocation of ROS from the mitochondrial matrix to the cytoplasm and increases ROS signalling (325). Targeting PDK signalling thus represents a novel means in which to target cancer cells.

Recent studies suggest that forcing cells into oxidative phosphorylation suppresses cancer growth (319-321). Inhibitors of PDKs attenuate inhibition of PDH activity (334). The increased PDH activity shifts metabolism from glycolysis to oxidative phosphorylation, decreases mitochondrial membrane potential hyperpolarization, which opens mitochondrial transition pores. This allows for the translocation of ROS from the mitochondrial matrix to the cytoplasm and increases ROS-signalling, as well as restoring normal metabolism, thereby decreasing lactate production in metabolically altered cells (310,325).

A group of researchers from University of Alberta, Canada has focused on anticancer activity of DCA for years. Bonnet *et al.* (2007) have reported that DCA has remarkable effects on cancer cell survival by reduced mitochondrial membrane potential, formation of ROS and release of pro-apoptotic effector cytochrome *c* (325). Michelakis *et al.* (2010) utilized DCA to treat glioblastoma patients for 15 months and found this small molecule has ability to induce apoptosis *in vitro* and *in vivo* (335). Sutendra *et al.* (2012) demonstrated DCA re-activates mitochondrial metabolism in cancer *in vitro* in the xenotransplant model, and *in vivo* though inhibition of HIF1 signalling and angiogenesis mediated by PDK (336). Currently, DCA has been used extensively in clinical trials for the treatment of brain tumors, breast cancer and lung cancer (316).

The *in vitro* and *in vivo* performance of DCA on different types of cancer is remarkable (323,337,338). DCA is able to reverse the cytosolic glycolytic phenotype in a number of cancer cell lines, depolarizing the inner mitochondrial membrane potential and increasing mitochondrial metabolism (323,325,337). DCA appears to leave non-tumorigenic cells unaffected as a result and can be considered as an effective anticancer agent without toxicity to normal cells (323,337,338). Sun *et al*. (2010) mentioned that DCA has passed phase I/II toxicity testing in humans and is currently in phase III clinical trials for the treatment of chronic lactic acidosis in congenital mitochondrial disorders (323). In the study of Mori and co-workers (2004), DCA was used for the treatment of mitochondrial encephalomyopathy, lactic acidosis, and stroke-like episodes syndrome (MELAS) (orally administered up to 50 mg/kg/day) with serum levels being maintained between 0.3-1.0 mM (339). DCA has been proven in human trials to be safe, it can be administered orally and easily penetrates tissues (338).

Sun *et al*. (2010) investigated the effects of DCA on metastatic breast cancer cell growth *in vitro* and *in vivo*. In order to conduct the tests, a panel of breast cancer cell lines such as MCF-7, T-47D, 13762 MAT, V14 and 4T1 were treated with 5 mM of DCA. A non-tumorigenic epithelial cell line MCF-10A was included in the experiment as a positive control. Results demonstrated that after four days exposure of DCA on MCF-7, T-47D, 13762 MAT and V14 cell lines, cell growth had significantly decreased to between 60% and 80%. On the other hand, DCA had no effect on the normal breast cell line MCF-10A cell growth (323). Xiao *et al.* (2010) used up to 40

mM DCA for the treatment of A549, HeLa, HCT116, and PLC cell lines *in vitro* and significant decrease in cell growth was demonstrated in all of these cell lines (337).

1.8 Antimitotic compound 9

One of the most researched classes of cancer chemotherapeutic drugs are antimitotic drugs (340-344). The microtubule-interfering class of antimitotic agents halts mitosis by interfering with microtubule dynamics in actively dividing cells such as cancer cells, which in turn activates the spindle checkpoint. Activation of the spindle checkpoint prevents actively dividing cells from completing mitosis and a prolonged block in mitosis usually results in cell death (95).

Compounds that interfere with microtubule dynamics can bind at the various sites of microtubules. Vinblastine, a compound originally derived from the *Catharanthus* flowering plant, binds at the plus end and inhibits microtubule polymerization (345). Paclitaxel, also known as Taxol, was first isolated from the bark of the Pacific yew tree and binds along the interior surface of the microtubule, thereby interfering with the dynamics of the microtubules (345). Derivatives of Vinblastine and Taxol are currently are part of various chemotherapy regimens including Hodgkin lymphoma ovarian, breast and lung cancers, as well as Kaposi sarcoma (345).

Colchicine is a compound that is derived from plants of the genus *Colchicum* and forms complexes between the alpha and beta tubulin dimers to suppress microtubule dynamics (345). Other compounds are also able to interfere with microtubule dynamics by binding at the Colchicine site including combretastatins and 2-methoxyestradiol (2ME, Figure 1.11A) and analogues of these compounds (346,347). 2ME is produced in trace amounts in the human body and is an endogenous metabolite derivative of estrogenic hormone 17β-estradiol with well documented antimitotic, anti-angiogenic, and pro-apoptotic properties *in vitro* (324,348-350). Antimitotic compounds such as 2ME are able to induce apoptotic cell death via the extrinsic pathway by up regulating DR5 in a variety of cell types (351). 2ME treatment results in the formation of excess reactive oxygen species that contribute towards cell death induction (324) and reactive oxygen species are known to mediate death receptor activation and apoptosis (352).

Under *in vitro* conditions 2ME inhibits the activity of anaphase-promoting complex, an ubiquitin ligase of which the activation is required for separation of sister chromatids, in MDA-MB-435 human breast cancer cells (353). 2ME induces tubulin-dependent G_2/M cell cycle arrest through regulation of genes involved in the mitotic

spindle assembly checkpoint, which results in inhibition of the APC/C and tubulin-independent inhibition of protein translation (353). Furthermore, 2ME exhibits anti-angiogenic activity and is mediated through down regulation of hypoxia-inducible factor-1α (HIF-1 α), which is an essential component for transcriptional activation of VEGF expression (353,354).

Stander *et al*. (2010) mentioned that in order to treat cancer effectively, it is important to maintain the plasma concentration of 2ME in the range of 3-17 ng/ml (10-56 nM) (324). Mooberry (2003) displayed that 2ME has a broad spectrum of antitumor activities. The author also revealed that 2ME does not bind to or induce the activity of estrogen receptors, therefore the mechanism of its actions are mediated through inhibition of other anticancer related channels, such as inhibition of the pro-angiogenic transcription factor HIF-1α, JNK signalling and the initiation of the apoptotic pathway via regeneration of the ROS (355). In addition, Stander *et al*. (2010) revealed a novel finding, which is the induction of both apoptosis, as well as autophagy as a possible combination of types of cell death induced by treatment of MCF-7 cells with one micromolar 2ME after 24 hours of exposure (324).

In the clinical setting, 2ME suffers from a lack of oral bioavailability and it has a short half-life because of degradation and conjugation (356,357). Novel formulations of 2ME such as nanocrystals have been developed to try and improve its bioavailability and potency in the clinical setting, however, without much success (358). Low oral bioavailability is likely caused by a degradation step by oxidation at the C3/C17 hydroxyl groups (359,360). Previous studies by Liu *et al.* (2005) and Newman *et al.* (2006) have emphasized the limitations of 2ME due to its potential for inactivation at the D-ring, C17 position (360,361). It is suggested that low aqueous solubility and extensive ‘first pass’ hepatic metabolism likely account for the poor bioavailability of 2ME (359). These characteristics of 2ME led to the development of various analogues or derivatives that are able to improve bioavailability and potency.

2ME analogs therefore draw great interest among scientists and these analogs are under extensive research in recent years. ENMD-1198 (2-methoxyestra-1,3,5(10)16-tetraene-3-carboxamide), 2-methoxymethyl estradiol and 2ME-Gly-Cap-NH2 (*O*-17-substituted 2ME analog) are analogs of 2ME which were developed to increase both the bioavailability and antitumor activities of the parent molecule (362-364). All of these analogs demonstrated an antiproliferative activity comparable to 2ME. Phase II

dose-escalation studies of ENMD-1198 conducted by Zhou *et al*. (2011) demonstrated that this analog is well tolerated by cancer patients with a recommended dose of 425 mg/m^2/day (362).

Recent investigations have demonstrated that sulphamoylated analogs of 2ME are estrogen sulphamates that are more potent than that of their parent estrogens (365-367). Newman *et al.* (2007) demonstrated for the first time that cyanomethyl group at C17 position significantly increased the efficacy of compounds STX640 and STX641 *in vitro* and *in vivo* (327). Subsequently, Foster *et al.* (2008) demonstrated that 2-MEOe2*bis*MATE (STX140) and 2-EtE2*bis*MATE (STX 243), which are compounds exhibiting A-ring (C3 and/or C2) and D-ring (C17) modifications of 2ME, have potent anti-proliferative and anti-angiogenic activity *in vitro*, *in vivo* and *ex vivo* (368-370). The same group also showed the efficacy of STX243 against the growth of both estrogen receptor positive and estrogen receptor negative breast cancer tumors *in vitro* and *in vivo* with promising pharmacokinetic properties (369). These estrogen sulphamates are proven to obtain a higher bioavailability since they are able to overcome the biotransformation encountered by liver metabolism due to the fact that they are capable of reversibly conjugating to cytosolic erythrocyte carbonic anhydrase II (CAII) (365,366,371,372). Binding of these estrogen sulphamates to intracellular erythrocyte CAII prevents it from coming into contact with various liver enzymes and thus avoids taking part in first-pass metabolism (365,366,371,372).

Carbonic anhydrases are a family of ubiquitously expressed, zinc containing isozymes that catalyze the interconversion between CO_2 and HCO_3^- (372,373). It was evidenced that the overexpression of carbonic anhydrases IX (CAIX) and XII (CAXII) is strongly associated with hypoxia, a condition favoured by most solid tumors. For example, the promoter of the CAIX gene, which contains a hypoxia response element (HRE), binds to HIF-α in response to increased cell density and hypoxia microenvironment and activate the transcription of CAIX (366,374). The increased formation of carbonic acid as a result of CAIX expression facilitates in forming an acidotic environment surrounding solid tumors acidosis and is known to enhance pathologic processes favoured by tumorigenicity (367,372,373). Prospective inhibitors capable of selective inhibition of hypoxia-activated CAIX therefore provide therapeutic promise for the treatment of metastatic tumors since it will be able to prevent extracellular acidification via CAIX.

Several promising sulphamoylated analogs of 2ME were designed using *in silico* docking and molecular modelling at the University of Pretoria by Dr B.A. Stander (Department of Physiology, University of Pretoria), Professor F. Joubert (Bioinformatics Units, Department of Biochemistry, University of Pretoria) and Professor A.M. Joubert (Department of Physiology, University of Pretoria). A recent publication by Stander *et al.* (2011) has revealed that the newly designed sulphamoylated compounds exhibit antimitotic activity via binding to the colchicine binding site of tubulin, as well as that they are carbonic anhydrases IX inhibitors (Figure 1.18 A-C) (366).

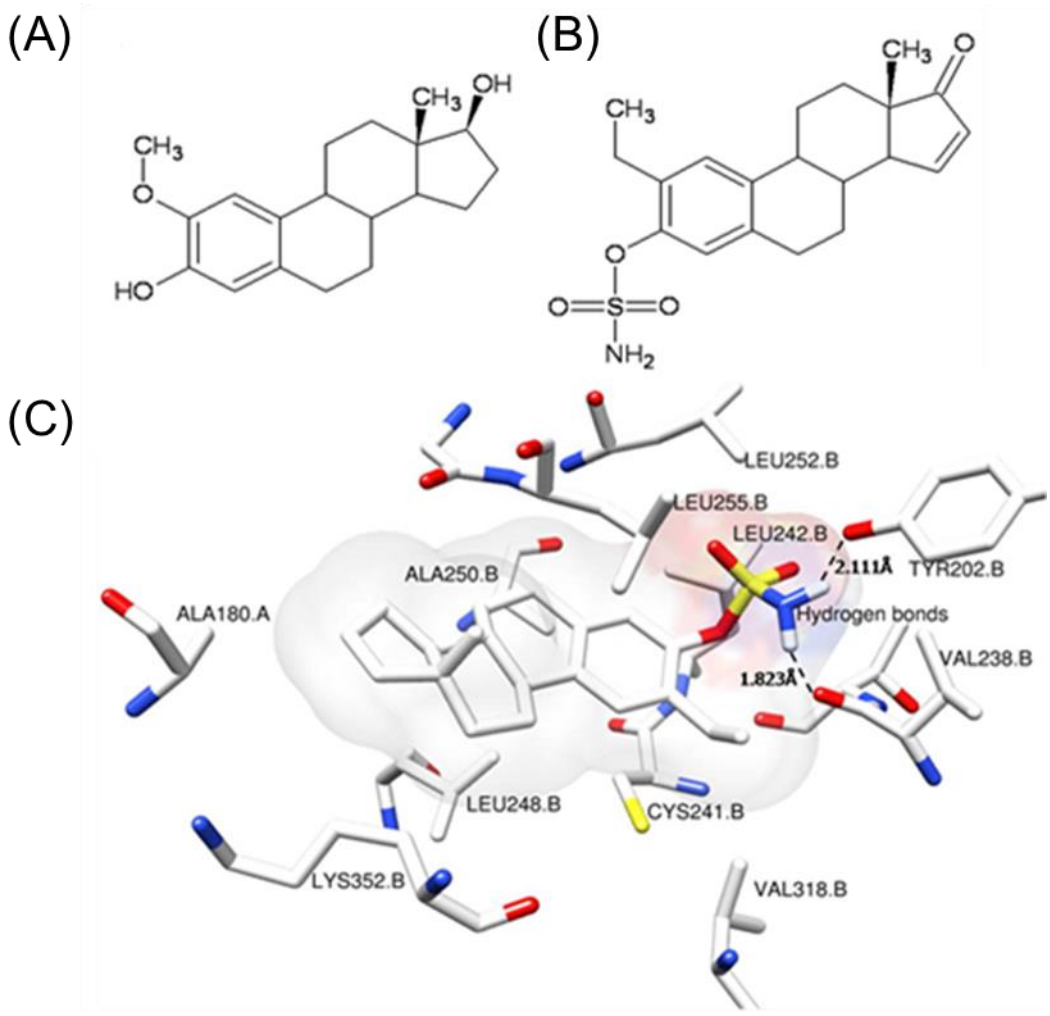

Figure 1.18: Chemical structure of 2-methoxyestradiol and *in silico*-designed compound 9 and the binding of compound 9 into tubulin. Chemical structure of 2-methoxyestradiol (2ME) (A) and 2-ethyl-3-*O*-sulphamoyl-estra-1,3,5(10),15-tetraen-3-ol-17-one (C9) (B) (ACD/ChemSketch freeware version 12.0). Docking of ESE-16 into the colchicine binding site of tubulin (C) (366).

In silico docking performed by Stander *et al.* (2011) revealed that the 2-ethyl derivatives displayed increased binding affinity to the colchicine-binding site when compared to other C2-modified analogs (366). This finding is in agreement with the results from another group Leese *et al.* (2006) earlier where it was discovered that an ethyl substitution at C2 position of estrone provided the optimal substituent for high antiproliferative activity (371,375). Therefore, based on the docking results of the analogs into the colchicine site and the CAIX/CAII ratio of the compounds, it was decided to synthesize C9 (Figure 1.19).

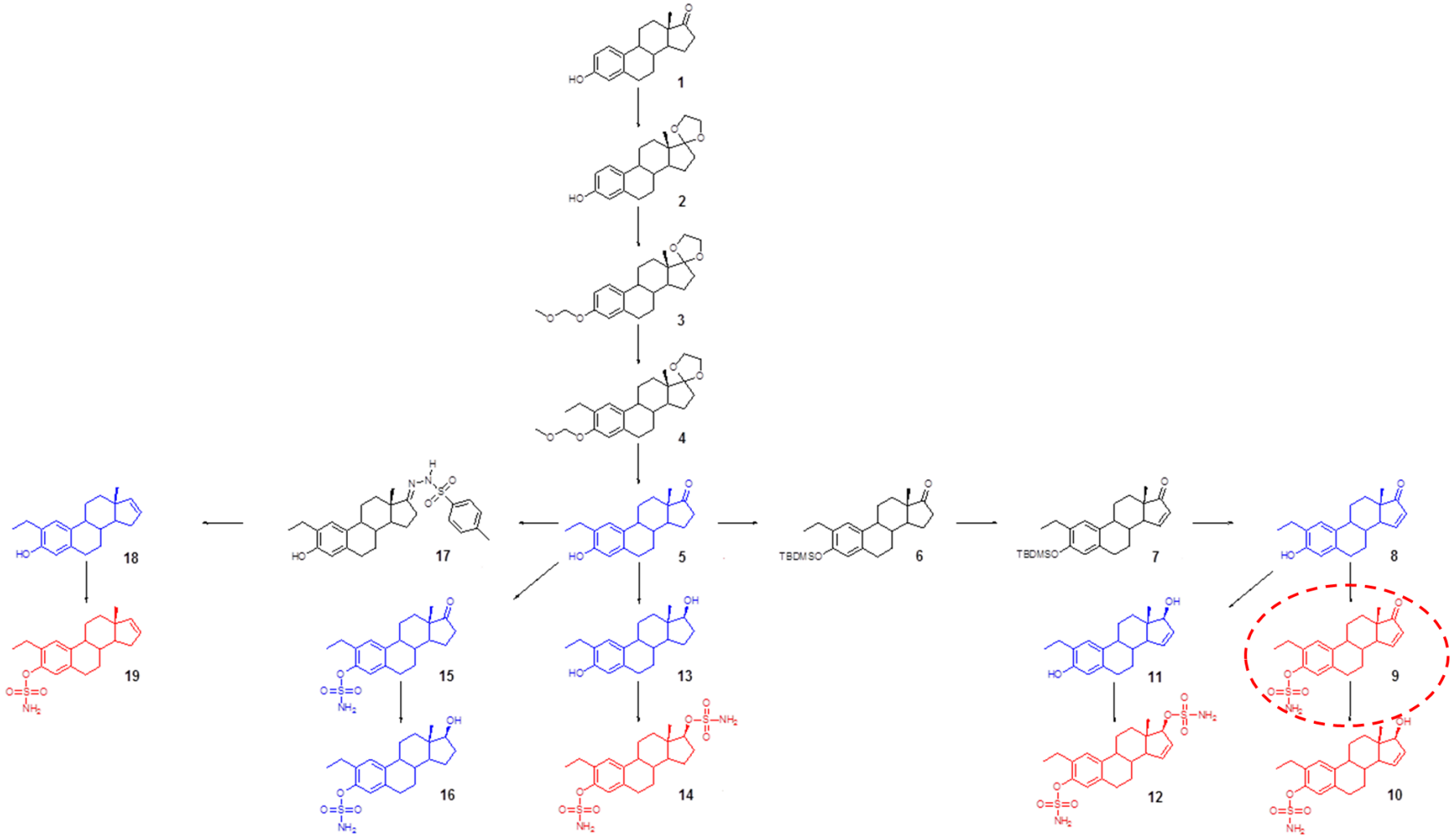

Figure 1.19: Synthetic pathways of compound 9 and other structural similar analogs. Final synthesis pathway as agreed upon between iThemba Pharmaceuticals (Pty) Ltd. and the Department of Physiology, University of Pretoria (From doctoral thesis B.A. Stander (294)).

A recent study on another 2ME analog ESE-16, which has been modified on the D-ring carbon 16 position, revealed that treatment caused activation of SAPKs p38 and JNK pathways in MCF-7 and metastatic human breast adenocarcinoma cell line (MDA-MB-231) respectively (187). Additionally, lysosomal rupture, iron metabolism, and abrogation of Bcl-2 phosphorylation were identified as important mediators of cell death in tumor cells (187).

Furthermore, a number of studies conducted in our laboratory (2011, 2012, 2013) have demonstrated that the newly designed antimitotic compounds C9, ESE-15-ol and ESE-16 (previously named compound 19 (C19)) exhibited anti-CAII, anti-CAIX, antiproliferative and pro-apoptotic (intrinsic mitochondrial pathway) and pro-autophagic properties on various cancer cell lines including MCF-7, MDA-MB-231, SNO and HeLa cells (187,366,376-378). Autophagy, particularly macroautophagy is activated during stress and the process involves cargo sequestering of cytoplasm contents to lysosomes for degradation (379). It is debatable whether the autophagic response of cancer cells to therapeutics serves as indication for cell death. In this context, only few studies reported that antimitotic drugs induce autophagy as drug target (380). Persistent autophagy may cause cells to become depleted in vital organelles and critical proteins which ultimately lead to cell death (381).

Evolutionary views about the origin of cancer help to explain why certain cancers become resistant to various treatment regimens (382). For example, sub-populations of colorectal tumors become more resistant after chemotherapy (383). Hanahan and Weinberg identified six hallmarks of cancer in 2000 (384) and the list was updated to include four additional hallmarks of cancer cell biology (329). Unstable genomes and tumor-promoting inflammation are two enabling features, while eight acquired features include self-sufficiency in growth signals, insensitivity to anti-growth signals, evading cell death, limitless replicative potential, sustained angiogenesis, evasion of the immune system, deregulated metabolism and tissue invasion, and metastasis (329). By making use of combination therapies that target many different signalling pathways, selection for chemotherapeutic resistant sub-population may be limited to a minimum.

Liu *et al.* (2001) have proposed that combination treatment of a glycolysis inhibitor in conjunction with a chemotherapeutic agent will open new windows for anticancer therapy (385). A recent study from Tagg *et al.* (2008) exhibited the glycolytic inhibitor 2-deoxy-D-glucose (2DG) in combination with STX140 significantly reduced tumor volume by 76% ($P < 0.001$) *in vivo* compared to 46% ($P < 0.05$) in STX140-only treated xenograft models (386). However, there is currently no literature available for the combination of both C9 and DCA for the treatment of cancer *in vitro*. The effects of C9 and DCA on tumorigenic and non-tumorigenic cell lines remain to be elucidated. Both C9 and DCA are regarded as potential anti-tumorigenic therapeutics with different targets and modes of action.

DCA and C9 are two compounds with different anticancer activities, one being a glycolytic inhibitor and other one an antimitotic compound. C9 is an antimitotic compound similar to 2-methoxyestradiol (366) and DCA is known to induce ROS level and apoptotic cell death (325). It is thus possible that combination treatment of cells with DCA and C9 may induce apoptosis via ROS-mediated pathway. There is currently no literature available for the combination of *in silico*-designed C9 and DCA for the treatment of cancer *in vitro*. It is of vital importance to examine and compare the effects of these compounds *in vitro* by utilizing tumorigenic and non-tumorigenic breast cells as a model.

Thus, it was decided to test C9+DCA on tumorigenic adenocarcinoma MCF-7 cells and non-tumorigenic MCF-12A breast epithelial cell lines. The aim of this study was to evaluate the influence and to elucidate the underlying mechanisms of action of C9 in combination with DCA on cell growth, cytotoxicity, morphology, cell cycle progression, autophagy and apoptotic induction, mitochondrial membrane potential, redox status, JNK activation, Bcl-2 phosphorylation, caspase activity and gene expression using a breast cell culture model namely tumorigenic MCF-7 and non- tumorigenic MCF-12A cells.

The present study contributes to the field of cellular and molecular anticancer by elucidating the mechanisms of combination treatment at the level of molecular biology, thus warranting further research projects to develop viable and functional combination treatment as clinically useable anticancer agents.

2. Chapter 2: Materials and Methods

2.1 Compounds and reagents

Gibco® Dulbecco's Modified Eagle's Medium (DMEM) and Ham's F-12 Nutrient Mixture (F-12) were purchased from Life Technologies™ South Africa Pty Ltd. (Fairland, JHB, RSA). Crystal violet, actinomycin D, Bouin's fixative, Hoechst 33342 (bisBenzimide), acridine orange, propidium iodide and 2′, 7′-dichlorodihydrofluorescein diacetate (H_2DCF-DA) were supplied by Sigma Aldrich (St. Louis, MO, USA). Heat-inactivated fetal bovine serum (FBS) (PAA Laboratories (Pty) Ltd. Morningside, QLD, AUS), sterile cell culture flasks and plates (96-well plates and 6-well plates) were obtained through Separations (Pty) Ltd. (Randburg, JHB, RSA). Trypsin/Versene (0.125% trypsin, 0.1 Versene - disodium ethylenediamine tetraacetic acid (EDTA)), penicillin, streptomycin and fungizone were purchased from Highveld Biological (Pty) Ltd. (Sandringham, JHB, RSA). Cholera toxin, glutaraldehyde, triton X-100, haematoxylin, eosin, ethanol, xylol and Entellam® fixative were purchased from Merck (Pty) Ltd. (Munich, Germany). The xCELLigence system which includes the Real-Time Cell Analyzer Single Plate (RTCA SP®) system, RTCA Analyzer and RTCA Control Unit (developed by ACEA Biosciences, Inc. (San Diego, CA, USA)) were kindly provided as a demonstration model by Roche Products (Pty) Ltd. (Randburg, JHB, RSA) and the E-plate 96 microtiter plates were purchased from Roche Products (Pty) Ltd. (Randburg, JHB, RSA). The primary monoclonal mouse anti-tubulin alpha antibody from IMGENE (Alexandria, VA, USA) (cat no. IMG-80196) was purchased from BIOCOM biotech (Pty) Ltd. (Clubview, PTA, RSA) and the fluorophore-labelled donkey anti-mouse heavy and light chain secondary IgG with Alexa Fluor 350 secondary antibody from Invitrogen™/Life Technologies™ (Carlsbad, CA, USA) were purchased from The Scientific Group (JHB, RSA). The Annexin V-fluorescein isothiocyanate (FITC) Kit was purchased from BIOCOM biotech (Pty) Ltd. (Clubview, PTA, RSA) and manufactured by MACS Miltenyi Biotech (GmbH, Germany). The Lactate Dehydrogenase Cytotoxicity Assay Kit from BioVision Inc. (Mountain View, CA, USA) was purchased through BIOCOM biotech (Pty) Ltd. (Clubview, PTA, RSA). FITC-conjugated anti-autophagy-related (LC3) antibody was purchased from Novus Biologicals Ltd. (NB600-1384) (Cambridge, UK). A rabbit antibody for anti-active caspase 7 from BioVision Inc. (Mountain View, CA, USA) and a

secondary anti-rabbit antibody conjugated to Dylight™ 488 from Rockland Inc (Gilbertsville, PA, USA) were purchased from BIOCOM biotech (Pty) Ltd. (Clubview, PTA, RSA). MitoCapture™ Apoptosis Detection Kit (K250-25) was purchased from BioVision (Mountain View, CA, USA). FlowCellect™ Bcl-2 Activation Dual Detection Kit produced by Millipore Corporation (Billerica, MA, USA) was purchased through Microsep (Pty) Ltd (Sandton, JHB, RSA). Qiagen® RNeasy Plant Mini Kit and RNase-free DNase were purchased from Southern Cross Biotechnology (Pty) Ltd. (Cape Town, RSA). Agilent's 44k 60-mer human oligo slides, Low RNA Input Fluorescent Linear Amplification Kit, 2x GEx Hybridization Buffer HI-RPM, Gene Expression (GE) Wash Buffer 1 and 2, Stabilization and Drying Solution were obtained from Agilent Technologies (Pty) Ltd. (Palo Alto, CA, USA). Cy-3 and Cy-5 fluorescent dyes were supplied by Amersham Biosciences (Pittsburgh, USA). All other chemicals were of analytical grade and were purchased from Sigma Aldrich (St. Louis, MO, USA), Southern Cross Biotechnology (Pty) Ltd. (Cape Town, RSA) and Amersham Biosciences (Pittsburgh, PA, USA).

2.2 Cell lines and cultures

The MCF-7 cell line is derived from a pleural effusion of human breast adenocarcinoma provided by American Type Culture Collection (ATCC™) (Manassas, VA, USA). The MCF-7 line retains several characteristics of differentiated mammary epithelium including ability to process estradiol via cytoplasmic estrogen receptors. The MCF-12A cell line (estrogen receptor negative) is a non-tumorigenic spontaneously immortalized adherent human breast epithelial cell line established from tissue taken at reduction mammoplasty from a nulliparous patient with fibrocystic breast disease that contained focal areas of intraductal hyperplasia. The original MCF-12A cell line was produced by long-term culture and forms a monolayer without domes when cell growth reaches confluency. MCF-12A cells were obtained as a gift from Prof MI Parker (Department of Cancer Biology of the University of Cape Town, CT, RSA).

MCF-7 breast adenocarcinoma tumorigenic cells were cultured in DMEM and supplemented with 10% heat-inactivated FBS (56˚C, 30 min), 1% penicillin G (100 U/ml),

streptomycin (100 µg/ml) and fungizone (250 µg/l). MCF-12A non-tumorigenic breast epithelial cells were cultured in a 1:1 mixture of DMEM and Ham's F12 medium supplemented with epidermal growth factor (20 ng/ml), cholera toxin (100 ng/ml), insulin (0.01 mg/ml), hydrocortisone (500 ng/ml), 10% heat-inactivated FBS, 1% penicillin G (100 U/ml), streptomycin (100 µg/ml) and fungizone (250 µg/l). All cells were grown at 37˚C in a humidified atmosphere containing 5% CO_2 in air. All medium used in this project contained phenol red which is used to monitor the pH of media. When phenol red turns yellow, it serves as indicator that the pH of the medium is low and needs replacement.

Experiments were conducted either in 25 cm^2 culture flasks, 96-well microculture plates or six-well culture plates. For 25 cm^2 culture flasks, exponentially growing cells were seeded at 500 000 cells per 5 ml maintenance medium per flask. For six-well plates, exponentially growing cells were seeded at 375 000 cells/well in three ml maintenance medium on heat-sterilized cover slips. For 96-well plates, exponentially growing cells were seeded at 5000 cells/well in 100 µl of maintenance medium. For E-Plate 96 microtiter plate, exponentially growing cells were seeded at 10 000 cells/well in 200 µl of medium. Cells used in all experiments were allowed a 24 h incubation period for cell adherence and medium was renewed prior to exposure.

General cell culture was maintained in 25 cm^2 culture flasks in a Forma Scientific water-jacketed incubator (Ohio, USA) contained in a humidified atmosphere with 5% CO_2. MCF-7 and MCF-12A cells were maintained by subculturing at regular intervals between two to three days. When cells almost reached stationary phase growth (approximately 90% full), they were subcultured and split into new flasks. Subcultivation of monolayers involved the breakage of cell-to-surface and cell-to-cell interactions which require enzymatic digestion of trypsin-EDTA. EDTA binds to Ca^{2+} and Mg^{2+} by sequestering them and preventing their interference with trypsin (387). The complete tissue culture media contains trypsin inhibitors (from FBS) and divalent cations such as Ca^{2+}- and Mg^{2+} ions. All of these factors inhibit the enzymatic activity of trypsin. Thus, prior to trypsinization, cells were washed with phosphate buffered saline (PBS) free from Ca^{2+} and Mg^{2+} to remove trypsin inhibitors contained in the media. Concentrated PBS solution (10 x) was prepared by dissolving 80 g NaCl, 2 g KCl, 11.5 g Na_2HPO_4

and 2 g KH_2PO_4 (all chemicals were purchased from Merck (Pty) Ltd. (Munich, Germany)) in one litre of distilled water. The pH of the concentrated solution was adjusted to 7.4 with a Thermo® Orion 3 star pH Benchtop pH meter. The 10 x PBS was diluted to 1 x solution and autoclaved for 20 minutes at 120˚C.

Cultured cells were observed regularly via light microscopy to monitor their density and morphology for subculture. The parent flask was rinsed with 1 x PBS buffer at least once followed by trypsinization. The progression of cell dissociation was monitored by light microscopic examination (magnification 10x, 20x and 40x). Trypsin was gently removed and the cell culture flask was agitated by shaking. Trypsin was inactivated by adding fresh medium and cell viabilities were tested by the trypan blue staining method before subculturing. Cells were also regularly cryopreserved in the liquid nitrogen cryo-freezer. A special freezing medium was prepared with a cryoprotectant property. The freeze medium consisted of 70% supplemented medium, 20% FBS and 10% dimethylsulfoxide (DMSO).

2.3 Chemical compounds and composition of appropriate controls

2-Ethyl-3-*O*-sulphamoyl-estra-1,3,5(10),15-tetraen-3-ol-17-one (C9) was *in silico*-designed in our laboratory and is therefore not commercially available. C9 was synthesized by iThemba Pharmaceuticals (Pty) Ltd. (Modderfontein, JHB, RSA) with analytical grade > 95% purity. DCA (powder) was purchased from Sigma Aldrich (St. Louis, MO, USA). Time- and dose-dependent cell growth studies were conducted for selection of optimal exposure conditions. A previous study conducted in our laboratory by Stander *et al.* (366) revealed that the concentration for 50% of maximal inhibition of cell proliferation (GI_{50}) value for C9-exposed MCF-7 cells is 130 nM after 48 h of exposure. This concentration served as benchmark for concentration selection for dual drug treatment. Selection of the concentration for combination therapy was conducted by setting up one non-variable constant (C9 with concentration of 130 nM) and combining this with a range of different concentrations of DCA (2.5 mM, 5.0 mM, 7.5 mM and 15.0 mM). Range of concentrations for DCA was based on previous literature using similar concentrations (323,388). The process of elimination was used to

determine the exposure time and concentrations. The pilot study indicated that C9 was active in nanomolar concentration against MCF-7 tumorigenic cell line (366) thus, a stock solution with micromolar concentration 0.75 μM in DMSO was prepared for experiments in this project. The final concentrations of C9 and DCA used for experiments were determined at early onset of this project and it was determined to be 130 nM and 7.5 mM respectively. More details are available in the result section.

The stock solution was diluted with culture medium to the required final concentrations prior to exposure. Several controls were incorporated. Firstly, cells grown under normal conditions propagated in culture medium only. Secondly, in order to determine whether the vehicle, DMSO, had an effect on proliferating cells, vehicle-treated controls were included and the final DMSO concentration used to expose cells never exceeded 0.1% (v/v) (389). Thirdly, in order to observe differences between combination/dual treatment of 130 nM C9 in conjunction with 7.5 mM of DCA and individual treatment of C9 (130 nM) or DCA (7.5 mM), cells exposed with either C9 (130 nM) or DCA (7.5 mM) were included as single treatment controls. Cells were treated with actinomycin D (0.2 μg/ml) to induce apoptosis and the latter served as a positive control for the induction of apoptosis (390).

2.4 Cell growth and proliferation

2.4.1 Real-time cell proliferation assays

The xCELLigence System (Real-Time Cell Analyzer Single Plate (RTCA SP®) system) was developed by ACEA Biosciences, Inc. (San Diego, CA, USA) in conjunction with Roche Diagnostics GmbH (Roche Applied Science, Mannheim, Germany) to monitor cellular events in real time without incorporation of dyes by measuring electrical impedance created by cells (391,392). The RTCA xCELLigence system utilizes micro-electronic sensor technologies for monitoring adherent cells. The core of the system is arrays of ultra-thin sheath of gold which serves as the microelectronic cell sensor that are integrated in the bottom of microtiter plates. In the absence of cells, strong current flow passes the microelectrodes with no disturbances. Presence of cells, quantity and

quality of cells affect the passage of electrons and ions on sensor surfaces; thus introducing impedance. The impedance may subsequently be converted to a Cell Index (CI) value. An increase in the presence of cells will lead to an increase in impedance and therefore cause a higher CI value. Likewise, when cells experience morphological changes such as cell shrinkage caused by apoptosis, the CI will decrease (Figure 2.1).

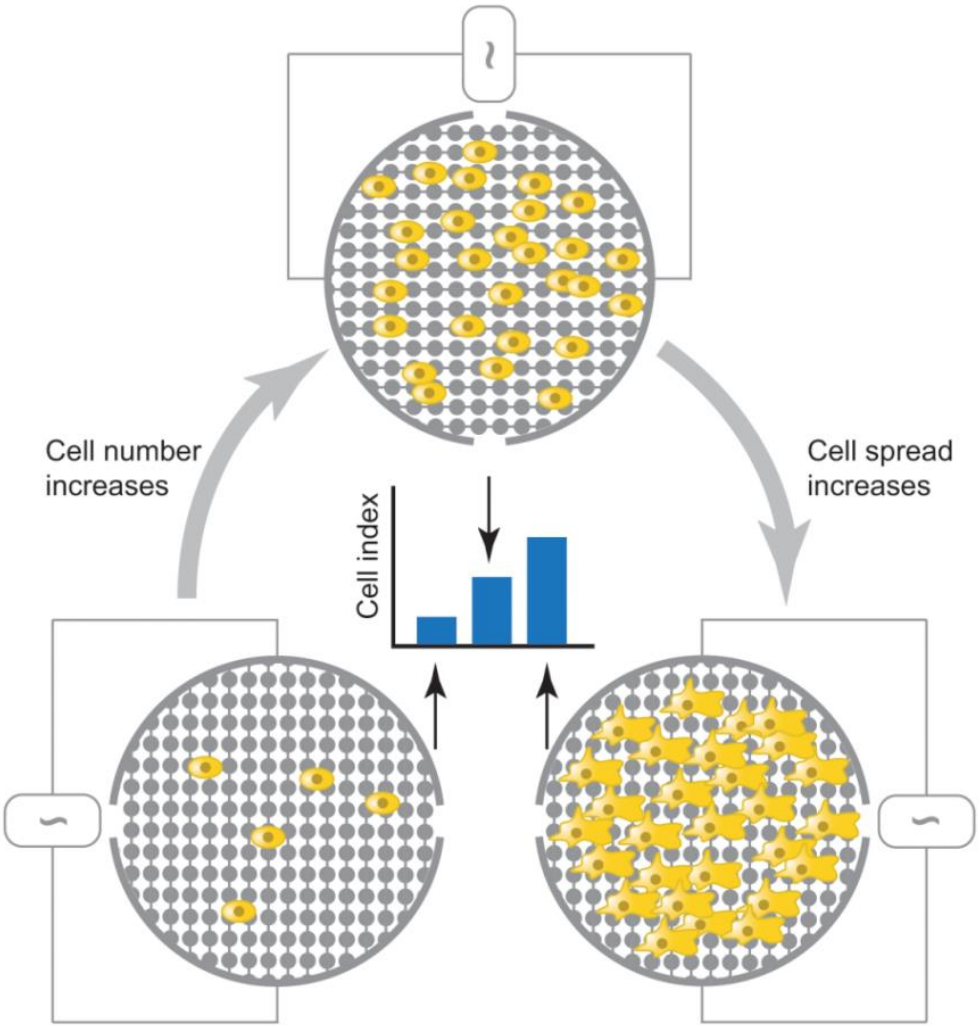

Figure 2.1: Real-Time Cell Analyzer Single Plate® system based on impedance technology detection of cell viability and motility. In the absence of cells, strong current flow passes the microelectrodes with no disturbances. The impedance introduced by presence of cell is converted to Cell Index (CI) value (393). (Adapted from Limame *et al.* (2012))

Materials

The Real-Time Cell Analyzer xCELLigence instrument and E-plate 96 were provided by Roche Diagnostics (Randburg, RSA).

Methods

The RTCA SP Station was connected to the RTCA Analyzer and subsequently joined the RTCA Control Unit. The xCELLigence System was connected and tested via Resistor Plate Verification before the RTCA SP Station was placed inside the incubator at 37°C and 5% CO_2. According to the ATCC Cell Culture Technical Resources (version 1825/CF/1111), approximately 0.5 x 10^5 cell/cm^2 to 1 x 10^5 cell/cm^2 is a typical yield for confluent continuous mammalian cell lines (cell line dependent). A 96-well plate occupies 0.32 cm^2 surface area and the cell yield should be 16 000 to 32 000 per well.

Cells were seeded at four different densities which were 20 000, 10 000, 5 000 and 2500 cells per well in E-Plate 96 microtiter plate devices (as suggested by supplier's manual). Briefly, cells were trypsinized, counted using the trypan blue exclusion method via a hemacytometer and resuspended in growth medium. Medium background measurements were taken by adding 100 µl of the appropriate medium to the wells of the E-Plate 96. When the plate was correctly placed into the RTCA SP station, the green indicator light was registered. RTCA Software Package 1.2 was used to automatically scan the plate with media and calibration of the plate was completed thereafter. Cells were trypsinized and prepared into a 400 000 cell/ml stock solution prior to exposure. A volume of 100 µl of the cell suspension was added to the wells of the E-Plate 96 which contained the 100 µl of growth medium with a final volume equal to 200 µl. MCF-7 and MCF-12A at densities of 20 000-, 10 000-, 5 000- and 2 500 cells per well were seeded and allowed to settle down at the bottom of the well at room temperature for 30 minutes before placing the E-Plate 96 onto the RTCA SP Station.

The RTCA Control Unit (laptop) was used to monitor cell attachment and proliferation continuously for a period of 48 h. At the same time, the impedance values were recorded and converted into CI value in real time and corresponding to each well

precisely. CI calculations for real-time dynamic cell proliferation assay (n=3) were automatically performed by the RTCA Software Package 1.2 of the xCELLigence system with error bars included on a cell proliferation curve. The CI curves of the plate are projected on RTCA Control Unit in real time.

2.4.2 Crystal violet assay

Crystal violet (*N*-hexamethylpararosaniline) is a colorimetric method that is commonly used to evaluate a new chemical entity on cell cultures in *in vitro* oncology discovery research (394). Crystal violet assay is used to obtain quantitative information about the cell number adhering to microtiter dishes (typically 96-well plate). In this project, dose- and time-dependent studies were conducted in order to determine the growth inhibitory effect on MCF-7 and MCF-12A cell lines of the combination compounds. Time-dependent studies were carried out at intervals of 24 h, 48 h and 72 h in order to determine the optimal compound exposure time for following experiments. Previously determined optimal seeding number for 96-well plate via xCELLigence RTCA system was used in crystal violet assays. The crystal violet dye generally binds nonspecific external to DNA molecule, with preference of two adjacent A-T base pairs (395). Thus, the cell number in monolayer culture can be quantified as a function of the absorbance of the amount dye incorporated by the DNA of these cells. This method allows for rapid, accurate and reproducible quantification of cell number in cultures proliferating in microtiter plates (396,397). Quantification is possible by solubilizing the adsorbed dye into a solution of triton X-100 and determining optical density (OD) spectrophotometrically at 570 nm (396).

Materials

Crystal violet, glutaraldehyde and triton X-100 were purchased from Merck (Munich, Germany). EL_x800 Universal Microplate Reader from Bio-Tek Instruments Inc. (Vermont, USA).

Methods

In order to determine the growth inhibitory effect of the dual treatment on both cell lines as well as the optimal exposure conditions, time- (24 h, 48 h and 72h) and dose- (C9: 100 nM - 200 nM; DCA: 2.5 mM - 40 mM)-dependent cell proliferation studies were conducted prior to final combination of dosage selection. Dosages chosen for C9 were based on previous *in vitro* proliferation assays conducted in our laboratory (366,377) and the concentrations selected for DCA were supported by literature (186,388,398).

Quantification of fixated monolayer cells was spectrophotometrically determined by employing crystal violet as a DNA stain. MCF-7 and MCF-12A cells were seeded in 96-well plates at a density of 5000 cells per well (200 µl medium/well). Cells were incubated at 37˚C for 24 h to allow for recovery and attachment. Cells were exposed to 130 nM of C9-, 7.5 mM of DCA-, C9+DCA and DMSO (v/v < 0.1%) for 24 h. At the end of the exposure period, medium was discarded and 100 µl of 1% glutaraldehyde was added to fixate cells for 15 min. Thereafter, glutaraldehyde was discarded and 100 µl of 0.1% crystal violet stain solution was added to cells and left at room temperature for 30 min. Subsequently, crystal violet stain was removed by immersing the plate under running tap water for 5 min. A 0.2% triton X-100 solution (200 µl) was added to the plate. Measurement of the absorbance of all treatments, as well as controls were conducted with an ELX800 Universal Microplate Reader from Bio-Tek Instruments Inc. (Vermont, USA) with 570 nm filter.

The percentage growth inhibition and half-maximal growth inhibitory concentration (IC_{50}) was calculated in order to compare the growth inhibition induced by the compounds on the various cell lines. The IC_{50} is the concentration that induces a percentage growth inhibition of 50.

$$Percentage\ growth\ inhibition = \frac{Blank-corrected\ absorbance\ of\ test\ condition\ after}{Blank-corrected\ absorbance\ of\ vehicle-treated\ control}\ x\ 100$$

Statistical analysis (n=6) was performed in Microsoft Excel and cell growth of treated cells was expressed as a percentage ratio to DMSO-exposed controls. Statistically significant results with $P < 0.05$ are indicated in the bar charts.

2.5 Cell viability

Lactate dehydrogenase assay

Cell viability assays are used for drug screening and one of the most robust tests is the lactate dehydrogenase (LDH) assay. Cell viability must be determined by counting the unstained live cells with a suitable instrument such as microscope or spectrophotometer. Cellular enzymes such as LDH is used as marker to indicate plasma membrane damage and indirect measurement of cell death (399). LDH is present in all cell types and is rapidly released into the cell culture medium upon damage of the plasma membrane (399). LDH oxidizes lactate to pyruvate and this reaction is coupled with formation of reduced NADH. Reagent WST-8 receives two electrons from NADH and changes to yellow. Quantification is possible by determining OD spectrophotometrically at 450 nm.

Materials

A lactate dehydrogenase Cytotoxicity Assay Kit from BioVision Inc. (Mountain View, CA, USA) was purchased through BIOCOM biotech (Pty) Ltd. (Clubview, PTA, RSA). Microplate Reader was supplied by Bio-Tek Instruments Inc. (Vermont, USA).

Methods

The effects of C9-, DCA- and C9+DCA on MCF-7 and MCF-12A cell viability were tested via the lactate dehydrogenase Cytotoxicity Assay Kit from BioVision Inc. (Mountain View, CA, USA) according to the manufacturer's instruction. MCF-7 and MCF-12A cells were seeded in 96-well plates at a density of 5000 cells per well (100 µl medium/well). Cells were incubated at 37˚C for 24 h to allow for recovery and attachment. Cells were exposed to 130 nM of C9-, 7.5 mM of DCA-, C9+DCA and DMSO (v/v < 0.1%) for 24 h prior to termination for LDH-cytotoxicity assay. Plates were gently shaken at the end of the incubation period to ensure LDH is evenly distributed in the culture medium. Thereafter, cells were centrifuged (300 x g) to ensure that no cell debris can influence the reading. Subsequently, 10 µl/well test plate medium was

transferred from tested plates into optically clear plates to obtain readings. In order to develop colour, 100 µl of LDH Reaction Mix solution was added and incubated for 60 min at room temperature. Measurement of the absorbance of all treatments, as well as controls were conducted with an ELX800 Universal Microplate Reader from Bio-Tek Instruments Inc. (Vermont, USA) with 450 nm filter and a reference wavelength of 650 nm.

A few important controls were included in the test protocol and they are listed as follows.

Control type	**Description**
Background control (BC)	100 µl culture medium per well with DMSO
Low control (LC)	100 µl cells propagated in medium with DMSO
High control (HC)	100 µl cells propagated in medium with DMSO, at the end of the 24 h experiment added 10 µl Cell Lysis Solution
Test samples (T)	100 µl cells with test substances

LDH cell viability percentages for the combination treatment, as well as appropriate controls were calculated with a specific formula. The background value was subtracted from all wells. Subsequently, the cytotoxicity was calculated as follows:

Cytotoxicity (%) = (Test samples – Low control) / (High control – Low control) x 100

Statistical analysis (n=6) was performed in Microsoft Excel and cytotoxicity of treated cells was expressed as a percentage ratio to cells that were propagated in medium only controls. Statistically significant results with $P < 0.05$ are indicated in the bar charts.

2.6 Cytotoxicity measurement and drug efficacy prediction

The xCELLigence System (Real-Time Cell Analyzer Single Plate (RTCA SP®) system) was developed by ACEA Biosciences, Inc. (San Diego, CA, USA) in conjunction with Roche Diagnostics GmbH (Roche Applied Science, 68298 Mannheim, Germany) to monitor cellular events in real time without incorporation of dyes by measuring electrical impedance created by cells (391,392). The principle of this technology was previously

described in section 2.4.1 and Figure 2.1. Addition of compound DCA, C9 and C9+DCA altered the cell proliferation and motility. This morphological change was immediately reflected on impedance conversion to CI. Subsequently, the RTCA Software Package 1.2 was used to calculate IC_{50} as well as drug efficacy prediction with aid of sigmoidal curve(s).

Materials

The Real-Time Cell Analyzer xCELLigence instrument and E-plate 96 were provided by Roche Diagnostics (Randburg, RSA).

Methods

Real-Time Cell Analyzer Single Plate (RTCA SP®) xCELLigence system was used to assess the cytotoxicity of compounds C9-, DCA- and C9+DCA on both MCF-7 and MCF-12A cells. Cells were seeded at 10 000 cells/well which is suitable for the surface area of E-Plate 96 microtiter plate devices (E-Plate™, as suggested by supplier's manual) (377). Briefly, background measurements were taken by adding 100 µl of the appropriate medium to the wells of the E-Plate 96. Subsequently, the RTCA Software Package 1.2 was used to calibrate the plate. Cells were trypsinized, counted using the trypan blue exclusion method via hemacytometer and resuspended in growth medium for preparation of a stock solution with density of 400 000 cell/ml. A volume of 100 µl of the cell suspension were added to the wells of the E-Plate 96 which contained the 100 µl of growth medium which made the final volume equal to 200 µl/well. MCF-7 and MCF-12A cells were seeded and allowed to settle down at the bottom of the well of the plate at room temperature for 30 minutes before placing it onto the RTCA SP Station. Cell attachment and proliferation were continuously monitored for a period of 24 h prior to exposure of compounds. Subsequently, exposure procedure were conducted by dissolving C9, DCA and C9+DCA into appropriate medium and then added into the wells. After exposure to different conditions, the RTCA Control Unit was used to monitor the real time cell proliferation and the impedance values were converted into a CI value corresponding to each well. The RTCA Software Package 1.2 was used to perform automated calculation of IC_{50} values as well as drug efficacy prediction with the aid of

sigmoidal curve(s). The CI value corresponded to the relative change in measured electrical impedance to represent cell status and was directly proportional to the quantity, size, and attachment forces of the cell. CI calculations for real-time dynamic cell proliferation assay (n=3) were automatically performed by the RTCA Software Package 1.2 of the xCELLigence system with error bars included on cell proliferation curve.

2.7 Morphological studies

2.7.1 Optical transmitted light differential interference contrast

Polarization-optical differential interference contrast (PlasDIC) is a polarization-optical transmitted light differential interference contrast method from Zeiss (Carl Zeiss MicroImaging GmbH, Göttingen, Germany). Unlike the traditional DIC method (Smith/Nomarski DIC method), the improved PlasDIC equipment positioned the polarizer and Wollaston prism after the light has already passed through the object and objective to create image qualities of excellences (400,401). PlasDIC contrast system allows the use of plastic dishes for microscopic examinations and deliver quality optical imaging, in particular, assessment of thick cells that lie in close proximity or form groups. Images of living cells were captured before and after the appropriate exposure in order to gain insight into the morphological effects of the newly synthesized compounds on these cells.

Materials

Zeiss inverted Axiovert CFL40 microscope and Zeiss Axiovert MRm monochrome camera were supplied by Carl Zeiss MicroImaging GmbH, Göttingen, Germany.

Methods

MCF-7 and MCF-12A cells were seeded in 6-well plates at a density of 375 000 cells/well (3 ml medium). Cells were exposed to DMSO-, C9-, DCA- and C9+DCA for 24

h respectively. All appropriate controls as discussed in paragraph 2.3 were also included in the experiment. At the end of the exposure period samples were simply observed under the Zeiss inverted Axiovert CFL40 microscope and Zeiss Axiovert MRm monochrome camera (Carl Zeiss MicroImaging GmbH, Göttingen, Germany). Morphological studies performed by means of PlasDIC microscopy were conducted in triplicates and a minimum of three representative images were captured from each sample. One representative set of images are displayed in the result section.

2.7.2 Light microscopy

Haematoxylin and eosin staining

Haematoxylin and eosin (H&E) stains are commonly used to recognize various cytoplasmic and nuclear morphologic changes that form the basis of contemporary cancer diagnosis. In basic cell culture, H&E staining method is used to monitor morphological changes introduced by certain compounds. Haematoxylin stains nucleic acids with a deep blue-purple colour (135). The cytoplasm can be contrasted and visualized with a pink eosin stain, because it binds non-specifically to protein (135). Various degrees of pink stain maybe used to distinguish cytoplasm and extracellular matrix (135). Moreover, images obtained from this technique were used to calculate the mitotic index which is the ratio of the number of cells undergoing mitosis (cell division) to the number of cells not undergoing mitosis (402).

Materials

Bouin's fixative was purchased from Sigma Aldrich (St. Louis, USA). Haematoxylin, eosin, ethanol, xylol and Entellam® fixative were purchased from Merck (Munich, Germany). The Zeiss Axiovert MRs microscope was purchased from Carl Zeiss MicroImaging GmbH, Göttingen, Germany.

Methods

MCF-7 and MCF-12A cells were seeded in 6-well plates at a density of 375 000 cells/3 ml medium/well on heat-sterilized cover slips. Cells were exposed to DMSO-, 130 nM C9-, 7.5 mM DCA- and C9+DCA for 24 h. All appropriate controls as discussed in paragraph 2.3 were also included in the experiment. Prior to staining, cover slips were transferred and fixed with Bouin's fixative for 30 min. The fixative was discarded and the cover slipimmersed in 70% ethanol for 20 min before rinsing with tap water. Mayer's haemalum was added and left for 20 min before rinsing it with tap water and ethanol (70%). Subsequently, 1% eosin was used to stain the cells for 5 min. Cover slips were rinsed twice with 70%, 96% and 100% ethanol and then xylol to ensure that excess water was removed. Samples were left to dry and observed under a Zeiss Axiovert MRs microscope (Carl Zeiss MicroImaging GmbH, Göttingen, Germany). In this experiment, data captures consisted of qualitative image examination, as well as quantitative mitotic indices. The latter was acquired by analysing and counting mitosis phase (prophase, metaphase, anaphase and telophase) of 1 000 cells per slide. Morphological studies performed by means of light microscopy were conducted in duplicates and a minimum of three representative images were captured from each sample. One representative set of images are displayed in the result section.

2.7.3 Fluorescent microscopy

Triple fluorescent staining: Hoechst 33342, acridine orange and propidium iodide

Fluorescent microscopy was employed to differentiate between viable and stressed cells. A triple fluorescent dye staining method was utilized to distinguish level of stress within cells. Fluorescent dyes such as acridine orange (green), Hoechst 33342 (blue) and propidium iodide (red) were used to indicate types of cell stress. Acridine orange is a lysosomotropic weak base which selectively accumulates in cellular acidic vacuolar compartments (403,404). The leakage of acridine orange from the acidic compartments to the cytosol shifts the fluorescence from red to green (405). Thus, increased green fluorescence within the cell may be used as indication of lysosome rupture. Hoechst

33342 is a fluorescent dye that penetrates both intact viable cell membranes and cells that are undergoing apoptosis to stain their nucleus. Propidium iodide (PI) is a fluorescent dye that is unable to penetrate an intact membrane and therefore stains the nucleus of cells that have lost their membrane's integrity due to oncotic and/or necrotic processes.

Materials

Hoechst 33342 (bisBenzimide), acridine orange and propidium iodide were purchased from Sigma Aldrich (St. Louis, USA). Zeiss inverted Axiovert CFL40 microscope (with Zeiss filter 2, 9 and 15) and Zeiss Axiovert MRm monochrome camera were supplied by Carl Zeiss MicroImaging GmbH, Göttingen, Germany.

Methods

Exponentially growing MCF-7 and MCF-12A cells were seeded at 375 000 cells per well in 6-well plates. After a 24 h attachment period, cells were exposed to treatments 130 nM C9-, 7.5 mM DCA- and C9+DCA respectively. All appropriate controls as discussed in paragraph 2.3 were also included in the experiment. After 24 h incubation period, Hoechst 33342 solution (500 µl with concentration of 3.5 µg/ml) was added to the medium to obtain a final concentration of 0.9 µM and plates were incubated for 25 minutes. Subsequently, 500 µl of acridine orange solution (4 µg/ml), as well as 500 µl propidium iodide solution (40 µg/ml) were added simultaneously to provide a final concentration of 1 µg/ml and 12 µM respectively. Plates were incubated further for five more minutes. In order to prevent fluorescent dye quenching, all procedures were performed in a dark room. Cells were examined with a Zeiss inverted Axiovert CFL40 microscope and Zeiss Axiovert MRm monochrome camera (Carl Zeiss MicroImaging GmbH, Göttingen, Germany) under Zeiss filter 2, 9 and 15 for Hoechst 33342- (blue), acridine orange- (green) and propidium iodide-stained cells respectively. Qualitative studies were repeated at least three times and a minimum of three representative images were captured from each sample. One representative set of images are displayed in the result section.

2.7.4 Confocal microscopy

Immunofluorescent detection of tubulin architecture

As mentioned previously, the newly synthesized C9 was designed to be an antimitotic compounds which interfere with microtubule dynamics. C9 was designed to bind to the colchicine site between α and β tubulins; thus it acts as spindle poison which has the ability to prevent cell division (366). Confocal microscopy was employed to observe the effect of the newly synthesized antimitotic compound C9 (130 nM), as well as the combination C9+DCA (7.5 mM) on MCF-7 and MCF-12A cells. The cytoskeletal microtubule architecture of control and treated MCF-7 and MCF-12A were compared after 24 h exposure time.

Materials

A primary monoclonal mouse anti-tubulin alpha antibody from IMGENE (Alexandria, VA, USA) (cat no. IMG-80196) was purchased from BIOCOM biotech (Pty) Ltd. (Clubview, PTA, RSA) and the fluorophore-labelled donkey anti-mouse heavy and light chain secondary IgG with Alexa Fluor 350 secondary antibody from Invitrogen (Carlsbad, CA, USA) was purchased from The Scientific Group (JHB, RSA).

Methods

Exponentially proliferating MCF-7 and MCF-12A cells were seeded (375 000 cells/well) on cover slips in the 6-well plate, incubated for 24 h. Cells were exposed to DMSO-, C9-, DCA- and C9+DCA for 24 h respectively. All appropriate controls as discussed in paragraph 2.3 were also included in the experiment. Cells were washed three times with pre-warmed 37˚C cytoskeletal buffer (CB) (60 mM 1,4 piperazinediethanesulfonic acid, 27 mM 4-(2-hydroxyethyl)-1-piperazineethanesulfonic acid, 10 mM ethylene glycol tetraacetic acid, 4 mM magnesium sulphate heptahydrate, pH = 7.0) and fixated with pre-warmed 0.3% glutaraldehyde at 37˚C for 10 min. Subsequently, cells were washed again with pre-warmed 37˚C cytoskeletal buffer by placing the 6-well plate onto a slowly rotating orbital shaker at 5 revolutions per min. In order to stain the intracellular

components, cellular membranes were permeabilized with 1% triton X-100 that was diluted in CB buffer. Thereafter, cells were washed once with CB and twice with PBS buffer.

Unreacted aldehydes were removed with reducing agent solution prepared by dissolving highly toxic sodium borohydride in PBS (1 mg/ml). Subsequently, cells were washed with PBS and blocked in 5% bovine serum albumin (BSA) for 60 min at room temperature. Mouse monoclonal anti-α-tubulin antibody (IMG-80196, Imgenex) was used with a 1:100 ratio for microtubule structure detection with an incubation period of 1.5 h in the incubator. Subsequently, cells were counter-stained with fluorophore-labelled donkey anti-mouse heavy and light chain secondary IgG with Alexa Fluor 350 (Invitrogen) fluorescent probe for 1 h with dilution factor of 1:125 in the incubator (protect the fluorophores from light by cover the sample with aluminium foil). Nuclei were stained with 4',6-diamidino-2-phenylindole (DAPI, Sigma) afterwards for 10 min at room temperature. Stained cells were mounted on microscopy slides and viewed with a Zeiss 510 META confocal laser microscope (Carl Zeiss MicroImaging GmbH, Göttingen, Germany) (376). Confocal microscopy was conducted in duplicates and a minimum of three representative images were captured from each sample. One representative set of images are displayed in the result section.

2.7.5 Transmission electron microscopy

Transmission electron microscopy (TEM) was used to determine the ultrastructure of intracellular components. Electron microscopy, especially the transmission electron microscopy (TEM), is able to detect the ultra-structural changes within the cell. Irregular cell outlines, extrusion of membrane-bound cytoplasm containing organelles, fragmented nucleus and increased density of microvilli are typical morphological observations from TEM micrograph of apoptotic cells (125).

Materials

Osmium tetroxide (aqueous), glutaraldehyde, phosphate buffer quetol, Reynolds' lead citrate and uranyl acetate (aqueous) were purchased from Merck (Munich, Germany). A Multi-purpose Philips 301 TEM was used to view the prepared samples.

Methods

Exponentially growing MCF-7 and MCF-12A cells were seeded at 1.2 x 10^6 cells/25 cm^2 flasks. Medium was discarded after allowing 24 h attachment and the cells were exposed to treatment of 130 nM C9, 7.5 mM DCA, C9+DCA respectively (24 h). All appropriate controls as discussed in paragraph 2.3 were also included in the experiment. After incubation, cells were trypsinized and resuspended in 1 ml of growth medium in eppendorf tubes. Cells were fixed in glutaraldehyde (2.5%) in phosphate buffer (0.075M, pH 7.4-7.6) for 1 h and samples were rinsed three times with PBS for 5 min. Thereafter, cells were fixed with aqueous osmium tetroxide for 30 min and were rinsed three times in distilled water. Samples were dehydrated with increasing concentrations of ethanol and infiltrated with 30% quetol in ethanol for 1 h. Samples were polymerized at 60˚C for at least 36 h before ultra-thin sections were prepared with the aid of a microtome and mounted on a copper grid. Subsequently, samples were contrasted with 4% uranyl acetate for 10 min and rinsed with water (406). Samples were observed under the Multi-purpose Philips 301 Transmission Electron Microscope situated at Electron Microscopy Unit, University of Pretoria, Pretoria, RSA. Transmission electron microscopy was conducted in duplicates and a minimum of three representative images were captured from each sample. One representative set of images are displayed in the result section.

2.8 Cell cycle analysis

Cell cycle analysis is based on univariate analysis of cellular DNA content following cell staining with PI and expression of the cellular DNA content frequency histograms. This experimental approach reveals distribution of cells in four major phases of the cycle namely G_1, S, G_2/M and cell population contains fractionated DNA (407). This type of analysis is made possible by employing flow cytometry technology where a number of detectors are focused at the point where the stream of cells passes through the light beam. Flow cytometry was utilized to analyse the effects of C9 and DCA on cell cycle progression of MCF-7 and MCF-12A cells. Propidium iodide fluorescence (relative DNA content per cell) was measured with a fluorescence activated cell sorting (FACS) FC500 System flow cytometer (Beckman Coulter SA (Pty) Ltd.) equipped with an air-cooled argon laser excited at 488 nm. Data from at least 10 000 cells per sample were analysed with CXP software (Beckman Coulter SA (Pty) Ltd). Data from cell debris (particles smaller than apoptotic bodies) and clumps of two or more cells were removed to display accurate data. Cell cycle distributions were calculated with non-commercialized Cyflogic software 1.2.1 (Pertu Therho, Turku, Finland) by assigning relative DNA content per cell to sub-G_1, G_1, S and G_2/M fractions. Propidium iodide dye emits light at 617 nm, therefore, data obtained from the fluorescent detector number 3 (Fl3, detects 630 nm emissions) are represented as histograms on the x-axis.

Materials

Propidium iodide and RNAse A were purchased from Sigma Aldrich (St. Louis, MO, USA). Ethanol and triton X-100 were purchased from Merck (Munich, Germany).

Methods

Exponentially growing MCF-7 and MCF-12A cells were seeded at 500 000 cells/25 cm^2 flask. After a 24 h attachment period, medium was discarded and cells were exposed to DMSO-, C9-, DCA- and C9+DCA for 24 h respectively. All appropriate controls as discussed in paragraph 2.3 were also included in the experiment. After a 24 h exposure period, cells were trypsinized and resuspended in 1 ml of growth medium. Cells were

centrifuged (300 x g) for five minutes and supernatant was discarded. Cells were resuspended in 200 µl of ice-cold PBS containing 0.1% FBS. Afterwards, ice-cold 70% ethanol (4 ml) were added in a drop wise manner and cells were stored for at least 24 h at 4˚C. Prior to the analyzing step, cells were pelleted by centrifugation at 300 x g for 5 minutes and resuspended in 1 ml of PBS containing propidium iodide (40 µg/ml), RNAse A (100 µg/ml) and triton X-100 (0.1%) and incubated at 37˚C for 45 minutes prior to FC500 System analysis. Experimental data from at least three biological repeats for cell cycle analysis were statically analysed with non-commercialized Cyflogic software 1.2.1 (Pertu Therho, Turku, Finland) by assigning relative DNA content per cell to sub-G_1, G_1, S and G_2/M fractions.

2.9 Apoptosis quantification

Phosphatidylserine outer membrane redistribution: Annexin V-fluorescein isothiocyanate

One of the earliest indications of apoptosis is the translocation of the membrane phospholipid phosphatidylserine (PS) from the inner to the outer leaflet of the plasma membrane (183). Once exposed to the extracellular environment, binding sites on PS become available for Annexin V, therefore PS externalization was chosen as the marker for apoptosis (183,184). Annexin V is a 35 kDa phospholipid-binding protein which has a high affinity for PS in the presence of physiological levels of calcium ions (1.2 mM) (182,185). Annexin V is conjugated to a fluorochrome, FITC and used for identification by flow cytometry for early stages of apoptosis. PS translocation also occurs during necrosis (408); therefore propidium iodide is used to distinguish between necrotic and early apoptotic cells.

Materials

The Annexin V-FITC kit (MACS, Miltenyi Biotech) was purchased from BIOCOM biotech Pty Ltd. (Clubview, PTA, RSA).

Methods

Exponentially growing MCF-7 and MCF-12A cells were seeded (500 000 cells/25 cm^2 flask), left to attach for 24 h and exposed to 130 nM C9, 7.5 mM DCA and C9+DCA respectively. All appropriate controls as discussed in paragraph 2.3 were also included in the experiment. After 24 h exposure time, cells were trypsinized and resuspended in 1 x Binding Buffer (1 ml) and were centrifuged at 300 x g for 10 min. The supernatant was removed and cells were washed and resupended in 100 µl of 1x Binding Buffer. Samples were incubated with Annexin V-FITC (10 µl) in the dark (covered in aluminium foil) for 15 minutes. Thereafter, cells were washed with 1 x Binding Buffer (1 ml) and were centrifuged at 300 x g for 10 minutes. The supernatant was discarded and cells were resuspended in 500 µl of 1 x Binding Buffer solution. Immediately prior to analysis, 5 µl of propidium iodide (100 µg/ml) was added and mixed gently. Propidium iodide fluorescence (oncotic cells) and annexin V fluorescence (apoptotic cells) were measured with a FACS FC500 System flow cytometer (Beckman Coulter SA (Pty) Ltd.) equipped with an air-cooled argon laser excited at 488 nm. Each sample with at least 10 000 cells/events were measured/collected with FACS FC500 System flow cytometer (Beckman Coulter SA (Pty) Ltd.). Experimental data from at least three biological repeats for PS outer membrane redistribution were statistically analysed with non-commercialized Cyflogic software 1.2.1 (Pertu Therho, Turku, Finland).

2.10 Autophagic activity

Microtubule-associated protein 1 light chain 3 (II) expression

The microtubule-associated protein 1 light chain 3 (LC3) associates with autophagosome membranes (409). The detailed biochemical involvement of LC3 and formation of autophagosomes is discussed in section 1.3.2. A commonly used marker for active autophagy is the autophagosome-associated form of LC3: LC3-II (410). Flow cytometry was employed to quantify elevated levels autophagy induction in MCF-12A and MCF-7 cells. Cells were stained with FITC-conjugated microtubule associated light

chain 3 (LC3) membrane protein antibodies to quantify the autophagy-related LC3 protein.

Materials

FITC conjugated anti-autophagy-related (LC3) antibody from Novus Biologicals Ltd. (NB600-1384) (Cambridge, UK) was purchased from BIOCOM biotech (Pty) Ltd. (Clubview, PTA, RSA). Bovine Serum Albumin BSA and triton X-100 were purchased from Sigma Aldrich (St. Louis, USA).

Methods

MCF-7 and MCF-12A cells were seeded at 500 000 cells/25 cm^2 flask. After 24 h of attachment, cells were treated with 130 nM C9 and 7.5 mM DCA respectively. All appropriate controls as discussed in paragraph 2.3 were also included in the experiment. Tamoxifen (20 µM) was used to induce autophagy. After 24 h exposure, cells were trypsinized, washed with ice-cold PBS, and fixed with 0.01% paraformaldehyde. Subsequently, cells were permeabilized with 1 ml of ice-cold methanol (stored at -20˚C) in a drop-wise manner. Cells were washed with cold PBS and mixed with 500 µl of the FITC-conjugated anti-autophagy-related LC3B antibody (0.5 µg/ml) (NB600-1384) (Novus Biologicals Ltd., Cambridge, UK) for 2 h at 4˚C in the dark. Thereafter, cells were washed twice with washing buffer (PBS, 0.05% triton X-100 and 1% BSA) and at least 10 000 events were measured with a fluorescence activated cell sorting (FACS) FC500 System flow cytometer (Beckman Coulter SA (Pty) Ltd.). Experimental data from at least three biological repeats for autophagic related LC3-II were statically analysed with non-commercialized Cyflogic software 1.2.1 (Pertu Therho, Turku, Finland).

2.11 Mitochondrial membrane potential depolarization

Mitochondrial-initiated apoptotic events are regarded as non-receptor-mediated intrinsic signalling pathways for apoptosis. In apoptotic cells, MitoCapture™ cannot aggregate in

the mitochondria due to the altered mitochondrial membrane potential and thus remains in the cytoplasm in its monomer form, generating a green fluorescence.

Materials

The MitoCapture™ apoptosis detection kit produced by BioVision Inc. (Mountain View, CA, USA) was purchased through BIOCOM biotech (Pty) Ltd. (Clubview, PTA, RSA).

Methods

MCF-7 and MCF-12A cells were seeded at 500 000 cells/25 cm^2 flask. After 24 h attachment the cells were exposed to the compound 130 nM C9, 7.5 mM DCA and C9+DCA (24 h) respectively. All appropriate controls as discussed in paragraph 2.3 were also included in the experiment. Cells were subsequently trypsinized and incubated with 1 ml of MitoCapture™ reagent for 15 min. At least 10 000 events with fluorescent dye were measured with a fluorescence activated cell sorting (FACS) FC500 System flow cytometer (Beckman Coulter SA (Pty) Ltd.). Experimental data from at least three biological repeats for mitochondrial membrane potential depolarization were statically analysed with non-commercialized Cyflogic software 1.2.1 (Pertu Therho, Turku, Finland).

2.12 Oxidative stress test via 2', 7'-dichlorofluorescein fluorescence

The fluorescent compound 2', 7'-dichlorofluorescein (DCF) (DCF test) is used to evaluate intracellular oxidative stress. 2′, 7′-Dichlorodihydrofluorescein diacetate (H_2DCF-DA) is a non-fluorescent lipophilic compound which readily passes through the plasma membrane to form hydrophilic dihydrodichlorofluorescein (H_2DCF). Subsequent oxidation of H_2DCF to fluorescence DCF is dependent on Fenton-type reactions, cytochrome *c* and H_2O_2 (411). The lysosome is the highest iron containing organelle within the cell, thus lysosomal rupture will result in an increased fluorescent signal for DCF. Cytochrome *c* and H_2O_2 are released when the mitochondria is stressed.

Consequently, a positive DCF test might be interpreted as a sign of oxidative stress from lysosomal membrane permeabilization and mitochondrial damage (142).

Materials

Non-fluorescent lipophilic compound H_2DCF-DA was purchased from Sigma Aldrich (St. Louis, MO, USA).

Methods

MCF-7 and MCF-12A cells were seeded at 500 000 cells/25 cm^2 flask. After 24 h attachment period was allowed the cells were exposed to 130 nM of C9, 7.5 mM of DCA and C9+DCA respectively for 24 h. All appropriate controls as discussed in paragraph 2.3 were also included in the experiment. Cells were trypsinized and incubated with 10 µM H_2DCF for 20 min. Fluorescence of the compound DCF was measured with a FACS FC500 System flow cytometer (Beckman Coulter SA (Pty) Ltd.). Ferric iron chelator deferoxamine mesylate salt (DFO, 100 µM) and antioxidant *N*-acetyl-*L*-cysteine (NAC, 5mM) were used as positive controls in this experiment. When complexed with DFO and NAC, iron and ROS are prevented from redox cycling and are unable to support Fenton-type reaction respectively (133,412). Each sample with at least 10 000 events were measured with FACS FC500 System flow cytometer (Beckman Coulter SA (Pty) Ltd.). Experimental data from at least three biological repeats for DCF test were statistically analysed with a Java-based flow cytometry data analysis program WEASEL v3.0.2 (trail version, available from Walter and Eliza Hall institute of Medical Research).

2.13 Kinase inhibition studies

The oxidative stress level alteration may trigger cascade events which result in the activation of p38 and JNK (413). Thus, it was decided to determine how p38 activation and JNK pathway was affected on untreated, as well as treated MCF-7 and MCF-12A cells. A p38 inhibitor (15 µM, SB239063) and JNK inhibitor (20 µM, SP600125) were

chosen based on literature (414) and added either in untreated or treated MCF-7 and MCF-12A cells.

Materials

p38 inhibitor SB239063 and JNK inhibitor SP600125 were purchased from Sigma Aldrich (St. Louis, MO, USA).

Methods

The effect of p38 inhibitor SB239063 and JNK inhibitor SP600125 on treated and untreated MCF-7 and MCF-12A cells were investigated by means of morphological observation via PlasDIC, influences on mitochondrial membrane potential depolarization via MitoCapture™ apoptosis detection kit and the cell proliferation curve via the RTCA xCELLigence system. The detailed protocols, as well as statistical analysis procedures of PlasDIC, MitoCapture™ and xCELLigence have been introduced previously in sections 2.7.1, 2.11 and 2.4.1 respectively.

2.14 Protein expression analysis

2.14.1 B cell leukaemia-2 expression and phosphorylation at Serine 70

Bcl-2 is an anti-apoptotic protein which is regulated at the level of phosphorylation by JNK at a multi-site phosphorylation loop namely serine 70, tryptophan 69 and serine 87 (415). Single-site hyper-phosphorylation at serine 70 leads to prevention of apoptosis. However, hyper-phosphorylation of Bcl-2 at multi-site (serine 70, tryptophan 69 and serine 87), hypo-phosphorylation at Bcl-2 serine 70, as well as a decrease in total Bcl-2 protein expression are factors associated with its pro-apoptotic properties (416). Merck Millipore's FlowCellect^{TM} Bcl-2 Activation Dual Detection Kit was used to investigate the total amount of Bcl-2 protein, as well as the phosphorylation status of Bcl-2 (serine 70 position) simultaneously within the same experimental sample. This kit contains two

antibodies that quantify the total amount of Bcl-2 protein (FL1 Log) and S70 phosphorylation status of Bcl-2 per cell simultaneously (FL3 Log). JNK inhibitor (JNKi) SP600125 (20 μM) and p38α inhibitor (p38i) SB239063 (15 μM) were included in the experiment to test whether these pathways play a roll with regards to activation/deactivation of Bcl-2 protein in MCF-7 and MCF-12A cells.

Materials

FlowCellect™ Bcl-2 Activation Dual Detection Kit produced by Millipore Corporation (Billerica, MA, USA) was purchased through Microsep (Pty) Ltd (Sandton, JHB, RSA).

Methods

Exponentially growing MCF-12A and MCF-7 cells were seeded at 500 000/25cm^2 flasks. After a 24 h attachment period the cells were exposed to 130 nM of C9, 7.5 mM of DCA and C9+DCA respectively for 24 h. All appropriate controls as discussed in paragraph 2.3 were also included in the experiment. After 24 h treatment time, cells were trypsinized and counted so that 500 000 cells were centrifuged (600 x g, 3 min) per sample. Samples medium were discarded and cells were resuspended in 1 X Wash Buffer (0.5 ml) and centrifuged at 600 x g for 3 min. The supernatant was removed and cells were suspended in 1 x Fixation Buffer (0.5 ml) (0.1% formaldehyde) and incubated for 20 min at room temperature. Afterwards, cells were centrifuged (600 x g) and the supernatant was removed prior to suspension in 1 x Assay Buffer (0.5 ml) (1% BSA). Cells were spun down at 600 x g for 3 min and buffers were discarded. Ice-cold 1 x Permeabilization Buffer (500 μl 100% methanol) was added and the cells were suspended and incubated on ice for 10 min. Samples were centrifuged at 600 x g for 3 min, then resuspended in 0.5 ml 1 x Assay Buffer.

Prior to the staining step, cells were centrifuged for 3 min at 600 x g. Samples were resuspended and stained by adding 100 μl of 1 x Assay Buffer containing an anti-Bcl-2 antibody conjugated to AlexaFluor® 488 and an anti-pBcl-2 (Ser^{70}) conjugated to phycoerythrin. The mixture was incubated for 60 min on ice in the dark, after which 900

µl of 1 x Assay Buffer was added to wash and pellet the cells at 600 x g (3 min). The cells were washed and centrifuged again (600 x g for 3 min) with 500 µl 1 x Assay Buffer. Samples were resuspended in 500 µl 1 x Assay Buffer before analysing it on the flow cytometer. Fluorescence of the FL1 (total Bcl-2 antibody expression) and FL3 (pBcl-2 Ser^{70}) channel were measured simultaneously with at least 10 000 events per sample by employing FACS FC500 System flow cytometer (Beckman Coulter SA (Pty) Ltd.). Experimental data from at least three biological repeats for FlowCellect™ Bcl-2 Activation Dual Detection were statistically analysed with a Java-based flow cytometry data analysis program WEASEL v3.0.2 (trail version, available from Walter and Eliza Hall institute of Medical Research).

2.14.2 Caspase 7 activity

Procaspase 7 is cleaved by executioner caspases 8, 9 and 10 into active caspase 7 (417). Active caspase 7 are effector caspases that cleave a number of substrates, which trigger cascade events that eventually result in morphological and biochemical features of apoptosis (417).

Materials

A rabbit antibody for active caspase 7 from BioVision Inc. (Mountain View, CA, USA) and an anti-rabbit immunoglobulin antibody conjugated to Dylight™ 488 from Rockland Inc (Gilbertsville, PA, USA) were purchased from BIOCOM biotech (Pty) Ltd. (Clubview, PTA, RSA).

Methods

Exponentially growing MCF-7 and MCF-12A cells were seeded at 500 000 cells/25 cm^2 flask. After 24 h of attachment, cells were treated with DMSO-, 130 nM C9-, 7.5 mM DCA-, C9+DCA- and actinomycin D respectively for 24 h. Cells were washed with PBS, trypsinized, and pelleted (300 x g). Subsequently, cells were fixed with 500 µl of 1% paraformaldehyde (in PBS) for 20 min at room temperature, pelleted (300 x g) and

resuspended in 500 µl PBS. Further permeabilization of the cells was achieved by adding 500 µl ice-cold 100% methanol. Subsequent washing and re-suspension steps were carried out consecutively in 100 µl 1% BSA buffer. Thereafter, cells were incubated with caspase 7 antibody-(15 µg/ml) (BioVision Inc., Mountain View, CA, USA) for 90 min in the dark. Anti-rabbit immunoglobulin antibody conjugated to Dylight™ 488 from Rockland Inc. (0.2 µg/ml) (Gilbertsville, PA, USA) was used as secondary antibodies for flow cytrometry analysis. Each sample was measured with a FACS FC500 System flow cytometer with at least 10 000 events (Beckman Coulter SA (Pty) Ltd.). Experimental data from at least three biological repeats for caspase 7 were statistically analysed with non-commercialized Cyflogic software 1.2.1 (Pertu Therho, Turku, Finland).

2.15 Microarrays

Gene expression analysis: Complimentary RNA microarray

Gene expression changes in MCF-12A and MCF-7 cells due to C9+DCA exposure for 24 h were carried out using Agilent's Human 1A Oligo 60-mer Microarray (V2) 44k slides. Qiagen® RNeasy Plant Mini Kit (Valencia, CA, USA) and RNase-free DNase (Valencia, CA, USA) were used to conduct RNA extraction.

(I) RNA extraction

Exponentially growing MCF-12A and MCF-7 cells were seeded at 750 000 cells/25cm^2 flasks. After 24 h of attachment, medium was discarded and cells were exposed to C9+DCA and incubated for 24 h. After exposure, cells were washed twice with PBS and lysed by adding 1 mL RLT buffer (RNeasy Plant Mini Kit, Qiagen®, Valencia, CA, USA) to each flask. Lysates was pipetted into Qiashredder columns (Qiagen®, Valencia, CA, USA) and centrifuged for 2 min at 9000 x g. The flow-through was collected and one volume of 70% ethanol was added and gently mixed. This solution was divided into Qiagen Plant Mini Kit columns (Qiagen®, Valencia, CA, USA) (700 µl per column) and centrifuged for 15 sec at 9000 x g. The flow-through was discarded. RW1 buffer (350 µl)

was added to each column in order to wash the column. The column was centrifuged for 15 sec at 9000 x g. A DNase mixture was prepared utilizing Qiagen's RNase-free DNase Set (Valencia, CA, USA) by adding 70 µl RDD buffer (Qiagen®, Valencia, CA, USA)to every 10 µl DNase1, adding 80 µl of this mixture in the middle of each column and leaving it at room temperature for 15 min. Another 350 µl RW1 buffer was added and the column was centrifuged for 15 s at 9000 x g. Flow-through was discarded and columns were transferred to new eppendorf tubes. A series of washing steps followed. RPE buffer (Qiagen®, Valencia, CA, USA) (500 µl) was added to each tube and centrifuged for 15 sec at 12000 x g, discarding the flow-through afterwards and replacing the eppendorf tubes. This step was repeated. Next, the column was centrifuged at 9000 x g for 1 min. In order to elute the total RNA from the column, RNase-free water (50 µl) was added to the column and centrifuged for 1 min at 9000 x g. Total RNA was suspended in RNase-free water (50 µl) and was quantified with the NanoDrop 1000 (Thermo Fisher Scientific Inc. Wilmington, Delaware, USA) and tested for integrity by means of electrophoresis.

(II) RNA integrity

Agarose powder (0.6 g) was dissolved in 40 ml RNase free water (for 1.5% gel). In addition, 6 ml 10 x 3-(N-morpholino)propanesulfonic acid (MOPS), 3.4 ml formaldehyde and 14 ml RNase-free water was used to make the gel. A sample mix to be loaded in the well was prepared by adding 3 µg total RNA (±8 µl), 2 µl tracking dye ((50% glycerol, 100 mM disodium ethylenediaminetetraacetic acid (Na_2EDTA), pH 8.0, 1% sodium dodecyl sulfate (SDS), 0.1% bromophenol blue 0.1%)) and 1 µl ethidium bromide (0.5 µg/mL final concentration). The mixture was heated for 15 min at 55˚C and rapidly chilled on ice afterwards. A sample (15 µl) was pipetted into a well of the agarose-formaldehyde RNA gel and electrophoresis was conducted at 80 mV for 45 min.

(III) Labelled cRNA synthesis

Agilent's Low RNA Input Fluorescent Linear Amplification Kit was used to generate fluorescently labelled complimentary ribonucleic acid (cRNA). Labelled cRNA was produced using the T7 RNA polymerase (from the Agilent Low RNA Input Linear

Amplification Kit PLUS, Two-Color) and purification of labelled cRNA was conducted using Qiagen's RNeasy Mini kits. For each sample, 2000 ng of total polyA RNA was added to a 1.5 ml microcentrifuge tube and filled with RNase free water to a final volume of 8.3 µl or less.

Spike A Mix (2.0 µl) containing the positive control mRNA for the cyanine 3-deoxycytosine triphosphate (CTP) dye reactions and the Spike B Mix (2.0 µl) containing the positive control mRNA for the cyanine 5-CTP dye reactions were added to their respective samples containing the extracted total RNA from either the vehicle-treated controls or the compound-treated experiments. T7 Promoter Primer (1.2 µl) was added to each sample and the primer and the template were denatured by incubating the reaction at 65˚C in a circulating water bath for 10 min. After 10 min the reactions were placed on ice and incubated for 5 min.

For each sample 4 µl 5X First Strand Buffer, 2 µl 0.1 M dithiothreitol (DTT), 1 µl 10 mM deoxyribonucleotide triphosphate (dNTP) mix containing 10 mM deoxyadenosine triphosphate (dATP), 10 mM deoxycytosine triphosphate (dCTP), 10 mM deoxyguanosine triphosphate (dGTP), and 10 mM deoxythymidine triphosphate (dTTP), 1 µl Moloney Murine Leukemia Virus Reverse Transcriptase (MMLV-RT) and 0.5 µl RNase inhibitor (RNaseOUT) were added and incubated at 40˚C in a circulating water bath for 2 h. Thereafter, samples were incubated on ice for 5 min and then incubated at 65˚C in a circulating water bath for 3 h.

Samples were briefly centrifuged to drive down any precipitation. To each sample 15.3 µl nuclease-free water, 20 µl of 4X Transcription Buffer, 6 µl of 0.1 M DTT, 8 µl nucleotide triphosphate (NTP) mix, 0.5 µl 50% polyethylene glycol (PEG) 6.4 RNaseOUT, 0.6 µl inorganic pyrophosphatase, 0.8 µl T7 RNA Polymerase and 2.4 µl of either cyanine 3-CTP or cyanine 5-CTP were added. Samples were incubated at 40˚C in a circulating water bath for 2 h.

Labelled cRNA was purified using Qiagen's RNeasy mini spin columns. To each sample, 20 µl of nuclease-free, 350 µl of Buffer RLT and 250 µl of ethanol (100% purity) were added and mixed thoroughly by pipetting. This solution was pipetted onto the RNeasy

mini spin columns columns (700 µl per column) and centrifuged for 15 sec at 9000 x g. The flow-through was discarded and 500 µl RPE buffer was added to each tube and centrifuged for 15 sec at 12000 x g, discarding the flow-through afterwards and replacing the eppendorf tubes. This step was repeated. The column was centrifuged at 9000 x g for 1 min in order to remove all residual liquid. In order to elute the total RNA from the column 35 µl RNase-free water was added to the column and centrifuged for 1 min at 9000 x g. Labelled cRNA was suspended in 35 µl RNase-free water and was spectrophotometrically quantified with the NanoDrop 1000 (Thermo Fisher Scientific Inc. Wilmington, Delaware, USA).

(IV) Hybridization of Cy-dye labelled cRNA

cRNA was considered pure of organic contamination (*e.g.* ethanol or phenol) with a 260/230 ratio greater than 1.5. Pure cRNA was hybridized to Agilent Human 1A (V2) oligonucleotide 44K microarray slides according to the manufacture's guidelines using Agilent's 2 x GEx Hybridization Buffer HI-RPM in Agilent's SureHyb chambers. A hybridization mixture was prepared by adding equal amounts of Cy-3 and Cy-5 labelled cRNA (825 ng), 11 µl 10 X blocking Agent, 2.2 of 25 x Fragmentation Buffer to a final volume of 55 µl. Samples were incubated at 60°C for exactly 30 minutes to fragment the RNA. After 30 min, 55 ml of the 2 x Hybridization Buffer was added to each sample. The backing slides were placed in Agilent's microarray hybridization chambers and the above prepared solution was pipetted (100 µl) onto each grid (four grids on one slide). The backing slide is a single-use, silicone gasket designed for Agilent microarray slides, that hold the sample and is assembled with the hybridization chamber.

The assembled slide chamber was placed in an Agilent's hybridization oven set to 65˚C and 10 rpm. Samples were hybridized for 17 hours. Afterwards the slides were washed twice for 1 min in Falcon tubes containing Agilent's Gene Expression Wash Buffer 1 at room temperature and once in Falcon tubes containing Agilent's Gene Expression Wash Buffer 2 at 37˚C for 1 min. The slide was transferred to acetonitrile Sigma Aldrich (St. Louis, MO, USA) for 1 min and then subsequently to Agilent's Stabilization and Drying Solution to help prevent ozone bleaching of the Cy-fluorochromes. The slides

were gently removed from the Stabilization and Drying Solution and scanned immediately.

(V) Scanning of Agilent microarray slides

Slides were scanned with the Axon Genepix 4000B Scanner (Molecular Devices, USA) provided by the African Centre of Gene Technology (ACGT) Microarray Facility at the University of Pretoria.

(VI) Spotfinding

Spotfinding was performed using Genepix Pro 6.1 (Molecular Devices Corporation, Sunnyvale, CA USA). GenePix Pro 6.1 uses a set of proprietary feature-finding algorithms to find circular features. Every pixel in a region around the feature is examined by a local alignment algorithm and assigned to feature or background. Global alignment algorithms determine the translation, rotation and skew of blocks of features. Saturated spots, spots with an uneven background, non-uniform spots and spots with a low intensity versus back ground ratio were removed from further analysis by excluding the spots that satisfied the following parameters. The excluded spots were assigned as “Bad” as previously described by Stander (2007) (418).

Saturated spots:
[F532 % Sat.] > 30 And
[Ratio of Means (635/532)] > 0.75 Or
[F635 % Sat.] > 30 And
[Ratio of Means (635/532)] < 1.3333

Spots with an uneven background:
([B635 Mean] > (1.5*[B635 Median]) Or
[B532 Mean] > (1.5*[B532 Median])) And
([B635 Median] > 40 Or
[B532 Median] > 40)

Non-uniform spots:

[Ratio of Medians (635/532)] > (4.0*[Rgn Ratio (635/532)]) Or
[Ratio of Medians (635/532)] < (0.25*[Rgn Ratio (635/532)])

Low intensity vs back ground ratio:

[% > B635+2SD] < 10 Or [% > B532+2SD] < 10

(VII) Limma statistical analysis

Statistical analysis after spotfinding was conducted using Limma with the LimmaGUI interface (419,420). Background correction was done with the normal+exponential (Normexp) convolution model to observed intensities. The normal part represents the background and the exponential represents the signal intensities (420). The Normexp offset value was set to 25 (418). A value of 25 maximized the df.prior is the numeric vector giving empirical Bayes estimated degrees of freedom associated with s2.prior for each gene. s2.post is the numeric vector giving posterior residual variances. A maximized df.prior is optimal and will allow for greater power to detect differentially expressed genes (420). Spot quality weighting was performed and Genepix Flag weightings that were flagged as “Bad” were excluded from further analysis. Normalization within arrays was performed to remove dye-bias at higher and lower intensities by normalizing M-values (log-ratios) with the Global Loess method (421). The M-value (M) represents a log2-fold change between two or more experimental conditions. The A-value (A) is the average log2-expression level for a gene across all the arrays and channels in the experiment.

The **M-value** is calculated as follows:
M = log2(Cy5)/Cy3)
(Cy5/Cy3 values are the normalized emission intensities of the spot)

The **A-value** is calculated as follows:
A = (log2(Cy5)*Cy3))/2

Aquantile normalization between arrays was performed in order to normalize expression intensities so that the intensities or log-ratios have similar distributions across a series of arrays (421). Aquantile normalization ensures that the A-values (average intensities) have the same empirical distribution across arrays leaving the M-values (log-ratios) unchanged (421). The Least squares linear model fit method was employed and the *P*-values were adjusted for multiple testing utilizing the Benjamini and Hochberg's step-up method for controlling the false discovery rate (422). Genes that had a *P*-value of less than 0.05 were considered statistically significantly differentially expressed and were included in further analyses.

(VIII) Gene expression analysis

Biological interpretation and functional analysis of gene lists were performed by mapping differentially expressed genes to biochemical pathways and Gene Ontology (GO) categories using Gene Annotation Co-occurrence Discovery (GENECODIS) (423). GENECODIS is a web-based tool for finding sets of biological annotations that frequently appear together and are significant in a set of genes (423). In order to determine common genes that were affected by the compounds between cell lines as well as the different compounds, differentially expressed gene lists were compared utilizing GeneVenn (424). GeneVenn is a simple, web-based application creating Venn diagrams from two or three gene lists.

2.16 Logistics

All *in vitro* experiments were conducted at the University of Pretoria, Pretoria, South Africa. All cell culture work and related experiments were completed at the Department of Physiology, Prinshof campus, University of Pretoria. Flow cytometric analysis was conducted at the Department of Pharmacology, Prinshof campus, University of Pretoria. Microarray gene expression study was conducted at the African Centre for Gene Technologies (ACGT) Microarray facility, Department of Plant Sciences, Hatfield campus, University of Pretoria. Transmission electron microscopy and confocal

microscopy were conducted at the Electron Microscopy Unit, Hatfield campus, University of Pretoria.

2.17 Statistics

Statistical analyses of the data were conducted as discussed with Professor Piet J Becker of the unit for Biostatistics at the Medical Research Council. The statistical microarray data analysis was accredited by Professor Fourie Joubert of the Bioinformatics Unit of University of Pretoria.

Qualitative studies

Morphological studies performed by means of light-, fluorescent-, confocal- and electron microscopy were conducted at least in duplicate and a minimum of three representative images were captured from each sample.

Quantitative studies

CI calculations for real-time dynamic cell proliferation assay (n=3) were performed automatically by the RTCA Software Package 1.2 of the xCELLigence system with error bars included on cell proliferation curve. Experimental data from at least three biological repeats for cell number, cell viability test, cell cycle, PS externalization, autophagic activity (LC3-II) expression, mitochondria membrane potential ($\Delta\Psi m$) assay, DCF test, Bcl-2 expression, Bcl-2 Ser^{70} phosphorylation and caspases 3 & 7 activity were statistically analysed.

Statistical considerations

The quantitative part of the study such as apoptosis, autophagy, cell cycle, spectrophotometry measurements (cell growth and cell viability) and flow cytometry measurements ($\Delta\Psi m$ reduction, DCF test, Bcl-2 expression, Bcl-2 Ser^{70} phosphorylation and caspase 7 activity) was assessed using a factorial experimental

design with two factors, i.e. cell type (cancer, non-cancer) and treatment (DMSO, DCA, C9, DCA+C9).

Sample size

Three replicates per factor combination will yield 16 degrees of freedom for the error term in the appropriate analysis of variance (ANOVA), which confirms with convention that requires at least 12 degrees of freedom for the error term.

Data analysis

Data summary employed mean, standard deviation and where appropriate 95% confidence intervals. Each of the quantitative variables was analysed in two-way ANOVA with main factors treatment and cell type along with a term for the interaction between treatment and cell-type. Comparisons between treatments were three active treatments compared to DMSO and the combination DCA+C9 versus DCA and C9 respectively. For the comparison within the same experimental study, two-tailed Student's *t*-test was used for appropriate contrasts with 0.05 level of significance regarded as statistically significant ($P < 0.05$).

3. Chapter 3: Results

3.1 Cell growth and proliferation

3.1.1 Real-time cell proliferation assays

The xCELLigence System allows for real-time dynamic monitoring of cell attachment, adhesion and proliferation. Dynamic cell proliferation of MCF-7 and MCF-12A cells plated on the E-Plates 96 was monitored in 30-minute intervals over 96 hours from the time of plating until the end of the experiment. The E-Plates 96 mimic the ordinary 96-well microtiter plates except for the addition of the ultra-thin sheath of gold beneath the plastic plate which serve as microelectrodes to conduct current across the plate. The presence of cells on top of the thin sheath of gold will disturb the local current and introduce electrode impedance to the local ionic environment. Thus, any type of cell morphological alteration will cause changes in the impedance value and ultimately convert it into a Cell Index (CI) value. The latter is directly proportional to impedance value.

MCF-7 and MCF-12A at densities of 20 000, 10 000, 5 000 and 2 500 cells/well in E-Plates 96 were seeded and observed for a period of 48 h (Figure 3.1). Growth curves generated via the xCELLigence system revealed that MCF-7 and MCF-12A each had distinctive cell proliferation profiles. MCF-7 displayed a rapid attachment over the first 2 h followed by approximately 20 h long exponential phase depending on the number of cells seeded per well and finally entered an stationary cell growth phase (Figure 3.1A). MCF-12A cells had increased cell index after 1 h seeding when compared to MCF-7 cells (Figure 3.1B). Negative controls (medium only without any cells) which are indicated in turquoise in Figure 3.1 recorded CI value of zero throughout the experiment. This result revealed the medium for culture was free from contamination (Figure 3.1). Impedance/CI of 20 000, 10 000, 5 000 and 2 500 cells/well increased proportionally to cell numbers of MCF-7 and MCF-12A cells (Figure 3.1). CI is directly proportional to the number of cells seeded per well with the exception of 20 000 cells/well MCF-12A cells.

Cell index difference values for MCF-7 and MCF-12A cells were statistically significant with $P < 0.05$ at 20 000 cells/well (Figure 3.2), indicating that this condition is not optimal for comparing the two cell lines with each other in terms of cell proliferation.

It is of vital importance to ensure cell quality and correct amount of cells per specific surface area for any *in vitro* cell experiments to avoid false positive or false negative results. Proliferation curves of MCF-12A cells revealed that at the higher densities, 20 000 cells/well (Figure 3.1B), cells numbers plateaued rapidly and CI declined. This is possibly caused by cell contact inhibition. At a density of 20 000 cells/well, MCF-7 and MCF-12A cells stopped proliferation at 40 h and at 5 h respectively post-seeding due to contact inhibition, thus, making it unsuitable to conduct 24 h cell growth studies with this starting amount of cells/well. In contrast, at 2 500 cells/well, neither cell line showed typical characteristics of proliferation. Furthermore, at the densities of 5000 and 10 000 cells/well, cells were still actively proliferating 24 h after seeding (Figure 3.1). It was demonstrated the most suited amount of cells per 0.32 cm^2 (surface area of a single well of 96-well plate), for this comparative studies was either 10 000 or 5 000 cells. Subsequently, 5000 cells/0.32 cm^2 were chosen for crystal violet experiments as the cells reached confluency later than that of the 10 000 cells/well.

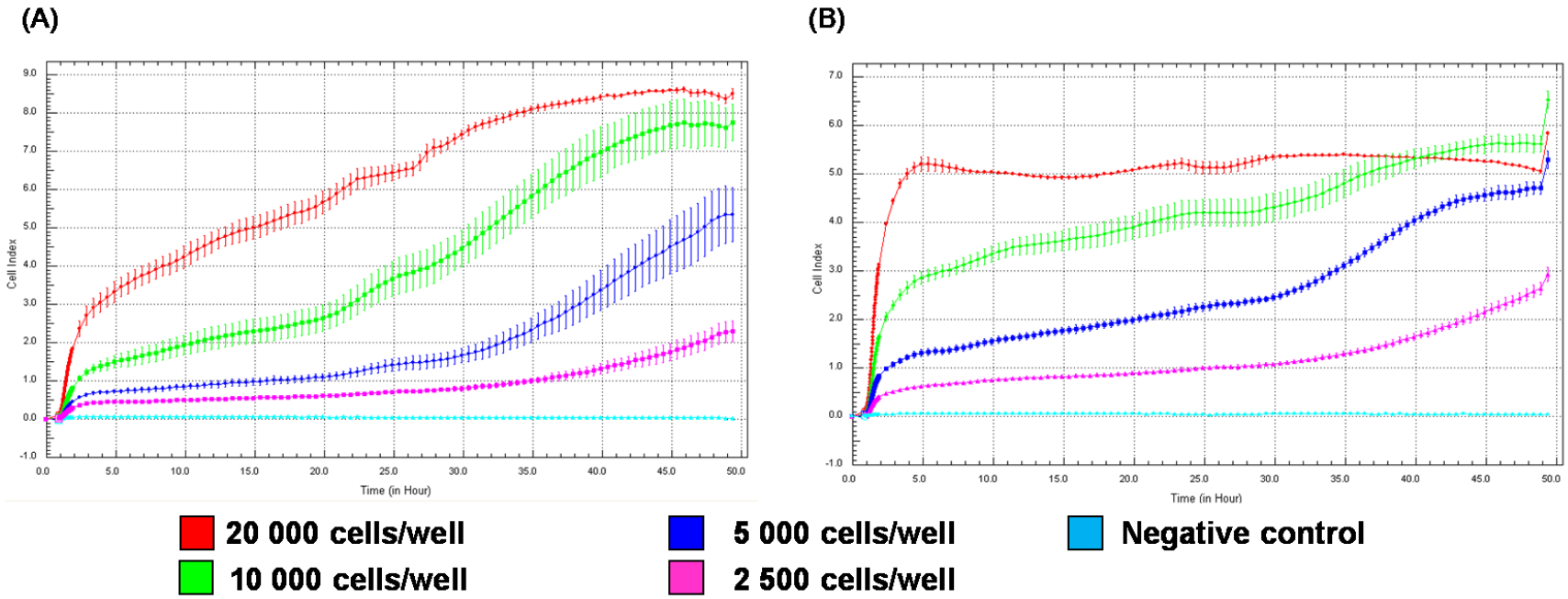

Figure 3.1: Real-time dynamic monitoring of cell adhesion and proliferation via the xCELLigence system. MCF-7 (A) and MCF-12A (B) seeded at densities of 20 000, 10 000, 5 000 and 2 500 cells per well in E-Plates 96 were observed for a period of 48 h. At density of 20 000 cells/well, MCF-7 and MCF-12A cells stopped proliferation at 40 h and at 5 h respectively post-seeding. At 2 500 cells/well, both cell line did not display typical characteristics of proliferation curve. The densities of 5000- and 10 000 cells/well, MCF-7 and MCF-12A cells exhibited smooth increase of CI. CI is directly proportional to the number of cells seeded per well with the exception of 20 000 cells/well MCF-12A cells which is possibly caused by cell contact inhibition.

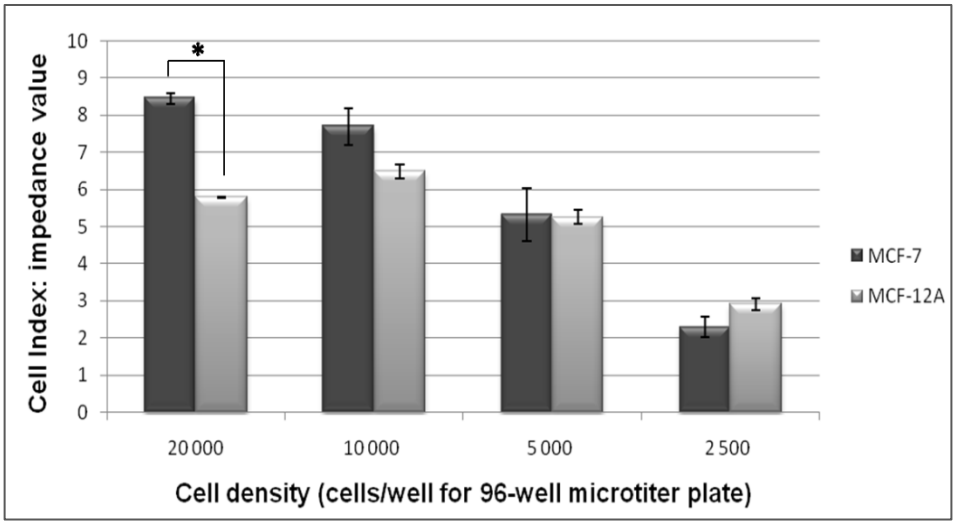

Figure 3.2: Cell number titration in the E-plate 96 after being monitored for 48 h. Cell number index expressed as impedance value for both MCF-7 and MCF-12A cells with cell densities of 20 000, 10 000, 5 000 and 2 500 cells/well in the E-plate 96 after being monitored for 48 h. An asterisk (*) indicates a *P*-value < 0.05 for CI index difference when MCF-7 and MCF-12A cells were compared.

3.1.2 Crystal violet assay

Time- and dose-dependent cell growth studies (Figure 3.3 and Figure 3.4) were conducted for selection of optimal exposure conditions. A previous study conducted in our laboratory by Stander *et al.* (366) has revealed the growth inhibitory effect (GI_{50}) value for C9-exposed MCF-7 cells to be 130 nM after 48 h of exposure. This concentration served as benchmark for concentration selection for combination drug treatment. Selection of concentrations for combination therapy was conducted by setting up one non-variable constant (C9 with concentration of 130 nM) and combining this with a range of different concentrations of dichloroacetic acid (2.5 mM, 5.0 mM, 7.5 mM and 15.0 mM). The range of concentrations for DCA was based on other studies using similar concentrations (388,398). A process of elimination was used to determine the exposure time and concentrations. Figure 3.4 illustrated the MCF-7 cell number reduction upon different kinds of exposure conditions over 72 h periods. The vehicle (DMSO) used to dissolve C9 was biologically and molecularly inert with no toxic effect observed on the cells with (v/v) not exceeding 0.01%. Addition of DMSO to proliferating cells had 100% growth rate compared to cells that propagated in medium only; thus indicating DMSO is well suited as a solvent for *in vitro* testing (Figure 3.3 and 3.4).

Percentage growth inhibition for C9 on MCF-7 cells calculated as described was 79%, 75% and 69% for 24 h, 48 h and 72 h respectively and was statistically significantly different when compared to the vehicle-treated control (Figure 3.3). DCA at concentrations of 2.5 mM, 5.0 mM and 7.5 mM had no adverse effect on MCF-7 growth (Figure 3.3). Tumorigenic cells that were exposed to 15 mM of DCA for 48 and 72 h showed significant cell number reduction to 70% and 50% respectively. Similarly, MCF-12A cells also showed adverse effect by higher dosage of DCA and longer exposure time (≥ 7.5 mM; 48 h and 72 h). Additional testing of 40 mM DCA on both cell lines exhibited powerful cell number reduction (data not shown). Therefore, concentrations of DCA which were higher than 15 mM were not suitable and excluded for further *in vitro* testing. When compared to its vehicle-exposed control, the combination of C9 and DCA reduced MCF-7 and MCF-12A cell number statistical significantly at any given dosage and time point. Furthermore, time- and dose-dependent trends for the treatment of C9+DCA on both cell lines were detected (Figure 3.3 and Figure 3.4).

It was decided to select condition(s) of dose and time for exposure purposes which inhibited cell growth by 50% (IC_{50}). Figure 3.3 demonstrated time- and dose-dependent cell growth study of tumorigenic MCF-7 cells. This result showed combination of 130 nM of C9 with 7.5 mM or 15.0 mM of DCA reduced MCF-7 cell proliferation to 55.9% and 43.1% respectively after 24 h exposure time (Figure 3.3). Under the same conditions (130 nM C9 with 7.5 mM or 15.0 mM DCA for 24 h), non-tumorigenic MCF-12A cells displayed high number of cell survival 70% and 65.4% respectively (Figure 3.4). This observation revealed the selectivity of C9+DCA towards tumorigenic cells for the 24 h exposure condition. Furthermore, neither 2.5 mM nor 5.0 mM of DCA in combination with 130 nM of C9 inhibited cell growth more than 30% in MCF-7 and MCF-12A cell lines after 24 h exposure, therefore these concentrations are not suitable for further testing (Figure 3.3 and Figure 3.4).

The selected window of DCA (7.5 – 15.0 mM) combined with 130 nM of C9 were repeated to ensure a correct protocol was followed and to confirm the specific concentration which would be used for further testing. Amongst concentrations of 7.5 mM, 10.0 mM, 12.5 mM and 15 mM DCA, C9 (130 nM) combined with 7.5 mM DCA still demonstrated 50% inhibition effect compared to control in MCF-7 cells (Figure 3.5). Yet, the MCF-12A cells showed a higher percentage of cell survival under the same given conditions (C9+DCA (7.5 mM) for 24 h) (Figure 3.6). In the end, after repeating the experiments three times and confirmed with the previous results, it was decided to use 130 nM of C9 in combination with 7.5 mM of DCA with 24 h exposure for all subsequent experiments. The exposure condition was chosen based on the principle of lowest concentration of drugs with maximal efficacy, which selectively target tumorigenic cells within a 24 h time frame.

Cell growth analysis by means of crystal violet DNA staining revealed that compound C9-exposed MCF-7 cells demonstrated approximately 20% cell growth inhibition (percentage growth inhibition = 80%) compared to vehicle exposed MCF-7 cells ($P < 0.05$) after 24 h of exposure (Figure 3.7). DCA-exposed (24 h) MCF-7 cells did not show significant cell inhibition compared to DMSO-exposed control (Figure 3.7). However, MCF-7 cell numbers after 24 h of exposure to 130 nM of C9 in combination with DCA

(7.5 mM) revealed a statistically significant decrease of 50.84% ($P < 0.05$) (Figure 3.7). Therefore, a synergistic effect of DCA in combination with C9 was observed, in which DCA serves as an adjuvant to enhance the pharmacokinetics of the microtubule disruptor, C9, in rapidly proliferating tumorigenic cells.

For the MCF-12A cells, C9 also induced cell inhibition in non-tumorigenic cells and revealed approximately 28% growth inhibition (percentage cell growth = 72%) compared to the vehicle-treated control ($P < 0.05$) (Figure 3.7). Growth inhibition for combination-exposed MCF-12A cells was approximately 29% and was not statistically significantly different from the C9-treated MCF-12A cells (Figure 3.7). Thus, no synergistic effect for combination-exposed MCF-12A cells was observed (Figure 3.7). MCF-12A cells responded statistically significantly differently to the combination treatment when compared to MCF-7 cells, with MCF-7 cell growth being inhibited to a greater extent (50.84%, percentage growth inhibition = 49.16%) when compared to the MCF-12A-treated cells (71%, percentage growth inhibition = 29%) ($P < 0.05$) (Figure 3.7).

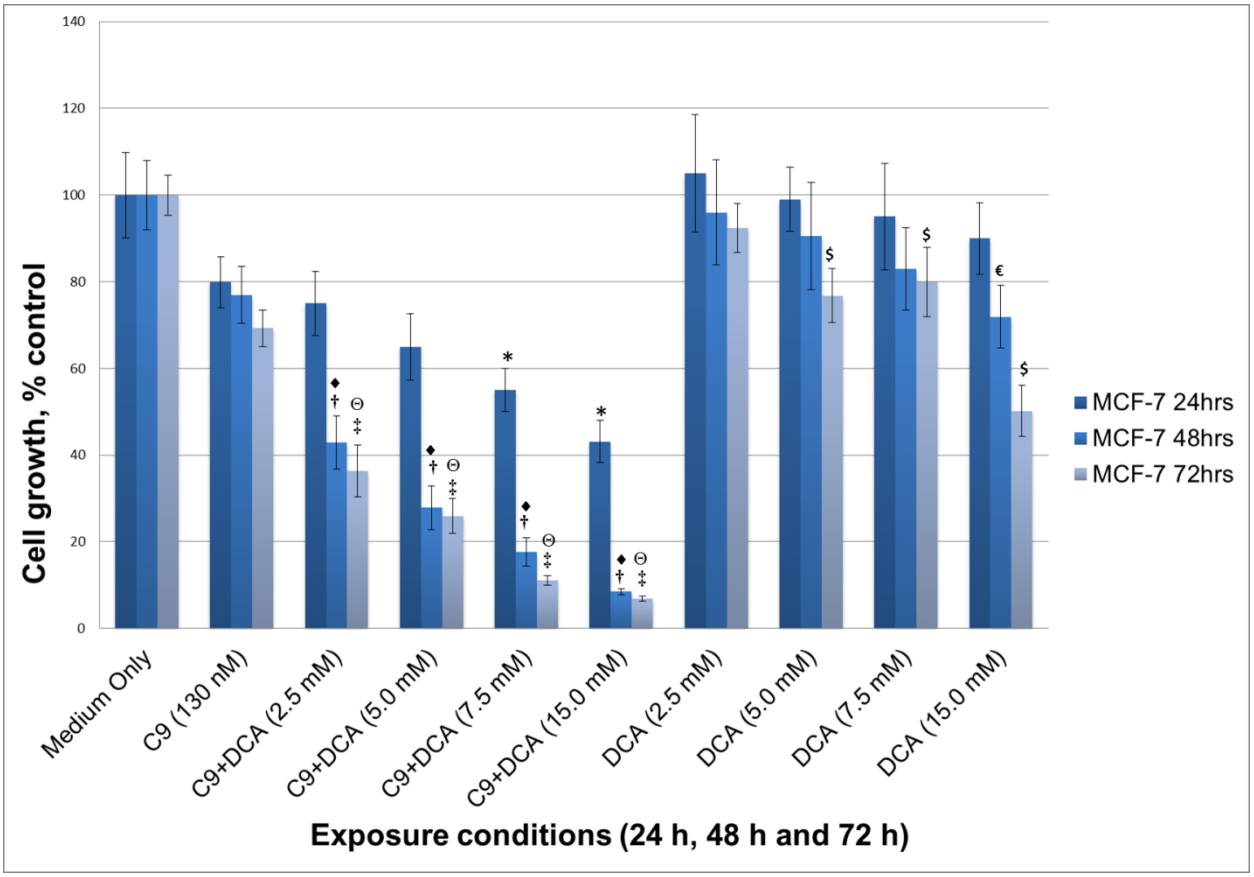

Figure 3.3: Time- and dose-dependent MCF-7 cell growth study via crystal violet assay. Cell growth expressed as a percentage of the control (cells propagated in medium and the vehicle, DMSO < 0.01%) after 24 h, 48 h and 72 h of exposure to different conditions. Four different concentrations of DCA (2.5 mM, 5.0 mM, 7.5 mM and 15.0 mM) were combined with 130 nM of C9. $^{*}P < 0.05$ when C9 and C9+DCA treatments were compared for 24 h exposure. $^{\dagger}P < 0.05$ when C9 and C9+DCA treatments were compared for 48 h exposure. $^{\ddagger}P < 0.05$ when C9 and C9+DCA treatments were compared for 72 h exposure. $^{\blacklozenge}P < 0.05$ when 24 h and 48 h exposure times were compared for a specific C9+DCA treatment concentration. $^{\Theta}P < 0.05$ when 24 h and 72 h exposure times were compared for a specific C9+DCA treatment concentration. $^{€}P < 0.05$ when DMSO- and DCA-exposed cells were compared for 48 h exposure. $^{\$}P < 0.05$ when DMSO- and DCA-exposed cells were compared for 72 h exposure.

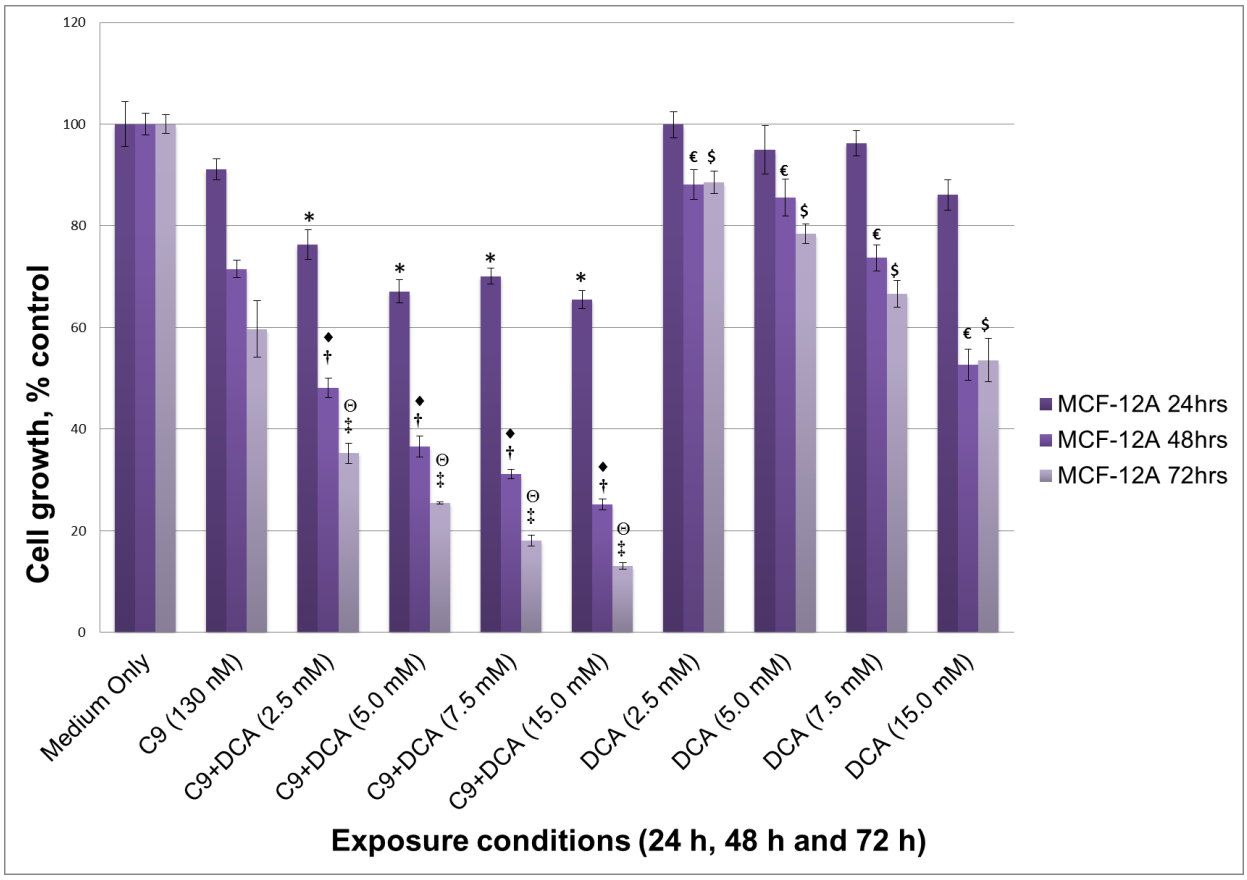

Figure 3.4: Time- and dose-dependent MCF-12A cell growth study via crystal violet assay. Cell growth expressed as a percentage of the control (cells propagated in medium and the vehicle, DMSO < 0.01%) after 24 h, 48 h and 72 h of exposure to different conditions. Four different concentrations of DCA (2.5 mM, 5.0 mM, 7.5 mM and 15.0 mM) were combined with 130 nM of C9. $^{*}P$ < 0.05 when C9 and C9+DCA treatments were compared for 24 h exposure. $^{\dagger}P$ < 0.05 when C9 and C9+DCA treatments were compared for 48 h exposure. $^{\ddagger}P$ < 0.05 when C9 and C9+DCA treatments were compared for 72 h exposure. $^{\blacklozenge}P$ < 0.05 when 24 h and 48 h exposure times were compared for a specific C9+DCA treatment concentration. $^{\Theta}P$ < 0.05 when 24 h and 72 h exposure times were compared for a specific C9+DCA treatment concentration. $^{€}P$ < 0.05 when DMSO- and DCA-exposed cells were compared for 48 h. $^{\$}P$ < 0.05 when DMSO- and DCA-exposed cells were compared for 72 h.

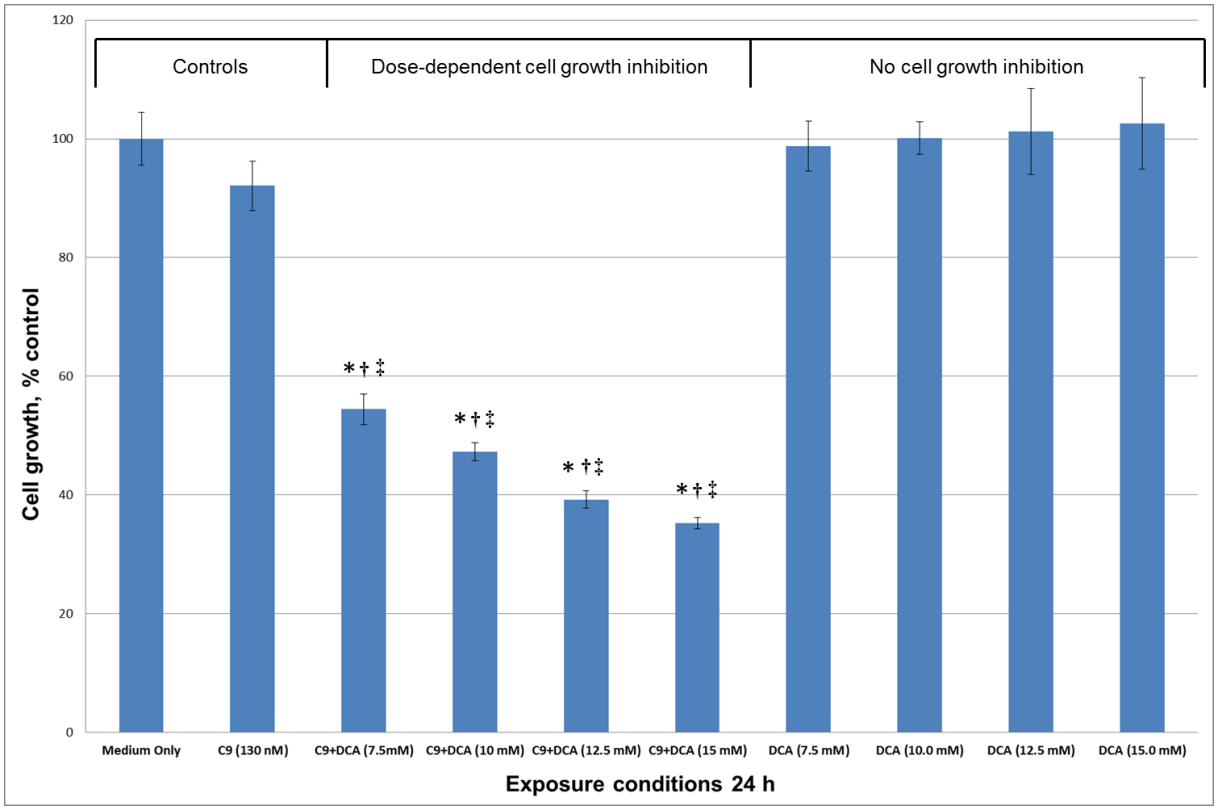

Figure 3.5: MCF-7 cell growth inhibition study via crystal violet assay. Cell growth expressed as a percentage of the control (cells propagated in medium and the vehicle, DMSO < 0.01%) after 24 h of exposure to different conditions. Four different concentrations of DCA (7.5 mM, 10.0 mM, 12.5 mM and 15.0 mM) were combined with 130 nM of C9. Combination of 130 nM of C9 with 7.5 mM, 1.0 mM, 12.5 mM and 15 mM DCA inhibited MCF-7 cell growth in dose-dependent manner. $^{\dagger}P$-value < 0.05 when C9+DCA-treated cells and DMSO-exposed were compared. $^{*}P$-value < 0.05 when C9- and C9+DCA-treated cells were compared. $^{\ddagger}P$-value < 0.05 when DCA- and C9+DCA-treated cells were compared.

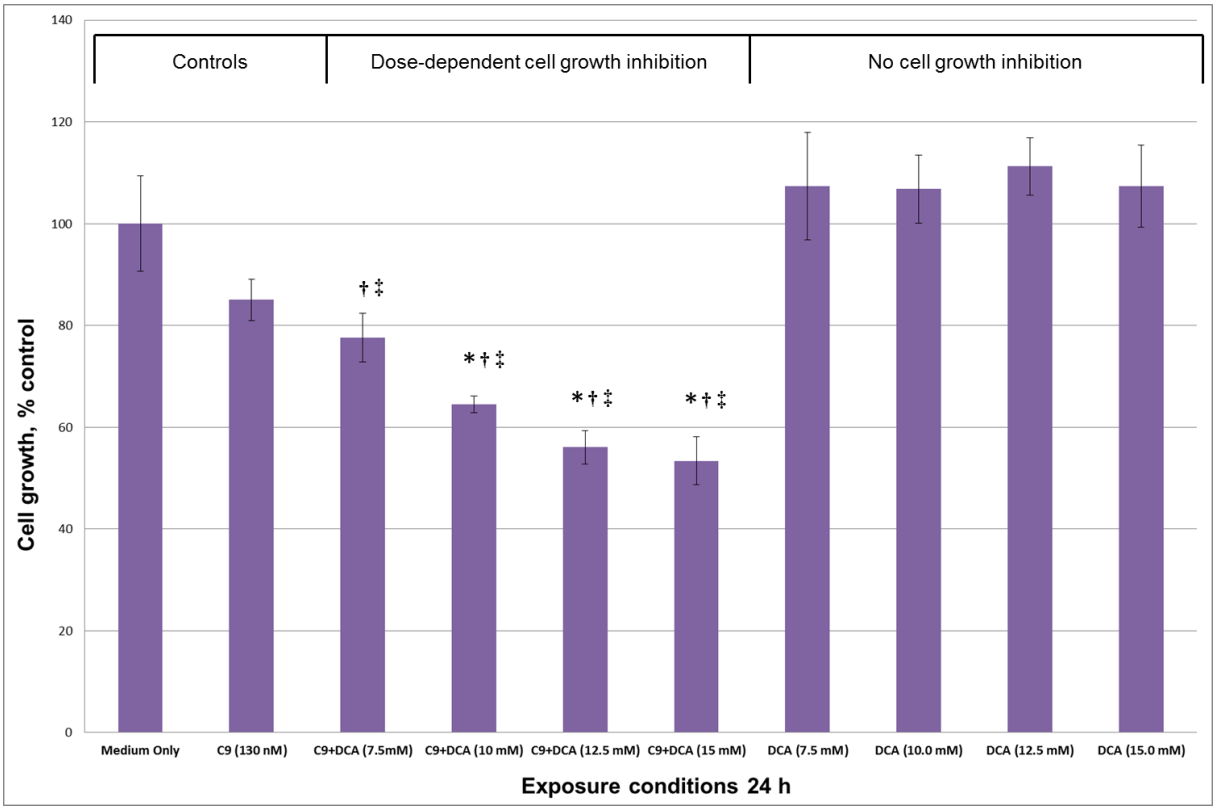

Figure 3.6: MCF-12A cell growth inhibition study via crystal violet assay. Cell growth expressed as a percentage of the control (cells propagated in medium and the vehicle, DMSO < 0.01%) after 24 h of exposure to different conditions. Four different concentrations of DCA (7.5 mM, 10.0 mM, 12.5 mM and 15.0 mM) were combined with 130 nM of C9. Combination of 130 nM of C9 with 7.5 mM, 1.0 mM, 12.5 mM and 15 mM DCA inhibited MCF-12A cell growth in dose-dependent manner. $^{\dagger}P$-value < 0.05 when C9+DCA-treated cells and DMSO-exposed were compared. $^{*}P$-value < 0.05 when C9- and C9+DCA-treated cells were compared. $^{\ddagger}P$-value < 0.05 when DCA- and C9+DCA-treated cells were compared.

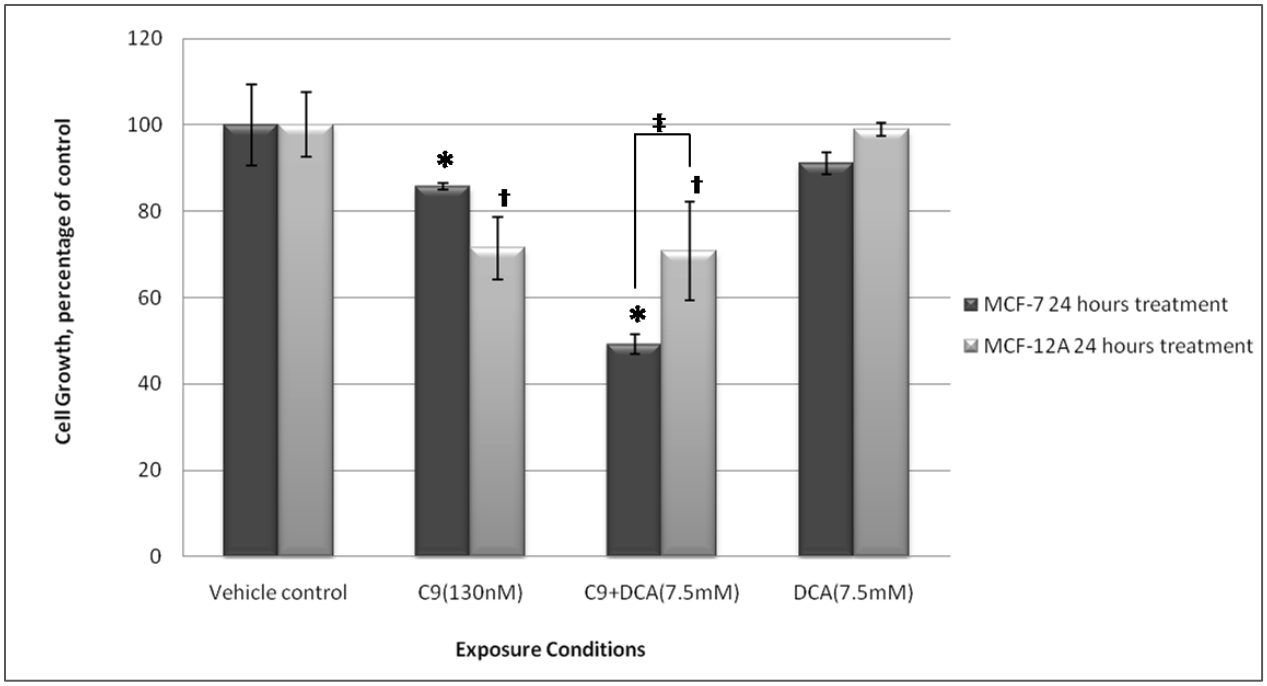

Figure 3.7: MCF-7 and MCF-12A cell growth after 24 h of exposure to 130 nM C9, 7.5 mM DCA and C9+DCA. MCF-7 and MCF-12A cell growth expressed as a percentage of the control (cells propagated in medium and the vehicle, DMSO<0.01%) after 24 h of exposure to 130 nM C9, 7.5 mM DCA and C9+DCA. *,†*P*-value < 0.05 when treated cells and controls were compared within the same cell line. ‡*P*-value < 0.05 when MCF-7 and MCF-12A cells were compared for the same treatment.

3.2 Cell viability test

Lactate dehydrogenase assay

Cell viability tests were performed with the aid of the LDH kit. It was previously mentioned that lactate dehydrogenase enzyme activity is directly proportional to plasma membrane damage. The LDH enzyme activity is converted to percentages of cell growth relative to vehicle-exposed cells. Thus, higher levels of cell damage correspond to more LDH enzyme released in the cytosol. In both MCF-7 and MCF-12A cells, compared to vehicle-exposed cells, neither 130 nM C9- nor 7.5 mM DCA-exposed cells showed significant cytosolic LDH enzymatic release after 24 h treatment (Figure 3.8). However, the number of viable MCF-7 and MCF-12A cells decreased to 83.53% and 92.40% respectively after 24 h treatment with C9+DCA compared to controls ($P < 0.05$) (Figure 3.8). The cell viability test results showed that there are more viable MCF-12A cells than MCF-7 cells after 24 h treatment of C9+DCA ($P < 0.05$). LDH activity is higher in combination (C9+DCA) exposed tumorigenic cells compared to non-tumorigenic cells as a result of higher levels of cell damages. The vehicle (DMSO) used to dissolve C9 (powder) had no effect on cell viability when used less than v/v 0.01% (Figure 3.8).

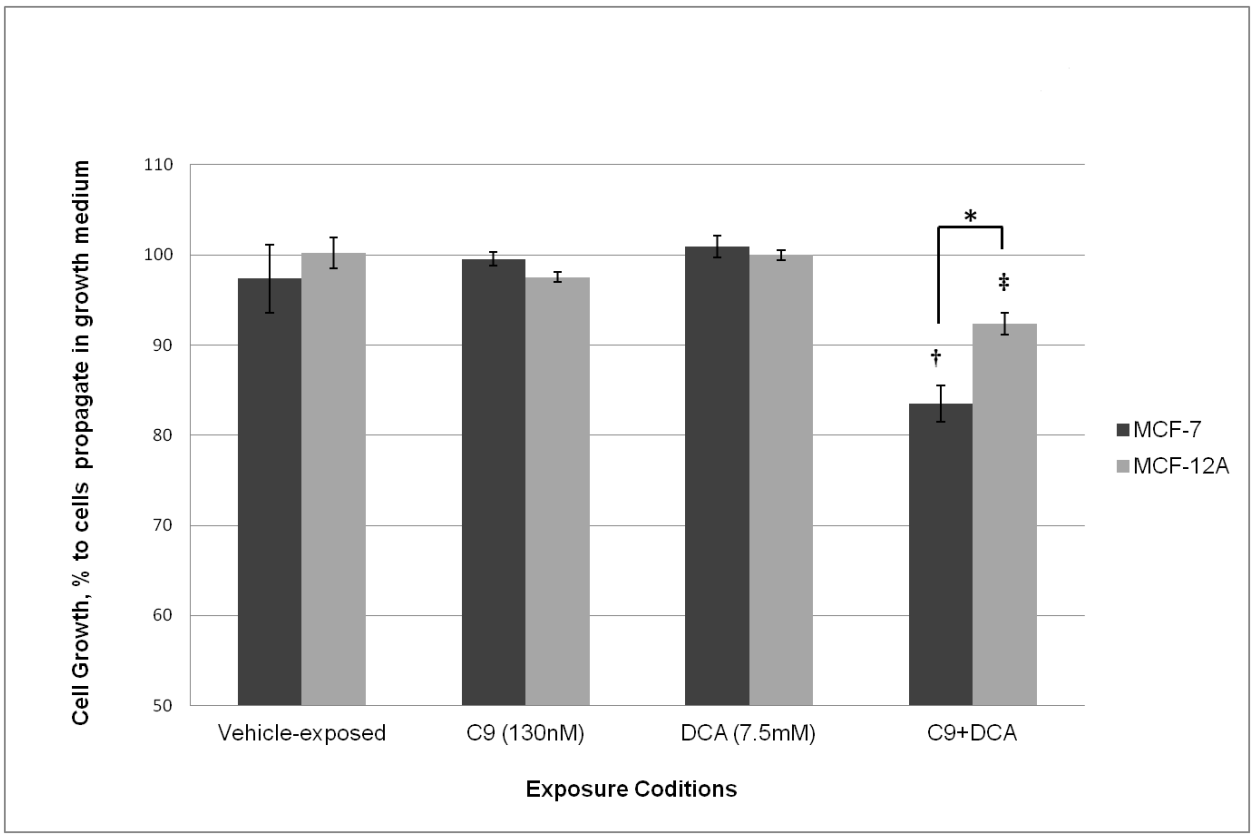

Figure 3.8: Lactate dehydrogenase cell viability test of MCF-7 and MCF-12A cells. MCF-7 and MCF-12A cell growth expressed as a percentage of the control (cells propagated in medium with addition of vehicle, DMSO < 0.01%) after 24 h of exposure to 130 nM C9, 7.5 mM DCA and C9+DCA. †, ‡*P*-value < 0.05 after comparison of exposed cells and controls within the same cell line. **P*-value < 0.05 when MCF-7 and MCF-12A cells were compared for the same treatment.

3.3 Cytotoxicity measurement and drug efficacy prediction

The xCELLigence system is capable of generating a dose-response curve for the calculation of IC_{50} values at a specific given time point. The RTCA SP® system was employed to monitor cellular morphological alterations such as cell proliferation, division, shrinkage, death or detachment. The impedance caused by cellular events would ultimately be converted into CI. Changes in CI directly imply changes in the impedance value as a result of above-mentioned events.

Firstly, it was necessary to ensure the integrity of cells as part of the quality control mechanisms. MCF-7 and MCF-12A were seeded at 10 000 cells/well (this concentration yielded the best results for the E-Plates 96) in triplicates in the E-Plates 96 and observed for a period of 48 h for a routine inspection. The sensitivity of the instrument allows it to collect information with regards to any contamination and cell behaviour changes. Figure 3.9 A demonstrates that both MCF-7 and MCF-12A with seeding density of 10 000 cell/well were propagating properly and free from contamination. Secondly, the effect of vehicle DMSO was re-evaluated to ensure the effect of compound C9 on cells was not influenced by DMSO prior to cytotoxicity testing. Results obtained from this part of the study confirmed the previous finding that the vehicle used in this study had no effect on cell proliferation (Figure 3.9 B). Thirdly, the effect of either C9 or DCA was assessed on MCF-7 and MCF-12A cells. Two concentrations, 130 nM and 200 nM of the antimitotic compound C9 were selected for testing in both cell lines (Figure 3.10). C9 did not have detrimental effects on MCF-12A cell growth even at 200 nM concentration (26% reduction) (Figure 3.10 B). On the other hand, different concentrations (130 or 200 nM) of C9-exposed MCF-7 cells displayed dissimilar inhibition patterns. At 24 h exposure, 130 nM and 200 nM of C9 reduced tumorigenic MCF-7 cell growth by 16% and 80% respectively (Figure 3.10 A). The C9-exposed cell index graph exhibited a spoon-shaped curve which is a distinctive shape for antimitotic compounds. Finally, the effect of DCA was evaluated with three concentrations, 7.5 mM, 15 mM and 40 mM, on MCF-7 and MCF-12A cells (Figure 3.11). DCA at all three concentrations had no adverse effect on MCF-12A cell growth; however, it negatively affected cell growth of MCF-7 cells at 40 mM (Figure 3.11).

Table 1 illustrates the raw data used to generate the sigmoidal curve. The concentrations of C9 was kept constant and it was combined with five different concentrations of DCA, 2.5 mM, 5.0 mM, 7.5 mM, 15 mM and 40 mM. After the raw data was captured by the xCELLigence system, the inbuilt statistical software utilized this information and generated the sigmoidal dose response curve with the IC_{50} calculation. The formula which the RTCA Software used to interpret and compute the IC_{50} value of DCA in combination therapy is displayed below. The IC_{50} values of DCA which combined with 130 nM of C9 were 6.44 mM and 5.74 mM for 24 h and 48 h exposure respectively (Figure 3.12).

Formula: $CI_{Bottom} + (CI_{Top} - CI_{Bottom})/(1 + 10\text{^}((\text{Log } EC_{50} - \text{Intercept}) * \text{Hill Slope}))$

In addition, the xCELLigence system has an extra feature which is the prediction of drug efficacy by means of slope value comparisons amongst treatments. The slope is used to describe the steepness, incline, gradient, or changing rate of a curve within the given time window. The mathematical relationship between the cell index values and the slope of a particular curve can be represented by a straight line equation y = m*x + c, where ‘m’ is the slope and ‘c’ is the intercept. This equation can be translated to represent cell index. The equation then becomes Cell Index = slope * time + intercept. In this case, the slope is the gradient value of CI change over time which means the rate of CI change. For each selected well, the RTCA Software calculates the slope of the Cell Index or Normalized Cell Index curve in the chosen Time period, after fitting the points to a straight line (Figure 3.13 A). The slope values are shown in the bar chart (Figure 3.13 B). A positive slope within a fix time period with certain drug treatment means that the drug has cytostatic effect on cells. In contrast, a negative slope means that at the time of assessment the particular drug has cytotoxic effect. Figure 3.13 B demonstrated toxicity profiles of five concentrations of DCA (2.5, 5.0, 7.5, 15 and 40 mM) in combination with 130 nM C9 over 24 h and 48 h. Data showed when DCA concentrations used in the combination treatment greater or equal to 15 mM, the slopes calculated for 24 h and 48 h exposure time were all negative. It means DCA ≥ 15 mM in the combination treatment were toxic to the MCF-7 cells and the degree of toxicity is directly proportional to DCA concentration. Quite the opposite, positive slopes were observed when DCA ≤ 5 mM were used in combination treatment. Interestingly, if 7.5

mM of DCA were used in the treatment, negative 24 h and positive 48 h slopes were displayed. This result confirmed 7.5 mM of DCA in combination with antimitotic C9 at 24 h exposure time produced cytotoxicity effect on MCF-7 cells (Figure 3.13 B).

Figure 3.14 was produced to illustrate the effect of 7.5 mM DCA with 130 nM C9 on tumorigenic MCF-7 and non-tumorigenic MCF-12A cells. The cytotoxic effect of 130 nM of C9 on tumorigenic MCF-7 is observed within three hours of drug exposure, however, this effect is not significant (Figure 3.14 A). At 24 h time point after C9 exposure, MCF-7 normalized CI decreased 18.33% compared to vehicle-exposed controls. Under the same condition (130 nM C9 24 h), MCF-12A normalized CI decreased only by 5.39%. Moreover, DCA (7.5 mM) treatment had no effect on MCF-7 and MCF-12A cells (Figure 3.14). Upon treatment of combination compounds C9+DCA, MCF-7 cells CI decreased sharply and reached its lowest point at 16 h after treatment to 0.39 compared to vehicle treated 2.65 (CI decreased 85.19%). The combination compounds exert their maximal effect at 16 h after exposure (Figure 3.14 A). At 24 h time point after C9+DCA treatment, MCF-7 the CI reduced 81.97%. The CI values may be used as indicators that point out a treatment's exact maximal effect time point *in vitro*. In contrast, MCF-12A cells also experienced reduced CI after C9+DCA treatment, however, the CI decrease was not as severe when compared to the MCF-7 cells. The CI of MCF-12A cells after 16 h and 24 h treatment with C9+DCA was reduced 51.3% and 36.91% respectively.

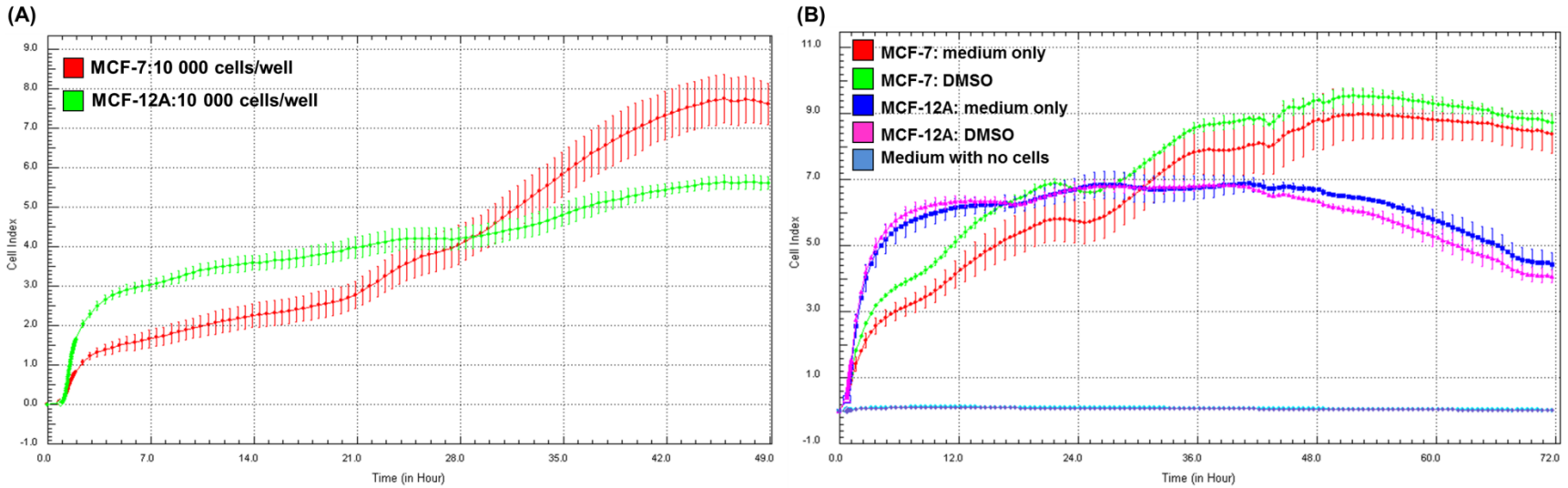

Figure 3.9: Cell quality assessment and evaluation of solvent's suitability as vehicle for subsequent experiments. Cell quality assessment (A) and evaluation of DMSO suitability as vehicle for subsequent experiments (B). MCF-7 and MCF-12A cell quality was assessed with 10 000 cells/well prior to cytotoxicity testing. MCF-7 and MCF-12A showed normal proliferation patterns and CI (A). Vehicle DMSO used to dissolve C9 had no effect on MCF-7 and MCF-12A cell proliferation when used at less than 0.01% in the media (B).

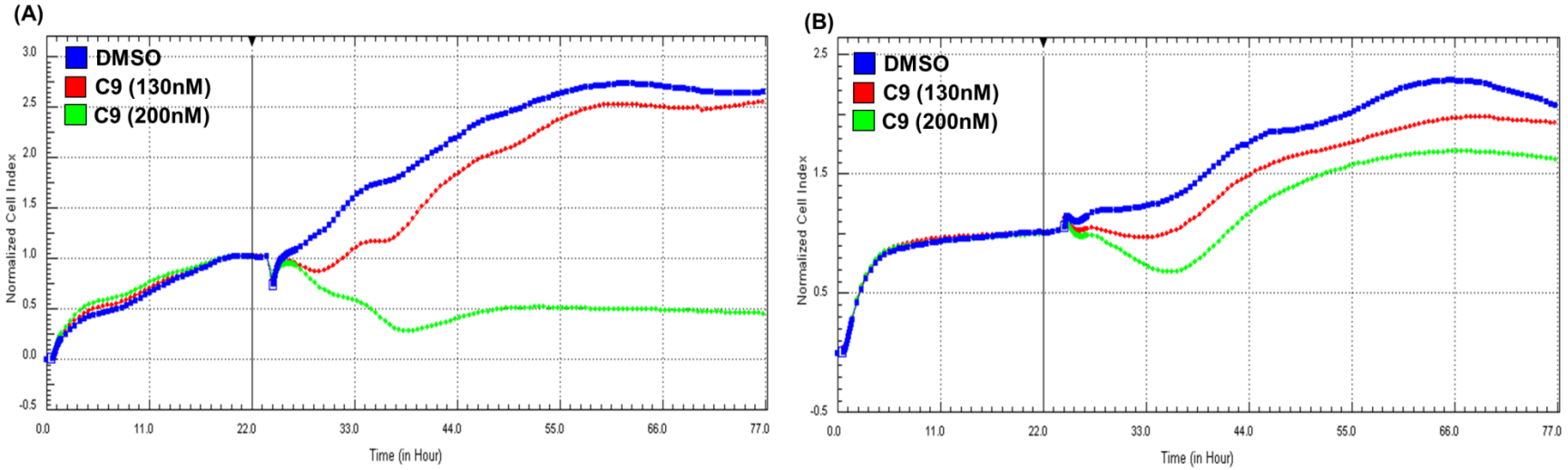

Figure 3.10: Cytotoxicity test of 130 nM and 200 nM C9 on MCF-7 and MCF-12 cells for 48 h. Cytotoxicity test of 130 nM (red) and 200 nM (green) C9 on MCF-7 (A) and MCF-12A (B) cells for 48 h. Treatment of C9 inhibited both MCF-7 and MCF-12A cell growth in dose-dependent manner. CI curve after C9 treatment showed typical antimitotic spoon-shaped inhibition curve.

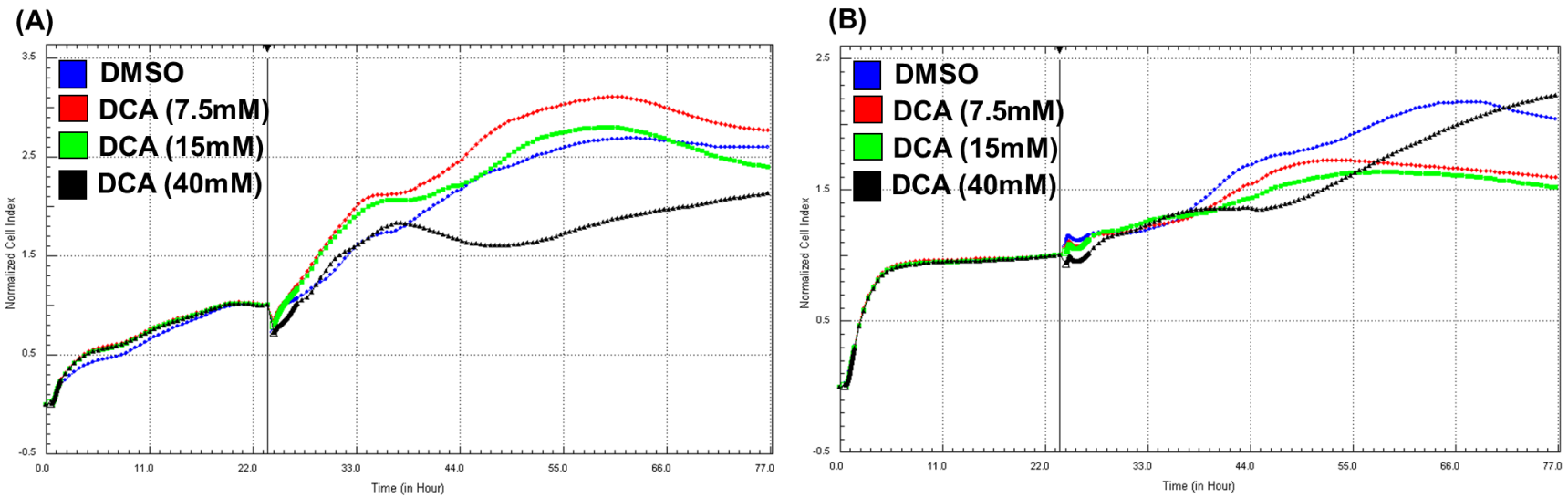

Figure 3.11: Cytotoxicity test of 7.5 mM, 15 mM and 40 mM DCA on MCF-7 and MCF-12A cells for 48 h. Cytotoxicity test of 7.5 mM (red), 15 mM (green) and 40 mM DCA (black) on MCF-7 (A) and MCF-12A (B) cells for 48 h. DCA treatments with all three concentrations had no drastic cell inhibition effect on MCF-12A cells. The highest concentration of DCA (40 mM) reduced MCF-7 cell growth from 12 hours after treatment.

Table 1: Cell index data at 24 h and 48 h exposure time point of C9+DCA treated MCF-7 cells. Five different concentrations of DCA (2.5 mM, 5.0 mM, 7.5 mM, 10.0 mM, 15.0 mM and 40.0 mM) were combined with 130 nM of C9. The normalized CI, as well as the log of concentrations are presented in the table.

MCF-7		**C9*+DCA**	**24 hours exposure**		**48 hours exposure**	
Compounds exposed	Well ID (Triplicates)	Concentration DCA (M)	Log Concentration(M)	Normalized Cell Index	Log Concentration(M)	Normalized Cell Index
C9+DCA (2.5 mM)	A10A11A12	2.50E-03	-2.6021	2.0868	-2.6021	2.4443
C9+DCA (5.0 mM)	B10B11B12	5.00E-03	-2.301	1.5976	-2.301	1.6482
C9+DCA (7.5 mM)	C10C11C12	7.50E-03	-2.1249	1.0542	-2.1249	1.073
C9+DCA (15 mM)	D10D11D12	1.50E-02	-1.8239	0.3843	-1.8239	0.3552
C9+DCA (40 mM)	E10E11E12	4.00E-02	-1.3979	0.4239	-1.3979	0.2455

* Concentration of C9 was kept constant at 130 nM.

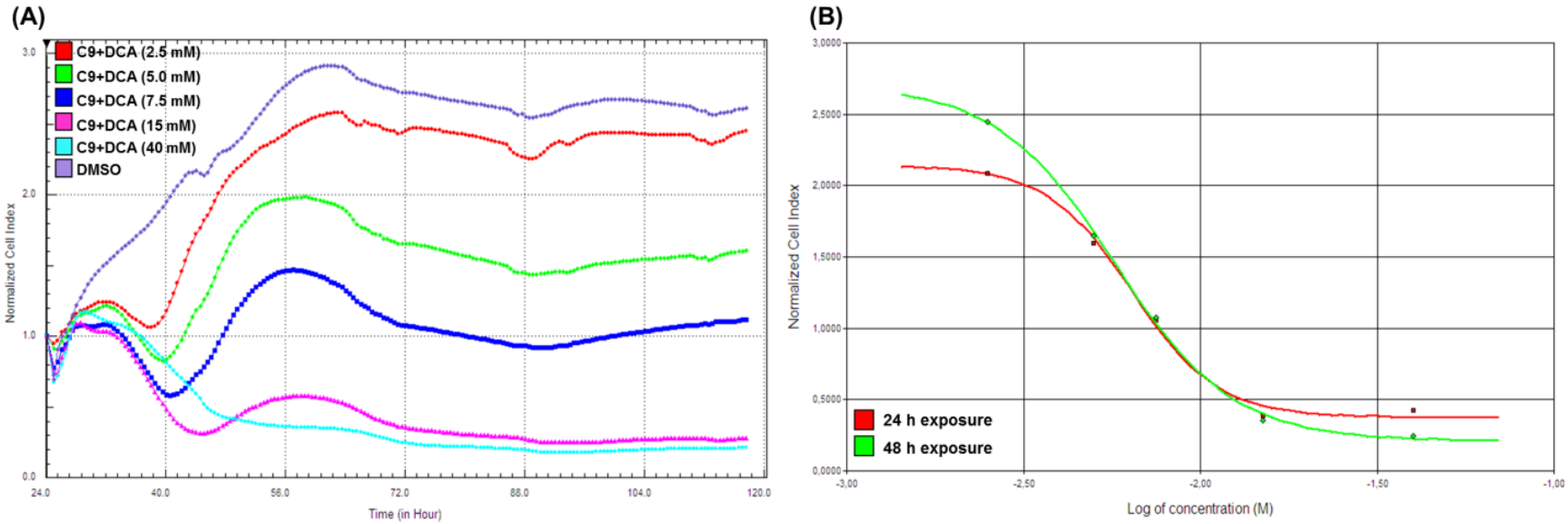

Figure 3.12: Cytotoxicity test of antimitotic C9 (130 nM) in combination with ranges of DCA (2.5 mM, 5 mM, 7.5 mM, 15 mM and 40 mM). Cytotoxicity test of antimitotic C9 (130 nM) in combination with ranges of DCA (2.5 mM, 5 mM, 7.5 mM, 15 mM and 40 mM) on MCF-7 cells for 72 h (A). Table 1 was used to plot the DCA dose-response sigmoidal curves of MCF-7 cells for 24 h (red) and 48 h (green) treatment (B). Treatment concentration and normalized cell index for 24 and 48 h exposure were converted to Log of concentration (M) versus normalized CI (B).

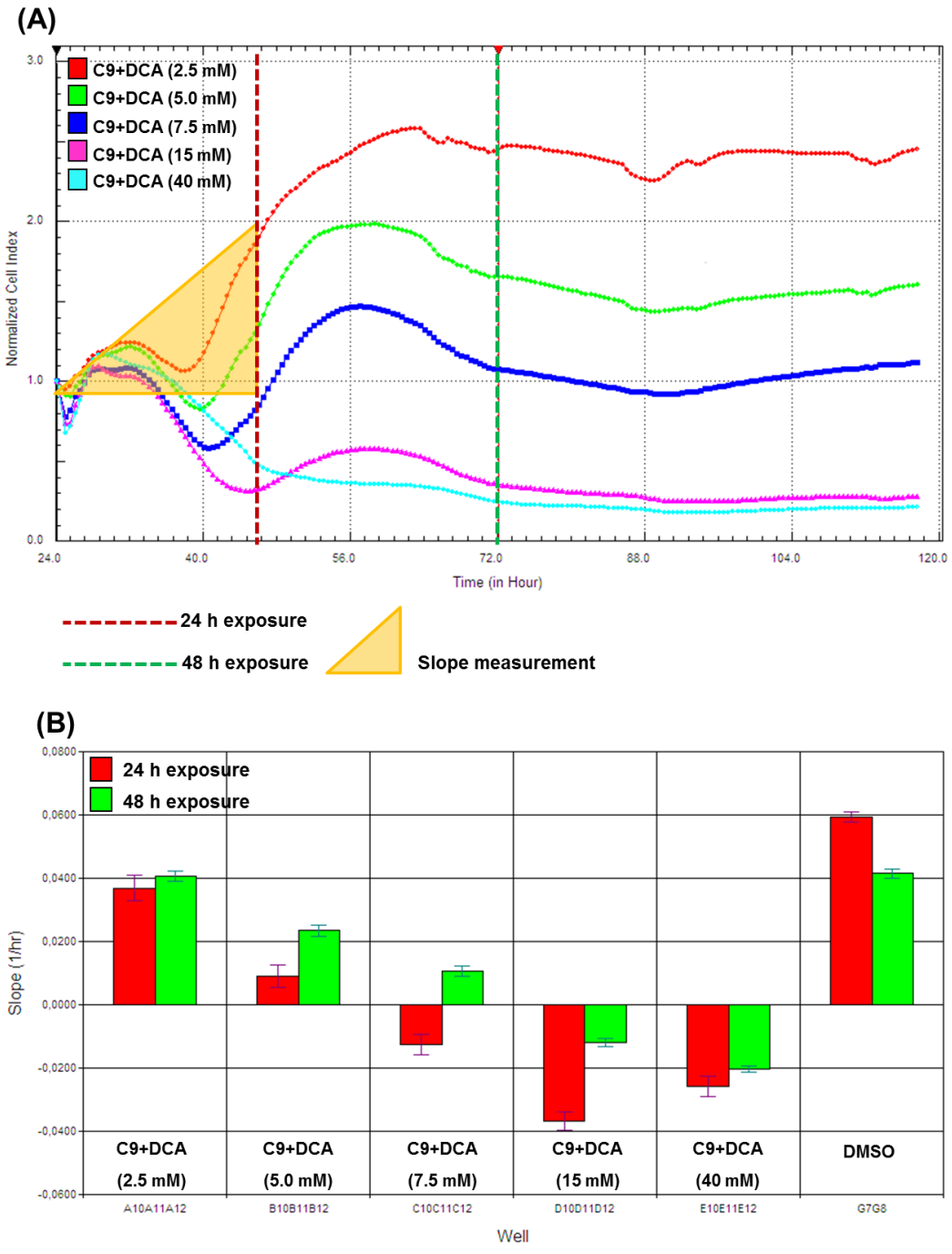

Figure 3.13: Dose-response cytotoxicity and efficacy predictions of C9+DCA on MCF-7 cells. Slope measurement of dose-response cytotoxicity test curves of MCF-7 cells (A). Treatment of C9+DCA (2.5 mM, 5 mM, 7.5 mM, 15 mM and 40 mM) efficacy predictions (B) via the calculated slope values from Table 1. Positive slope indicates cytostatic effect and negative value indicates cytotoxic effect.

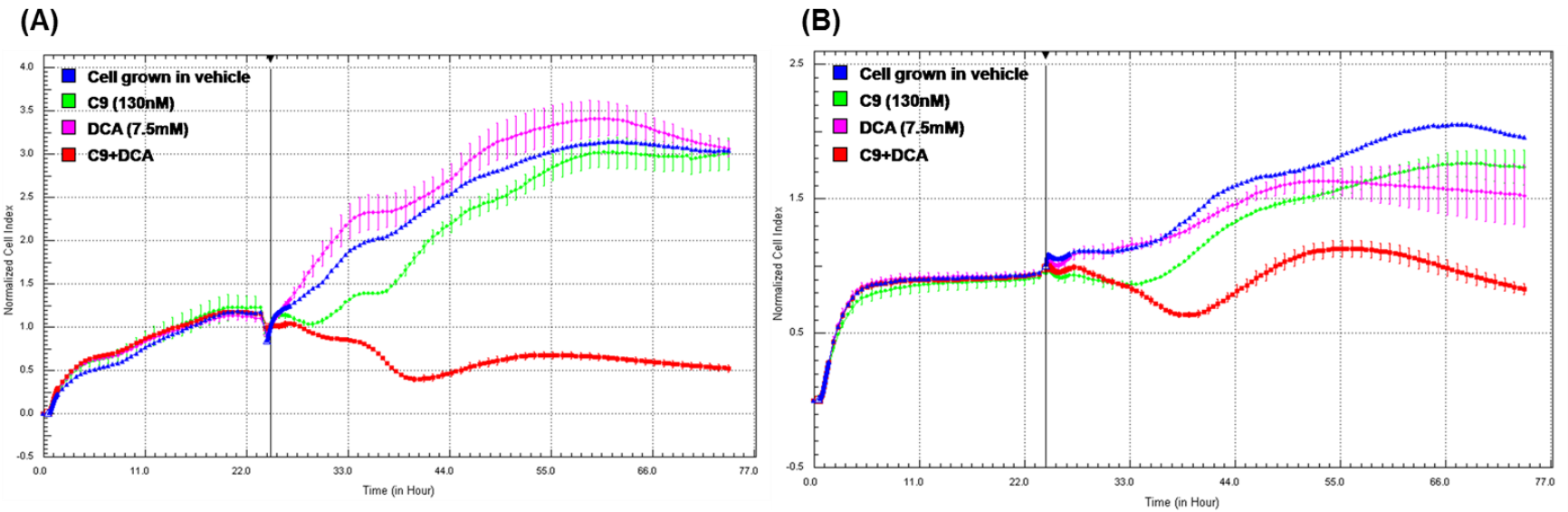

Figure 3.14: xCELLigence system cytotoxicity test of C9+DCA on MCF-7 and MCF-12A cells for 48 h. xCELLigence system cytotoxicity test of C9+DCA (7.5 mM) on MCF-7 (A) and MCF-12A (B) cells for 48 h. DCA-exposed (7.5 mM, pink) MCF-7 and MCF-12A cells showed no CI reduction. CI curve of C9-exposed (130 nM, green) MCF-7 and MCF-12A cells had slight reduction in cell number. C9+DCA-exposed (red) MCF-7 and MCF-12A cells displayed drastic reduction CI curve.

3.4 Morphological studies

3.4.1 Optical transmitted light differential interference contrast

PlasDIC images of both MCF-7 and MCF-12A C9-treated cells (Figure 3.15 B and G) showed an increase in metaphase and formation of apoptotic bodies. DCA-treated cells (Figure 3.15 C and H) revealed shrunken cells compared to cells grown to confluency in the vehicle-treated control (Figure 3.15 A and F). Cells exposed to C9 in combination with DCA (Figure 3.15 D and I) displayed characteristics of cells in metaphase, formation of apoptotic bodies, shrunken cells, compromised cell density and even appearance of ghost cells. Upon dual treatment with C9 and DCA, MCF-7 cells (Figure 3.15 D) displayed not only severe degree of compromised cell density but also vast numbers of existing cells that are either in metaphase, shrunken or display characteristics of cell death (apoptosis) compared to MCF-12A cells. Therefore, when looking at morphology, MCF-7 cells (Figure 3.15 D) appeared more susceptible when compared to MCF-12A cells (Figure 3.15 I).

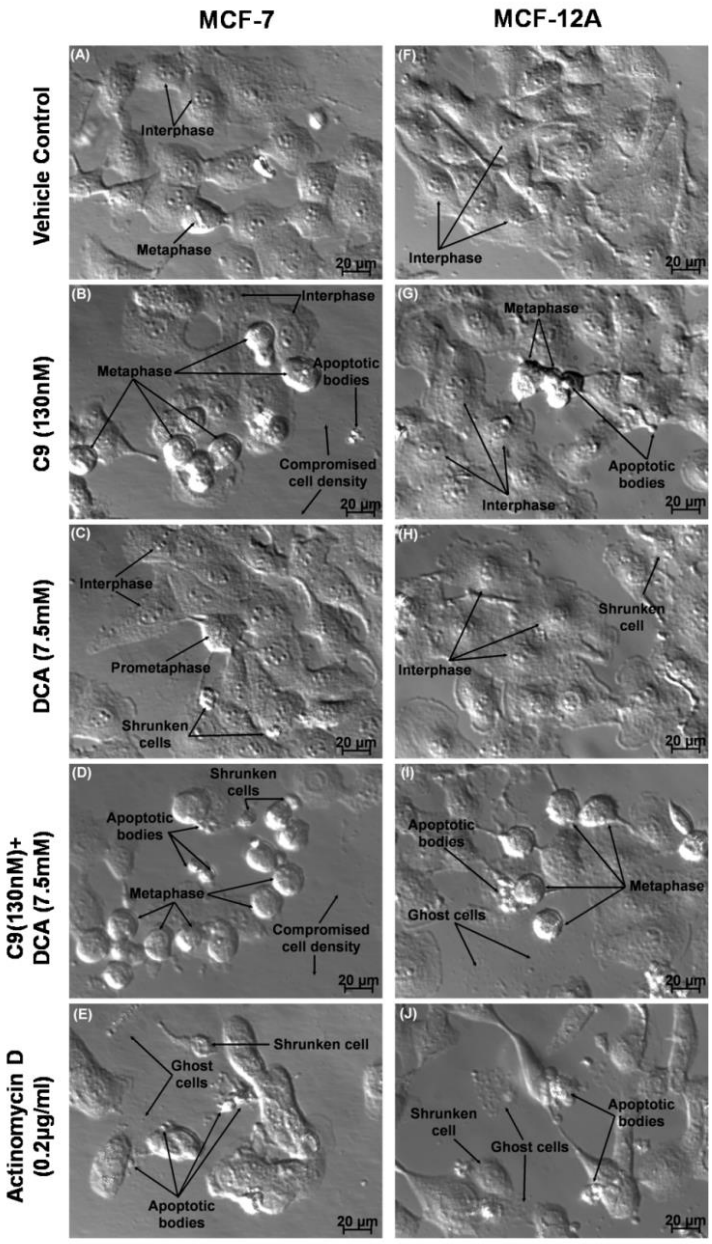

Figure 3.15: Optical transmitted light differential interference contrast images of MCF-7 and MCF-12A cells after 24 h treatment exposure. PlasDIC images of MCF-7 cells (left column, images A to E) compared to MCF-12A cells (right column, images F to J) after 24 h exposure to different conditions. Vehicle-treated (A and F) cells were confluent and showed no sign of distress. C9 (130 nM)-exposed (B and G) cells showed decreased cell density and an increase in metaphase. Cells exposed to 7.5 mM of DCA (C and H) indicated no significant decrease in cell number. Cells exposed to C9 (130 nM) in combination of DCA (7.5 mM) (D and I) showed significant inhibition of cell growth. Actinomycin D (0.2 µg/ml)-treated cells (E and J) exhibited hallmarks of late stages of apoptosis.

3.4.2 Light microscopy

Haematoxylin and eosin staining

Haematoxylin and eosin (H & E) staining was performed to observe cellular morphological changes in large scale. After exposure to combination treatment of C9+DCA, MCF-7 cells exhibited a decrease in cell density, as well as the formation of apoptotic bodies (Figure 3.16) when compared to the vehicle-expose tumorigenic cells (Figure 3.16). MCF-12A also showed decreases in cell density after exposure to combination treatment (Figure 3.16), however, only less so when compared to MCF-7-treated cells. The haematoxylin and eosin staining cell morphology study has demonstrated that the MCF-7 cells are more susceptible to the combination treatment, further confirming the cell growth and PlasDIC studies.

MCF-7 and MCF-12A cells mitotic indices were derived from the H & E stained slides by counting 1000 cells per slide. This experiment was repeated twice and the averages of the two repeats were counted and data is presented in Table 2. Data has been divided into four categories: vehicle-, C9-, DCA- or C9+DCA-exposed respectively for MCF-7 and MCF-12A cells. Cells in the mitotic phase were subdivided into prophase, metaphase, anaphase, telophase and tripolar metaphase. Non-mitotic cells were subdivided into interphase and hypercondensed chromatin with the latter indicating the amount of cells undergoing apoptosis. In general, MCF-12A cell is a faster dividing cell type when compared to MCF-7 cells as the mitotic indices for cells in interphase are 86.4% and 91.3%, respectively (Figure 3.16 E compared to A). Treatment with C9 and C9+DCA on MCF-7 cells caused increased mitotic indices of metaphase from 2.9% (DMSO-exposed) to 9.4% and 16.3% respectively, as well as increased the count for cells exhibiting hypercondensed chromatin from 1.5% (DMSO-exposed) to 5.8% and 10.3% respectively. This result shows compound C9 has antimitotic effects and also promotes apoptosis. Furthermore, addition of DCA combined with C9 exhibited synergistic effects, where the number of cells in metaphase and cells exhibiting hypercondensed chromatin almost doubled (16.3% and 10.3%, respectively) compared to C9-exposed (9.4% and 5.8%) MCF-7 cells.

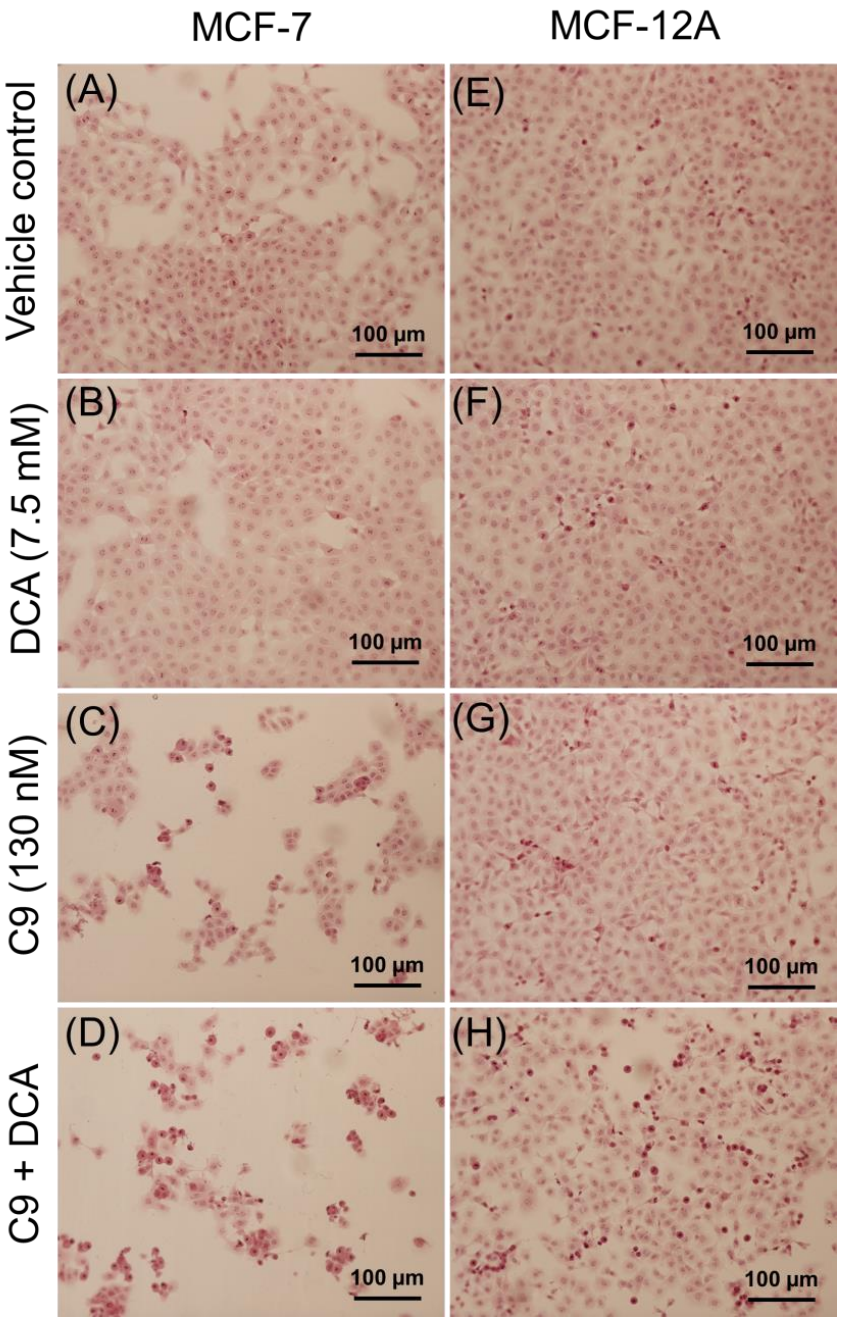

Figure 3.16: Haematoxylin and eosin stained images of MCF-7 and MCF-12A cells after 24 h treatment exposure. Haematoxylin and eosin stained images of MCF-7 cells (left column, images A-D) compared to MCF-12A cells (right column, images D-H) after 24 h exposure to different conditions. Vehicle-treated (A and E) cells were confluent and showed no sign of distress. Cells exposed to 7.5 mM of DCA (B and F) indicated no significant decrease in cell number. C9 (130 nM)-exposed MCF-7 cells (C) showed decreased cell density and an increase in metaphase. Cells exposed to C9 (130 nM) in combination of DCA (7.5 mM) (D and H) showed significant inhibition of cell growth and formation of apoptotic bodies.

Table 2: MCF-7 and MCF-12A cell mitotic indices. Data has been divided into vehicle-, C9-, DCA- or C9+DCA-exposed cells respectively. Cells in the mitotic phase were subdivided into prophase, metaphase, anaphase, telophase and tripolar metaphase. Non-mitotic cells were subdivided into interphase and hypercondensed chromatin, the latter indicating cells undergoing apoptosis.

MCF-7	**Vehicle control**	**C9**	**DCA**	**C9+DCA**
Mitotic cells				
Prophase	1.9	0.4	1.6	0.3
Metaphase	2.9	9.4	2.2	16.3
Anaphase	1.5	0.2	0.8	0
Telophase	1.2	0	0.9	0
Tripolar metaphase	0	0	0	0
Non-mitotic cells				
Interphase	91.3	86.1	92.6	73.1
Hypercondensed chromatin	1.5	5.8	1.9	10.3
MCF-12A	**Vehicle control**	**C9**	**DCA**	**C9+DCA**
Mitotic cells				
Prophase	2.9	0.8	1.4	0.4
Metaphase	3.7	5.5	2.9	13.9
Anaphase	1.8	0.2	0.9	0
Telophase	2.4	0.1	1.8	0
Tripolar metaphase	0.7	1.9	1.0	0.8
Non-mitotic cells				
Interphase	86.4	87.6	88.9	81.6
Hypercondensed chromatin	2.1	3.9	3.1	3.3

3.4.3 Fluorescent microscopy

Triple fluorescent staining: Hoechst 33342, acridine orange and propidium iodide

The fluorescent microscopy study revealed an increase of MCF-7 cells present in metaphase after 24 h of exposure to C9 (130 nM) (Figure 3.17 B). DCA-exposed (7.5 mM) MCF-7 cells showed slightly increased acridine orange staining (Figure 3.17 C) when compared to the control (Figure 3.17 A). However, combination treatment of C9+DCA-exposed MCF-7 displayed severe degree of compromised cell density, increased acridine orange staining and large numbers of existing cells in metaphase (Figure 3.17 D). Furthermore, the microscopy study showed a slight increase in acridine orange staining in C9-, DCA- and C9+DCA-exposed MCF-12A cells (Figure 3.17 G, H and I). The effect of C9 or combination treatment on MCF-12A cells (Figure 3.17 G and I) is moderate in comparison with MCF-7 cells (Figure 3.17 B and D) that were treated under the same exposure conditions. This observation is in agreement with findings from previous cell number studies where the addition of DCA enhanced the efficacy of compound C9 in tumorigenic cells.

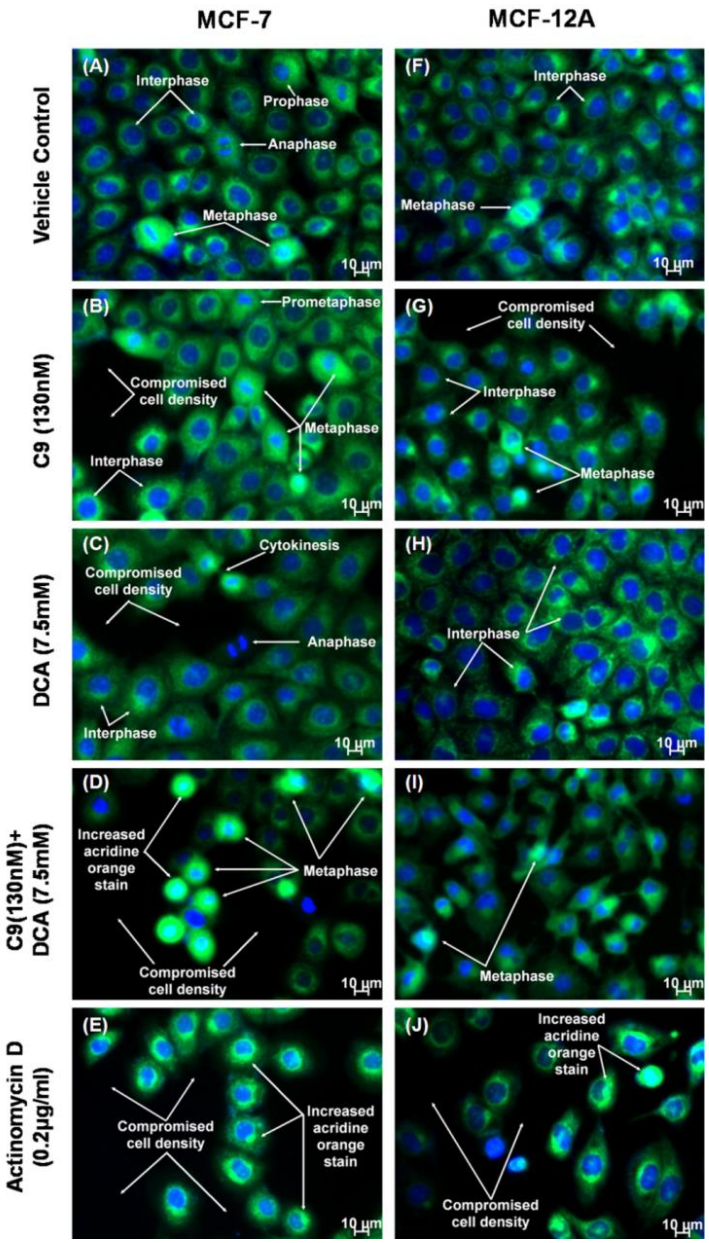

Figure 3.17: Fluorescent microscopy utilizing triple fluorescent stains of Hoechst 33342, acridine orange and propidium iodide. Fluorescent images of MCF-7 cells (left column, images A to E) compared to MCF-12A cells (right column, images F to J) after 24h of exposure to different conditions. Vehicle-treated (A and F) cells were confluent and showed no sign of distress. C9 (130 nM) -exposed (B and G) cells showed decreased cell density and an increase in metaphase. Cells exposed to 7.5 mM of DCA (C and H) indicated no significant decrease in cell number. Cells exposed to C9 (130 nM) in combination of DCA (7.5 mM) (D and I) showed significant inhibition of cell growth. Actinomycin D (0.2 µg/ml) -treated cells (E and J) exhibited hallmarks of late stages of apoptosis.

3.4.4 Confocal microscopy

Immunofluorescent detection of tubulin architecture

Confocal microscopy revealed the cytoskeletal microtubule architecture of α-tubulin for both MCF-7 and MCF-12A cells. The confocal microscopy study revealed an increase in cell size of both MCF-7 and MCF-12A cells after 24 h of exposure to DCA (7.5 mM) when compared to the control (Figure 3.18). This result is in agreement with the morphological observations from the other technique, namely, PlasDIC where the cells were flattened and stretched out (Figure 3.15 C and H). An increased portion of MCF-7 cells showed characteristics of cells arrested in metaphase and abnormal spindle formation after exposed to C9 (130 nM) for 24 h (Figure 3.18 C9). The combination exposed tumorigenic cells exhibited characteristics that were similar to C9-exposed MCF-7 cells with additional hallmarks of fragmented DNA and destruction of α-tubulin architecture (Figure 3.18 C9+DCA). Furthermore, this study demonstrated abnormal multinucleated MCF-12A cells after treatment with C9 for 24 h (Figure 3.18 C9). The effect of the combination treatment on MCF-12A cells is moderate in comparison with MCF-7 cells that were treated under the same exposure conditions (Figure 3.18 C9+DCA). This observation is consistent with findings from previous cell number studies where the addition of DCA enhanced the efficacy of compound C9 in tumorigenic cells.

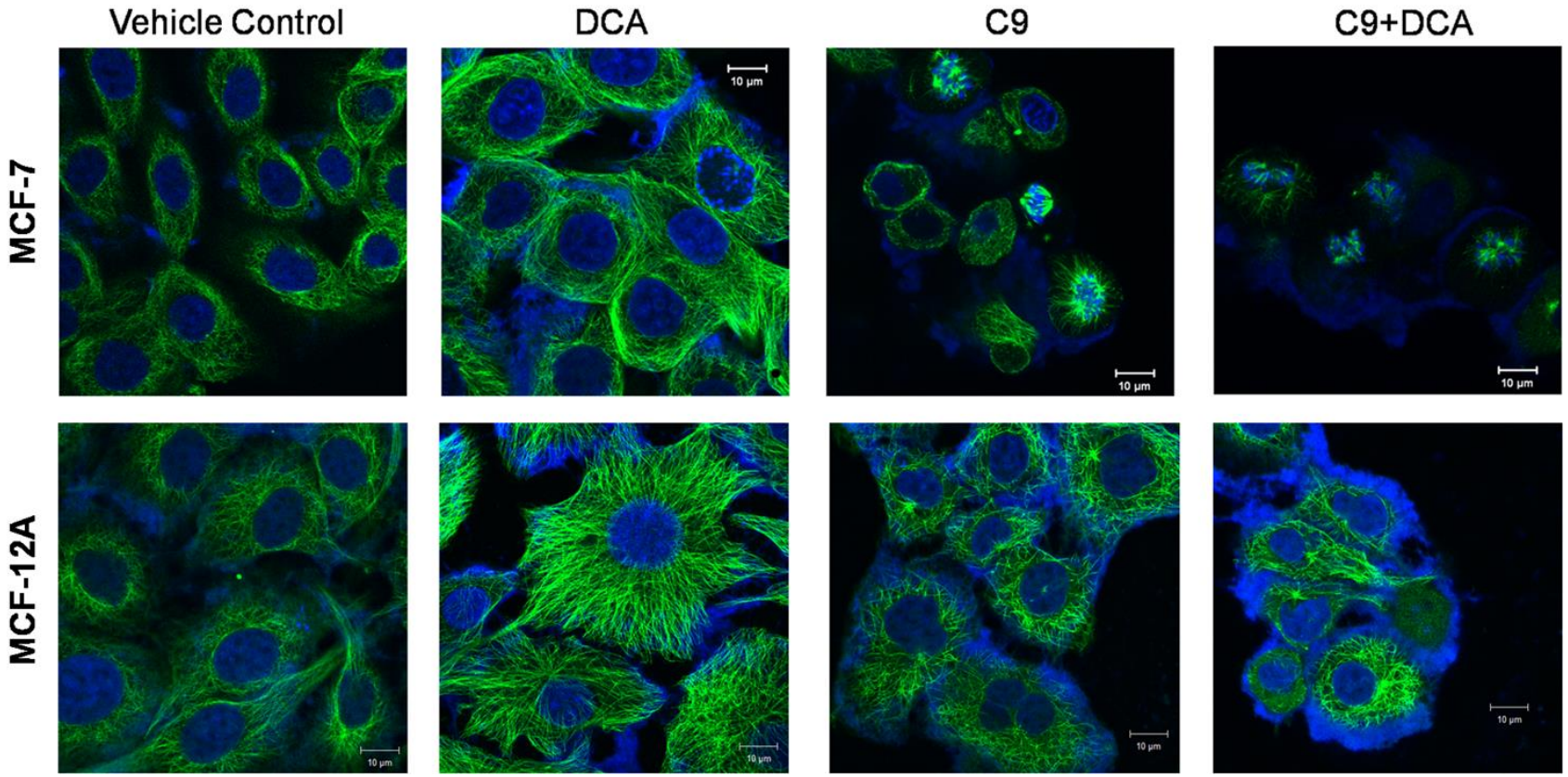

Figure 3.18: Immunofluorescent staining of α-tubulin (green) for MCF-7 and MCF-12A cells. Fluorescent images of MCF-7 cells (top row) compared to MCF-12A cells (bottom row) after 24h of exposure to DCA (7.5 mM), C9 (130 nM) and C9+DCA. Vehicle-treated MCF-7 and MCF-12A cells were confluent and showed no sign of distress. DCA-exposed cells showed no significant decrease in cell number, but displayed slightly larger and flattened morphology. C9 (130 nM)-exposed MCF-7 and MCF-12A cells decreased in cell number; MCF-7 displayed formation of abnormal spindle, as well as cell arrested in metaphase after treatment. Cells exposed to C9 (130 nM) in combination of DCA (7.5 mM) showed significant inhibition of cell growth, abnormal spindle formation and fragmentation of genomic material.

3.4.5 Transmission electron microscopy

Normal nuclear- and cytoplasmic physiology was observed in vehicle treated MCF-7 and MCF-12A cells (Figure 3.19 A and E). The untreated control cells were round with smooth cell membrane and limited number of apical microvilli protrusions. Furthermore, the nucleus usually presented indentation and contained one or two prominent nucleoli. The volume ratio between nucleus and cytoplasm was roughly 1:1 for a healthy untreated cell. The cytoplasm possessed considerably quantities of mitochondria and endoplasmic reticulum. An extensive network of Golgi apparatus, centriole and specialized ER for the production of human mammary milk fat globule protein (MFGP) was also observed in untreated MCF-7 and MCF-12A cells. Transmission electronic micrographs did not illustrate any stress caused by DCA treatment on both cell lines compared to controls. Compromised cell density, endosomes, metaphase chromatid formation and autophagosome were, however, observed in MCF-7 cells treated with C9 (Figure 3.19 B). In contrast, MCF-12A cells affected by the antimitotic C9 (130 nM) were limited. Ordinary appearance of a pair of centrioles was spotted in MCF-12A cells after C9 treatment, indicating occurrences of regular cell division (Figure 3.19 F). The combination of C9+DCA-exposed MCF-7 cells displayed distorted cell shape, high density of digit-like apical microvilli, formations of vacuoles, lysosomes and apoptotic bodies, highly condensed chromatin (heterochromatin), as well as fragmented DNA compared to the control (Figure 3.19 C and D). The above mentioned characteristics were also observed in MCF-12A cells treated with the combination therapy, however, the intensity was in moderation when compared to MCF-7 cells (Figure 3.19 G and H). Fragmented nuclei and apoptotic bodies were detected within combination compounds exposed tumorigenic cells thus indicating late stages of apoptosis (Figure 3.19 C and D). Furthermore, several autophagic related structures were identified within the cells that had been treated with the combination treatment. These autophagic related structures include autophagosome, multi-vascular endosome, amphisome, lysosome and autolysosome (Figure 3.20).

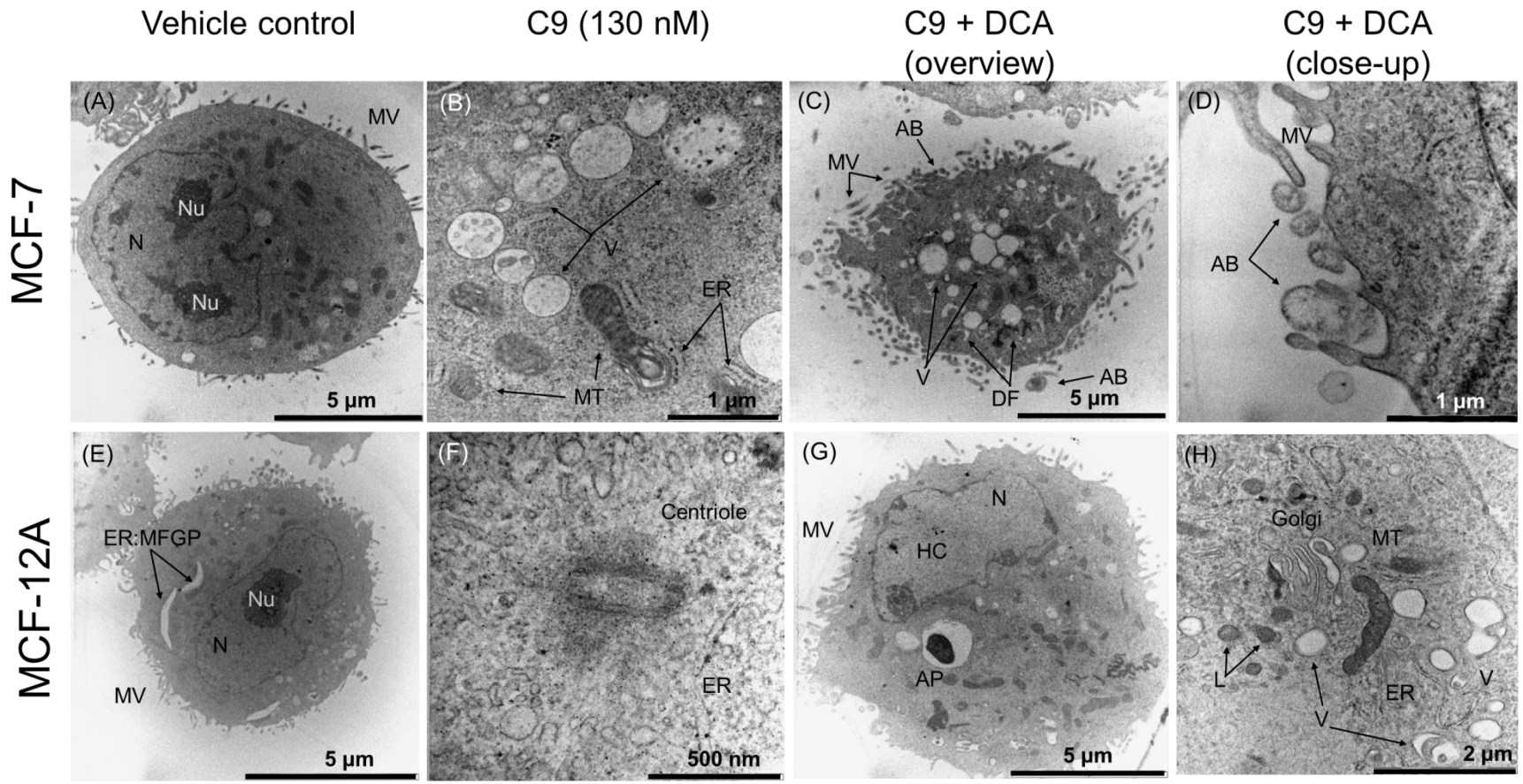

Key: **N**: Nucleus, **Nu**: Nucleoli, **HC**: Heterochromatin, **MV**: Apical Microvilli, **AB**: Apoptotic Bodies, **DF**: DNA Fragmentation, **V**: Vacuoles, **MT**: Mitochondrial, **ER**: Endoplasmic Reticulum, **C**: Centriole, **MFGP**: specialized ER for the production of human mammary milk fat globule protein, **Golgi**: Golgi apparatus, **AP**: Autophagosome and **L**: Lysosome.

Figure 3.19: Transmission electron micrographs of MCF-7 cells compared to MCF-12A cells after 24 h exposure to different conditions. Transmission electron micrographs of MCF-7 cells (top row, images A-D) compared to MCF-12A cells (bottom row, images E-H). Vehicle-exposed cells (A and E) showed smooth cell membrane with limited apical microvilli surrounding the cells. C9 (130 nM)-exposed MCF-7 (B) cells exhibited formation of vacuoles, however, large number of MCF-12A cells remain unaffected and standard cell proliferation followed after treatment. Cells exposed to C9 in combination with DCA (7.5 mM) (C, D, G and H) showed significant amount of microvilli increase, distorted cell shapes, enlarged mitochondrion, increased number of vacuoles (autophagosome and lysosomes) formation and DNA damage (heterochromatin and DNA fragmentation).

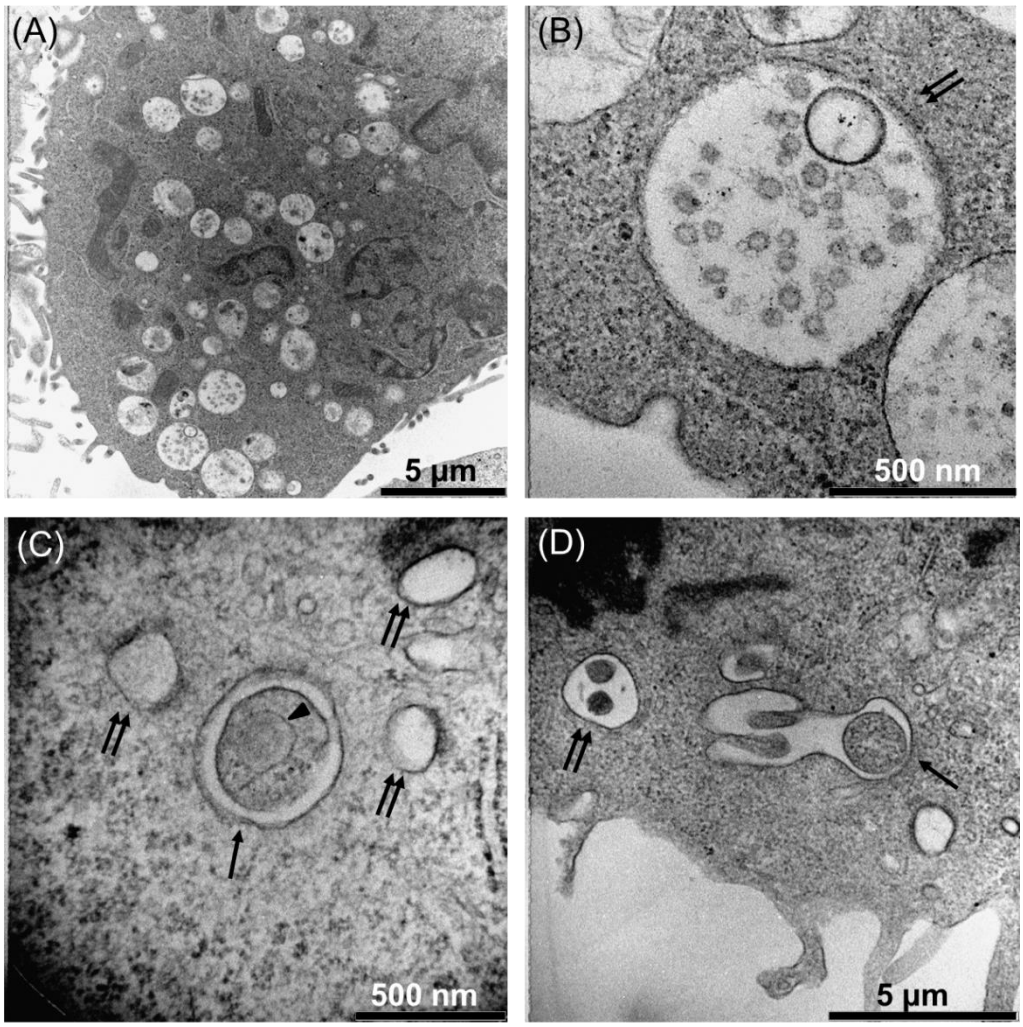

Figure 3.20: Electron microscopic analysis of C9+DCA-treated MCF-7 and MCF-12A cells. Increased number of vacuoles formation in C9+DCA-exposed (24 h) MCF-7 (A and B) and MCF-12A (C and D) cells. Autophagosome and autolysosome morphology: arrows indicate autophagosomes, double arrows indicate autolysosomes/amphisomes and arrowhead indicate fragments of endoplasmic reticulum inside the autophagosome.

3.5 Cell cycle analysis

Previous studies demonstrated that sulphamoylated derivatives of 2ME are able to induce cell cycle arrest in a number of tumorigenic cell lines *in vitro*, as well as xenograft models (366,368). In this study, the effect of an *in silico*-designed novel C-17 modified sulphamoylated derivatives in conjunction with a glycolysis inhibitor on cell cycle arrest were examined in the hormone-dependent MCF-7 and hormone-independent MCF-12A cell lines. In vehicle-exposed MCF-7 cells, less than 1% of the cells were present in sub-G_1 phase and 27% were present in G_2/M phase (Figure 3.21 A and Figure 3.22 A). The antimitotic agent C9-exposed (130 nM) MCF-7 cells showed slightly elevated levels of cells present in sub-G_1 (5%, $P = 0.13$) (Figure 3.21 A and Figure 3.22 A). However, C9 induced tumorigenic MCF-7 cell cycle arrest with 36% of cells present in G_2/M phase ($P < 0.05$) when compared to the control (Figure 3.21 A and Figure 3.22 A). After treatment with 7.5 mM of DCA on MCF-7 cells, no significant change in cell cycle events was observed. In contrast, we have observed that when DCA was added together with the antimitotic agent C9, the efficacy of combination therapy was superior than that of C9 alone exposed MCF-7 cells, with increased sub-G_1 (19%, $P < 0.05$) and G_2/M (35%, $P < 0.05$) phases compared to control (Figure 3.21 A and Figure 3.22 A). Alternatively, agent C9 at 130 nM after 24 h exposure did not induce non-tumorigenic MCF-12A G_2/M (22%) cell cycle arrest compared to control (23%) (Figure 3.21 B and Figure 3.22 B). The combination of C9 and DCA-exposed MCF-12A showed a statistically significant increase in sub-G_1 (10%) compared to control (5%) ($P < 0.05$). No sign of elevated G_2/M with the combination treatment was observed on MCF-12A cells (Figure 3.21 B and Figure 3.22 B). Combination treatment of the antimitotic agent with the glycolysis inhibitor resulted in 19% of the tumorigenic cells to be present in sub-G_1. However, only 10% of non-tumorigenic cells were in sub-G_1 when given the same circumstances. These observations were statistically significant ($P < 0.05$) (Figure 3.22).

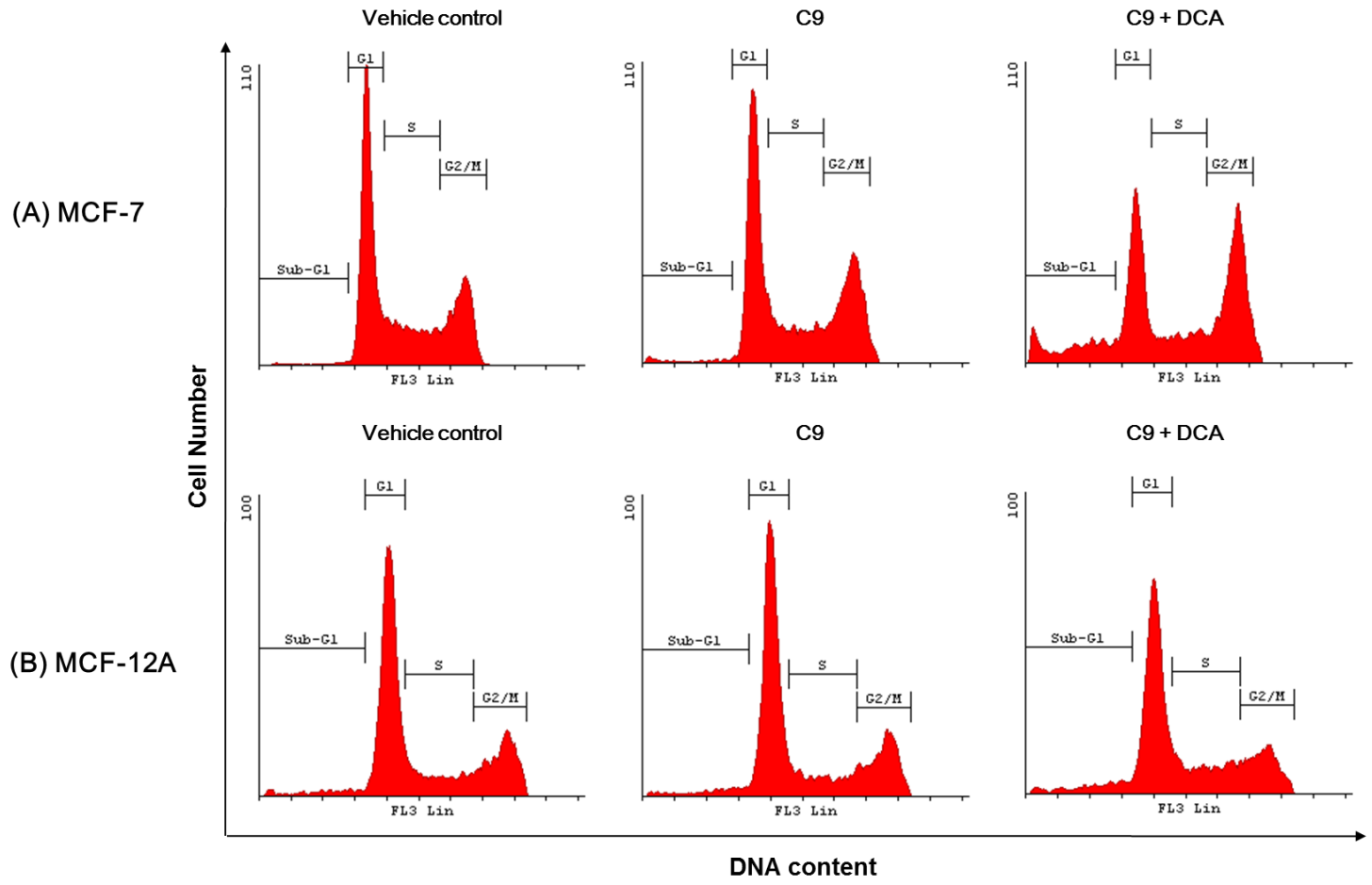

Figure 3.21: Cell cycle histograms of vehicle-, C9- and C9+DCA-exposed cells after 24 h treatment for (A) MCF-7 and (B) MCF-12A cells. This figure represents DNA content (X) versus number of cells (Y). C9 (130 nM) induced G_2/M MCF-7 (A) cell cycle arrest. Addition of DCA (7.5 mM) with C9 exhibited synergistic effects and induced G_2/M cell cycle arrest and increased sub-G_1 phase population. MCF-12A (B) cells were less affected when compared to MCF-7 cells.

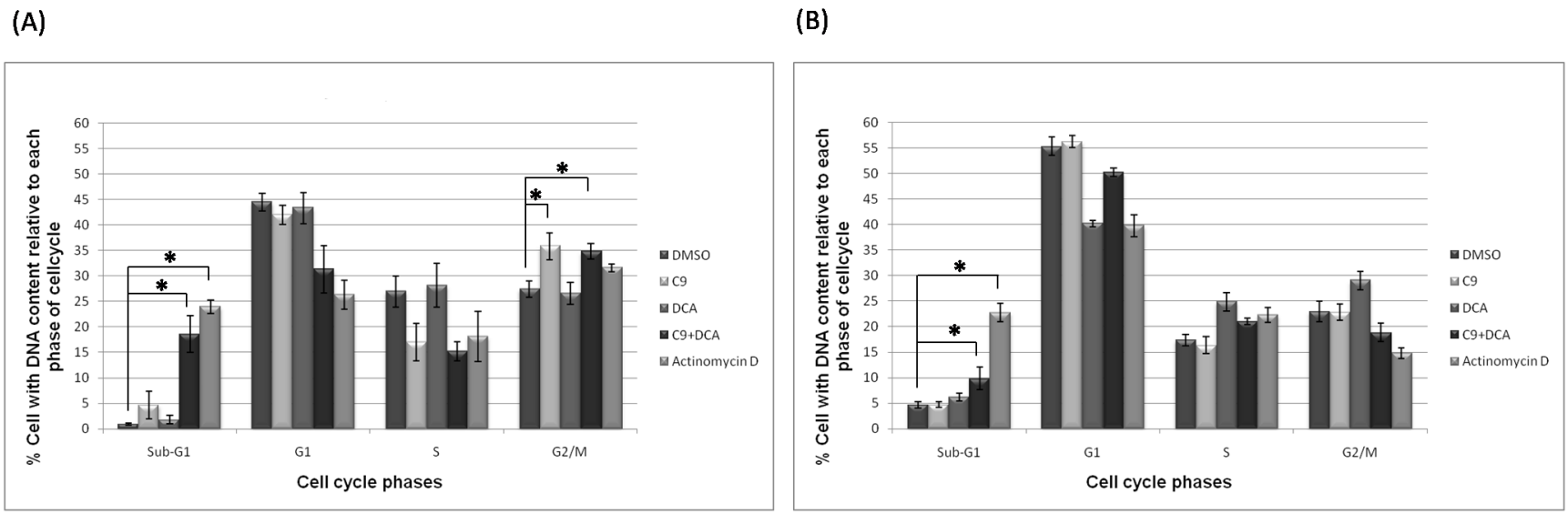

Figure 3.22: Distribution of DNA content relative to phase of cell cycle of both MCF-7 and MCF-12A cells. Data is sub-ordered to vehicle-, C9-, DCA-, C9 plus DCA- and actinomycin D (positive control for apoptosis)-exposed cells. Both cell lines indicated a statistically significant increase in the sub-G_1 phase of the C9+DCA-exposed samples compared to vehicle-treated cells. MCF-7 (A) cells were more susceptible to the combination compounds treatment when compared to MCF-12A (B) cells. An asterisk (*) indicates a *P*-value < 0.05 when compared to the vehicle control.

3.6 Apoptosis quantification

Phosphatidylserine outer membrane redistribution

Analysis of cellular apoptosis is one of the methods to understand the possible mechanisms for C9+DCA mediated cell death. Externalization of phosphatidylserine was detected with Annexin V-FITC and measured with a flow cytometer. In terms of apoptosis induction, in both types of cells, neither the antimitotic agent C9 (130 nM) nor the glycolysis inhibitor DCA (7.5 mM) alone had a significant effect compared to controls (Figure 3.23). However, when both cell types were exposed to the combination therapy (C9+DCA) for 24 h, there were 15.3% MCF-7 and 5.7% MCF-12A cells present in early apoptosis phase and the increase was statistically significant when compared relative to the controls ($P < 0.05$) (Figure 3.23). These findings are in agreement with the previous cell cycle analyses with the sub-G_1 results (Figure 3.22). Evaluation of apoptosis induction results between the two cell lines revealed that the difference between early apoptosis for MCF-7 (15.3%) and MCF-12A (5.7%) cells were statistically significant ($P < 0.05$) (Figure 3.23).

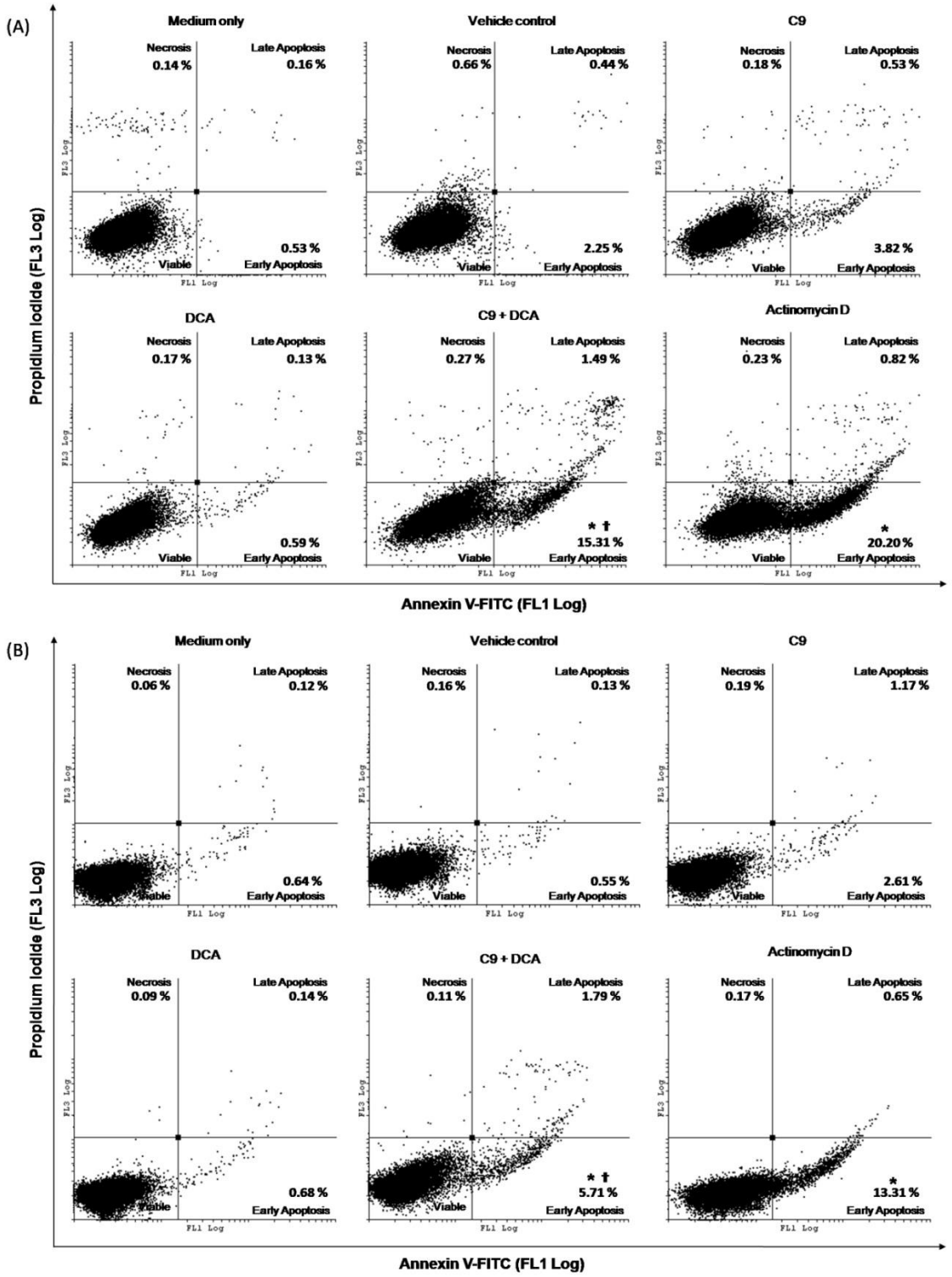

Figure 3.23: Propidium iodide (FL3 Log) vs. Annexin V-FITC (FL1 Log) dot-plot of cells propagated in growth medium, vehicle (DMSO)-, C9-, DCA-, C9+DCA- and actinomycin D-exposed MCF-7 (A) and MCF-12A (B) cell. Cells treated with vehicle control (DMSO

v/v < 0.01%) revealed no toxic effect. Neither C9-treated nor DCA-treated MCF-7 cells caused severe degree of apoptosis when compared to C9+DCA-exposed cells. Apoptosis induction results between the two cell lines revealed the difference between early apoptosis for MCF-7 (15.3%) and MCF-12A (5.7%) cells were statistically significant ($^{\dagger}P < 0.05$). $^{*}P$-value < 0.05 after comparison of exposed cells and controls within the same cell line.

3.7 Autophagic activity

Microtubule-associated protein 1 light chain 3 (II) expression

Microtubule-associated protein 1 light chain 3 (LC3) is the only known mammalian protein identified that stably associates with the autophagosome membranes. Hence LC3-I is cytosolic, while the identification and quantification of membrane bound LC3-II can be utilized as a specific marker for mammalian cells undergoing autophagic process. C9+DCA-treated MCF-7 and MCF-12A cells after 24 h exposures showed statistically significant increases (23.2% and 25.8% respectively) in LC3-II expression when compared to the vehicle-treated control as well as C9-treated samples ($P < 0.05$) (Figure 3.24). Tamoxifen (2.5 μM) was used as a positive control for autophagy induction in breast cancer cells. This finding suggests that autophagic induction is increased due to the combination treatment and this result appears to support the previously displayed TEM micrographs (Figure 3.19 and Figure 3.20).

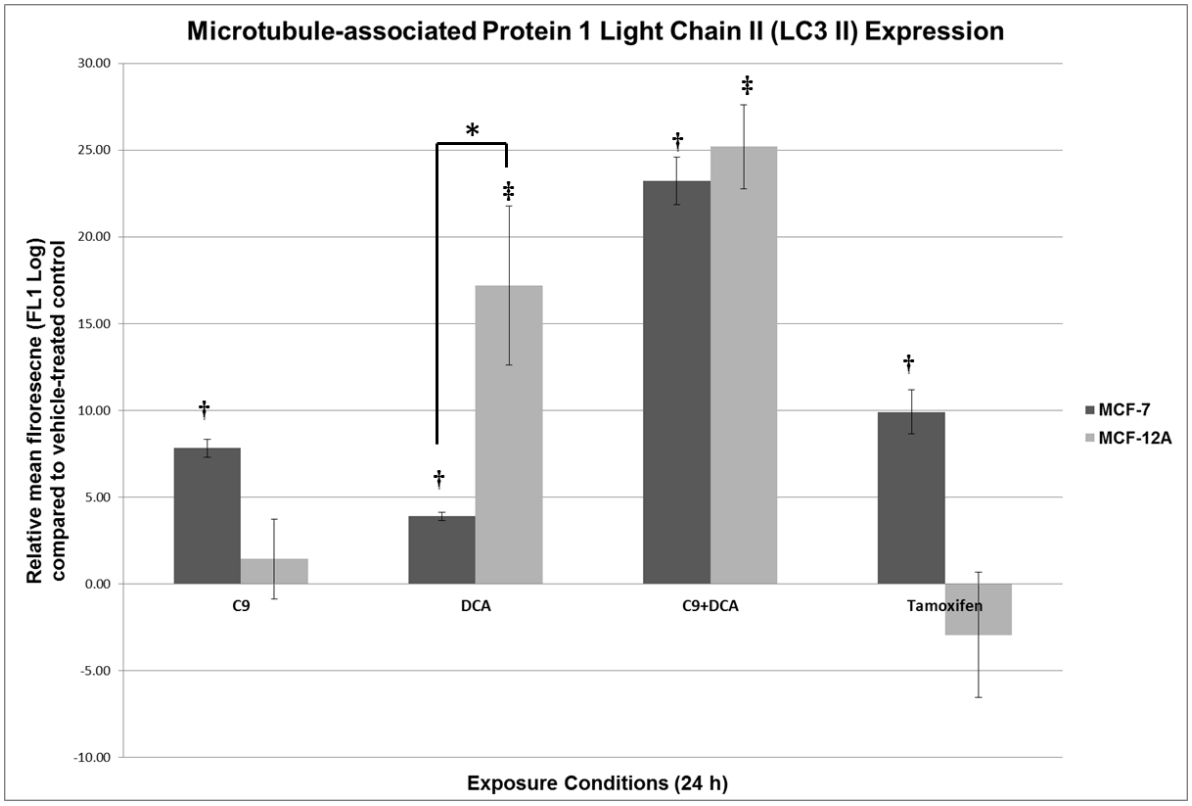

Figure 3.24: Autophagic related quantification of specific microtubule-associated protein 1 light chain 3 II (LC3 II) expression in MCF-7 and MCF-12A cells. 130 nM of C9 induced 7.8% LC3 II expression in MCF-7 cells compared to DMSO-exposed control (*P*-value < 0 .05). Treatment of DCA (7.5 mM) induced 17.2% of LC3 II expression in MCF-12A cells compared to DMSO-exposed control (*P*-value < 0 .05). C9+DCA-exposed MCF-7 and MCF-12A cells induced LC3 II expression 23.2% and 25.2% respectively, when compared to control (DMSO-exposed). **†, ‡***P*-value < 0.05 after comparison of exposed cells and controls within the same cell line. **P*-value < 0.05 when MCF-7 and MCF-12A cells were compared for the same treatment.

3.8 Mitochondria membrane potential depolarization

MitoCapture™, a cationic dye that fluoresces differently in healthy verses apoptotic cells, was used to detect mitochondrial membrane potential depolarization ΔΨm. In apoptotic cells, the reagent cannot aggregate in the mitochondria due to the altered membrane potential and remains in monomeric form in the cytoplasm which subsequently generating a green fluorescence. The assay was conducted according to manufacturer's instruction. After treatment with C9 and C9+DCA for 24 h, there was more than a two-fold significant depolarization of ΔΨm in MCF-7 compared to vehicle-exposed controls (2.2-fold increase, $P < 0.05$) (Figure 3.25), but not for MCF-12A cells. However, treatment of DCA did not cause any membrane potential loss in MCF-7 or MCF-12A cells. In order to elucidate the possible cause of ΔΨm loss in MCF-7, NAC (5 mM) was utilized as a broad spectrum reactive oxygen species (ROS) inhibitor. Addition of the general ROS inhibitor NAC into cell propagated in medium reduced the mitochondrial membrane potential in both cell lines. Furthermore, NAC completely attenuated the antimitotic compound C9 and the combination of C9+DCA's effects on MCF-7 cells ($P < 0.05$) (Figure 3.25). This result serves as possible indication that treatment with C9 and C9+DCA caused increased ROS production in MCF-7 cells.

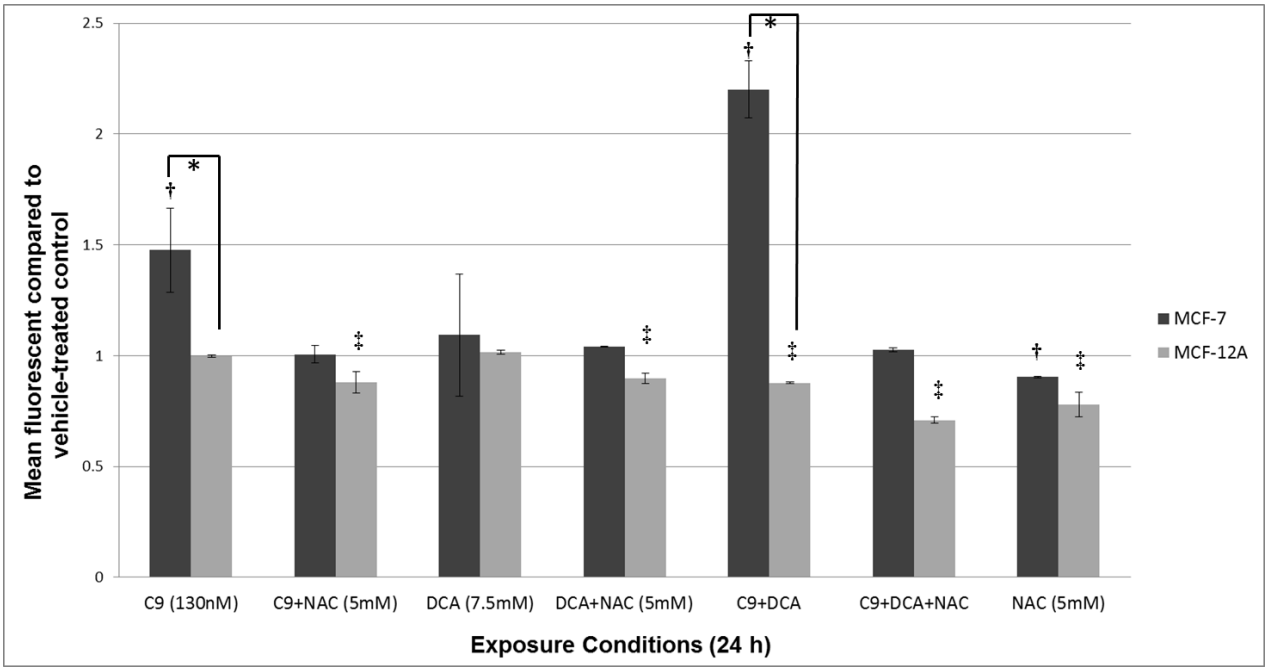

Figure 3.25: MitoCapture^{TM} cationic dye detection of mitochondrial membrane potential (ΔΨm) depolarization. Treatment with C9 (130 nM) and C9+DCA increased MCF-7 cell mitochondrial membrane potential (ΔΨm) depolarization compared to vehicle-exposed controls to 1.5 and 2.2-fold respectively ($P < 0.05$). None of the treatments influenced ΔΨm depolarization of MCF-12A cells. The influence of the antioxidant, NAC (5 mM), was investigated and used in conjunction with C9 (130 nM), DCA (7.5 mM) and C9+DCA. NAC attenuated the ΔΨm depolarization induced by C9 (1.5-fold) and C9+DCA (2.2-fold) on MCF-7 cells to 1.0 ($P < 0.05$). $^{\dagger}P$-value < 0.05 after comparison of exposed cells and controls within the same cell line. *P-value < 0.05 when MCF-7 and MCF-12A cells were compared for the same treatment.

3.9 Oxidative stress test via 2', 7'-dichlorofluorescein fluorescence

The altered mitochondrial membrane potential (ΔΨm) results suggested that ROS may be playing an important role in cell signalling in C9+DCA-treated tumorigenic MCF-7 cells. In order to explore and determine the hypotheses of increased ROS production (through mitochondrial damage) and/or lysosome rupture of C9+DCA-treated cells, flow cytometric analyses of MCF-7 cells loaded with the H_2O_2/Fe^{2+} sensitive fluorophore H_2DCF-DA were utilized. This result showed C9-, DCA- and C9+DCA-treated MCF-7 cells (24 h) exhibited statistically significant increases in DCF fluorescence signal compared to vehicle-treated control ($P < 0.05$) (Figure 3.26 i and ii (A)). MCF-12A cells with increased levels of H_2O_2/Fe^{2+} production were, however, not detected when provided with same treatments (C9-, DCA- and C9+DCA) (Figure 3.26 i and ii (C)). Also, C9- and C9+DCA-treated MCF-7 cells (24 h) had significant increases in DCF fluorescence signal compared to DCA-treated samples ($P < 0.05$) (Figure 3.26 i). This data suggest C9 and C9+DCA are able to induce cellular changes that resulted in increased formation of H_2O_2/Fe^{2+} in MCF-7 cells. This theory has been investigated by adding broad spectrum ROS inhibitor NAC and ferric iron chelator deferoxamine (DFO, 100 μM). Both NAC and DFO attenuated the effect of C9+DCA on MCF-7 cells in a negative manner ($P < 0.05$) (Figure 3.26 i and ii (B)). The addition of NAC and DFO into C9+DCA-treated MCF-7 cells resulted in an the x-mean shift to the left compared to the combination treatment (Figure 3.26 ii (B), indicating that ROS formation was suppressed by NAC and DFO. On the other hand, NAC suppressed ROS formation in treated, as well as untreated MCF-12A cells, but DFO did not have any significant effect on these cells (Figure 3.26 i and ii (D)). Interestingly, the effects of NAC on treated and untreated non-tumorigenic MCF-12A were not statistically significant (Figure 3.26 i and ii (D)). Flow cytometric data presented in Figure 3.26 ii displays the x-mean shift compared to vehicle-exposed control.

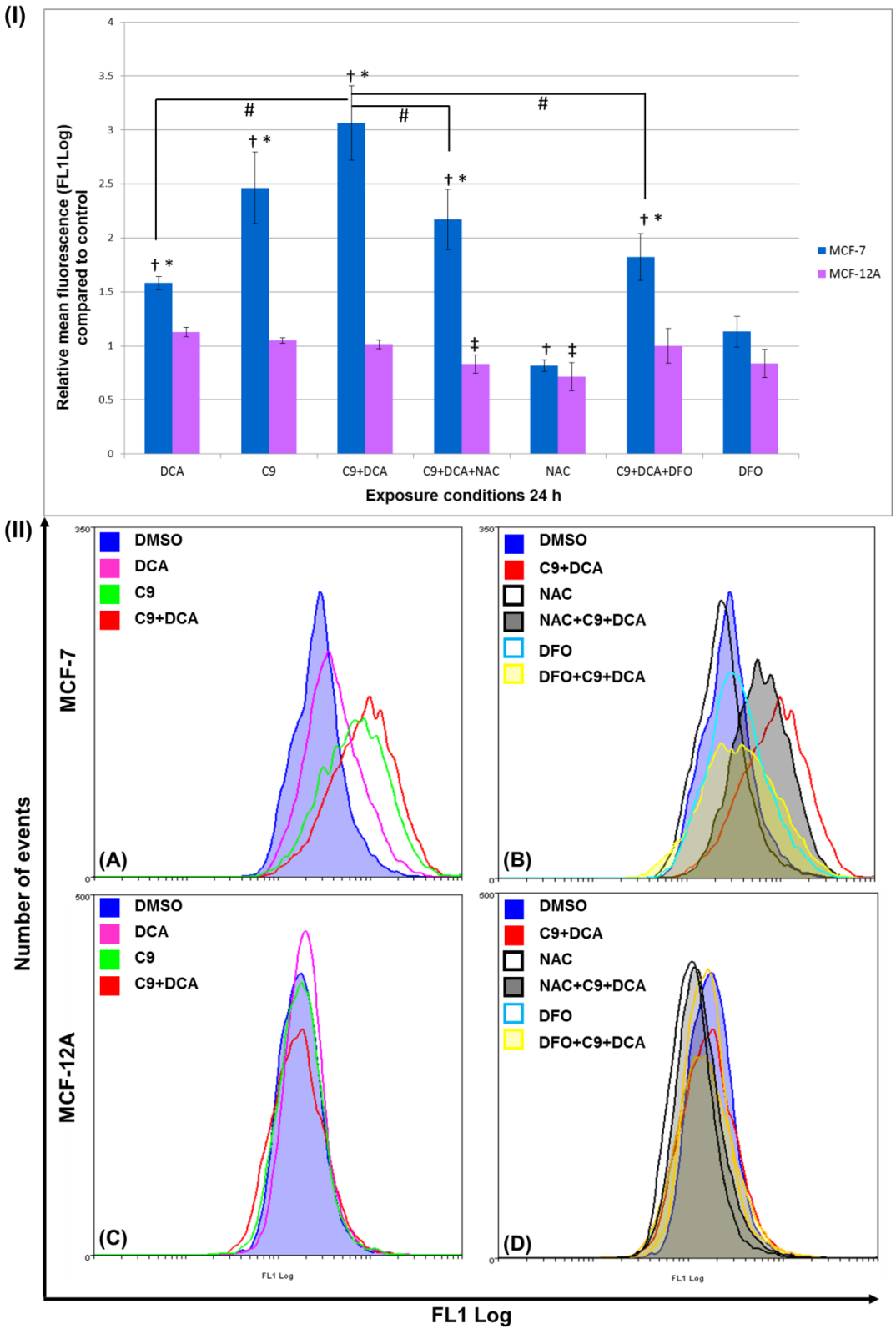
(I)
Relative mean fluorescence (FL1Log) compared to control
Exposure conditions 24 h
DCA
C9
C9+DCA
C9+DCA+NAC
NAC
C9+DCA+DFO
DFO
MCF-7
MCF-12A
(II)
Number of events
FL1 Log
MCF-7
MCF-12A
DMSO
DCA
C9
C9+DCA
NAC
NAC+C9+DCA
DFO
DFO+C9+DCA
(A)
(B)
(C)
(D)

Figure 3.26: Oxidative stress test via dichlorofluorescein fluorescence measurement for hydrogen peroxide or ferrous ions level. Relative mean fluorescence (FL1 Log) of C9-, DCA-, and C9+DCA-treated MCF-7 and MCF-12A cells compared to vehicle-exposed controls (i). Flow cytometric data of FL1 Log versus count illustrated the x-mean shift (ii) of treated MCF-7 (A) and MCF-12A (C) cell. The influence of the antioxidant, NAC (5 mM), and a ferric iron chelator, desferoxamine (100 μM), was investigated and results showed NAC and DFO reduced effect of C9+DCA treatment on MCF-7 (B) and MCF-12A (D) cell. $^{\dagger, \ddagger}$*P*-value < 0.05 after comparison of exposed cells and controls within the same cell line. **P*-value < 0.05 when MCF-7 and MCF-12A cells were compared for the same treatment. $^{\#}$*P*-value < 0.05 when C9+DCA-treatment were compared to other treatments within MCF-7 cell line.

3.10 Kinase inhibition studies

Previous mitochondrial membrane potential (ΔΨm) assays and oxidative stress test indicated the formation of ROS within MCF-7 cells after C9+DCA treatment for 24 h. Increases in intracellular ROS level may trigger the activation of p38α JNK MAPK signalling, causing induction of apoptotic events. Thus, it was decided to determine the effect on p38α and the JNK pathway in untreated, as well as treated MCF-7 and MCF-12A cells. In order to achieve this goal, a p38α inhibitor SB239063 (15 μM) and JNK inhibitor SP600125 (20 μM) were used either in untreated cells or in conjunction with treatment compounds. PlasDIC images of MCF-7 cells and MCF-12A after 24 h of exposure to the above-mentioned inhibitors were compared (Figure 3.27). Addition of p38α inhibitor SP239063 (15 μM) to either untreated or treated MCF-7 and MCF-12A cells slightly increased cell proliferation. In contrast, JNK inhibitor SP600125-exposed (20 μM) untreated MCF-7 showed signs of distress and decreased cell density. However, addition to treated MCF-7 cells attenuated the effect of C9+DCA. Similar results were observed when MCF-12A cells (treated and untreated) were exposed to JNK inhibitor SP600125 (20 μM) compared to vehicle-exposed cells. Decreased cell density was observed when the JNK inhibitor was added to MCF-12A ells. However, compared to the C9+DCA-treated cells, the effect that the C9+DCA had was attenuated by the addition of SP600125 (Figure 3.27). SP600125 (20 μM) reduced cell numbers in untreated MCF-7 and MCF-12A cells which indicates the importance of JNK pathway in promoting cell proliferation. The addition of SP600125 to treated cells masked the effect of treatment (Figure 3.27). This result indicated that inhibition of the JNK pathway interfered with treatment (C9+DCA)-induced apoptosis.

The RTCA xCELLigence system was employed to explore the possible activation of JNK or p38α MAPK after C9+DCA treatment. RTCA xCELLigence inhibition studies supported the morphological observation with p38i-exposed (SB239063, 15 μM) cells (treated or untreated) exhibited slightly higher CI curve than the cells without p38i treatment. This result showed p38α inhibition attenuated the C9+DCA treatment on MCF-7 and MCF-12A cells. However, the ability of the p38α inhibitor to reduce the effects of C9+DCA was not pronounced. On the contrary, inhibitory effects of 20 μM SP600125 on untreated MCF-7 and MCF-12A cells were demonstrated, since the CI

value was decreased statistically significant. Furthermore, these observations illustrated during morphological kinase inhibition studies were well translated into the xCELLigence experiment where SP600125 reduced treatment (C9+DCA) effect on MCF-7 and MCF-12A cells (Figure 3.28).

These inhibition studies indicate that the JNK pathway is playing an important role in normal MCF-7 and MCF-12A cell development as well as activation of apoptosis after cells encounter stress. However, p38α role in MCF-7 and MCF-12A cells' normal proliferation and apoptosis activation after stress is not pronounced.

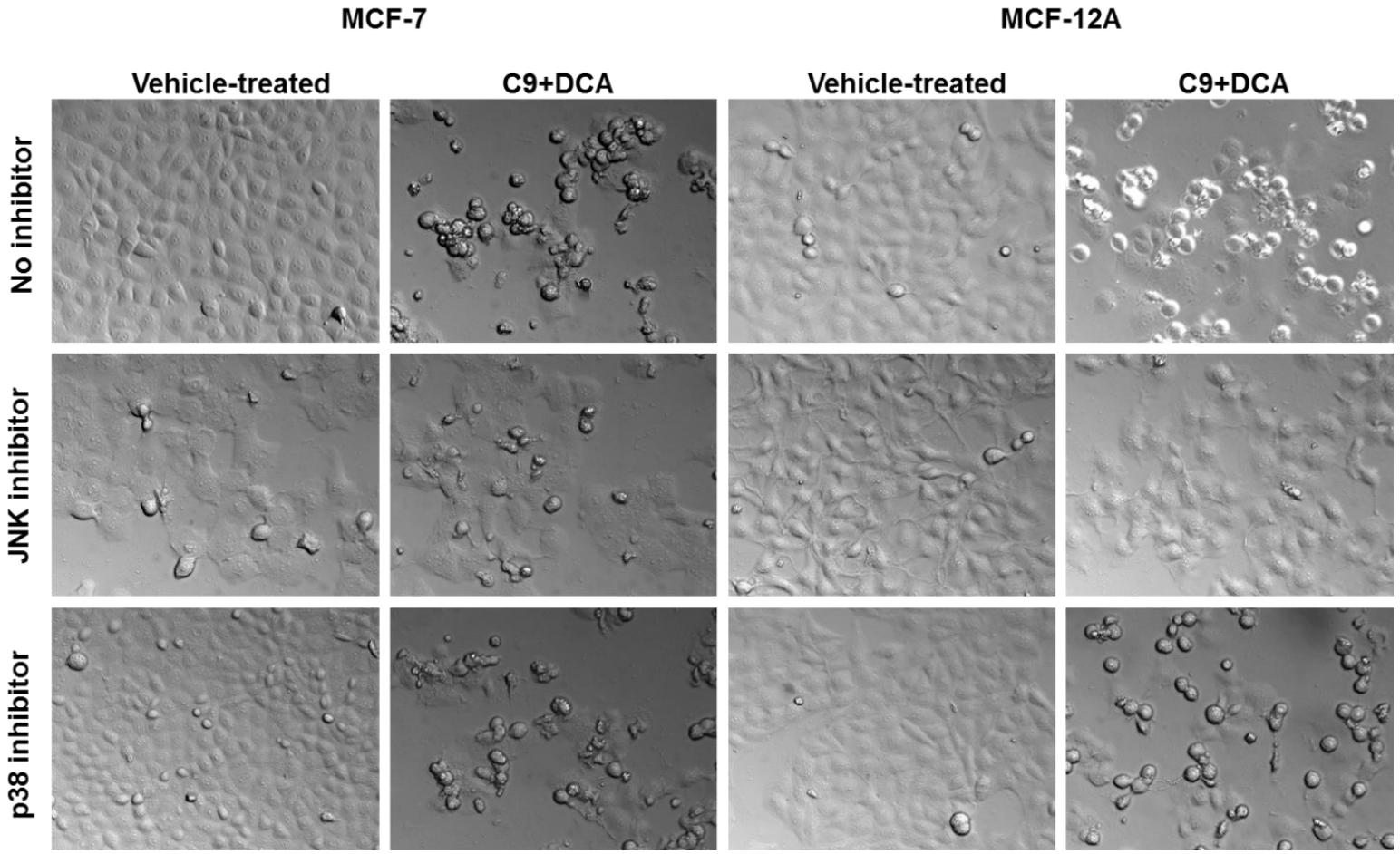

Figure 3.27: Optical transmitted light differential interference contrast images of MCF-7 cells and MCF-12A after 24 h exposure to different conditions. Vehicle-treated cells were confluent and showed no sign of distress. Cells exposed to C9 (130 nM) in combination with DCA (7.5 mM) showed significant inhibition of cell growth. JNK inhibitor SP600125-exposed (20 µM) untreated MCF-7 and MCF-12A cells were negatively affected with decreased density; however, it reduced the effect of C9+DCA on these cells. The addition of a p38 inhibitor, SB 239063 (15 µM), did not change MCF-7 and MCF-12A cells from its original appearance. (Magnification 20 X)

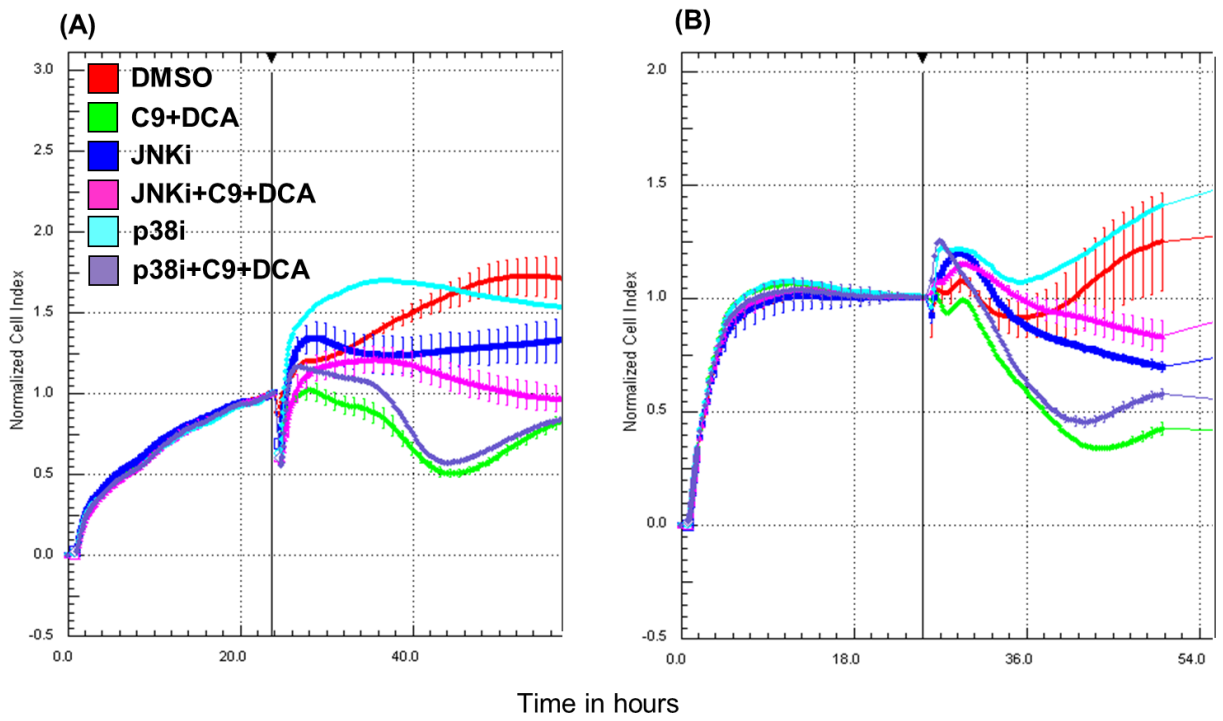

Figure 3.28: Real-time cell analyser xCELLigence system analysis of kinase inhibition studies. JNKi SP600125-exposed (20 µM) (blue) untreated MCF-7 and MCF-12A cells (red) displayed decreased CI after 8 h of treatment. JNKi+C9+DCA-exposed MCF-7 and MCF-12A cells (pink) showed increased CI compared to C9+DCA-treated cells (green) within 2 h of treatment. Addition of p38i SB239063 (15 µM) had no statistically significant effect on C9+DCA-treated MCF-7 and MCF-12A cells. Inhibition of p38 pathway in normal cells increased CI in both cell lines for 20 h after addition (24 h – 44 h) and declined CI thereafter 44 h.

3.11 Protein expression analysis

3.11.1 B cell leukaemia-2 expression and phosphorylation at Serine 70

Bcl-2 is the product of proto-oncogene *bcl-2* and functions as a prominent apoptosis suppressor (176). In response to a variety of extracellular stimuli, Bcl-2 releases pro-apoptotic factors such as Bax, thereby diminishing its inhibitory action and enables Bax oligomerization on the mitochondrial membrane (2). Thus, Bcl-2 is an anti-apoptotic protein that plays a role in modulating the membrane potential of mitochondria. An intracellular increase in the expression of Bcl-2 protein is associated with its anti-apoptotic effects by preventing mitochondrial depolarization through its interaction and ultimate inhibition of Bax (415). However, Bcl-2/Bax heterodimerization is not sufficient for full Bcl-2 anti-apoptotic function. Phosphorylation of Bcl-2 serine 70 (Ser^{70}) is a crucial requirement to complete its death suppressor signalling activity (176). Dephosphorylation of Bcl-2 at Ser^{70} is considered pro-apoptotic (415). In contrast, phosphorylation of Bcl-2 at Ser^{70} single-sited is anti-apoptotic, while multi-site phosphorylation at Ser^{70}, Trp^{69} and Ser^{87} is pro-apoptotic (416).

Merck Millipore's FlowCellect^{TM} Bcl-2 Activation Dual Detection Kit was employed to investigate the total amount of Bcl-2 protein, as well as the phosphorylation status of Bcl-2 (Ser^{70} position) in treated and control samples of MCF-7 and MCF-12A cells. The kit contains two antibodies that quantify the total amount of Bcl-2 protein (FL1 Log) and S70 phosphorylation status of Bcl-2 per cell simultaneously (FL3 Log).

The observations that C9+DCA induces mitochondrial membrane depolarization suggests that Bcl-2 may play a mechanistic role in the effects of C9+DCA. In addition, the altered oxidative status after treatment of C9+DCA suggested that ROS play a role in inducing mitochondrial membrane potential, and this finding might be linked to SAPKs such as JNK and p38. These kinases are known to be able to phosphorylate Bcl-2 protein. Therefore, a JNK inhibitor (JNKi) SP600125 (20 μM) and p38α inhibitor (p38i) SB239063 (15 μM) were included in the experiments to test whether these pathways

played roles with regards to activation/deactivation of Bcl-2 protein in MCF-7 and MCF-12A cells. NAC was also added together with C9+DCA in MCF-7 cells to determine whether it has a protective effect on this cell line.

WEASEL v3.0.2 program was used to perform the analysis for Bcl-2 protein expression and phosphorylation status. Dot-plots, histograms and bar-charts were generated for both MCF-7 and MCF-12A treated and untreated cells. Data displayed in this section is arranged in the following order: MCF-7 FL1 Log dot-plots (Figure 3.29), FL3 Log dot-plots (Figure 3.30), FL1 Log and FL3 Log histograms (Figure 3.31); MCF-12A FL1 Log dot-plots (Figure 3.32), FL3 Log dot-plots (Figure 3.33), FL1 Log and FL3 Log histograms (Figure 3.34); MCF-7 and MCF-12A total Bcl-2 protein quantification (Table 3 and Figure 3.34); MCF-7 (Figure 3.36) and MCF-12A (Figure 3.37) Bcl-2 protein phosphorylation status (S70) (Table 3).

The total expression of Bcl-2 in the treated MCF-7 samples was statistically significant lowered in C9+DCA- and actinomycin D-treated cells compared to vehicle-exposed control (Table 3 and Figure 3.35). Its level, however, increased in p38i-, C9+DCA+p38i-, JNKi- and C9+DCA+JNKi-exposed MCF-7 cells (Table 3 and Figure 3.35). Decreased expression of total Bcl-2 in C9+DCA-treated cells suggests that the anti-apoptotic effects of Bcl-2 may be inhibited by C9+DCA treatment. Also, the increased expression of Bcl-2 in p38i- and JNKi-treated cells suggests that inhibition of these proteins is anti-apoptotic.

In MCF-12A cells, total Bcl-2 expression decreased in actinomycin D-treated cells and increased in DCA-, JNKi and C9+DCA+JNKi-exposed cells (Table 3 and Figure 3.35). Total Bcl-2 expression was unaffected in MCF-12A cells exposed to C9+DCA (Table 3 and Figure 3.35). This result means 130 nM of C9 in combination with 7.5 mM of DCA effectively inhibited the anti-apoptotic effects of Bcl-2 protein expression in MCF-7 cells, but not in MCF-12A cells.

When measuring the phosphorylation status (FL3 = pBcl-2 at Ser^{70}) of MCF-7 and MCF-12A cells it was observed that > 90% of vehicle-treated cells had a fluorescence

intensity (FI) of 7.5-75 which is considered the normal range phosphorylation status for healthy proliferating cells (Figure 3.31, and Figure 3.34). For the viewer's convenience, dotted lines have been drawn to create divisions amongst sub-population on the FL3 Log histograms with label (i) hypo-p-S70, (ii) normal and (iii) hyper-p-S70. Those histograms are derived from flow cytometric analysis of dot-plots (Figure 3.30 and Figure 3.33). Three sub-populations per sample were obtained based on the FL3 Log fluorescence intensity unit measured. Cells that had an increase in FL3 fluorescence intensity of above 75 where considered to be cells that contained more phosphorylated Ser^{70} Bcl-2 intracellular proteins when compared to the control and thus an indication of hyper-phosphorylated Bcl-2 (hyper-p-S70). On the other hand, cells that had an increase in FL3 fluorescence intensity of below 7.5 were considered to be cells that contained less phosphorylated Ser^{70} Bcl-2 intracellular proteins when compared to the control and thus an indication of hypo-phosphorylated Bcl-2 (hypo-p-S70).

Figure 3.36 revealed that six treatments including C9, C9+DCA, C9+DCA+JNKi, JNKi, C9+DCA+p38i and actinomycin D decreased normal Bcl-2 S70 phosphorylation sub-population of MCF-7 cell compared to DMSO-exposed control. In turn, these six treatments resulted in a significant increase in Bcl-2 S70 hypo-phosphorylation sub-populations compared to DMSO control (Figure 3.36A and Table 4).

In MCF-7 cells, C9+DCA treatment resulted in a decrease in the number of cells with an FL3 FI of 7.5-75 (normal) when compared to the vehicle-treated control (Figure 3.36 and Table 4). Both JNK inhibition and ROS inhibition (NAC treatment, data not shown) in C9+DCA-treated MCF-7 cells also decreased the number of cells with an FL3 FI of 7.5-75 (normal) when compared to the vehicle-exposed control. However, addition of JNKi and NAC in C9+DCA-treated cells resulted the amount of cells with hypo- and hyper-phosphorylated Bcl-2 (S70) statistically significantly decreasing when compared to C9+DCA-treated cells (Figure 3.36 and Table 4). MCF-7 cells treated with C9+DCA together with the p38i showed no difference when compared to the C9+DCA cells. Results indicated that C9+DCA treatment abrogates the phosphorylation status of Bcl-2 and that JNK inhibition, as well as NAC treatment (but not p38 inhibition) prevents the C9+DCA-mediated abrogation of Bcl-2 phosphorylation. This in turn suggests that ROS

and JNK activation (possibly via ROS) in C9+DCA-treated cells has pro-apoptotic effects which may relate to how they change the S70 phosphorylation status of Bcl-2.

In MCF-12A cells, similar effects were observed, however, the effect was more pronounced in the MCF-7 cell line when compared to the MCF-12A cell line (Figure 3.37 and Figure 3.38). Figure 3.37 revealed that C9+DCA, C9+DCA+p38i and actinomycin D had a decreased 'normal' sub-population compared to the DMSO-exposed control. All three treatments caused significant increase in hypo-phosphorylation sub-population compared to DMSO control. C9+DCA and C9+DCA+p38i increased the amount of cells that entered the hyper-phosphorylation sub-population when compared to vehicle-exposed control. When compared to the Bcl-2 phosphorylation status of different treatments within the same cell line, C9+DCA-treated MCF-12A cells displayed statistically significant increase in hypo-p-S70 and hyper-p-S70 cell populations than DCA-, C9-, C9+DCA+JNKi- and p38i-treated cells ($P < 0.05$) (Figure 3.37). MCF-12A results also indicate that the combination treatment C9+DCA abrogates the phosphorylation status of Bcl-2 and that JNK inhibition, but not p38 inhibition, stops the C9+DCA-mediated abrogation of Bcl-2 phosphorylation.

Interestingly, actinomycin D-treated cells resulted in a decrease in the amount of cells in both cell lines with "normal" phosphorylation and corresponded with only an increase the amount of cells that are hypo-phosphorylated on Bcl-2 (S70). In contrast, C9+DCA treatment also resulted in a decrease in the amount of cells in both cell lines with "normal" phosphorylation, however, these cells had an increase in cells with both hypo- and hyper-phosphorylated Bcl-2 (S70). C9 is an antimitotic compound and blocks cells in G_2/M and it is also known that multi-site phosphorylation of Bcl-2 is associated with a G_2/M block in MCF-7 and MDA-MB-231 cells (416). Therefore, the data suggest that C9+DCA treatment can result in multi-site phosphorylation of Bcl-2, however, this proposed mechanism needs to be confirmed.

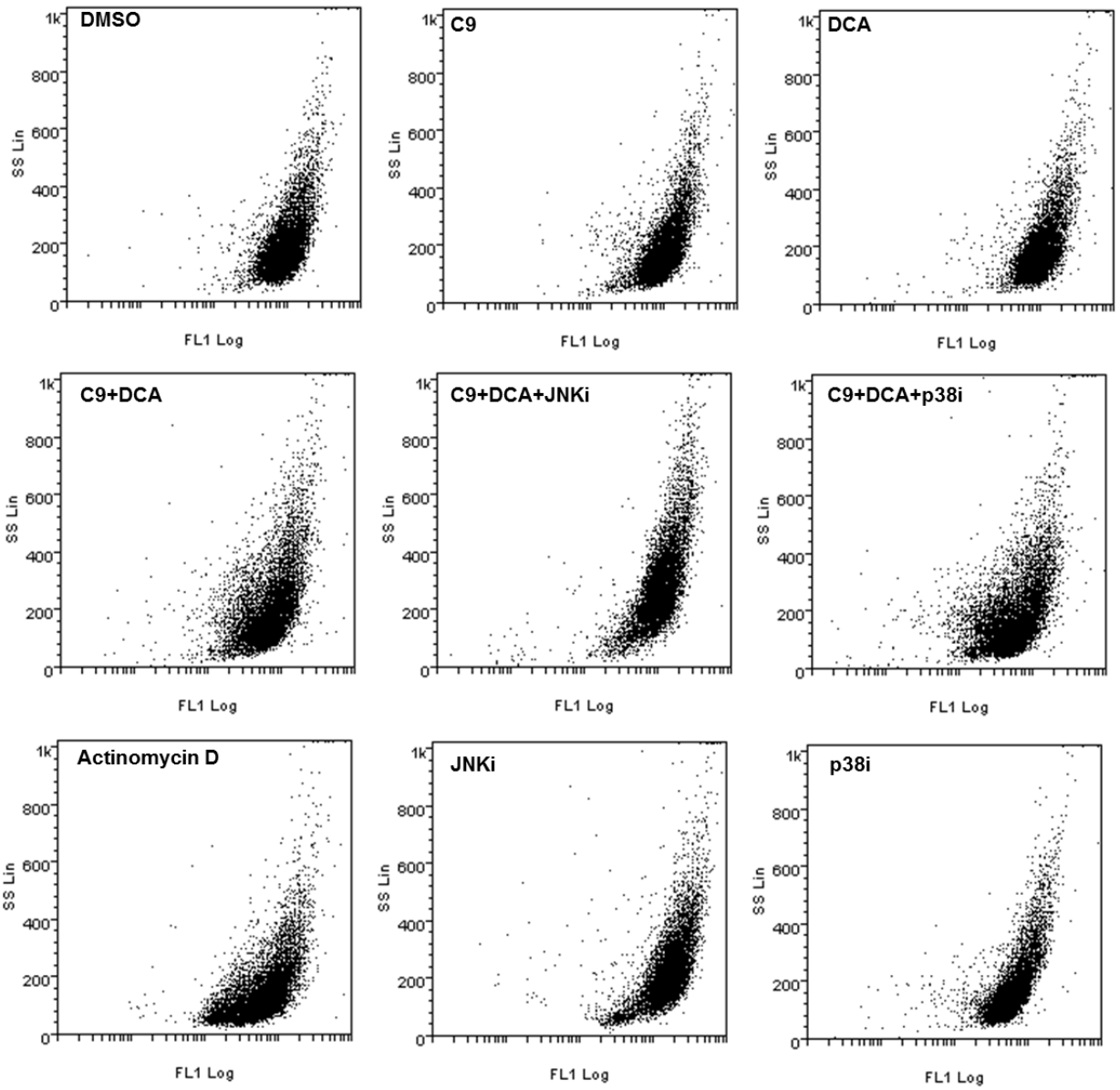

Figure 3.29: Total B cell leukaemia-2 protein expression (FL1 Log) dot-plots of treated MCF-7 cells 24 h. Exposure conditions: DCA (7.5 mM), C9 (130 nM), C9+DCA, p38 inhibitor (p38i: SB 239063) (15 µM), C9+DCA+p38i, JNK inhibitor (JNKi: SP600125) (20 µM) and actinomycin D (2 µg/ml). C9-, DCA- and p38i-exposed MCF-7 cells displayed similar dot-plot pattern compared to DMSO-exposed cells. Treatment of C9+DCA, C9+DCA+p38i and actinomycin D displayed a portion of cell population decreased in total Bcl-2 stains compared to DMSO-exposed (reflected on x-axis left shift). C9+DCA+JNKi-exposed cells attenuated the population x-axis left shift effect produced by C9+DCA-exposed cells. Further analyses (demonstrating the x-axis shift) are included in subsequent histograms.

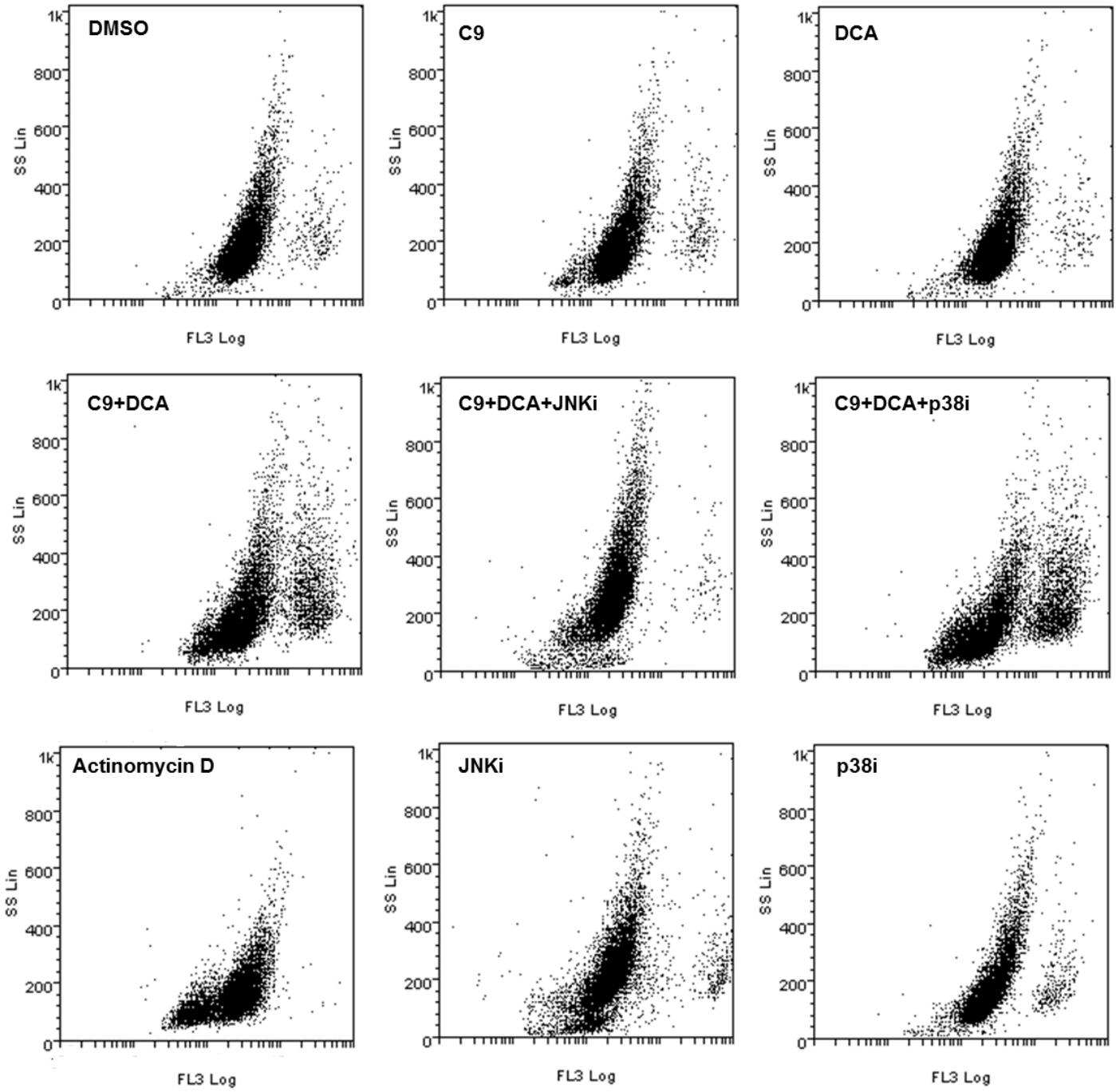

Figure 3.30: Phosphorylated B cell leukaemia-2 protein quantification (FL3 Log) dot-plots of treated MCF-7 cells 24 h. Exposure conditions, DCA (7.5 mM), C9 (130 nM), C9+DCA, p38 inhibitor (p38i: SB 239063) (15 µM), C9+DCA+p38i, JNK inhibitor (JNKi: SP600125) (20 µM) and actinomycin D (2 µg/ml). The DMSO control MCF-7 cells mainly showed a large population which correlates to normal phosphorylation status as previously defined. Treatments affected this Bcl-2 phosphorylation status with C9+DCA displaying three cell populations with a large normal Bcl-2 S70 in the middle and two smaller populations appears to either the left or right of the 'normal' population. The left and right smaller populations represent 'hypo-p-S70' and 'hyper-p-S70' respectively. Further analyses (demonstrating the x-axis) are included in subsequent histograms.

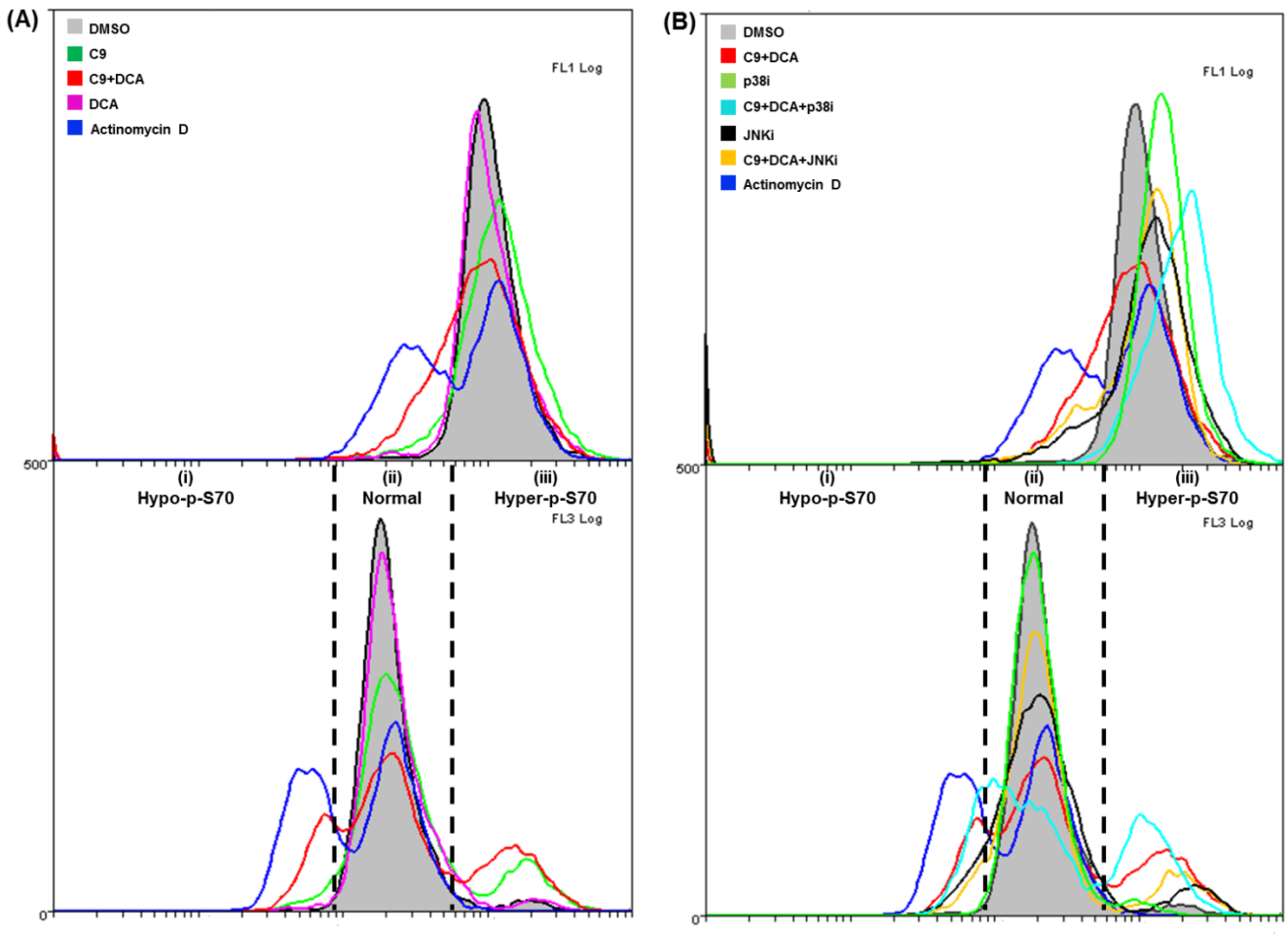

Figure 3.31: Histograms of total (FL1 Log) and phosphorylated (FL3 Log) B cell leukaemia-2 protein quantification of treated MCF-7 cells for 24 h. Exposure conditions: DCA (7.5 mM), C9 (130 nM), C9+DCA, p38 inhibitor (p38i: SB 239063) (15 µM), C9+DCA+p38i, JNK inhibitor (JNKi: SP600125) (20 µM) and actinomycin D (2 µg/ml). Effects of treatment DCA, C9 and C9+DCA on MCF-7 Bcl-2 protein expression (FL1 Log) and serine 70 phosphorylation statuses (FL3 Log) are

displayed in (A). Inhibition studies (JNK and p38) on MCF-7 Bcl-2 protein expression (FL1 Log) and serine 70 phosphorylation statuses (FL3 Log) are displayed in (B).

C9- or DCA-exposed MCF-7 cells displayed similar histogram patterns compared to DMSO-exposed cells (A, FL1 Log). Treatment with C9+DCA and actinomycin D displayed a portion of cell population decreased in total Bcl-2 stain compared to DMSO-exposed (reflected on x-axis left shift) (A, FL1 Log). C9+DCA+p38i, p38i, C9+DCA+JNKi, JNKi-exposed MCF-7 cells showed increased Bcl-2 expression compared to DMSO-exposed (reflected on x-axis right shift) (B, FL1 Log).

FL3 Log (A and B) histograms displayed DCA- and p38i-exposed MCF-7 cells showed similar patterns compared to DMSO-exposed cells, where more than 90% of the cell population displayed normal Bcl-2 phosphorylation at S70. C9-exposed MCF-7 cells displayed increased hyper-p-S70 population compared to DMSO control. C9+DCA- and C9+DCA+p38i-exposed MCF-7 cells displayed increased hypo-, as well as hyper-p-S70 population compared to DMSO control. C9+DCA+JNKi showed an increased number of cells in the normal population in terms of Bcl-2 S70 phosphorylation compared to C9+DCA-treated MCF-7 cells.

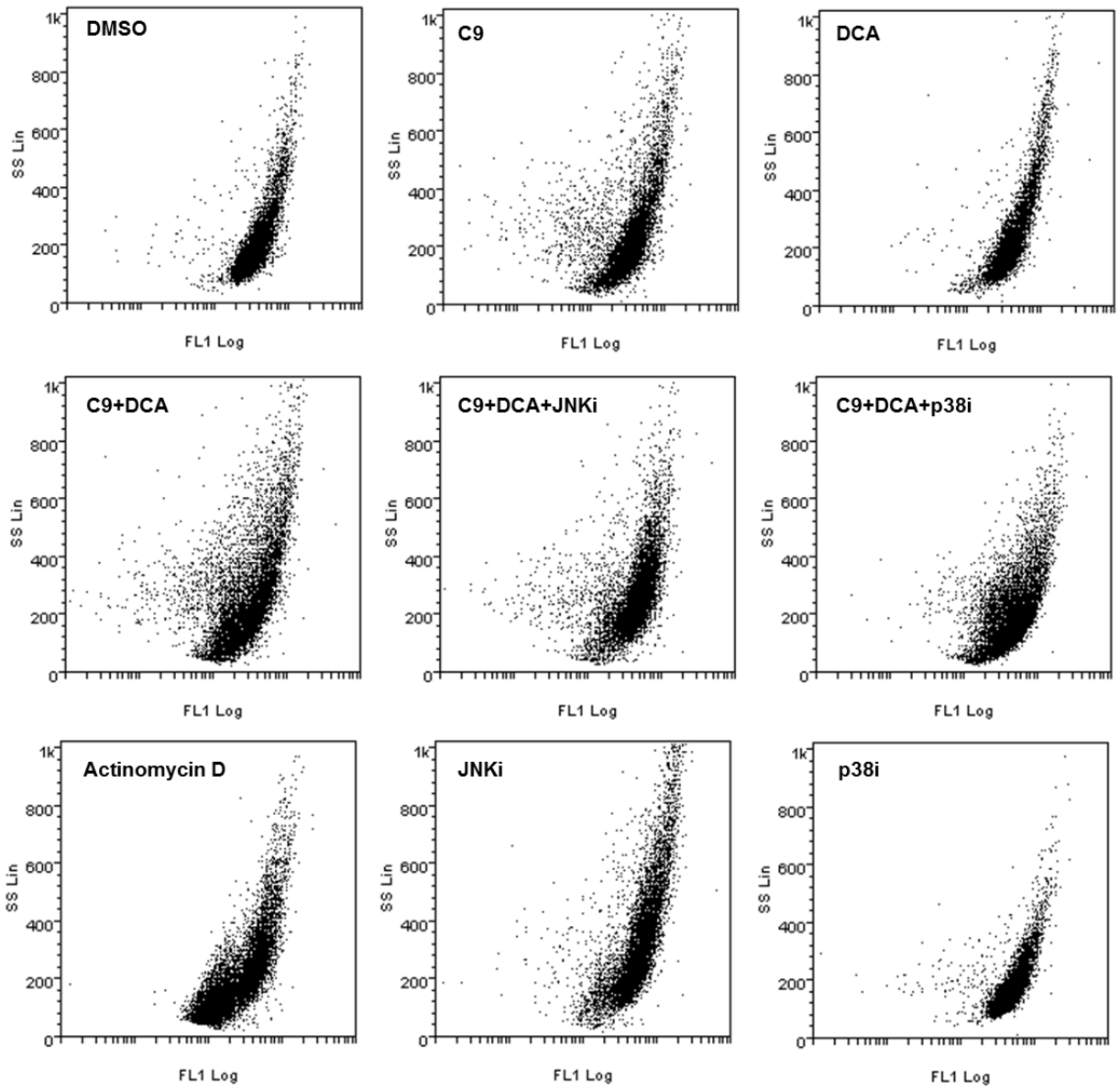

Figure 3.32: Total B cell leukaemia-2 protein expression (FL1 Log) dot-plots of treated MCF-12A cells 24 h. Exposure conditions: DCA (7.5 mM), C9 (130 nM), C9+DCA, p38 inhibitor (p38i: SB 239063) (15 µM), C9+DCA+p38i, JNK inhibitor (JNKi: SP600125) (20 µM) and actinomycin D (2 µg/ml). DCA- and p38i-exposed MCF-7 cells displayed similar dot-plot pattern compared to DMSO-exposed cells. C9, C9+DCA, C9+DCA+p38i, C9+DCA+JNKi, actinomycin D and JNKi-treated cells displayed a portion of cell population decreased in total Bcl-2 stains compared to DMSO-exposed (reflected on x-axis left shift). Further analyses (demonstrating the x-axis) are included in subsequent histograms.

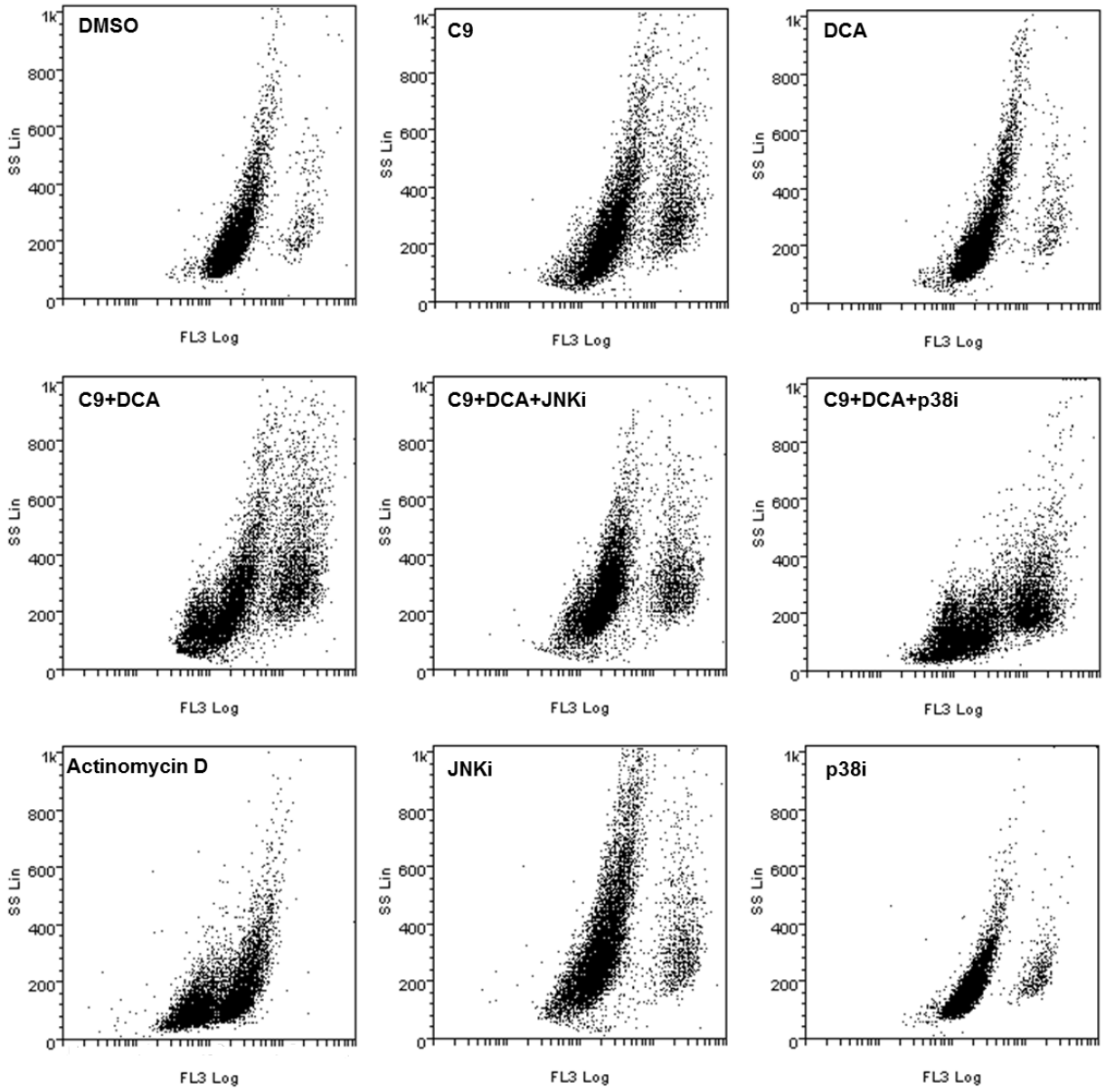

Figure 3.33: Phosphorylated B cell leukaemia-2 protein quantification (FL3 Log) dot-plots of treated MCF-12A cells at 24 h. Exposure conditions, DCA (7.5 mM), C9 (130 nM), C9+DCA, p38 inhibitor (p38i: SB 239063) (15 µM), C9+DCA+p38i, JNK inhibitor (JNKi: SP600125) (20 µM) and actinomycin D (2 µg/ml). The purpose of this set of dot-plot was to illustrate that DMSO control MCF-12A cells showed mainly a large middle population which correlates to normal phosphorylation status. Treatments affected this Bcl-2 phosphorylation status with C9+DCA displaying three cell population with a large normal Bcl-2 S70 in the middle and two smaller populations appears to either the left or right of the 'normal' population. The left and right smaller populations represent 'hypo-p-S70' and 'hyper-p-S70'. Further analyses (demonstrating the x-axis) are included in subsequent histograms.

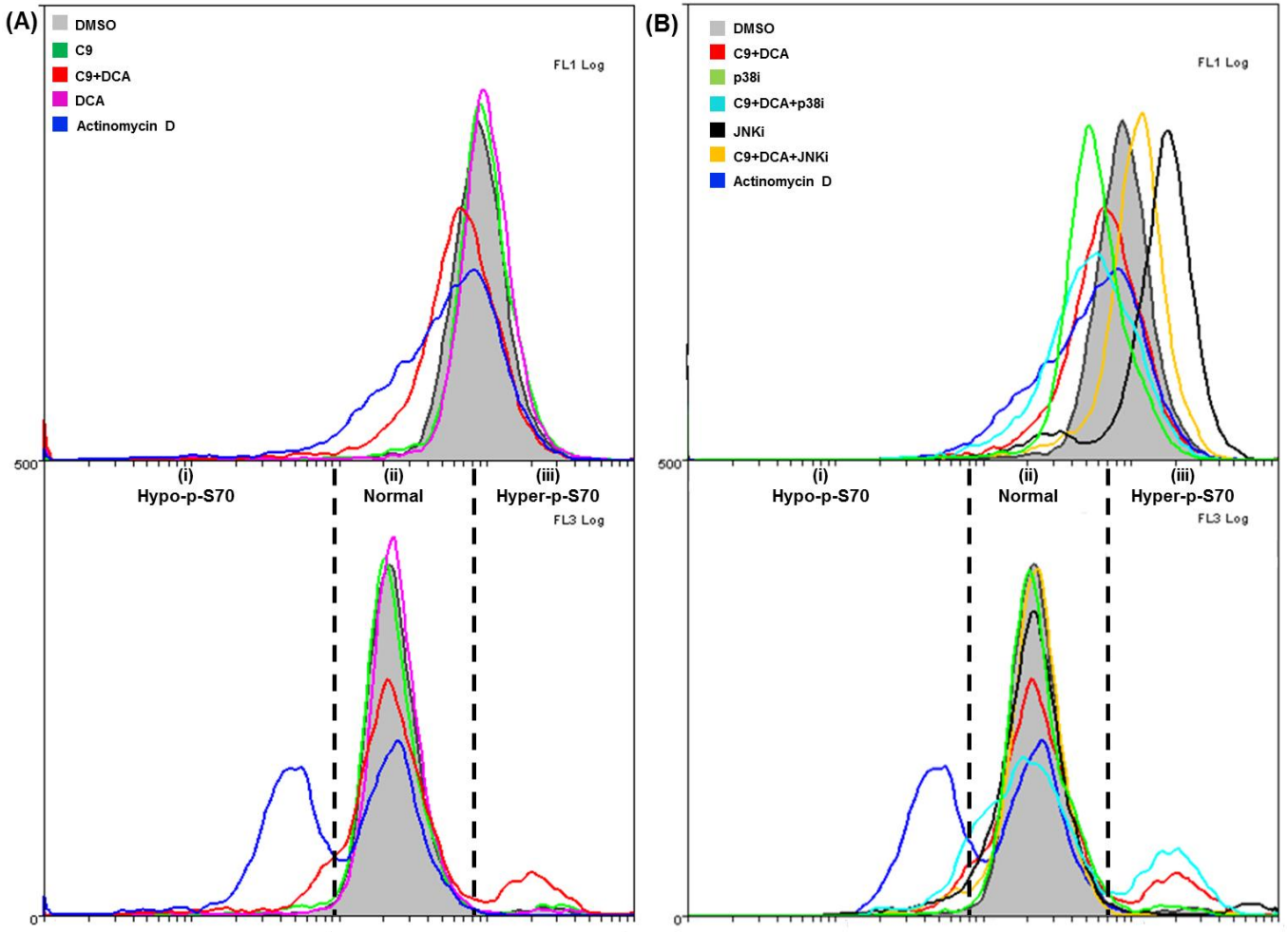

Figure 3.34: Histograms of total (FL1 Log) and phosphorylated (FL3 Log) Bcl-2 protein quantification of treated MCF-12A cells for 24 h. Exposure conditions: DCA (7.5 mM), C9 (130 nM), C9+DCA, p38 inhibitor (p38i: SB 239063) (15 µM), C9+DCA+p38i, JNK inhibitor (JNKi: SP600125) (20 µM) and actinomycin D (2 µg/ml). Effects of treatment DCA, C9 and

C9+DCA on MCF-12A Bcl-2 protein expression (FL1 Log) and serine 70 phosphorylation statuses (FL3 Log) are displayed in (A). Inhibition studies (JNK and p38) on MCF-12A Bcl-2 protein expression (FL1 Log) and serine 70 phosphorylation statuses (FL3 Log) are displayed in (B).

C9- or DCA-exposed MCF-12A cells displayed similar histogram patterns compared to DMSO-exposed cells (A, FL1 Log). Treatments with C9+DCA, C9+DCA+p38i, p38i and actinomycin D displayed a portion of cell population decreased in total Bcl-2 stain compared to DMSO-exposed (reflected on x-axis left shift) (A and B FL1 Log). C9+DCA+JNKi and JNKi exposed MCF-12A cells showed increased Bcl-2 expression compared to DMSO-exposed (reflected on x-axis right shift) (B, FL1 Log).

FL3 Log (A and B) histograms displayed C9-, DCA-, p38i-, JNKi and C9+DCA+JNKi-exposed MCF-12A cells. Similar patterns compared to DMSO-exposed cells, where 90% or more of the cell population displayed normal Bcl-2 phosphorylation at S70 were observed. Actinomycin D-exposed MCF-12A cells displayed increased hypo-p-S70 population compared to DMSO control. C9+DCA- and C9+DCA+p38i-exposed MCF-12A cells displayed increased hypo-, as well as hyper-p-S70 population compared to DMSO control.

Table 3: Total B cell leukaemia-2 protein expression ratio compared to vehicle-exposed control.

Exposure conditions	MCF-7		MCF-12A	
(24 h)	Average	StdEV	Average	StdEV
DCA	1.100	0.094	1.102	0.013
C9	1.050	0.128	1.033	0.057
C9+DCA	0.907	0.043	0.857	0.194
C9+DCA+p38i	1.659	0.301	1.070	0.062
p38i	1.455	0.159	1.041	0.040
C9+DCA+JNKi	1.293	0.025	1.285	0.067
JNKi	1.646	0.132	1.943	0.243
C9+DCA+NAC	0.825	0.261	-	-
Actinomycin D	0.844	0.080	0.675	0.065

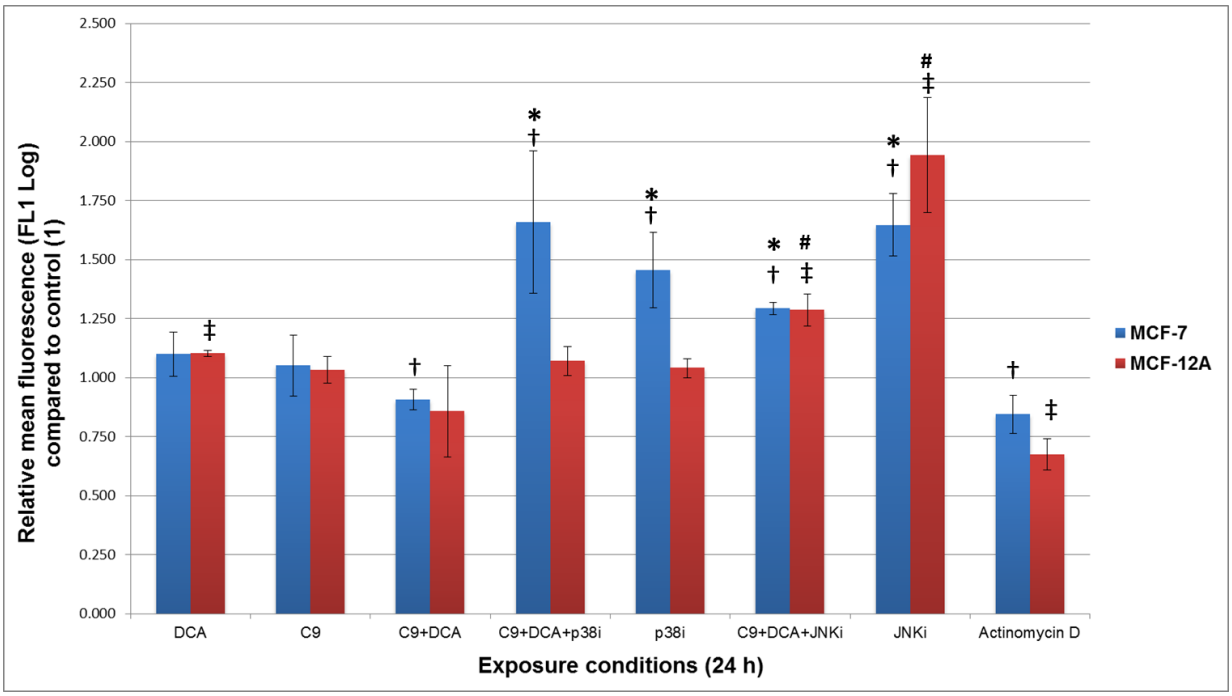

Figure 3.35: Total B cell leukaemia-2 protein expression of treated MCF-7 and MCF-12A cells. Exposure conditions: DCA (7.5 mM), C9 (130 nM), C9+DCA, p38 inhibitor (p38i: SB 239063) (15 µM), C9+DCA+p38i, JNK inhibitor (JNKi: SP600125) (20 µM) and actinomycin D (2 µg/ml). Total Bcl-2 expression was statistically significant lowered in C9+DCA- and actinomycin D-treated MCF-7 cells compared to DMSO control. Bcl-2 level increased in p38i-, C9+DCA+p38i-, JNKi- and C9+DCA+JNKi-exposed MCF-7 cells. DCA-, JNKi and C9+DCA+JNKi-exposed MCF-12A cells revealed increased expression of total Bcl-2 protein. Statistically significant effects on total Bcl-2 expression were observed when comparing MCF-7 and MCF-12A for the same treatment of p38i- and p38i+C9+DCA ($P < 0.05$). $^{\dagger}P$-value < 0.05 when each treatment was compared to DMSO-exposed control within MCF-7 cell line. $^{\ddagger}P$-value < 0.05 when each treatment was compared to DMSO-exposed control within MCF-12A cell line. $^{*}P$-value < 0.05 when each treatment was compared to C9+DCA-treated cells within MCF-7 cell line. $^{\#}P$-value < 0.05 when each treatment was compared to C9+DCA-treated cells within MCF-12A cell line.

Table 4: Sub-population of cells (percentages) with hypo-, normal and hyper-phosphorylation statuses of B cell leukaemia-2 protein at serine 70 position.

MCF-7	Hypo-p-S70	StdEV	Normal	StdEV	Hyper-p-S70	StdEV
DMSO	2.40	1.08	93.82	0.99	4.10	0.71
DCA	5.71	3.74	91.31	1.83	5.83	1.21
C9	7.41	2.45	77.56	2.57	15.35	1.52
C9+DCA	23.06	2.91	53.81	2.05	23.73	1.35
C9+DCA+JNKi	7.56	0.49	80.64	2.98	12.13	3.03
JNKi	11.28	1.16	78.82	1.51	10.33	1.96
C9+DCA+p38i	15.65	5.82	54.66	7.41	30.00	4.63
p38i	3.62	1.40	92.94	1.56	3.74	0.61
C9+DCA+NAC	4.05	1.46	89.17	2.04	7.05	0.95
Actinomycin D	40.87	2.28	57.92	2.97	1.77	1.19

MCF-12A	Hypo-p-S70	StdEV	Normal	StdEV	Hyper-p-S70	StdEV
DMSO	1.49	0.97	95.71	1.92	2.57	0.83
DCA	2.27	0.79	95.07	1.23	2.94	0.39
C9	3.37	1.41	93.57	2.09	3.00	1.32
C9+DCA	12.73	3.69	72.12	9.21	16.66	5.64
C9+DCA+JNKi	3.62	2.60	93.35	1.41	2.94	2.02
JNKi	5.32	2.79	89.97	2.13	3.80	1.30
C9+DCA+p38i	13.46	1.06	65.20	6.10	21.23	5.18
p38i	1.94	2.36	94.42	3.87	3.15	2.04
Actinomycin D	40.94	7.77	65.44	11.87	1.07	0.23

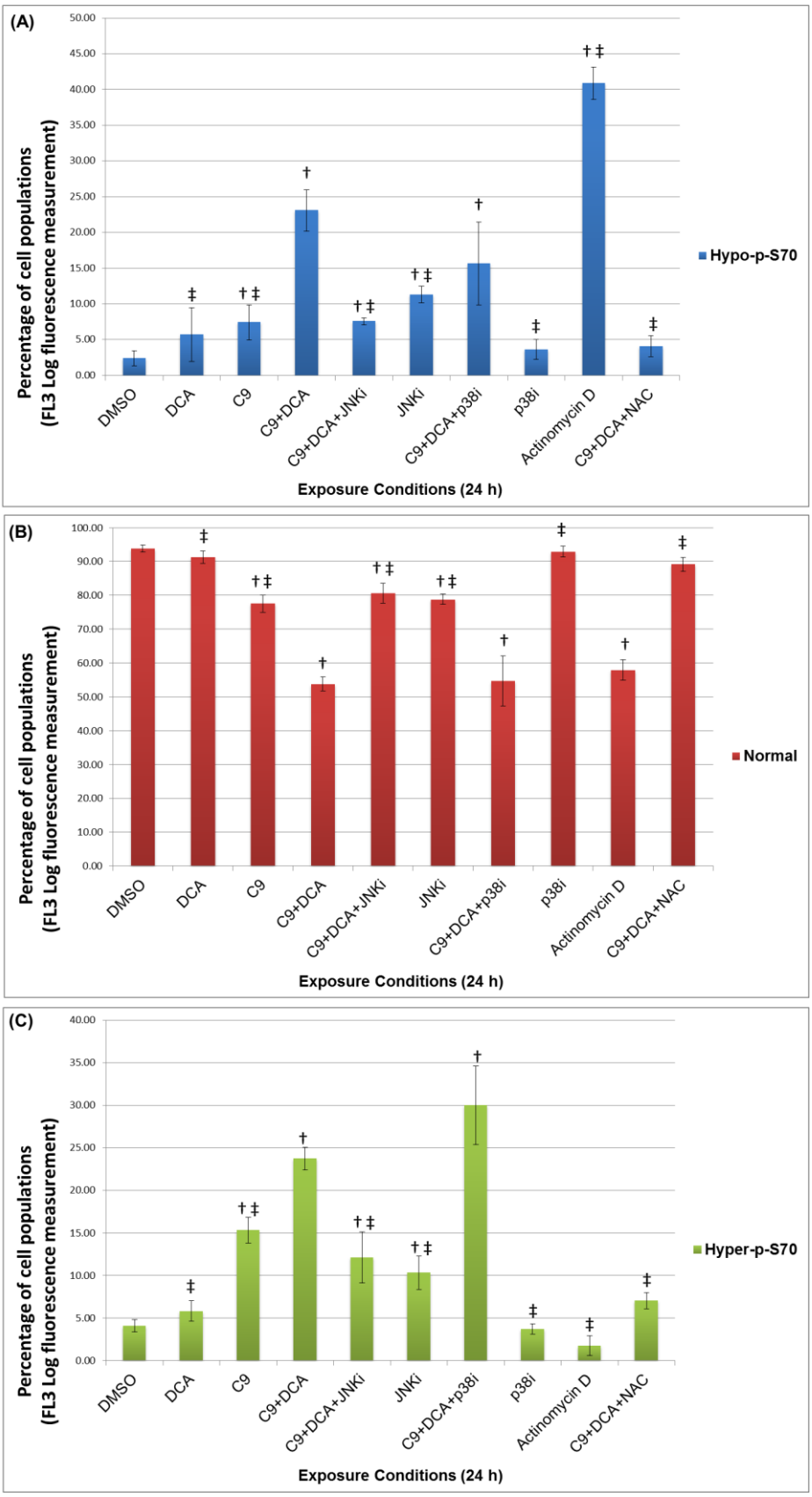
(A)
Percentage of cell populations (FL3 Log fluorescence measurement)
Exposure Conditions (24 h)
DMSO
DCA
C9
C9+DCA
C9+DCA+JNKi
JNKi
C9+DCA+p38i
p38i
Actinomycin D
C9+DCA+NAC
Hypo-p-S70
(B)
Percentage of cell populations (FL3 Log fluorescence measurement)
Exposure Conditions (24 h)
Normal
(C)
Percentage of cell populations (FL3 Log fluorescence measurement)
Exposure Conditions (24 h)
Hyper-p-S70

Figure 3.36: Sub-population of cells (percentages) with (A) hypo-, (B) normal- and (C) hyper-phosphorylation status of MCF-7 cells B cell leukaemia-2 protein at serine 70. Exposure conditions for 24 h: DCA (7.5 mM), C9 (130 nM), C9+DCA, p38 inhibitor (p38i: SB 239063) (15 µM), C9+DCA+p38i, JNK inhibitor (JNKi: SP600125) (20 µM) and actinomycin D (2 µg/ml). Six treatments including C9, C9+DCA, C9+DCA+JNKi, JNKi, C9+DCA+p38i and actinomycin D decreased normal sub-population (B) of MCF-7 cell compared to DMSO-exposed control. All six treatments caused significant increase in hypo-phosphorylation sub-population (A) compared to DMSO control. Exposure of the MCF-7 cells to C9, C9+DCA, C9+DCA+JNKi, JNKi, C9+DCA+p38i increased amount cell that entered hyper-phosphorylation sub-population (C) compared to vehicle-control. When comparing Bcl-2 phosphorylation status of different treatments within the same cell line, C9+DCA-treated MCF-7 cells displayed a statistically significant increase in Hypo-p-S70 and Hyper-p-S70 cell populations compared to DCA-, C9-, C9+DCA+JNKi-, JNKi-, C9+DCA+p38i- and p38i-treated cells ($P < 0.05$). $^{\dagger}P$-value < 0.05 after comparison of exposed cells and DMSO control. $^{\ddagger}P$-value < 0.05 when treated cell compared to C9+DCA-treated cells.

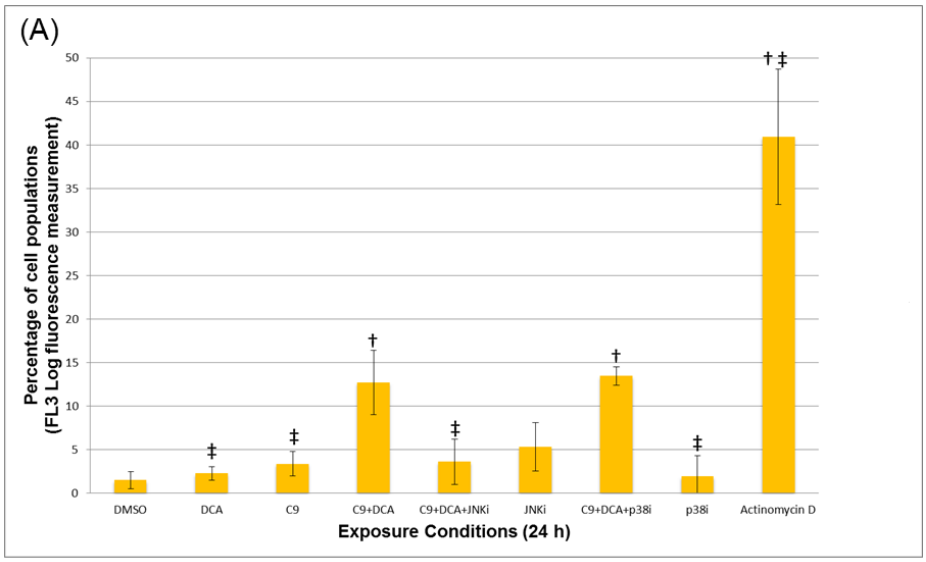
(A)
Percentage of cell populations (FL3 Log fluorescence measurement)
0
5
10
15
20
25
30
35
40
45
50
† ‡
† ‡ ‡ ‡
DMSO
DCA
C9
C9+DCA
C9+DCA+JNKi
JNKi
C9+DCA+p38i
p38i
Actinomycin D
Exposure Conditions (24 h)

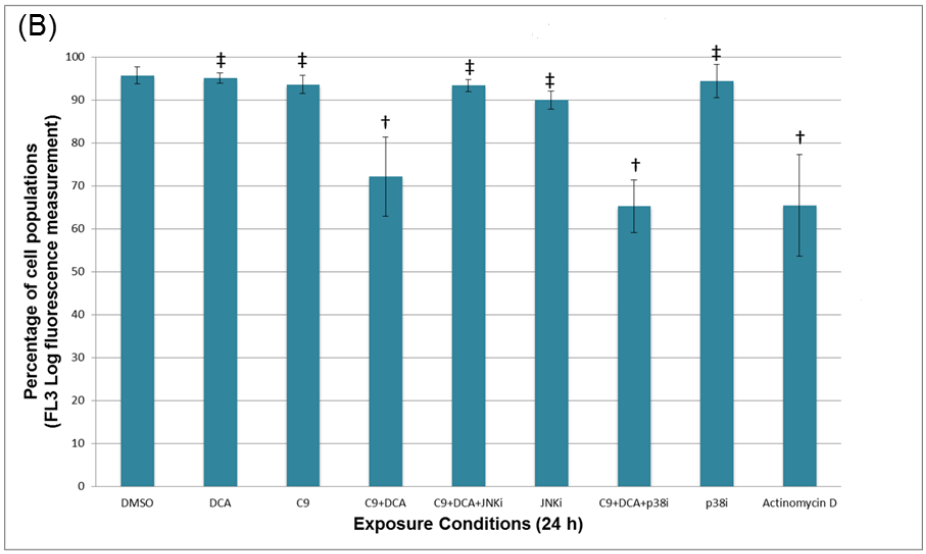
(B)
Percentage of cell populations (FL3 Log fluorescence measurement)
0
10
20
30
40
50
60
70
80
90
100
‡ ‡ ‡ † ‡ ‡ † ‡ †
DMSO
DCA
C9
C9+DCA
C9+DCA+JNKi
JNKi
C9+DCA+p38i
p38i
Actinomycin D
Exposure Conditions (24 h)

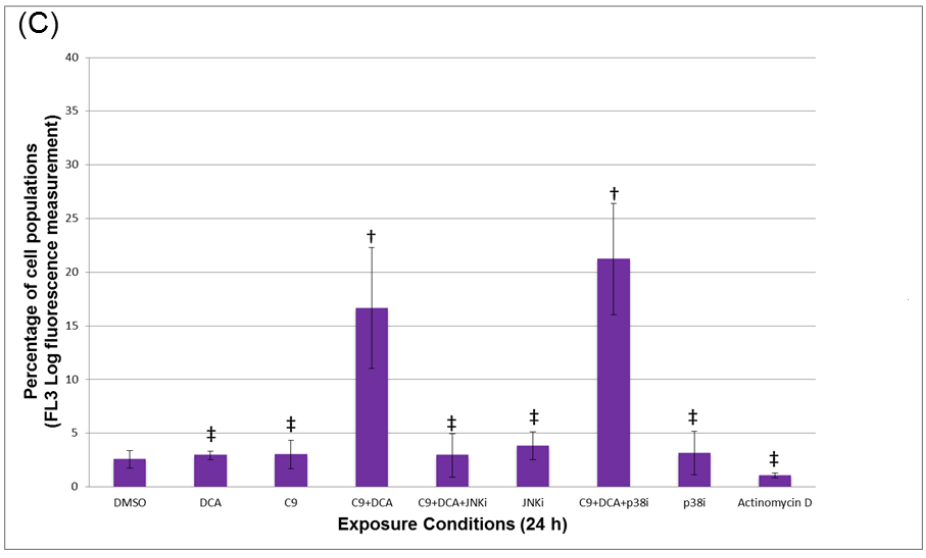
(C)
Percentage of cell populations (FL3 Log fluorescence measurement)
0
5
10
15
20
25
30
35
40
‡ ‡ † ‡ ‡ † ‡ ‡
DMSO
DCA
C9
C9+DCA
C9+DCA+JNKi
JNKi
C9+DCA+p38i
p38i
Actinomycin D
Exposure Conditions (24 h)

Figure 3.37: Sub-population of cells (percentages) with (A) hypo-, (B) normal- and (C) hyper-phosphorylation status of MCF-12A cells B cell leukaemia-2 protein at serine 70. Exposure conditions for 24 h: DCA (7.5 mM), C9 (130 nM), C9+DCA, p38 inhibitor (p38i: SB 239063) (15 µM), C9+DCA+p38i, JNK inhibitor (JNKi: SP600125) (20 µM) and actinomycin D (2 µg/ml). Treatments C9+DCA, C9+DCA+p38i and actinomycin D decreased normal phosphorylation sub-population compared to DMSO-exposed control (B). These three treatments caused a significant increase in Bcl-2 hypo-p-S70 compared to DMSO control (A). Treatments C9+DCA and C9+DCA+p38i increased Bcl-2 hyper-p-S70 compared to vehicle-exposed control (C). In general, C9+DCA-treated MCF-12A cells displayed statistically significant increase in both Bcl-2 hypo-p-S70 and hyper-p-S70 statuses when compared to C9-, DCA-, C9+DCA+JNKi- and p38i-treated cells ($P < 0.05$). $^{\dagger}P$-value < 0.05 after comparison of exposed cells and DMSO control. $^{\ddagger}P$-value < 0.05 when treated cell compared to C9+DCA-treated cells.

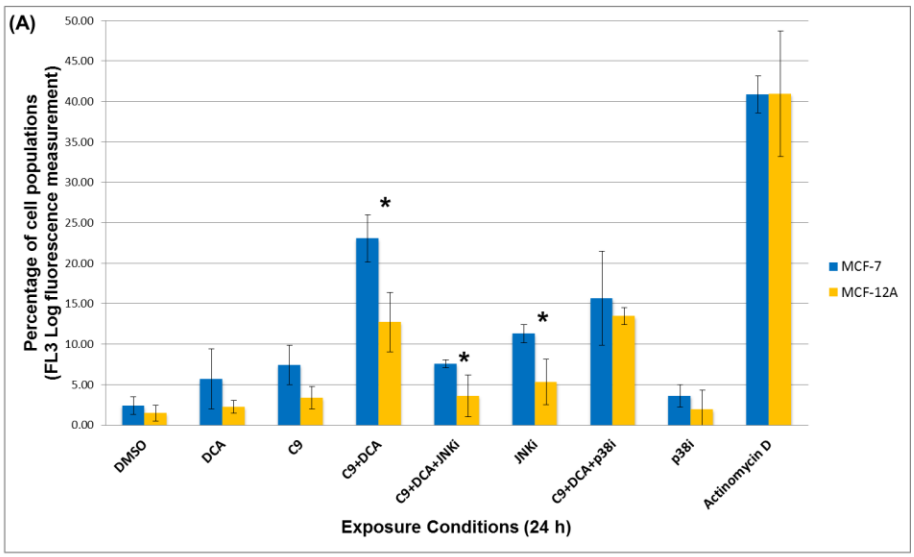
(A)
Percentage of cell populations (FL3 Log fluorescence measurement)
50.00
45.00
40.00
35.00
30.00
25.00
20.00
15.00
10.00
5.00
0.00
*
*
*
MCF-7
MCF-12A
DMSO
DCA
C9
C9+DCA
C9+DCA+JNKi
JNKi
C9+DCA+p38i
p38i
Actinomycin D
Exposure Conditions (24 h)

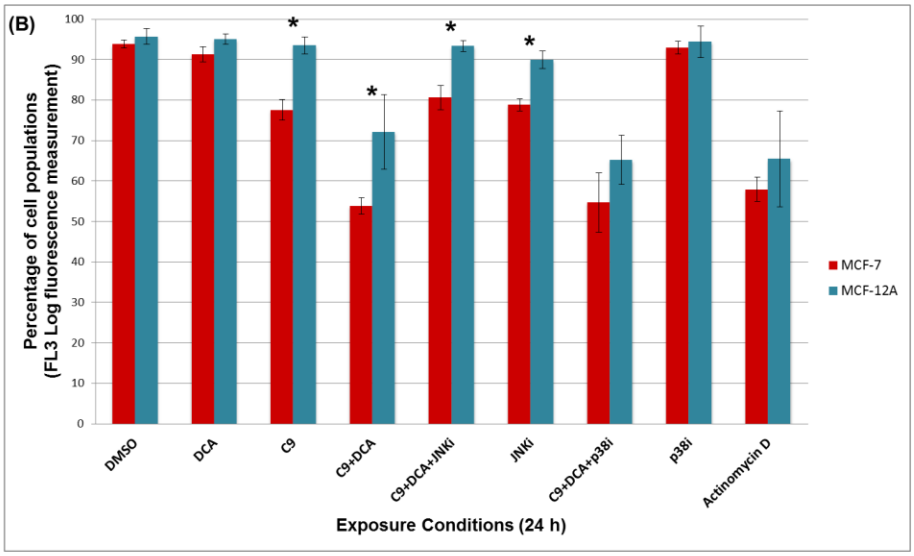
(B)
Percentage of cell populations (FL3 Log fluorescence measurement)
100
90
80
70
60
50
40
30
20
10
0
*
*
*
*
MCF-7
MCF-12A
DMSO
DCA
C9
C9+DCA
C9+DCA+JNKi
JNKi
C9+DCA+p38i
p38i
Actinomycin D
Exposure Conditions (24 h)

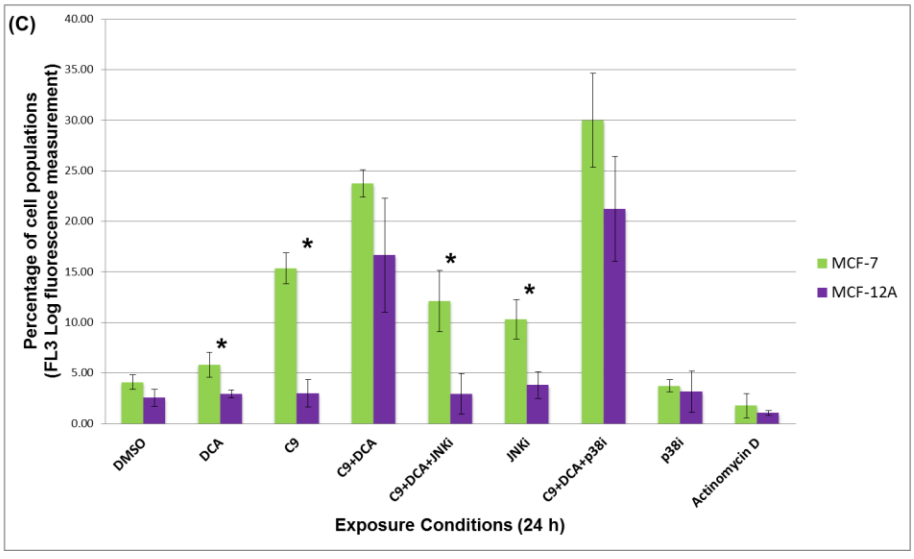
(C)
Percentage of cell populations (FL3 Log fluorescence measurement)
40.00
35.00
30.00
25.00
20.00
15.00
10.00
5.00
0.00
*
*
*
*
MCF-7
MCF-12A
DMSO
DCA
C9
C9+DCA
C9+DCA+JNKi
JNKi
C9+DCA+p38i
p38i
Actinomycin D
Exposure Conditions (24 h)

Figure 3.38: Comparisons between MCF-7 and MCF-12A sub-populations of cells (percentages) with (A) hypo-, (B) normal- and (C) hyper-phosphorylation status B cell leukaemia-2 protein at serine 70. Exposure conditions for 24 h: DCA (7.5 mM), C9 (130 nM), C9+DCA, p38 inhibitor (p38i: SB 239063) (15 µM), C9+DCA+p38i, JNK inhibitor (JNKi: SP600125) (20 µM) and actinomycin D (2 µg/ml). When two cell lines MCF-7 and MCF-12A were compared, Bcl-2 normal-p-S70 fluorescent unit showed a statistically significant difference when treatments C9-, C9+DCA-, C9+DCA+JNKi or JNKi-exposed cells were compared (B). Decrease in Bcl-2 normal-p-S70 sub-population means increase in either hypo-p-S70 or hyper-p-S70 statuses. C9+DCA, C9+DCA+JNKi or JNKi-exposed cells displayed a statistical significance in Bcl-2 hypo-p-S70 statuses when MCF-7 and MCF-12A results were compared (A). C9-, C9+DCA+JNKi- and JNKi-exposed cells displayed a statistical significance in Bcl-2 hyper-p-S70 statuses when MCF-7 and MCF-12A results were compared (B). *P-value < 0.05 after comparison of exposed MCF-7 and MCF-12A cells.

3.11.2 Caspases 7 expression

Caspases are divided into initiator caspases (caspase 1, 2, 4, 5, 8, 9, 10, 11, 12) and effector caspases (caspase 3, 6, 7) (144). Caspases 3, 6 and 7 are effector caspases which play a key role in apoptosis processes by destroying vital components of cellular infrastructure and activate factors that damage the cell. Initiator caspases such as caspases 1, 4 and 5 appear to be more specific proteases that cleave few substrates with the preferred tetrapeptide WEHD (425). Considering effector caspases are responsible for most of the substrate proteolysis during apoptosis, it is not easy to identify the functionally targets (144). Studies revealed caspase 2, 3 and 7 have the ability to recognize tetrapeptide motifs DEXD (425).

Primary antibodies against active (i.e. cleaved) caspase 7 were used to study protein expression changes in the MCF-7 and MCF-12A cells after 24 h treatment of C9-, DCA- and C9+DCA. Actinomycin D (0.2 µg/ml) was used as a positive control for apoptosis induction. Figure 3.39 A and B showed that caspase 7 protein expression was elevated in C9-, and C9+DCA-exposed (24 h) MCF-7 cells. Caspase 7 levels also increased in C9+DCA-treated (24 h) MCF-12A cells. Furthermore, the differences between the active

caspase 7 expression level in C9+DCA-treated MCF-7 and MCF-12A cells were statistically significant ($P < 0.05$). Data captured from at least three biological experiments were used to calculate the relative mean fluorescence. The average of these three data sets are presented in Figure 3.39 A. Representative histogram of caspase 7 expression in MCF-7 cell is provided in Figure 3.39 B.

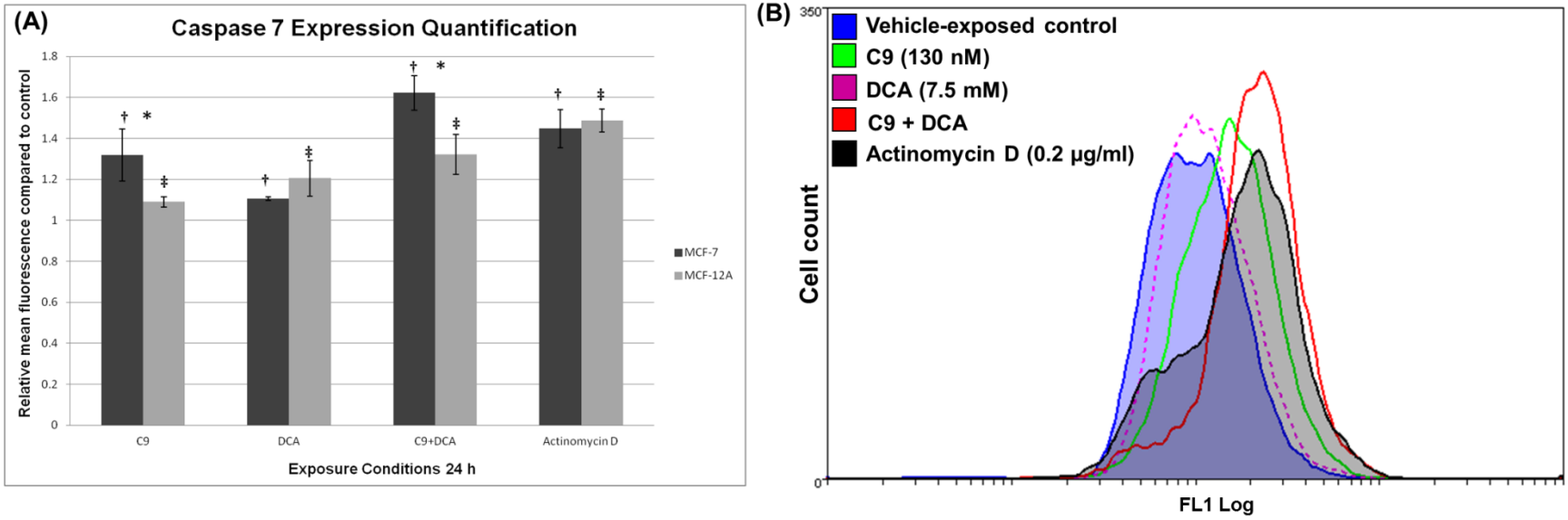

Figure 3.39: Apoptosis-related quantification of cleaved executioner caspase 7 expression in MCF-7 and MCF-12A cells. Caspase 7 expression in treated and untreated MCF-7 and MCF-12A cells (A), as well as one representative MCF-7 data of FL1 log against cell count (B). Caspase 7 protein expression was elevated in C9-, and C9+DCA-exposed (24 h) MCF-7 cells. Caspase 7 levels also increased in C9+DCA-treated (24 h) MCF-12A cells. Differences between the active caspase 7 expression level in C9+DCA-treted MCF-7 and MCF-12A cells were statistically significant ($P < 0.05$). †, ‡, P-value < 0.05 after comparison of exposed cells and controls within the same cell line. *, P-value < 0.05 when MCF-7 and MCF-12A cells were compared for the same treatment. Actinomycin D (0.2 µg/ml) was used as a positive control for apoptosis induction.

3.12 Microarrays

Gene expression analysis

Global gene expression analysis was conducted by employing the Agilent's Human 1A Oligonucleotide Microarray slides. MCF-7 and MCF-12A cells were exposed to C9 (130 nM) in combination of DCA (7.5 mM) for 24 h prior to collection of gene expression information. After treatment of C9+DCA (24 h), 684 and 830 genes were considered statistically significantly differentially expressed in MCF-7 and MCF-12A cells. Mapping of differentially expressed genes to biochemical pathways and Gene Ontology (GO) categories were performed by utilizing GeneCodis3 (3.0 versions) (426). Differentially expressed genes exclusively responsive in C9+DCA-treated (24 h) MCF-7 and -MCF-12A cells were mapped to cell death, cell cycle, cytoskeleton, metabolism, transcription, epigenetic regulation, protein kinases and phosphatases, reactive oxygen species metabolism and ribosomal proteins. Data were categorized and statistically differentially affected genes are summarized Table 5. Furthermore, the statistically differentially ($P < 0.05$) expressed genes responsive to combination treatment in both cell lines were compared using GeneVenn and 74 genes were found to be affected in both cell lines after 24 h exposure (Figure 3.40).

As shown in Table 5, C9+DCA induced the expression of a number of genes related to the p53 pathway in MCF-7 cells including tumor protein p53 binding protein 1 (*TP53BP1*), transformed 3T3 cell double minute 2 (*MDM2*) and BCL2 binding component 3 (*BBC3/PUMA*). Cell growth and proliferation depend on the general mRNA translation processes. The circularization of the mRNA 5' cap and 3' poly(A) tail structure is dependent on the interactions between eukaryotic initiation factor 4G (eIF4G) and poly(A) binding protein (PABP) (427). Poly(A) binding protein interaction protein 1 (PAIP1) is able to interact with both eIF4G (428) and PABP to stimulate translation (427). In this study, the expression of *PAIP1* was down-regulated after exposed to MCF-7 cells with C9+DCA treatment for 24 h. Moreover, two genes involved in DNA repair namely poly (ADP-ribose) polymerases 1 (*PARP1*) and breast cancer 1 (*BRCA1*) were down-regulated. The combination treatment also affected several genes of the PI3K/AKT/mTOR pathway namely eukaryotic translation initiation factor 1 (*EIF1*), eukaryotic translation initiation factor 4E (*EIF4E*), mitogen-activated protein kinase 14 (*MAPK14*), phosphoinositide-3-kinase regulatory

subunit 1 (*PIK3R1*), protein tyrosine phosphatase non-receptor type 6 (*PTPN6*), tyrosine 3-monooxygenase/tryptophan 5-monooxygenase activation protein (*YWHAE*), proto-oncogene *c*-Fos (*FOS*) and jun proto-oncogene (*JUN*).

The NF-κB pathway is important for normal mammary gland development, as well as breast cancer formation (429). There are five structurally related proteins within the NF-κB family namely, RelA (p65), RelB, *c*-Rel, NF-κB1 (p105 and p50), and NF-κB2 (p100 and p52) (429,430). Activities of these five NF-κB proteins are inhibited by inhibitor of NF-κB (IκB) and activated by IκB kinase (IKK) (429). NF-κB is activated by two distinct pathways: the classic RelA/p50 pathway and the alternative RelB/p52 pathway (429). *v*-rel Reticuloendotheliosis viral oncogene homolog B, nuclear factor of kappa light polypeptide gene enhancer in B-cells 3 (*RELB*) gene expression was up-regulated in both cell lines. Up-regulation of *RELB* protein levels is usually associated with an up-regulation of cyclin D mRNA and protein (429). However, the present study found no significant changes in cyclin D expression levels. Therefore, the increase in *RELB* mRNA expression levels in both cell lines in response to C9+DCA exposure likely does not correlate with an increase in protein levels of *RELB.* The Notch pathway target gene hairy and enhancer of split 1 (*HES1*) gene represses the expression of a cell cycle inhibitor cyclin-dependent kinase inhibitor, $p27^{Kip1}$, independently of a cell differentiation role (431). *HES1* expression was down-regulated in both cell lines after treatment of C9+DCA, thus indicating the possible activation of $p27^{Kip1}$ and cell cycle inhibition. Cyclin K encoding gene *CCNK* expression was down-regulated in MCF-7 cells treated with C9+DCA. Cyclin K plays an important role in transcriptional elongation regulation by its interaction with RNA polymerase II C-terminal domain (432).

A number of genes such as thioredoxin-like 4A (*TXNL4A*), thioredoxin-like 4B (*TXNL4B*) and peroxiredoxin 3 (*PRDX3*) that are involved in reactive oxygen species metabolism were down-regulated in MCF-7 cells. Ferritin, both heavy and light polypeptide genes (*FTH1* and *FTL*) were induced. C9 being the antimitotic agent, suppressed a large number genes related to cellular structural integrity. Actin (*ACTG1*), microtubule-associated protein 7 (*MAP7*), tubulin alpha 1, 6 and 8, as well as tubulin beta 2A (*TUBA1*, *TUBA6*, *TUBA8* and *TUBB2A*) genes were down-regulated. These structural related genes encode proteins that are important to cell motility and maintenance of the cytoskeleton (433-435).

For C9+DCA-exposed MCF-12A cells, a number of genes related to p53 pathway were differentially expressed. Similarly to the MCF-7 gene expression profile, *BBC3/PUMA*, *MDM2* were up-regulated. On the other hand, proto-oncogene *c*-Myc (*MYC*), cyclin D1 (*CCND1*) and retinoblastoma 1 (*RB1*) were down-regulated. DNA-damage-inducible transcript 3 (DDIT3) and growth arrest and DNA-damage-inducible (GADD45A) genes expression were induced. Unlike the MCF-7 gene expression profile, PARP2 and PARP8 genes were up-regulated in C9+DCA-exposed MCF-12A. ATP-binding cassette, sub-family B (MDR/TAP), member 1 (*ABCB1*) and ATP-binding cassette, sub-family C (CFTR/MRP), member 5 (*ABCC5*) multidrug resistance genes were induced in treated MCF-12A cells, perhaps partly accounted for the treatment resistance. *ABCB1* functions as an energy-dependent drug efflux transporter that lowers concentrations of various anticancer drugs, such as colchicine, paclitaxel, doxorubicin and vinblastine (436,437). Genes involved in ROS metabolism namely, *FTH1*, glutathione S-transferase A2 (*GSTA2*), nitric oxide synthase 2A (*NOS2A*), spermine oxidase (*SMOX*), superoxide dismutase 1 (*SOD1*) and superoxide dismutase 2 mitochondrial (*SOD2*) were up-regulated. The ferredoxin reductase (*FDXR*) gene was down-regulated. FDXR gene product ferredoxin reductase protein transfers electron from NADPH to cytochrome P450 via ferredoxin in mitochondria (438). The ferredoxin reductase gene is reported regulating by the p53 family and sensitizes cells to oxidative stress-induced apoptosis (439).

It was also shown that spermidine/spermine N^1-acetyltransferase 1 (*SAT1*) mRNA was up-regulated in response to C9+DCA treatment in non-tumorigenic cell line. High levels of spermidine/spermine N^1-acetyltransferase protein reduce polyamine content, as well as cause a fall in acetyl-CoA level (440). Depletion of spermidine and spermine cause an arrest in cell growth (441). The function of apoptosis antagonizing transcription factor (*AATF*) is to complete blockade of the pro-apoptotic signalling. This apoptosis antagonizing effect is possibly achieved by protecting cells against oxidative and apoptotic damage (442). *AATF* gene transcription is lowered in MCF-12A cells after treatment with C9+DCA, showing the treatment has ability to interfere with apoptotic signalling pathway at the transcript level. Another gene E2F transcription factor 4, p107/p130-binding (*E2F4*) related to gene transcription is also down-regulated in treated MCF-12A cells. *E2F4* protein product binds to pRB, p107

and p130. Cyclin D/CDK4/6 phosphorylates p107 and p130, which deactivate the repression activity of E2F4 for cyclin E gene transcription and G_1 transition (57).

Apoptotic-related genes such as *BBC3/PUMA*, *MDM2*, Cbp/p300-interacting transactivator (*CITED4*), B-cell translocation gene 1 (*BTG1*), IKK interacting protein (*IKIP*), dual-specificity phosphatase 13 (*DUSP13*) and *FTH1* were commonly up-regulated in both cell lines after 24 h treatment. Several of the above-mentioned genes are linked to the p53 pathway which serves as the common pathway that introduced apoptosis in both MCF-7 and MCF-12A cells.

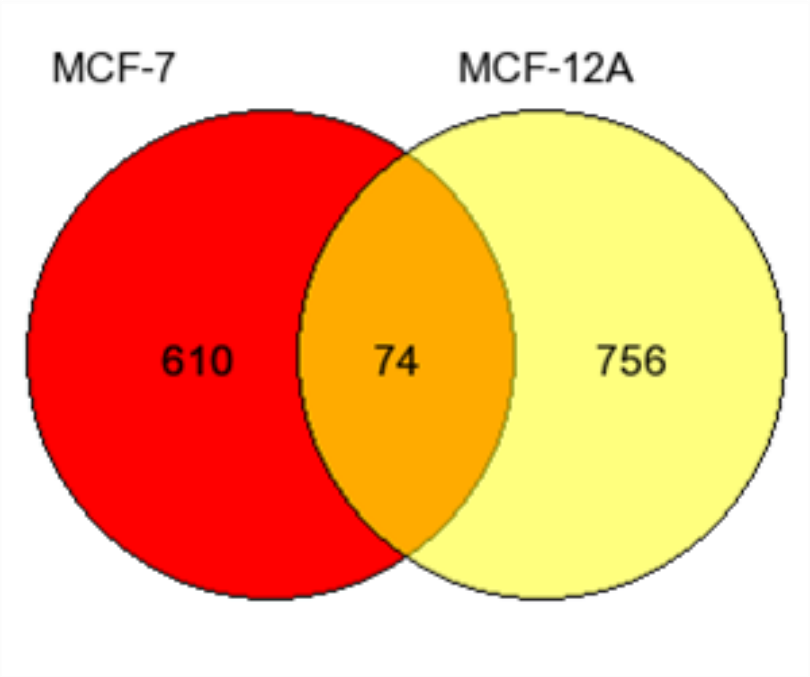

Figure 3.40: GeneVenn diagram showing 74 commonly affected genes in MCF-7 and MCF-12A cells after 24 h exposure to C9 (130 nM) in combination with DCA (7.5 mM). Treatment C9+DCA caused 610 and 756 statistically differentially expressed genes in MCF-7 and MCF-12A cell lines respectively.

Table 5: Differentially expressed genes mapped to functional cellular pathways in MCF-7 and MCF-12A cells exposed to 130 nM of C9 and 7.5 mM of DCA for 24 h. M-values represent a log2-fold change between two or more experimental conditions.

GeneBank number	Gene name	Description	MCF-7	MCF-12A
			Log M	
Cell proliferation and cell senescence				
NM_014417	**BBC3**	BCL2 binding component 3	1.217	0.904
NM_006879	**MDM2**	Mdm2, transformed 3T3 cell double minute 2, p53 binding	1.111	0.624
NM_001731	**BTG1**	B-cell translocation gene 1, anti-proliferative	0.740	0.798
NM_005766	**FARP1**	FERM, RhoGEF (ARHGEF) and pleckstrin domain protein 1	0.200	0.513
NM_005657	**TP53BP1**	Tumor protein p53 binding protein, 1	0.191	
NM_178234	**TUSC3**	Tumor suppressor candidate 3	0.172	
NM_004083	**DDIT3**	DNA-damage-inducible transcript 3		1.551
NM_005118	**TNFSF15**	Tumor necrosis factor (ligand) superfamily, member 15		0.775
NM_015124	**DIP**	Death-inducing-protein (DIP)		0.694
NM_003932	**ST13**	Suppression of tumorigenicity 13 (Hsp70 interacting protein)	-0.254	
NM_006451	**PAIP1**	Poly(A) binding protein interaction protein 1	-0.543	
NM_002467	**MYC**	v-myc Myelocytomatosis viral oncogene homolog		-0.707
NM_006761	**YWHAE**	Tyrosine 3-monooxygenase/tryptophan 5-monooxygenase activation protein	-0.179	-0.585
NM_006509	**RELB**	v-rel Reticuloendotheliosis viral oncogene homolog B, nuclear factor of kappa light polypeptide gene enhancer in B-cells 3	0.266	0.885
NM_002228	**JUN**	Jun oncogene	0.155	
NM_201612	**IKIP**	IKK interacting protein	0.440	0.521
Cell cycle, cytoskeleton and DNA repair				
NM_001614	**ACTG1**	Actin, gamma 1	-0.454	-0.610
NM_005524	**HES1**	Hairy and enhancer of split 1	-0.291	-2.020
NM_005517	**HMGN2**	High-mobility group nucleosomal binding domain 2	-0.430	-0.545
NM_006306	**SMC1A**	Structural maintenance of chromosomes 1A	-0.287	-0.604
NM_032704	**TUBA6**	Tubulin, alpha 6	-0.366	-0.653
NM_006000	**TUBA1**	Tubulin, alpha 1	-0.482	
NM_018943	**TUBA8**	Tubulin, alpha 8	-0.425	
NM_001069	**TUBB2A**	Tubulin, beta 2A	-0.282	
NM_002374	**MAP2**	Microtubule-associated protein 2		0.574
NM_003980	**MAP7**	Microtubule-associated protein 7	-0.689	
NM_001618	**PARP1**	Poly (ADP-ribose) polymerase family, member 1	-0.195	
NM_005484	**PARP2**	Poly (ADP-ribose) polymerase family, member 2		0.492
NM_024615	**PARP8**	Poly (ADP-ribose) polymerase family, member 8		0.929
NM_001924	**GADD45A**	Growth arrest and DNA-damage-inducible, alpha		0.793

NM_001237	**CCNA2**	Cyclin A2		-0.373
NM_053056	**CCND1**	Cyclin D1		-0.729
NM_000321	**RB1**	Retinoblastoma 1		-0.544
NM_002577	**PAK2**	p21 (CDKN1A)-activated kinase 2		-0.900
NM_003390	**WEE1**	WEE1 homolog	0.257	
NM_003858	**CCNK**	Cyclin K	-0.479	
NM_007295	**BRCA1**	Breast cancer 1, early onset	-0.209	
NM_015894	**STMN3**	Stathmin-like 3 (STMN3)	-0.289	
Metabolism				
NM_000927	**ABCB1**	ATP-binding cassette, sub-family B (MDR/TAP), member 1		0.679
NM_005688	**ABCC5**	ATP-binding cassette, sub-family C (CFTR/MRP), member 5		0.534
NM_006066	**AKR1A1**	Aldo-keto reductase family 1, member A1 (aldehyde reductase)	0.439	
NM_005603	**ATP8B1**	ATPase, Class I, type 8B, member 1	0.460	
NM_201444	**DGKA**	Ddiacylglycerol kinase, alpha 80kDa	0.383	
NM_002633	**PGM1**	Phosphoglucomutase 1	0.334	
NM_181523	**PIK3R1**	Phosphoinositide-3-kinase, regulatory subunit 1 (p85 alpha)	-0.181	
Reactive oxygen species metabolism				
NM_002032	**FTH1**	ferritin, heavy polypeptide 1	0.201	0.604
NM_000146	**FTL**	Ferritin, light polypeptide	0.272	
NM_006701	**TXNL4A**	Thioredoxin-like 4A	-0.320	
NM_017853	**TXNL4B**	Thioredoxin-like 4B	-0.241	
NM_006793	**PRDX3**	Peroxiredoxin 3 (PRDX3), nuclear gene encoding mitochondrial protein	-0.176	
NM_004110	**FDXR**	Ferredoxin reductase, nuclear gene encoding mitochondrial protein		0.741
NM_031894	**FTHL17**	Ferritin, heavy polypeptide-like 17		0.567
NM_000846	**GSTA2**	Glutathione S-transferase A2		1.133
NM_000625	**NOS2A**	Nitric oxide synthase 2A (inducible, hepatocytes)		0.840
NM_000603	**NOS3**	Nitric oxide synthase 3 (endothelial cell)		0.419
NM_002970	**SAT1**	Spermidine/spermine N1-acetyltransferase 1		1.402
NM_175839	**SMOX**	Spermine oxidase		1.007
NM_000454	**SOD1**	Superoxide dismutase 1		0.614
NM_001024465	**SOD2**	Superoxide dismutase 2, mitochondrial		1.159
NM_002133	**HMOX1**	heme oxygenase (decycling) 1 (HMOX1), mRNA		-0.429
NM_006819	**STIP1**	Stress-induced-phosphoprotein 1 (Hsp70/Hsp90-organizing protein)		-0.729
Regulation of transcription				
NM_133467	**CITED4**	Cbp/p300-interacting transactivator	0.343	0.728
NM_006079	**CITED2**	Cbp/p300-interacting transactivator, with Glu/Asp-rich carboxy-terminal domain, 2		-0.901
NM_012138	**AATF**	Apoptosis antagonizing transcription factor		-0.666
NM_001950	**E2F4**	E2F transcription factor 4, p107/p130-binding		-0.887
NM_001968	**EIF4E**	Eukaryotic translation initiation factor 4E	-0.501	-1.799
NM_005194	**CEBPB**	CCAAT/enhancer binding protein, beta	0.284	
NM_001455	**FOXO3A**	Forkhead box O3A (FOXO3A)	0.131	
NM_005801	**EIF1**	Eukaryotic translation initiation factor 1	-0.389	
NM_001968	**EIF4E**	Eukaryotic translation initiation factor 4E	-0.501	
NM_005252	**FOS**	v-fos FBJ murine osteosarcoma viral	0.557	

		oncogene homolog		
NM_000937	**POLR2A**	Polymerase (RNA) II (DNA directed) polypeptide A	-0.161	
ENST00000373575	**ENST00000373575**	Eukaryotic translation initiation factor 4E type 2	-0.193	
Protein kinases and phosphatases				
NM_001007271	**DUSP13**	Dual specificity phosphatase 13	0.483	0.488
NM_017572	**MKNK2**	MAP kinase interacting serine/threonine kinase 2	0.421	0.706
NM_002831	**PTPN6**	Protein tyrosine phosphatase, non-receptor type 6	0.156	
NM_000455	**STK11**	Serine/threonine kinase 11	0.323	
NM_203351	**MAP3K3**	Mitogen-activated protein kinase kinase kinase 3	0.116	-0.610
NM_145109	**MAP2K3**	Mitogen-activated protein kinase kinase 3 (MAP2K3)		-1.453
NM_138957	**MAPK1**	Mitogen-activated protein kinase 1		-0.462
NM_002752	**MAPK9**	Mitogen-activated protein kinase 9	0.145	
NM_001315	**MAPK14**	Mitogen-activated protein kinase 14	-0.253	

4. Chapter 4: Discussion

The approach of combining the antimitotic C9 with the glycolytic inhibitor DCA as a combination therapy for *in vitro* testing as an anticancer treatment is novel. In the present study, the MCF-7 human breast carcinoma cell line and MCF-12A non-tumorigenic breast cells were used as an experimental model system to examine the anticancer effect of C9 and DCA in combination.

C9, along with other 2ME analogs (ESE-15-ol and ESE-16), are a novel class of *in silico*-designed inhibitors of microtubule dynamics (187,366,376,377). Stander *et al.* (2011) utilized bioinformatics software namely Autodock 4.0 to develop an *in silico* protocol in order to design and select therapeutically viable antimitotic compounds (366). The development of C9, ESE-15-ol and ESE-16 advanced the pioneer research on 2ME analogs conducted by Seegers *et al.* (443-447), as well as Reed, Purohit and their associates (368,369,448-454). (353).

2ME induces G_2/M cell cycle arrest (353), exhibits anti-angiogenic property, as well as inhibits HIF-1α expression (353,354). This source molecule (2ME) exerts antiproliferative activity in MCF-7 and MDA-MB-231 cell lines at 1-4 μM (294). Newly designed compounds are active at nanomolar concentration (294). Thus, these new analogs are proven five to 20 times more potent than their source molecule, 2ME. Clinical studies in humans demonstrated the bioavailability of 2ME is as low as 1 to 2% (455) owning to oxidation (360,361).

Newman *et al.* (2007 and 2008) demonstrated modifications at carbon positions 3 and 17 of 2ME significantly increased the *in vitro* and *in vivo* efficacy of 2ME analogs, STX140 and STX641 (327,456). 2-Methoxyoestradiol-3,17-*O*,*O*-bis-sulphamate (STX140) and 2-methoxy-3-*O*-sulphamoyl-17β-cyanomethyloestra-1,3,5(10)-triene (STX641) inhibited cell proliferation in MCF-7 cells with IC_{50} values of 250 nM and 150 nM respectively (327). Their effects on cancer cells were due to the ability to induce a G_2/M cell cycle arrest and apoptosis (327). The mechanism of action of the sulphamate derivative STX140 on cancer cells is possibly through the repression of anti-apoptotic Bcl-2 phosphorylation and induction of the pro-apoptotic protein p53 in MCF-7 wild type cells, as well as the multidrug-resistant cancer cell lines (MCF-7_{DOX}) (327,456).

In vivo experiments showed that 20 mg kg^{-1} STX140 (twice weekly) completely inhibited tumor growth over a 28-day treatment period when compared to a clinically relevant drug, vinorelbine, at 80 mg kg^{-1} (twice weekly) (327). Foster *et al.* (2008) showed additional modifications to carbon positions 3 and 17 of 2ME, namely 2-ethyl group, significantly increased its efficacy against MDA-MB-231 cancer cells (368). The authors demonstrated the IC_{50} values for 2-ethylestradiol-3,17-*O*,*O*-bissulfamate (2-EtE2bisMATE or STX243), STX140, as well as 2ME against MDA-MB-231 to be 273 nM, 618 nM and 4930 nM, respectively (368). They showed that the increased antiproliferative and anti-angiogenic activity *in vitro*, *in vivo* and *ex vivo* of STX243 are associated with carbon modifications at positions 2, 3 and 17 (368-370). The same group also showed the efficacy of STX243 against the growth of both estrogen receptor positive- and estrogen receptor negative breast cancer tumors *in vitro* and *in vivo* with promising pharmacokinetic properties (369). These estrogen sulphamates are proven to obtain a higher bioavailability since they are able to delay the biotransformation encountered by liver metabolism due to the fact that they are capable of reversibly conjugating to cytosolic erythrocyte carbonic anhydrase II (CAII) (365,366,371,372). Binding of these estrogen sulphamates to intracellular erythrocyte CAII prevents contact with various liver enzymes and first-pass metabolism is avoided (365,366,371,372).

C9 was modified at carbon positions 2, 3 and 17 from its source molecule, 2ME. At carbon position three of C9, a sulphamate group was added as it is known that the sulfonamido nitrogen facilitates binding to the zinc ion present in carbonic anhydrases (457). This change is argued to improve bioavailability due the potential of aryl sulphamoyl-containing compounds to reversibly bind to carbonic anhydrase II present in erythrocytes and in turn circumvent first pass liver metabolism (458). The 2-ethoxy group at carbon position two of C9 is known to improve the antimitotic activity of estradiol analogs (459) and dehydration at carbon positions 14 and 15 was shown to have increased antiproliferative and antitumor activities (460).

C9 inhibits the activity of the wild-type CAII (K_i = 167 ± 19 nM) and the activity of a the CAIX mimic (K_i = 453 ± 43 nM) (294). While C9 is less selective towards CAIX when compared to CAII, it is still active in the sub 500 nM range and would thus still play a relevant role in inhibiting CAIX in cancer cells that express this protein (461). Recent studies from our laboratory demonstrated that MCF-7- and/or MDA-MB-231

cancer cell lines exhibited sensitivity towards *in silico*-designed compounds C9 (366), ESE-15-ol (C10) (366,378) and ESE-16 (C12) (366,376). These newly designed and synthesized antimitotic compounds induce G_2/M arrest and apoptosis by docking into the colchicine binding site between α and β tubulin (366).

Antimitotic compounds are capable of targeting hallmarks of cancer that promote a hyperproliferative phenotype. Combinations of antimitotic compounds with additional compounds that target the deregulated metabolism of many cancers are being investigated (462). Liu *et al.* proposed that chemotherapeutics would target the fast-dividing tumor cells on edges of tumor tissue, while the glycolysis inhibitor would focus on cells at the hypoxic center of the tumor (385). A small molecule, DCA (two carbon molecule), which is the by-product of drinking water by chlorination, targets PDK signalling and represents a novel means to target PDK (318). DCA is a non-patentable well-characterized inhibitor of PDK that forces cells into oxidative phosphorylation subsequently suppresses cancer growth. DCA binds to PDK and attenuates inhibition of PDH (334).

Most cancer cells rely on aerobic glycolysis even under conditions of sufficient oxygen supply to support OXPHOS (329). Oxygen is the first substrate that becomes limited during neoplastic growth (312). The persistent oxic-anoxic cycle subsequently exerts selection pressures which lead to the constitutive activation of glycolysis even in the presence of abundant oxygen (310). Following hypoxia in neoplastic cells, the expression of HIF1 increases, subsequently induceing a key enzyme PDK1, which in turn inactivates PDH that functions to convert pyruvate to acetyl-coenzyme A and deliver it to the TAC (336). The anticancer activity of DCA against lung (325), prostate (463), endometrial (186) and breast (323) tumorigenic cell lines were demonstrated in recent years. The common mechanisms of action of DCA was described to target the aerobic glycolysis, also known as the “Warburg Effect” in cancerous cell lines by reversing the metabolic changes in cancers cells, without affecting normal cells (323,337,338). Bonnet and colleagues (2007) reported that DCA has an anticancer effect by reducing mitochondrial membrane potential, leading to formation of ROS and the release of the pro-apoptotic effector cytochrome *c* (325). Sutendra *et al.* (2012) reported that DCA re-activates mitochondrial metabolism in cancer (*in vitro*, xenotransplant model and *in vivo*) through inhibition of HIF1 signalling and angiogenesis-mediated by PDK (336). Lower doses of DCA (5-10 mM)

have the ability to reactivate PDH complex by aerobic glycolysis inhibition in multiple myeloma cells (464). Higher doses of DCA (10-25 mM) successfully suppressed myeloma cell proliferation with G_0/G_1- and G_2/M cell cycle arrest and apoptosis possibly linked to ROS production (464).

Utilization of glycolytic inhibitors in combination with conventional chemotherapeutic treatment was proposed to hypersensitize tumor cells towards treatment as early as 2001 (385). The approach of combining the antimitotic compound C9, which is believed to target fast dividing cancer cells with the glycolysis inhibitor DCA, was pursued in our laboratory. Stander *et al.* (2011) exhibited synergistic effects of 130 nM C9 in combination with 7.5 mM DCA on tumorigenic MCF-7 and normal breast cell MCF-12A cell lines. Selective killing of tumorigenic MCF-7 cells was demonstrated through increased apoptotic cell population, as well as G_2/M cell cycle arrest (377). Similar types of studies conducted by Tagg *et al.* showed that 2DG in combination with a sulphamoylated analog STX140 eradicates tumorigenic cell proliferation of MCF-7 and prostate cancer cells (LNCaP) in xenograft models *in vivo* by arresting the cell cycle at G_2/M phase, increasing apoptotic cell population, as well as targeting glycolytic ATP production in hypoxic environment (386).

Raez and co-workers (2013) reported a phase I dose-escalation trial of the 2DG in combination with an antimitotic agent, docetaxel, in patients with advanced solid tumors. Authors recommended a dose of 2DG of 63 mg/kg/day in combination with weekly docetaxel (2 mg kg^{-1}) with tolerable adverse effect and no evidence of pharmacokinetic interactions (462). Shen *et al.* (2013) explored DCA's ability to reactivate OXPHOS in hepatocellular carcinoma (HCC) resistant cells with decreased lactate and increased ROS production (465). Activation of OXPHOS by DCA markedly sensitized HCC sorafenib-resistance cells towards sorafenib-induced apoptosis (465). A recent study conducted by Xie and co-workers demonstrated a synergistic apoptotic effect of DCA in combination with a chemotherapeutic compound cisplatin (DNA chelator) on HeLa cells (466). The latter was mediated by a shift in metabolism from glycolysis to glucose oxidation with increased H_2O_2 and reduced MMP (466). Latest research conducted by Tavares-Valente *et al.* (467) determined the influence of DCA on conventional mitotic inhibitors, paclitaxel and doxorubicin, on breast carcinoma MCF-7 cells. They demonstrated DCA is able to

reduce both ATP and lactate production in MCF-7 cells; in turn reducing the multidrug resistance phenotype which is energy- and pH-dependent (467).

Based on these pioneer results, it was hypothesized that the novel combination of C9 and DCA could selectively exhibit anticancer effects towards cancer cells. Up to date, there is limited scientific literature aimed at elucidation of the mechanism of combination therapy of glycolytic inhibitors and antimitotic agents on cancer cells.

The present study demonstrated that DCA (7.5 mM) in combination with C9 (130 nM) selectively inhibited half of MCF-7 cells' population (50.8%) within 24 hours. Under the same treatment condition, MCF-12A cells displayed higher numbers of cell survival of around 70%. Qualitative morphological studies revealed decreased cell density in both cell lines, as well as hallmarks of apoptosis and autophagic processes including formation of apoptotic bodies, DNA fragmentation and formation of autophagic vacuoles. Cell cycle- and apoptosis quantification analysis revealed C9+DCA treatment induced sub-G_1 population, G_2/M cell cycle arrest and apoptosis in both cell lines with higher induction levels displayed in carcinoma cells. Formation of autophagosome was observed and LC3-II expression was elevated after exposure. Tumorigenic MCF-7 cells mitochondrial membrane potential depolarization was demonstrated, but not in MCF-12A cells. Oxidative stress in C9+DCA-treated cell is induced in MCF-7 cells but not in MCF-12A cells and this induction may be due to altered levels of H_2O_2 and Fe^{2+}. Kinase inhibition studies revealed transient activation of JNK plays an important role in cell proliferation. However, C9+DCA stimulated prolonged JNK activation and in turn promoted Bcl-2 phosphorylation, thereby facilitating apoptotic cell death. The combination treatment C9+DCA abrogates the phosphorylation status of Bcl-2 in MCF- and MCF-12A cells. However, JNK inhibition, as well as NAC treatment, but not the p38 inhibitor, prevents the C9+DCA-mediated abrogation of Bcl-2 phosphorylation in MCF-7 cells. C9+DCA-treatment possibly disturbed the distribution and transport of ferritin, thus contributing towards higher concentration of ferritin within the lysosome. Prolonged autophagy, lysosomal instability, compromised microtubule integrity and activation of apoptosis together orchestrated the programmed cell death. Gene expression revealed C9+DCA induced expression of a number of genes related to stress in MCF-7 treated cells including *TP53BP1*, *MDM2* and *BBC3/PUMA*. Genes related to cell motility and maintenance of the cytoskeleton such as *ACTG1*, *MAP7*, *TUBA1*,

TUBA6, *TUBA8* and *TUBB2A* genes were down-regulated. In MCF-12A cells, treatment of C9+DCA induced expression of multidrug resistance gene *ABCB1*. Moreover, genes involved in reactive oxygen species metabolism *FTH1*, *GSTA2*, *NOS2A*, *SMOX*, *SOD1* and *SOD2* were also up-regulated. It was proposed that selectivity of the combination treatment is associated with restoration of mitochondrial OXPHOS in tumorigenic MCF-7 cells, which in turn contributes to reactive oxygen species formation, mitochondrial permeabilization and activation of ROS-JNK-Bcl-2-mediated apoptotic pathways.

Real-time dynamic monitoring of cell adhesion and proliferation via the xCELLigence system revealed that the optimal seeding number of cells for this comparative studies in a 96-well plate is between 5000 to 10 000 cells per well (377). Cell population growth studies employing crystal violet as a DNA stain revealed that the combination treatment of DCA at a concentration of 7.5 mM and C9 at a concentration of 130 nM inhibited cell proliferation in the tumorigenic MCF-7 cells to 50.84% after 24 h of exposure (IC_{50}). The same concentration inhibited cell population growth by only 29.29% in the non-tumorigenic MCF-12A cells, indicating that the non-tumorigenic MCF-12A cells are less susceptible to growth inhibition when compared to the tumorigenic MCF-7 cell line for this specific combination of DCA and C9. Previous research has demonstrated similar results for DCA when combined with antimitotic compounds whereby normal cells show lower cytotoxicity when compared to tumorigenic cells (468-470). Olszewski *et al.* (2011) demonstrated that HEK293 normal epithelial kidney cells exhibited less cytotoxity at 10 mM DCA in combination with selected platinum drugs (468). Fiebiger *et al.* (2011) demonstrated that DCA potentiates the cytotoxicity of selected platinum drugs, including satraplatin (469). Dhar and Lippard (2009) showed that mitaplatin, a platinum-based anticancer compound in combination with DCA, selectively kills cancer cells (470). Tavares-Valente *et al.* (467) determined IC_{50} for conventional mitotic inhibitors paclitaxel and doxorubicin on breast carcinoma MCF-7 cells when cells were pre-treated with 10.44 mM DCA. The results showed DCA pre-treatment reduced the MCF-7 IC_{50} from 1.58 µM paclitaxel and 4.27 µM doxorubicin to 0.01 µM and 0.35 µM, respectively (467). Thus, the present study display promising results as we were able to achieve IC_{50} on MCF-7 cells with lower concentrations of drugs: 7.5 mM DCA and 0.13 µM C9 for a 24 h study.

The initial determination of optimal concentration of combination compounds for this project was performed via crystal violet assay. The GI_{50} value of 130 nM for C9 served as a benchmark and was selected for this project. Initially, wide ranges of DCA concentrations were selected according to research conducted by Xiao *et al.* (337) and Sun *et al.* (323). The lowest DCA concentration used was 2.5 mM and it was adjusted with an increment of 2.5 mM until the highest concentration reached 15 mM. A final decision of 7.5 mM DCA for combination treatment was made based on the IC_{50} value of MCF-7 cells after 24 h exposure. Crystal violet assay data revealed the antiproliferative property of a combination of C9+DCA on MCF-7 and MCF-12A were time- and dose- dependent.

LDH cell viability experiments demonstrated statistically significant different percentages of viable cells when compared to the vehicle-treated controls (100%) of 83.53% for MCF-7 cells and 92.40% for MCF-12A cells when treated with C9+DCA. The difference is not major, however, because the LDH assay measures the content of LDH released from cells due to damage to cell membranes as a result of necrosis and/or late apoptotic processes (471,472). The lack of propidium iodide staining of the nucleus in treated cells indicated that necrotic processes were not up-regulated. Apoptosis assays showed only slight increases in the late apoptotic stages after 24 h exposure. These results support the small difference observed in LDH cell viability assay after 24 h exposure. It would also suggest that the more pronounced selectivity that was observed in cell growth assays (crystal violet and xCELLigence) and light microscopy micrographs is more likely due to the combination treatment having a negative effect on cell proliferation rather than increased induction of late stages of apoptosis. A possible reason for this lack of increased induction of late stages of apoptosis may in part be explained by the increase in autophagic activity that was observed after 24 h treatment. Autophagy is known to have a protective effect for cancer cells under various stress situations and in this may be another example of this phenomenon (239,240).

xCELLigence impedance technology is able to generate characteristic kinetic patterns to predict the mode of action of specific compound exposure. Depending on the type, concentration, exposure time and the mechanism of action of particular compound, a specific CI curve is generated. For example, a tubulin interfering antimitotic agent Epothilone B (473) (0.26 nM) was tested and showed a spoon-

shaped CI curve when exposed to Hela cells (data obtained from ACEA Biosciences, Inc.). In this project, C9- and C9+DCA-exposed cells also exhibit spoon-shaped CI curves. This phenomenon may be explained as follows and is summarized in Figure 4.1: (1) Normal cell proliferation/cell propagation reaches confluency; (2) compound exposure time point; (3) G_2/M cell cycle arrest, cell morphology appears rounded which caused cell lifting from plate surface; (4) initiation of apoptosis, cell morphology transit from G_2/M block to formation of apoptotic bodies; and (5) late stages of apoptosis cause cell to detach from plate surface and decrease in CI.

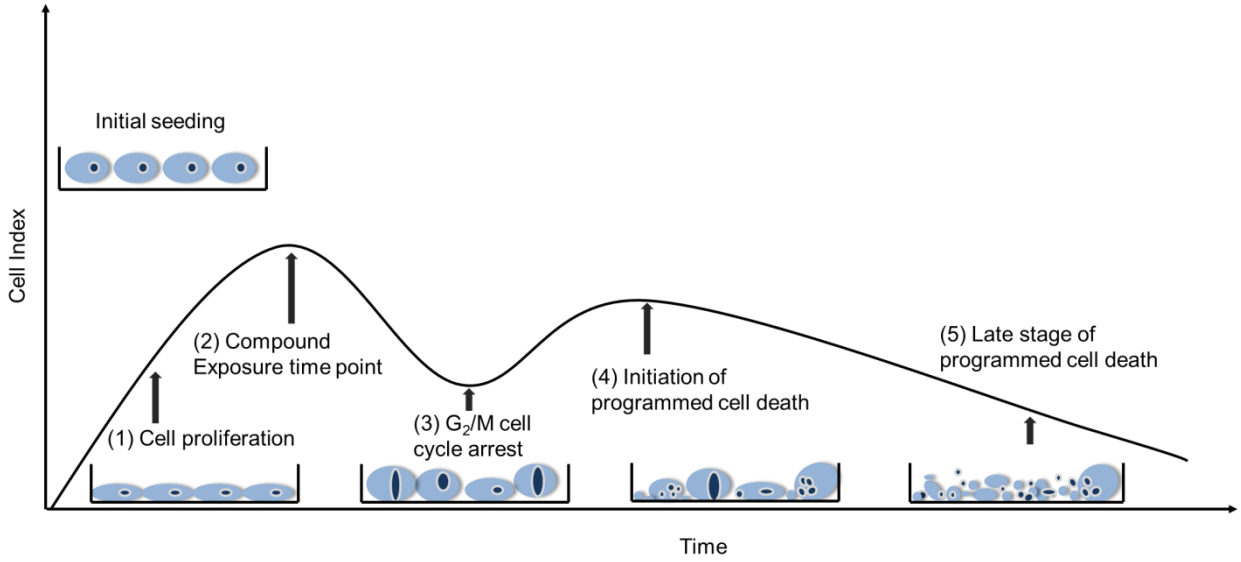

Figure 4.1: An antimitotic compound generates characteristic spoon-shaped kinetic CI patterns. (1) Normal cell proliferation/cell propagation reaches confluency; (2) compound exposure time point; (3) G_2/M cell cycle arrest, cell morphology appears rounded which caused cell lifting from plate surface; (4) initiation of apoptosis, cell morphology transit from G_2/M block to formation of apoptotic bodies; and (5) late stages of apoptosis cause cell to detach from plate surface and decrease in CI.

Cytotoxicity tests of the compounds were conducted via the RTCA xCELLigence system. Cytotoxicity results revealed C9+DCA exert its maximal effect at 16 h after exposure and when cell index value decreased by 85.19% compared to control. However, under the same treatment condition (C9+DCA for 16 h), MCF-12A cells CI value reduced by 51.3% compared to vehicle-exposed control. Cytotoxicity results confirmed our former findings that C9+DCA selectively reduced the tumorigenic MCF-7 cells growth by 50.84% after 24 h exposure with the crystal violet study. The advantage of the xCELLigence system is that the CI curve is produced in real time,

so that the exact time point when the compound exerts its effect on a certain cell line is demonstrated. A similar cytotoxicity study conducted by Visagie *et al.* (2012) in our laboratory utilized the xCELLigence system to test the effect of C16 on various breast cell lines (402). This study revealed that C16 exerted antiproliferative activity against MDA-MB-231 and MCF-7 cells (402).

The IC_{50} of DCA used in combination therapy was determined by employing the RTCA SP xCELLigence system and five different concentrations. Quantification via the RTCA Software allowed the plotting of a sigmoidal dose response curve and calculation of IC_{50} of 6.44 mM for 24 h exposure on MCF-7 cells. This value obtained via the xCELLigence system was similar to the value of 7.5 mM obtained by means of crystal violet DNA staining. Data from both xCELLigence and crystal violet DNA staining techniques determined that lower doses of DCA (2.5-15 mM) did not exhibit anti-proliferative properties against MCF-7 or MCF-12A cells. However, higher doses of DCA (40 mM) suppressed MCF-7 and MCF-12A cell proliferation. In addition, DCA increased MCF-7 carcinoma cell line sensitivity towards the mitotic inhibitor C9 regardless of the DCA concentrations used. Sanchez *et al.* demonstrated that lower concentrations of DCA (5-10 mM) have the ability to inhibit aerobic glycolysis, while DCA (10-25 mM) at higher concentrations exhibited anti-proliferative property with G_0/G_1 and G_2/M cell cycle arrest and induction of apoptosis in multiple myeloma cell (464). Previous studies suggested similar effects of DCA on colorectal cancer cells (463). A recent study demonstrated that 10.44 mM DCA pre-treatment markedly sensitized MCF-7 cells towards mitotic inhibitor paclitaxel and doxorubicin as the IC_{50} reduced from 1.58 µM and 4.27 µM to 0.01 µM and 0.35 µM, respectively (467).

The RTCA Software of the xCELLigence system was employed to predict combination drug efficacy. As described in the results section, the slope of the CI curve was used to describe the rate of CI change. If addition of compounds caused a CI decrease within short a period of time, the slope appears negative indicating that the compounds exerted toxic effect on the cells. The goal for this project was to identify a suitable DCA concentration via the slope for subsequent C9+DCA combination usage while minimizing the dosage. The lowest dosage that produced cytotoxic effects was 7.5 mM DCA combined with C9 (130 nM).

The xCELLigence system has been utilized in this project with regards to establishment of MCF-7 and MCF-12A cell proliferation profiles, cell quality control, cytotoxicity testing, signature CI kinetic curve generation, RTCA Software IC_{50} calculation, as well as drug efficacy prediction. Compared to conventional end-point cell-based assays, dynamic monitoring of cell response is one of the biggest advantages of the xCELLigence system, which is almost impossible to achieve by the currently established end-point assays as in crystal violet DNA stain or LDH cell viability assays. Thus, the xCELLigence RTCA system is an excellent tool for real-time evaluation of cytotoxic agents involving *in vitro* cell culture techniques.

Crystal violet DNA staining assay, LDH cell viability assay, as well as the xCELLigence RTCA system demonstrated that vehicle DMSO used to dissolve C9 was biologically and molecularly inert with no toxic effect observed on the cells when (v/v) not exceeding 0.01%. Addition of DMSO to proliferating cells had 100% growth rate compared to cell propagate in medium only, thus indicating DMSO is well suited as a solvent for *in vitro* testing.

Morphological investigation via PlasDIC light microscopy indicated that DCA-treated MCF-12A and MCF-7 cells showed no significant qualitative morphological differences when compared to the vehicle-treated controls. Compromised cell density was, however, observed in both cell lines treated with C9 when compared to vehicle-treated controls. Formation of apoptotic bodies and compromised cell density in MCF-7 and MCF-12A cells treated with C9+DCA were observed. Increase in acridine orange suggested an increase in lysosomal leakage. Treatment with C9 and C9+DCA respectively, on MCF-7 cells, caused increased mitotic indices of metaphase, as well as an increased count for cells exhibiting hypercondensed chromatin. This result suggested that C9 exhibits characteristics of a typical antimitotic compound where it induced an increase in the number of cells in metaphase after treatment. Previous studies suggested similar effects of sulphamoylated mitotic inhibitor with regards to mitotic indices on MCF-7, as well as MDA-MB-231 cells (402). Addition of DCA with C9 showed synergistic effect against MCF-7 cells, with the number of cells in metaphase and cells exhibiting hypercondensed chromatin almost doubling when compared to C9-exposed cells. However, the MCF-12A cells were less affected when compared to the MCF-7 cells for the same treatment.

Qualitative morphological examination via light microscopy indicated that DCA-treated MCF-7 and MCF-12A cells showed no significant differences compared to DMSO-treated vehicle controls. C9-exposed MCF-7 cells exhibited characteristics of compromised cell density and signs of G_2/M cell cycle arrest. These characteristics were not observed in C9-treated MCF-12A cells. Compromised cell density, G_2/M cell cycle arrest, membrane blebbing and formation of apoptotic bodies were observed in both cell lines after C9+DCA treatment for 24 h compared to controls. Confocal micrographs demonstrated that the mitotic spindle integrity was compromised after treatment with C9+DCA. Cells that divided in the presence of the C9+DCA treatment proceeded from being arrested at the mitotic phase to forming multiple micronuclei and apoptotic bodies. Studies conducted by Stander *et al*., Visagie *et al*. and Wolmarans *et al*. also showed similar results where a sulphamoylated antimitotic compound-treated MCF-7, and/or MDA-MB-231 or esophageal carcinoma cells (SNO) cells showed a decrease in cell density along with morphological indicators of apoptosis (366,402,474).

Distorted cell shape, high density of digit-like apical microvilli, formations of vacuoles, lysosomes and apoptotic bodies, heterochromatin, as well as fragmented DNA were detected in both cell lines by means of transmission electron microscopy. The non-tumorigenic MCF-12A cells were less affected by the combination compounds compared to MCF-7 cells. This observation is supported by a recent study where 17β estradiol analog-treated MDA-MB-231, MCF-7 and MCF-12A cells demonstrated the presence of apoptotic bodies and vacuoles (475). Fragmented nucleus and apoptotic bodies were detected within tumorigenic cells that were exposed to combination compounds thus indicating late stages of apoptosis, which also supported previous cell cycle and apoptotic quantification (Annexin V-FITC) studies, as well as other studies demonstrating similar results for antimitotic compounds (402,474).

Cell cycle analyses revealed an increase in G_2/M phase in C9-exposed and C9+DCA-exposed MCF-7 cells. A decrease in cells present in the S-phase, as well as an increase in the amount of cells present in the sub-G_1 phase in MCF-7-treated C9+DCA cells were observed. This observation of MCF-7 agrees with previous studies which showed similar findings on MCF-7 cells by Tagg *et al.* (2008) (386). There was also an increase in the sub-G_1 phase in C9+DCA-treated MCF-12A cells

and the difference between the two cell lines were statistically significant. Apoptosis analyses revealed treatment with C9 alone is not able to induce significant sub-G_1 cell cycle arrest in both MCF-7 and MCF-12A cells, which suggest that C9 at a concentration of 130 nM and 24 h exposure time is not able to induce late apoptosis. DCA-treated cells showed no statistically significant difference in early and late apoptotic cells when compared to the vehicle-treated control. However, treatment with C9+DCA demonstrated a synergistic effect when treated MCF-7 cells had about three-fold increase in early apoptosis populations compared to C9-treated cells. This effect was not as pronounced in the MCF-12A cells (two-fold increase), suggesting that the combination treatment is selective towards the tumorigenic cells.

Our previous study has demonstrated that C9+DCA is an agent that caused apoptosis in both MCF-7 and MCF-12A cells, with increased cell cycle sub-G_1 phase as well as Annexin V-FITC staining (377). These results indicated that the ability of C9+DCA to induce apoptosis is more pronounced in tumorigenic MCF-7 cells (377). The apoptosis study demonstrated that approximately 16% of the cells are apoptotic after 24 h exposure to C9+DCA. Thus, from the data it can be concluded that apoptosis is one mechanism of growth inhibition. The morphological studies qualitatively confirm that apoptotic processes are present. Fukui *et al.* (2008) demonstrated that 1.5-2.0 µM of 2ME inhibited cell growth in MDA-MB-435 cells after 48 h to 50% when compared to the vehicle-treated control and 1.5 µM only induced apoptosis in 18.1% of the cells (476). Also, our group has demonstrated that 2ME inhibits growth cell growth in MCF-7 cells after 48 h to 50% at 1 µM and that it induces apoptosis in 15% of the cells at the same concentration (324).

Autophagy, particularly macroautophagy, is conserved over a broad spectrum of organisms and is mediated by a special organelle named the autophagosome. The outcome for this “self-eating” process is digestion of organelles in lysosomes to sustain cellular metabolism (477). Cancer cells take advantage of this process and may utilize the autophagic process to survive in hostile environments (240). LC3-II autophagic protein expression increased in both cell lines when treated with C9+DCA for 24 h. A possible explanation for this observation is that both MCF-7 and MCF-12A use autophagy as protective pathway for survival. Several autophagic related structures were identified which include the autophagosome, multi-vesicular endosome, amphisome, lysosome and autolysosomes within the cells that have

been treated with the combination treatment. In addition, the gene expression profile demonstrated that the *SMOX* gene, which encodes protein spermine oxidase, was induced in MCF-12A cells. Spermine oxidase catalyzes the conversion of spermine to spermidine (478). The latter has been proven to prolong the life span of several model organisms via the induction of autophagic processes while retarding necrotic cell death (478). Madeo *et al.* (2010) revealed the induction of macroautophagy in yeast cells, *C. elegans*, *Drosophila* and human tumor cells (478). As previously mentioned in Introduction, the autophagic process often occurs upstream of apoptosis (238) or inhibits apoptosis (239) to provide cells with a protective function. During stress situations, autophagy functions as a pro-survival mechanism to support the cell with essential nutrients (239). Our cell viability tests, apoptosis assay (no major increase in late stage apoptosis), fluorescent morphology studies (lack of propidium iodide staining), as well as equal levels of LC3-II autophagic protein expression in MCF-7 and MCF-12A cells all support the conclusion that autophagy plays a protective role after C9+DCA treatment.

One of the most important downstream key players for the activation of the apoptotic intrinsic pathway is the depolarization of the mitochondrial membrane potential (125). The current study has demonstrated that C9- and C9+DCA treatment reduced the mitochondrial potential of MCF-7 cell. The reduced ΔΨm was completely inhibited by the addition of a broad spectrum of ROS inhibitor, NAC, in MCF-7. This result revealed that C9+DCA induced apoptosis via the intrinsic pathway through the production of ROS. However, C9+DCA did not have any effect on ΔΨm of MCF-12A cells. Other antimitotic compounds were also tested for their ability of reduce mitochondrial membrane potential in our laboratory. Data showed that C19 (200 nM) and C10 (50 nM) caused the mitochondrial membrane potential depolarization in MCF-7 and MDA-MB-231 cancer cell lines (187,376). Sun *et al.* (2011) (on arsenic trioxide and DCA) and Shen *et al.* (2013) (on sorafenib and DCA) demonstrated that combination of dichloroacetate with another chemotherapeutic agents induced apoptosis by reduced mitochondrial ΔΨm and production of ROS in breast cancer cells and hepatocellular carcinoma respectively (479,480).

Oxidative stress test via 2', 7'-dichlorofluorescein fluorescence was used to examine the oxidative stress status of MCF-7 and MCF-12A cells. For many years, DCF fluorescence within cells was considered as direct indication of increased level of

reactive oxygen species such as superoxide or hydrogen peroxide (481,482). H_2DCF-DA is a non-fluorescent lipophilic compound and is able to cross the biomembrane to form hydrophilic H_2DCF (411). A recent study revealed that the DCF-dependent fluorescence reflects the relocation of lysosomal iron and/or mitochondrial cytochrome *c* to the cytosol (411). The relocation of these membrane enclosed materials (iron and cytochrome *c*) is largely caused by the organelle membrane integrity being compromised (411). The current study demonstrated that the antimitotic compound C9- and C9+DCA-treatments were able to induce DCF fluorescence in MCF-7 cells. This data suggest that treatments with C9 and C9+DCA are able to induce lysosomal rupture and/or mitochondrial damage in tumorigenic MCF-7 cells. As a consequence, large quantities of H_2O_2, Fe^{2+} and cytochrome *c* were released into the cytosol. When a broad spectrum ROS inhibitor NAC and ferric iron chelator deferoxamine (DFO, 100 μM) were added in conjunction with C9+DCA treatment, both NAC and DFO attenuated the drug effect on MCF-7 cells in terms of mitochondrial membrane depolarization. This result confirmed that ROS as well as Fe^{2+} play an important role in apoptosis induction via mitochondrial membrane depolarization (Figure 4.2).

Transmission electron microscopy techniques revealed an increase in the production of autophagosomes after C9+DCA treatment on MCF-7 cells. The acidic organelle lysosomes function as degradative machinery for the ingestion and digestion of autophagic and heterophagic materials (142). Furthermore, when compared to other organelles, lysosomes contain much higher quantities of iron in a low-mass redox-active form (142,483). In normal cells, lysosomes utilize the iron-binding proteins, such as apoferritin, ferritin, metallothioneins and heat shock protein of 70 kDa (HSP70) to reduce tension exerted by free Fe (II) before protein degradation process occurs (142,483). Hasan and co-workers (484) demonstrated that the cytoskeletal component microtubule structures are responsible for the transportation of ferritin *in vitro* and *in vivo*, and that the ferritin is transported as oligomers. Inhibitors of microtubule polymerization are known to lead to changes in iron metabolism leading to increases in ferrous iron and this in turn contributes towards increased ROS formation (484). The combination treatment, especially with C9 being an antimitotic agent, likely disturbed the distribution and transport of ferritin and thus contributed towards a higher concentration of ferritin within the cytosol. The results suggested that the mechanism of action of compound C9 and C9+DCA on tumorigenic cells

and the treatment's ability to increase ROS are likely linked to its antimitotic property of targeting the microtubules (Figure 4.2).

Subsequently, specific primary antibodies to caspases 7 which were conjugated with Daylight^{TM} 488 were used to confirm apoptotic cell death. The flow cytometric results from caspase quantification showed increased levels of active caspases 7 in both cells lines after C9+DCA treatment for 24 h. It is well known that the activation of executioner caspases 7 during apoptosis can cause the cleavage and activation of PARP, a major contributing enzyme of apoptosis (485). In MCF-12A cells, the expression of mRNA for *GSTA2*, *SOD1*, *SOD2* and *SMOX*, which are involved in ROS metabolism, were up-regulated in response to C9+DCA exposure. Perhaps, a possible reason for no mitochondrial membrane potential ($\Delta\Psi m$) reduction observed may be attributed to the oxidative stress neutralizing effect of enzymes encoded by *GSTA2*, *SOD1* and *SOD2* genes.

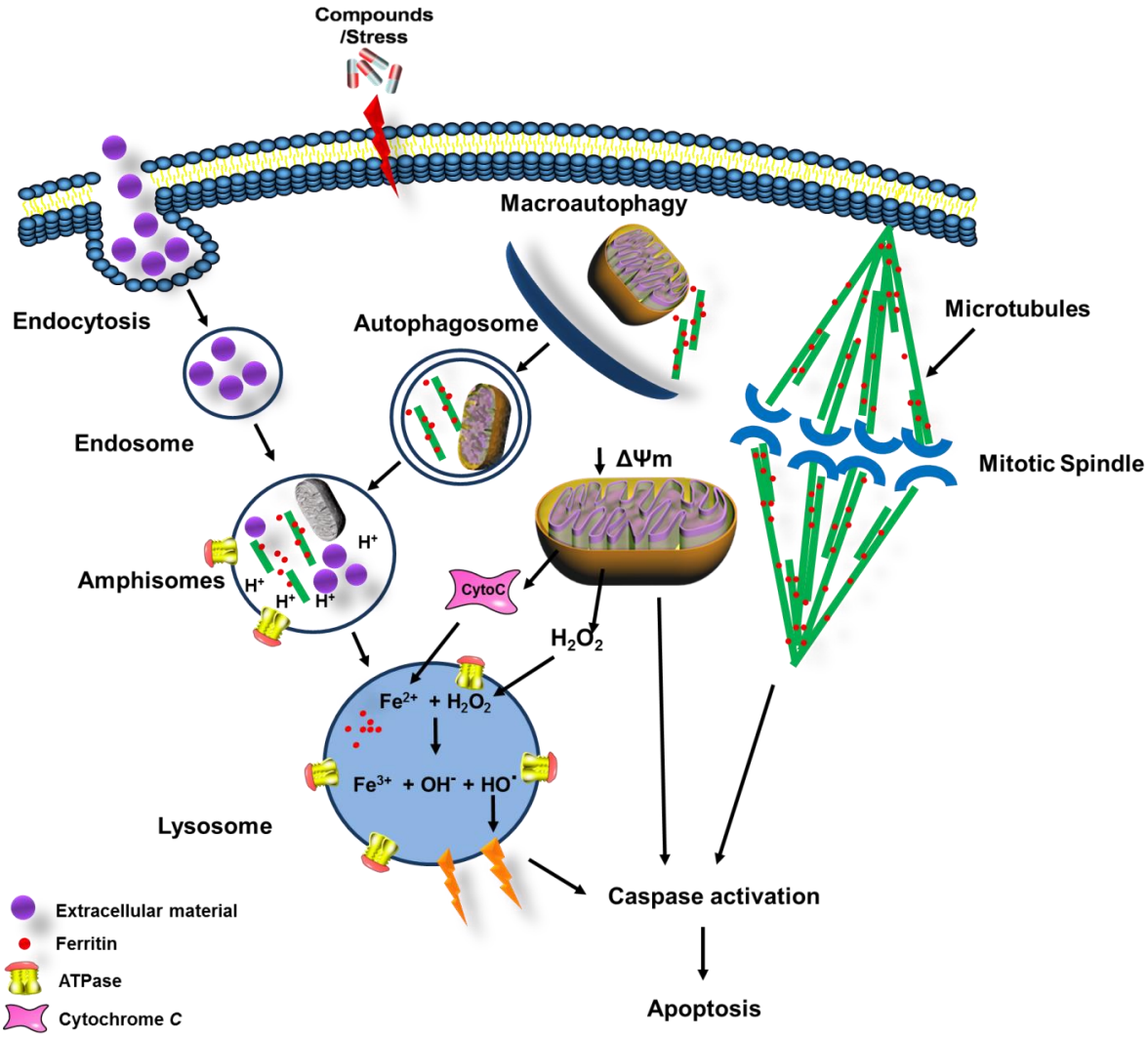

Figure 4.2: Cross-talk between intracellular structural (spindle) stability, autophagy, mitochondrial depolarization, lysosomal iron and apoptosis. Ferritin is known to be associated with microtubules which are the main constituents of the mitotic spindle. Combination compounds C9+DCA inhibited microtubules polymerization and caused cellular distress. Autophagy (endocytosis and macroautophagy) was initiated as survival mechanism to compensate for stress. The reduced mitochondrial membrane potential indicates the possibility of membrane pore formation and leakage of cytochrome *c*, as well as H_2O_2 into the cytosol. Consequently, redox-active iron and H_2O_2 accumulates within the lysosome, which facilitates Fenton-type reaction and the production of high reactive hydroxyl radicals that contribute to lysosomal rupture. Mitotic spindle arrest, mitochondrial depolarization and lysosomal rupture send out signals to activate caspases activation and eventually triggered apoptosis.

Reactive oxygen species play a significant role in cell senescence signalling pathways (352). Mitochondrial membrane potential depolarization and increased cytosolic fluorescent DCF-test confirmed that treatment of C9+DCA caused a significant increase in ROS formation and oxidative stress. It is well recognized that excessive ROS act as signals for the activation of stress related JNK and/or p38 pathways through the ASK1-Trx signalsome (169,254). ASK1 is one type of mitogen-activated protein kinase (MAPK) kinase kinase (MAPKKK) where it functions as part of the MAPK cascade toolkit for the activation of JNK/p38 pathway (2,254). Under normal conditions, ASK1 is inhibited by direct binding of its N-terminal region with reduced form of thioredoxin Trx-$(SH)_2$. When ROS formation is increased, it oxidizes Trx-$(SH)_2$ to Trx-S_2 and facilitates the release of ASK1 into the cytosol. Tobiume *et al.* (169) showed ASK1 is required for sustained activations of JNK/p38 MAP kinases and apoptosis. Several other types of MAPKKK such as, MEKK group (MEKK1-4), MLK1-3, TAK1 and TPL2 have been reported to activate the JNK signalling pathway (254). Yujiri *et al.* (1998 and 2000) demonstrated MEKK1 (type of MAPKKK) was required for JNK activation in response to microtubule disruption and cold shock (255,256).

Upstream activation of the JNK pathway can also be achieved by TNFα and Fas cytokine signalling. Activation of the TNFα-JNK pathway requires the recruitment of TNF receptor associated factor 2 (TRAF2) adaptor protein (257). Binding of TRAF2 adaptor protein to MEKK1 (258) and ASK1 (259) illustrated the importance of TRAF2 to mediate MAPKKK activation. The TNFα cytokine-mediated JNK activation require assistance from TRAF2 (257) to activate MAPKKK ASK1 (169). This cascade activation process cannot be completed without TNF-stimulated production of ROS (250,260). The JNK pathway may also act as apoptosis antagonist by NF-κB and Akt signalling pathways induced by AP-1 activity. This interpretation suggests that cell fate is orchestrated by the interaction between NF-κB, TNF-stimulated ROS production and type of JNK activation (sustained or transient) (261,262).

Morphologically, addition of p38 inhibitor promoted cell growth slightly, regardless of whether or not cells were treated with any compound(s). The RTCA xCELLigence inhibition study supported the morphological observation with p38i-exposed cells (treated or untreated) exhibited a higher CI curve than the cells without p38i

treatment. Results demonstrated that the combination treatment targeted p38 pathway moderately, but the exact mechanisms remain to be elucidated.

Inhibition studies results indicated that the JNK pathway plays an important role in MCF-7 and MCF-12A cell development, as well as mediating activation of apoptosis pathways after cells encounter stress. JNK inhibition results demonstrated that cell proliferation was negatively affected (decreased) in untreated cells and positively affected (increased) in C9+DCA-treated compared to DMSO-exposed controls. Results obtained from morphology, RTCA xCELLigence and ΔΨm with regards to JNK inhibition studies supported and confirmed that the JNK pathway was differentially activated in untreated (cells propagated in medium) and treated cells (C9+DCA). One explanation for this phenomenon is that transient JNK activation stimulated cell survival and growth, while sustained activation of JNK pathway by combination treatment motivated apoptotic signalling (Figure 4.3). This proposed mechanistic theory was previously tested by Ventura *et al.* (2006) where the authors tested the signal transduction of JNK and demonstrated that JNK activation can have a biphasic effect (250). Weston and Davis (2007) also mention the possibility of this theory in their review paper on the JNK signal transduction pathway (251). It is therefore suggested that the combination treatment of resulted in a sustained activation of the JNK pathway due to ROS signalling and subsequent induction of cell death. Furthermore, Lee *et al.* (486) demonstrated that JNK basal activity is indispensable for normal cell cycle progression and loss of JNK activity induces permanent cell cycle arrest following inhibition of Bcl-2 phosphorylation and generation of ROS. This result is in agreement with the JNK inhibition study results, where inhibition of JNK pathway in untreated cells elevated ROS production and slowed cell growth.

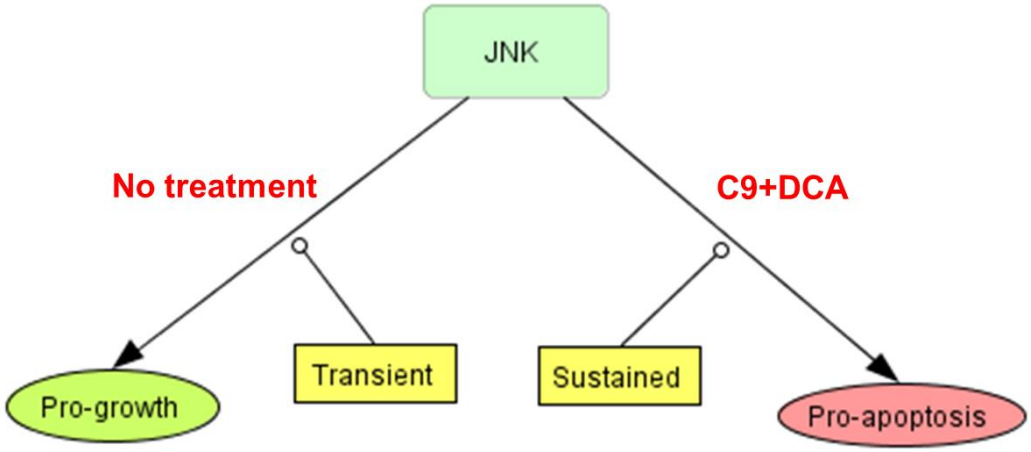

Figure 4.3: Biphasic time-dependent activation of *c*-Jun N-terminal kinase pathway. Untreated cells use transient activation of JNK pathway to promote cell growth. The combination treatment C9+DCA caused sustained activation of JNK pathway by subsequently switching on the apoptotic pathway.

Stress signals such as ROS and cytokines such as TNFα may stimulate and accelerate the production of ceramide. The generation of ceramide, which is the main bioactive messenger lipid, begins with the hydrolysis of sphingomyelin via enzymatic reaction catalyzed by sphingomyelinase. When receptor sensitive stimuli such as TNFα and Fas couples with their plasma membrane anchored receptors, the hydrolysis of sphingomyelin is activated and formation of ceramide is initiated. This ceramide that is released is believed to promote lipid rafts and subsequent clustering of death receptors on a large scale (487,488).

A study conducted by Wu *et al.* (2005) provided evidence that the generation of ceramide by a G-protein coupled receptor, the Ca^{2+}-sensing receptor, sequentially stimulates stress-activated protein kinase/extracellular signal regulated kinase kinase 1 (SEK1) and JNK activities, *c*-Jun phosphorylation, caspase activation, and DNA fragmentation (489). Ceramide is not only formed at the plasma membrane, but also in the lysosome by the enzyme acidic sphingomyelinase from sphingomyelin. This bioactive messenger has the ability to activate a couple of downstream effectors, such as ceramide-activated protein kinases (CAPK), ceramide-activated protein phosphatases (CAPP) and cathepsin D, to promote cell cycle arrest and apoptosis (490). The downstream effect of cathepsin D, for example, converts Bid into tBid to bind and promote oligomerization of Bax, a pro-apoptotic protein situated on the

outer mitochondrial membrane. It has been reported that permeabilization of the mitochondrial membrane was directly linked to oligomerization of Bax (174).

As previously mentioned, Bid and Bax protein belong to the Bcl-2 protein superfamily. More than 30 proteins are classified within the Bcl-2 superfamily and they can be categorized into three subgroups: Bcl-2-like survival factors, Bax-like death factors and BH3-only death factors (174). The Bcl-2 family of proteins are essential for regulation of apoptosis and autophagy (174). The intrinsic apoptotic pathway is primarily regulated by Bcl-2 superfamily proteins (2). Bcl-2-like survival factors Bcl-2, Bcl-X_L, Bcl-w and Mcl-1 promote cell survival, whereas Bax and Bak provoke the mitochondria-mediate intrinsic cell death. The activation of apoptosis depends on balances and interactions between BH3-only, Bax-like proteins and Bcl-2-like survival factors (175). The pro- and anti-apoptotic subgroups of the superfamily dynamically interact with each other through their conserved Bcl-2 homology (BH) domains. The BH-3 only subgroup (with only BH3 domain) is able to collect information and pass it on to multi-domain (BH) members (Bax-like and Bcl-2 like) of the family, which will carry out downstream effects (2).

Not only the transcription factors *c*-Jun, p53 and *c*-Myc can be phosphorylated by JNK (254,271), but also the non-transcription factors such as members of the Bcl-2 superfamily (Bcl-2, Bcl-XL, Bim and BAD) (491). B cell leukaemia-2 (Bcl-2) is a product of proto-oncogene *bcl-2* and functions as a prominent anti-apoptotic suppressor (176). In response to a variety of extracellular stimuli, Bcl-2 releases pro-apoptotic factors such as Bax, thereby diminishing its inhibitory action and enabling Bax oligomerization on the mitochondrial membrane (2). Bcl-2/Bax heterodimerization is not sufficient for full Bcl-2 anti-apoptotic function. Phosphorylation of Bcl-2 serine 70 (Ser^{70}) is a crucial requirement, which completes its death suppressor signalling activity (176). However, JNK-mediated Bcl-2 multi-site phosphorylation of the non-structured loop at residues Thr^{69}, Ser^{70} and Ser^{87} was shown to interfere with its binding to pro-apoptotic, as well as pro-autophagic BH3 domain-containing proteins (248,252). Thus, it was important to test overall protein expression and phosphorylation status of Bcl-2 in this study.

Flow cytometric analyses results demonstrated that combination treatment is able to alter the total Bcl-2 content, as well as Bcl-2 Ser^{70} phosphorylation dynamics in

MCF-7 and MCF-12A cell lines. The total Bcl-2 expression increased in C9+DCA+p38i-, JNKi- and C9+DCA+JNKi-exposed MCF-7 cells. The decreased expression of total Bcl-2 in C9+DCA-treated cells suggests that the anti-apoptotic effects of Bcl-2 may be inhibited by C9+DCA treatment. Also, the increased expression of Bcl-2 in p38i- and JNKi-treated cells suggests that inhibition of these proteins is anti-apoptotic. Total Bcl-2 expression was unaffected in MCF-12A cells exposed to C9+DCA. As mentioned previously, the total expression level of Bcl-2 cannot be the only measurement against its level of activity. Post-translational modifications such as phosphorylation should be taken into consideration.

When measuring the phosphorylation status of MCF-7 and MCF-12A cells it was observed that > 90% of vehicle-exposed cells had fluorescence intensity (FI) of 7.5-75. Treatments stressed cells with regards to the Bcl-2 phosphorylation status and it reflected with an increase in the amount of cells with both hypo- and hyper-phosphorylated Bcl-2 (ser70) (Figure 4.4). Hypo-phosphorylation/dephosphorylation at Ser^{70} is associated with apoptosis induction through the mitochondrial pathway (416). Hyper-phosphorylation at Ser^{70} position of the Bcl-2 protein is required for Bcl-2's full and potent anti-apoptotic function (492). However, studies have demonstrated that an increase in the Bcl-2 hyper-phosphorylation at multisite, which includes Ser^{70} is linked to G_2/M block in MCF-7 cells and lead to apoptosis induction (416) (Figure 4.4).

Compound 9 and combination therapy C9+DCA treated MCF-7 cells exhibited decreased normal level of Ser^{70} phosphorylated Bcl-2, and increased levels of hypo- and hyper-phosphorylated Ser^{70} Bcl-2 proteins per cell. A similar result was observed for C9+DCA-exposed MCF-12A cells, but not for treatment C9 on this cell line. This result suggests treatment C9 and C9+DCA have the ability to activate anti-apoptotic Bcl-2 protein in MCF-7 cells at the post-translational level of phosphorylation. The same statement is true for MCF-12A cells. However, it is only applicable for combination C9+DCA-treated MCF-12A cells. Hypo-phosphorylation at Ser^{70} of Bcl-2 protein is related to the intrinsic mitochondrial pathway of apoptosis induction; thus treatment of C9 or C9+DCA possibly induced apoptosis of MCF-7 cells through the intrinsic pathway. Treatments of C9- or C9+DCA against MCF-7 cells induced Bcl-2 Ser^{70} hyper-phosphorylation 15.35% and 23.73%, respectively. An increase in Ser^{70}, Trp^{69} and Ser^{87} multi-site phosphorylation is associated with apoptosis induction and

related to drugs causing G_2/M arrest in MCF-7 cells (416). Previous MitoCapture™ and DCF-test results demonstrated that treatments with C9- or C9+DCA against MCF-7 cells caused MMP depolarization as well as possible ROS formation. Together with these Bcl-2 results, it is therefore argued that Bcl-2 multi-site phosphorylation (Ser^{70}, Trp^{69} and Ser^{87}) might be induced by treatment with C9 and C9+DCA in MCF-7 cells.

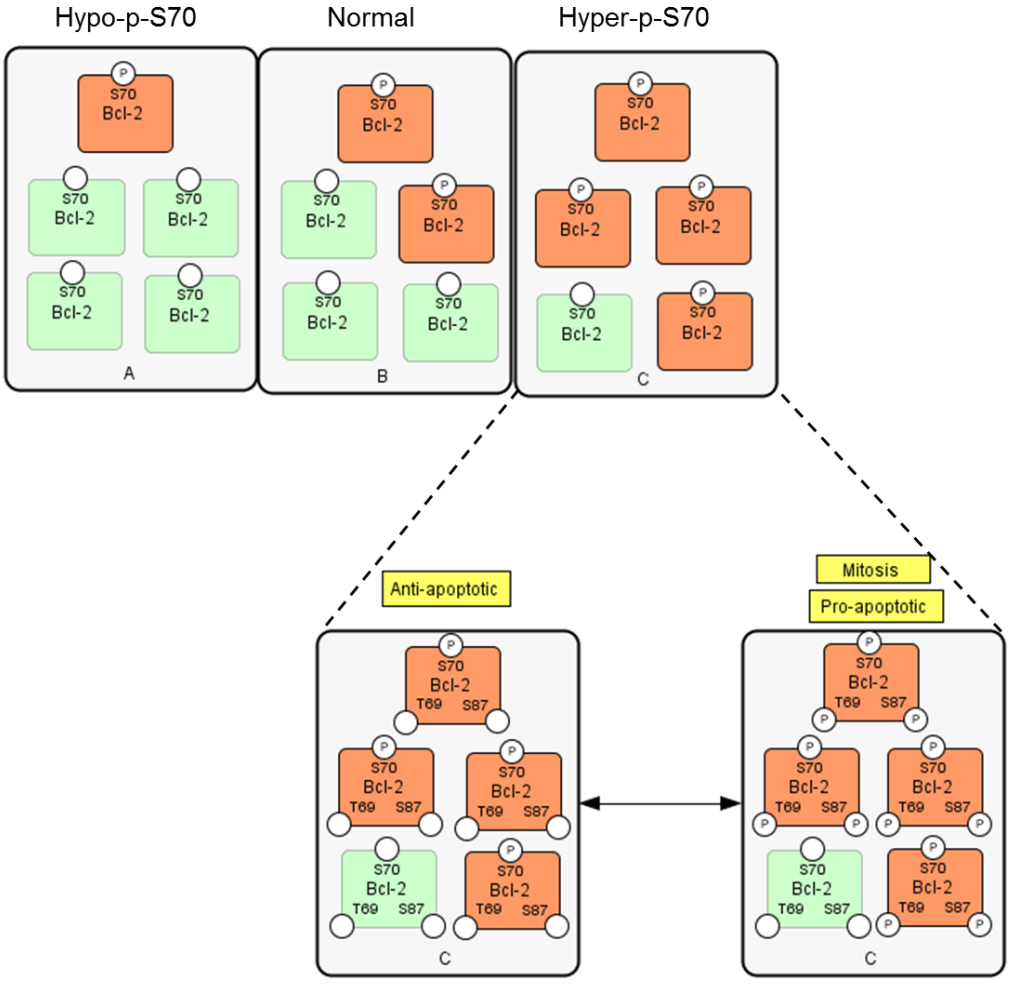

Figure 4.4: Implication of phosphorylation status of the cell concerning the serine 70 position. Three sub-populations of cells were identified signifying different protein expression levels of Ser^{70} phosphorylated Bcl-2, namely, 'hypo-phosphorylation' (Hypo-p-S70), 'normal' and 'hyper-phosphorylation' (Hyper-p-S70). Bcl-2 multi-site hyper-phosphorylation (serine 70, tryptophan 69 and serine 87) and Bcl-2 serine 70 hypo-phosphorylation are associated with its pro-apoptotic properties (416).

Sub-populations of cells (percentages) with hypo-, normal- and hyper-phosphorylation status of MCF-7 cells Bcl-2 protein at Ser^{70} (Figure 3.39) clearly

displayed that treatment with C9 and C9+DCA increased hypo- and hyper-phosphorylation at Ser^{70} of Bcl-2 at a statistically significant level. Previous cell cycle studies showed the antimitotic tubulin poison C9 caused MCF-7 proliferation to arrest at G_2/M phase of the cell cycle. Our Bcl-2 results demonstrated C9 induced Bcl-2 phosphorylation, together with the apoptosis study, suggesting that microtubule damage may lead to cancer cell apoptosis through a mechanism involving Bcl-2 phosphorylation. This study result is in accordance with research conducted by Haldar *et al.* (252,493), who showed that the spindle poison/antimitotic compounds induced cancer cell death through phosphorylation of Bcl-2. Furthermore, our result showed the addition of DCA together with C9 exhibited a synergistic effect and increased Bcl-2 phosphorylation. This observation can be attributed to DCA causing substantial amount of ROS formation, which served as signal to stimulate MAPK pathway and subsequently activate Bcl-2 phosphorylation (494).

In order to evaluate the role of mitogen-activated protein kinases (MAPKs) in Bcl-2 phosphorylation, the activation of JNK and p38 was examined. In untreated MCF-7 cells, if JNK activation was blocked by addition of JNK inhibitor SP600125, Bcl-2 phosphorylation was induced which served as a pro-apoptotic signal.

As previously explained, transient JNK activation stimulates cell survival and growth (Figure 4.3). JNK basal activity is indispensable for normal cell cycle progression. Loss of JNK activity may induce permanent cell cycle arrest and apoptosis (250,486). In MCF-7 cells treated with C9+DCA, addition of JNK inhibitor SP600125 lowered the level of hypo-, as well as hyper-phosphorylation Bcl-2 to one-third and half, respectively. The DCF-test results suggested that treatment with C9+DCA increased formation of ROS. Many reports showed that ROS activates the JNK pathway in a sustained manner. As a result, Bcl-2 phosphorylation status changes because it is the downstream target of JNK. This cascade of events contribute towards the release of pro-apoptotic Bcl-2 family protein Bax, which is located on the outer mitochondrial membrane. ROS appears to play a critical role in the regulation of sustained activation of the JNK pathway and JNK mediated Bcl-2 phosphorylation. Our results demonstrated that the generation of ROS was achieved by combination treatment.

The tumor suppressor p53 pathway is situated at the crossroads of a network of signalling pathways serving as a gate keeping molecule (495). Gene expression analysis has revealed several differentially expressed genes related to p53 pathway. *TP53BP1* is up-regulated in MCF-7 cells and this gene encode p53-binding protein 1 (53BP1), which detect early DNA damage and response by rapid recruitment to the site of nicked double-strand DNA. Histone proteins H2AX then become phosphorylated and available for 53BP1 to bind to DNA double-strand breakages (496). The signal transduction to the p53 protein is through mediator kinases such as ataxia telangiectasia mutated (ATM) and checkpoint kinase-2 (Chk2) phosphorylation (497). Thus, the induction of the *TP53BP1* gene serves as an indicator for cellular stress after combination treatment and possible activation of the p53 pathway. The expression of several p53-related pro-apoptotic genes were increased in both MCF-7 and MCF-12A cell lines including *BBC3/PUMA*, B-cell translocation gene 1 (*BTG1*), IKK interacting protein (*IKIP*), dual-specificity phosphatase 13 (*DUSP13*) and *FTH1*. The *BBC3/PUMA* and *NOXA* are p53-inducible genes which produce BH3-only proteins and are now known to be essential for DNA damage-induced apoptosis (498).

The combination compounds might exert their cytotoxic effect by inducting the *BTG1* gene to achieve inhibition of anti-apoptotic protein Bcl-2. Nahta *et al.* (2006) showed knockdown of *BTG1* gene reduced antisense Bcl-2-mediated cytotoxicity in breast cancer MCF-7 and MDA-MB-231 cells (499). Cytochrome *c* release plays a prominent role in formation of the apoptosome and its activation is completed by apoptotic protease activating factor 1 (*APAF1*). The *IKIP* gene and the *APAF1* gene share common bidirection promoters and they are p53 target genes with pro-apoptotic function. In particular, *IKIP* protein products may be involved in the ER-mediated apoptosis pathway by integrating with cascade NF-κB pathway signalling (500).

Emerging evidence suggests the *DUSP13* gene encodes two proteins DUSP13A and DUSP13B, however, the functions of the two proteins are distinct (501,502). DUSP13A activates *ASK1* and in turn initiate a MAPKKK that activates JNK and p38 kinases (501,503). Quite the opposite, DUSP13B has significant inhibitory effects on stress-activated MAPKs (502). The expression of FTH1 was up-regulated in both MCF-7 and MCF-12A cells in response to C9+DCA exposure. FTH1 gene products

contribute towards the synthesis of an iron-sequestering protein, ferritin. Microtubules serve as a scaffold for the intracellular distribution and transport of ferritin (484). Interfering with microtubule dynamics by antimitotic agents like C9 may therefore contribute towards iron metabolism imbalance and facilitate iron-mediated cell death (484). The increased FTH1 gene expression is induced by enlarged cytoplasmic liable iron pool (484), thus it means the cells are producing more iron under compound-induced stress. The increase in cytosolic iron may be sourced from lysosome permeabilization as a result of compromised lysosomal membrane integrity triggered by autophagy (142).

The present study is the first to demonstrate the *in vitro* effects of an antimitotic compound in combination with DCA on tumorigenic and non-tumorigenic cells. The novel *in silico*-designed 17β-estradiol derivative C9 in combination with DCA is a potent antiproliferative treatment with properties of selectivity towards tumorigenic MCF-7 cells. C9 may serve as a chemotherapeutic agent which targets rapidly growing tumor cells, while DCA may preferentially target the hypoxic tumorigenic cells. This study provides new insight to the field of combination therapy. It elucidated the mechanisms of combination treatment at the molecular and cellular level. Results obtained contribute to elucidate the functional roles of the pathways involved in selectively killing of cancer cells by a glycolytic inhibitor and an antimitotic compound. This project warrants further research to develop viable and functional combination treatments as clinically useable anticancer agents.

5. Chapter 5: Conclusion

The present study demonstrates that the combination of a new antimitotic compound in conjunction with the PDK inhibitor, DCA, has the potential to selectively target tumorigenic MCF-7 cells over non-tumorigenic MCF-12A cells by inducing apoptosis. MCF-7 cells have a high glycolytic capacity and they also have a significantly higher hyperpolarized mitochondrial membrane potential compared to normal cells (325,504). Inhibitors of PDKs such as DCA attenuate inhibition of PDH activity (334). Increased PDH activity shifts metabolism from glycolysis to oxidative phosphorylation, decreasing mitochondrial membrane potential hyperpolarization which in turn opens mitochondrial transition pores (325). This allows for the translocation of ROS from the mitochondrial matrix to the cytoplasm and increases ROS-signalling, as well as restoring normal metabolism (325). Restoring normal mitochondrial membrane potential in turn results in sensitizing cells to apoptotic signalling (325).

C9 is a more potent antimitotic analogue of 2ME (366,377). However, it is suggested that its mechanism of action with regards to induction of apoptosis is similar to that of 2ME (324,366,377). In 2ME-treated cells, cell cycle arrest leads to apoptosis via reactive oxygen species generation and the intrinsic apoptosis induction pathway as a result of an increase in mitochondrial permeabilization and cytochrome *c* leakage (324). Autophagic activity is also regulated by reactive oxygen species (505). It is proposed that the selectivity of the combination treatment is associated with the restoration of oxidative phosphorylation in MCF-7 cells, which in turn contributes to reactive oxygen species formation, mitochondrial permeabilization and ultimately culminating in apoptosis and/or autophagy induction.

Our present study has demonstrated that the antimitotic agent C9 and glycolytic inhibitor DCA synergistically inhibited the proliferation of MCF-7 and MCF-12A cells. Additionally, the combination treatment selectively induced apoptosis in MCF-7 cells *in vitro*. Morphological changes such as compromised cell density, membrane blebbing, and formation of apoptotic bodies were observed. Intracellular alterations especially with regards to the formation of various types of autophagic vacuoles were detected. Mitochondrial membrane potential reduction as well as cytosolic active caspase 7 activation were remarkably increased. Gene expression revealed there

are large numbers of apoptotic genes related to p53 pathway that were up-regulated. Genes that are related to structural integrity were affected negatively. The combined treatment with C9 and DCA significantly inhibited the growth of MCF-7 cells without severe adverse effects on MCF-12A, suggesting that this combination of compounds has promising value in treating breast cancer.

It was proposed that selectivity of our combination treatment is associated with restoration of mitochondrial OXPHOS in tumorigenic MCF-7 cells, which in turn contributes to reactive oxygen species formation and mitochondrial permeabilization. Here, the C9+DCA synergistic effect was tested on tumorigenic MCF-7 and non-tumorigenic MCF-12A cell lines. Cell growth and proliferation was investigated via real-time cell proliferation and crystal violet assays. Cell viability and cytotoxicity were tested by employed lactate dehydrogenase assay kit, as well as Roche xCELLigence real-time cell analyser system. Various morphological techniques such as, light-, fluorescent-, confocal- and transmission electron microscopy were utilized to exam the inter- and intra-cellular morphology changes. Cell cycle analysis, apoptosis quantification, autophagic activity, mitochondrial membrane potential depolarization study, oxidative stress test, Bcl-2 expression and phosphorylation status at S70, executioner caspase 7 quantification and global gene expression analysis via microarray technology were employed to elucidate the mechanism of action of C9+DCA combination treatment (Figure 5.1).

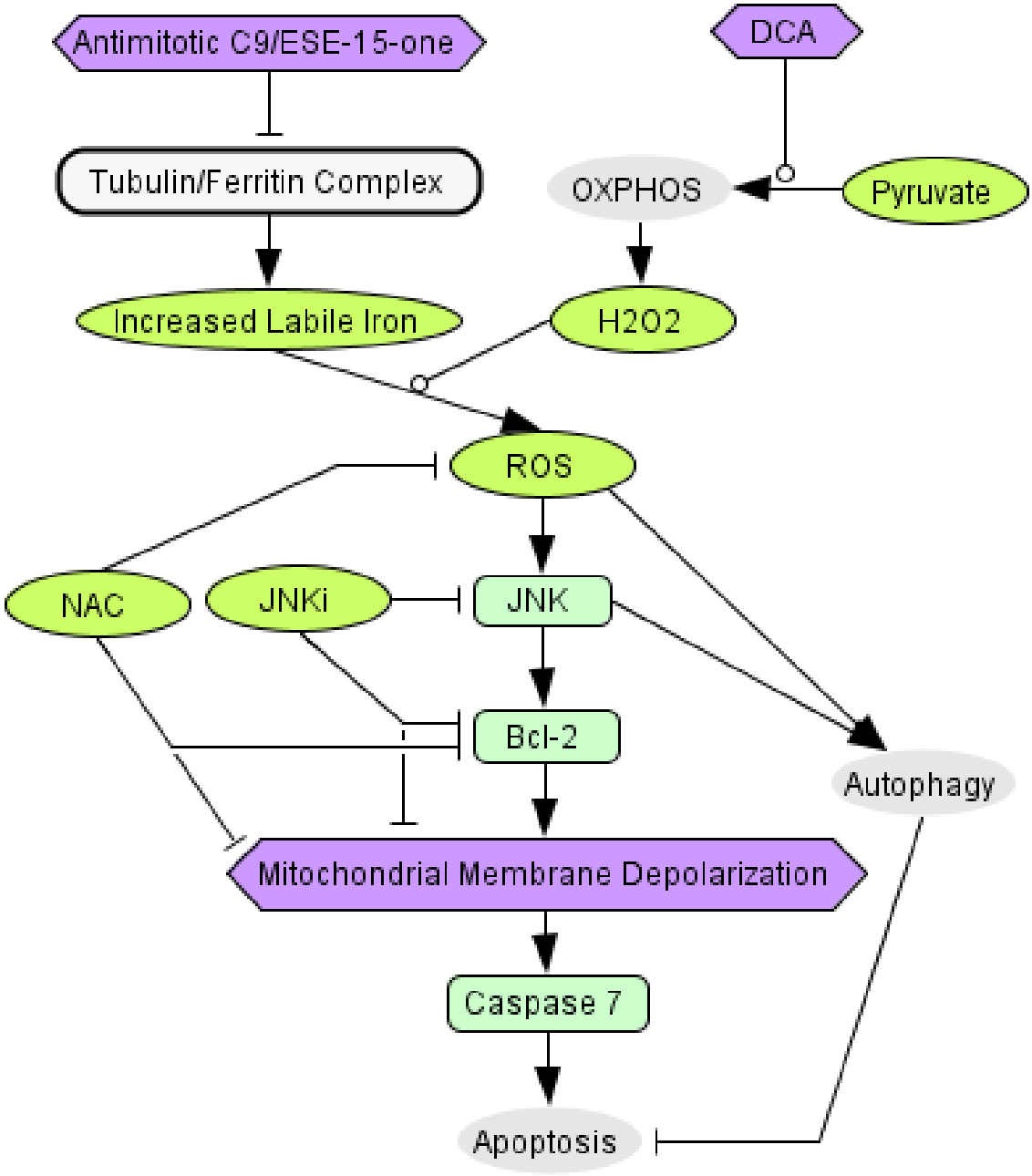

Figure 5.1: Proposed mechanism of action of compound 9 in combination with dichloroacetic acid on breast adenocarcinoma cells. C9+DCA combination treatment increases the formation of ROS which in turn activates JNK, phosphorylating Bcl-2 and results in mitochondrial-mediated induction of caspase 7 activity. Both inhibition of ROS formation (via NAC treatment) and inhibition of JNK result in abrogating the pro-apoptotic effects of C9+DCA. Formation of ROS and JNK activity by C9+DCA treatment can also induce an initial protective effect via autophagy that inhibits late apoptotic events.

In conclusion, the synergistic effect of a novel antimitotic compound in conjunction with DCA on tumorigenic and non-tumorigenic cells was demonstrated for the first time. The novel *in silico*-designed 17β-estradiol derivative C9 in combination with DCA is a potent antiproliferative treatment with properties of selectivity towards tumorigenic cells. This study suggests that the specific combination of DCA and C9 is more harmful for tumorigenic cells than treatment with DCA or C9 alone. Results elucidated the mechanisms of combination treatment at the molecular and cellular level. Future research may now be focused on the development of a viable and functional combination treatment as anticancer agents for clinical trials.

6. References

1. Spessard GO. ACD Labs/LogP dB 3.5 and ChemSketch 3.5. J Chem Inf Comput Sci 1998;38(6):1250-1253.

2. Berridge MJ. Cell Signalling Biology. Portland Press Ltd.; 2012.

3. Hwang D, Rhee SH. Receptor-mediated signaling pathways: potential targets of modulation by dietary fatty acids. Am J Clin Nutr 1999;70(4):545-556.

4. Alberts B, Johnson A, Lewis J, Raff M, Roberts K, Walter P. Molecular Biology of the Cell. New York: Garland Science; 2002.

5. Robinson-Rechavi M, Escriva Garcia H, Laudet V. The nuclear receptor superfamily. J Cell Sci 2003;116(Pt 4):585-586.

6. Maudsley S, Martin B, Luttrell LM. The origins of diversity and specificity in g protein-coupled receptor signaling. J Pharmacol Exp Ther 2005;314(2):485-494.

7. Drake MT, Shenoy SK, Lefkowitz RJ. Trafficking of G protein-coupled receptors. Circ Res 2006;99(6):570-582.

8. Chabre M, le Maire M. Monomeric G-protein-coupled receptor as a functional unit. Biochemistry 2005;44(27):9395-9403.

9. Zhang Z, Melia TJ, He F, Yuan C, McGough A, Schmid MF, et al. How a G protein binds a membrane. J Biol Chem 2004;279(32):33937-33945.

10. Neer EJ. G proteins: critical control points for transmembrane signals. Protein Sci 1994;3(1):3-14.

11. Lodish H, Berk A, Matsudaira P, Kaiser C, Krieger M, Scott MP, et al. Molecular Cell Biology. Sixth ed. New York: W.H.Freeman and Company; 2008.

12. Whittard JD, Akiyama SK. Positive regulation of cell-cell and cell-substrate adhesion by protein kinase A. J Cell Sci 2001;114(Pt 18):3265-3272.

13. Vecchi C, Montosi G, Garuti C, Corradini E, Sabelli M, Canali S, et al. Gluconeogenic signals regulate iron homeostasis via hepcidin in mice. Gastroenterology 2014;146(4):1060-1069.

14. Thiel G, Al Sarraj J, Stefano L. cAMP response element binding protein (CREB) activates transcription via two distinct genetic elements of the human glucose-6-phosphatase gene. BMC Mol Biol 2005;6(1):2.

15. Herzig S, Long F, Jhala US, Hedrick S, Quinn R, Bauer A, et al. CREB regulates hepatic gluconeogenesis through the coactivator PGC-1. Nature 2001;413(6852):179-183.

16. Badeaux AI, Shi Y. Emerging roles for chromatin as a signal integration and storage platform. Nat Rev Mol Cell Biol 2013;14(4):211-224.

17. Pietenpol JA, Stewart ZA. Cell cycle checkpoint signaling: cell cycle arrest versus apoptosis. Toxicology 2002;181-182:475-481.

18. Campbell NA, Reece JB. Biology. 7th ed. San Francisco, CA: Pearson Education, Inc., Benjamin Cummings; 2005. (Chapter 12: The cell cycle).

19. Luch A. Cell cycle control and cell division: implications for chemically induced carcinogenesis. Chembiochem 2002;3(6):506-516.

20. Sherr CJ, Roberts JM. CDK inhibitors: positive and negative regulators of G1-phase progression. Genes Dev 1999;13(12):1501-1512.

21. Lea NC, Orr SJ, Stoeber K, Williams GH, Lam EW-F, Ibrahim MA, et al. Commitment point during G0→ G1 that controls entry into the cell cycle. Mol Cell Biol 2003;23(7):2351-2361.

22. Johnson GL, Lapadat R. Mitogen-activated protein kinase pathways mediated by ERK, JNK, and p38 protein kinases. Science 2002;298(5600):1911-1912.

23. Nelson WJ, Nusse R. Convergence of Wnt, beta-catenin, and cadherin pathways. Science 2004;303(5663):1483-1487.

24. Hawkins PT, Anderson KE, Davidson K, Stephens LR. Signalling through Class I PI3Ks in mammalian cells. Biochem Soc Trans 2006;34(Pt 5):647-662.

25. Orphanides G, Lagrange T, Reinberg D. The general transcription factors of RNA polymerase II. Genes Dev 1996;10(21):2657-2683.

26. Alberts AS, Thorburn AM, Shenolikar S, Mumby MC, Feramisco JR. Regulation of cell cycle progression and nuclear affinity of the retinoblastoma protein by protein phosphatases. Proc Natl Acad Sci U S A 1993;90(2):388-392.

27. Lewis B. Cell Cycle Control in Pancreatic Cancer Pathogenesis. In: Pancreatic Cancer: Springer; 2010. p. 333-367.

28. Depoortere F, Pirson I, Bartek J, Dumont JE, Roger PP. Transforming Growth Factor β1 Selectively Inhibits the Cyclic AMP-dependent Proliferation of Primary Thyroid Epithelial Cells by Preventing the Association of Cyclin D3–cdk4 with Nuclear p27kip1. Mol Biol Cell 2000;11(3):1061-1076.

29. Derynck R, Zhang YE. Smad-dependent and Smad-independent pathways in TGF-beta family signalling. Nature 2003;425(6958):577-584.

30. Taylor WR, Stark GR. Regulation of the G2/M transition by p53. Oncogene 2001;20(15):1803-1815.

31. Liu Q, Hilsenbeck S, Gazitt Y. Arsenic trioxide-induced apoptosis in myeloma cells: p53-dependent G1 or G2/M cell cycle arrest, activation of caspase-8 or caspase-9, and synergy with APO2/TRAIL. Blood 2003;101(10):4078-4087.

32. Crick F. Central dogma of molecular biology. Nature 1970;227(5258):561-563.

33. Pertea M, Salzberg SL. Between a chicken and a grape: estimating the number of human genes. Genome Biol 2010;11(5):206.

34. Russell P. iGenetics: A Molecular Approach. 2nd ed. San Francisco: Pearson Education, Inc. Benjamin Cummings; 2006.

35. Fischer OM, Hart S, Gschwind A, Ullrich A. EGFR signal transactivation in cancer cells. Biochem Soc Trans 2003;31(Pt 6):1203-1208.

36. Schlessinger J. Cell signaling by receptor tyrosine kinases. Cell 2000;103(2):211-225.

37. Yu X, Sharma KD, Takahashi T, Iwamoto R, Mekada E. Ligand-independent dimer formation of epidermal growth factor receptor (EGFR) is a step separable from ligand-induced EGFR signaling. Mol Biol Cell 2002;13(7):2547-2557.

38. Lemmon MA, Schlessinger J. Cell signaling by receptor tyrosine kinases. Cell 2010;141(7):1117-1134.

39. Hubbard SR, Till JH. Protein tyrosine kinase structure and function. Annu Rev Biochem 2000;69:373-398.

40. Lowenstein EJ, Daly RJ, Batzer AG, Li W, Margolis B, Lammers R, et al. The SH2 and SH3 domain-containing protein GRB2 links receptor tyrosine kinases to ras signaling. Cell 1992;70(3):431-442.

41. Lewitzky M, Kardinal C, Gehring NH, Schmidt EK, Konkol B, Eulitz M, et al. The C-terminal SH3 domain of the adapter protein Grb2 binds with high affinity to sequences in Gab1 and SLP-76 which lack the SH3-typical P-x-x-P core motif. Oncogene 2001;20(9):1052-1062.

42. Rodriguez-Viciana P, Sabatier C, McCormick F. Signaling specificity by Ras family GTPases is determined by the full spectrum of effectors they regulate. Mol Cell Biol 2004;24(11):4943-4954.

43. Jun JE, Yang M, Chen H, Chakraborty AK, Roose JP. Activation of extracellular signal-regulated kinase but not of p38 mitogen-activated protein kinase pathways in lymphocytes requires allosteric activation of SOS. Mol Cell Biol 2013;33(12):2470-2484.

44. Locasale JW, Shaw AS, Chakraborty AK. Scaffold proteins confer diverse regulatory properties to protein kinase cascades. Proc Natl Acad Sci U S A 2007;104(33):13307-13312.

45. Kim J, Lee JH, Iyer VR. Global identification of Myc target genes reveals its direct role in mitochondrial biogenesis and its E-box usage in vivo. PLoS One 2008;3(3):e1798.

46. Pelengaris S, Khan M, Evan GI. Suppression of Myc-induced apoptosis in beta cells exposes multiple oncogenic properties of Myc and triggers carcinogenic progression. Cell 2002;109(3):321-334.

47. Adhikary S, Eilers M. Transcriptional regulation and transformation by Myc proteins. Nat Rev Mol Cell Biol 2005;6(8):635-645.

48. Meyer N, Penn LZ. Reflecting on 25 years with MYC. Nat Rev Cancer 2008;8(12):976-990.

49. Ayer DE, Eisenman RN. A switch from Myc:Max to Mad:Max heterocomplexes accompanies monocyte/macrophage differentiation. Genes Dev 1993;7(11):2110-2119.

50. Hooker CW, Hurlin PJ. Of Myc and Mnt. J Cell Sci 2006;119(Pt 2):208-216.

51. Grinberg AV, Hu CD, Kerppola TK. Visualization of Myc/Max/Mad family dimers and the competition for dimerization in living cells. Mol Cell Biol 2004;24(10):4294-4308.

52. Vervoorts J, Luscher-Firzlaff JM, Rottmann S, Lilischkis R, Walsemann G, Dohmann K, et al. Stimulation of c-MYC transcriptional activity and acetylation by recruitment of the cofactor CBP. EMBO Rep 2003;4(5):484-490.

53. Sears R, Nuckolls F, Haura E, Taya Y, Tamai K, Nevins JR. Multiple Ras-dependent phosphorylation pathways regulate Myc protein stability. Genes Dev 2000;14(19):2501-2514.

54. Yeh E, Cunningham M, Arnold H, Chasse D, Monteith T, Ivaldi G, et al. A signalling pathway controlling c-Myc degradation that impacts oncogenic transformation of human cells. Nat Cell Biol 2004;6(4):308-318.

55. Meyerson M, Harlow E. Identification of G1 kinase activity for cdk6, a novel cyclin D partner. Mol Cell Biol 1994;14(3):2077-2086.

56. Ray A, James MK, Larochelle S, Fisher RP, Blain SW. p27Kip1 inhibits cyclin D-cyclin-dependent kinase 4 by two independent modes. Mol Cell Biol 2009;29(4):986-999.

57. Viglietto G, Motti ML, Bruni P, Melillo RM, D'Alessio A, Califano D, et al. Cytoplasmic relocalization and inhibition of the cyclin-dependent kinase inhibitor p27(Kip1) by PKB/Akt-mediated phosphorylation in breast cancer. Nat Med 2002;8(10):1136-1144.

58. Pietenpol JA, Kastan MB. Abeloff's clinical oncology. 4th ed: Churchill Livingstone/Elsevier Philadelphia; 2008. (Chapter 5: Control of the Cell Cycle).

59. Siu KT, Rosner MR, Minella AC. An integrated view of cyclin E function and regulation. Cell Cycle 2012;11(1):57-64.

60. Zhao J, Kennedy BK, Lawrence BD, Barbie DA, Matera AG, Fletcher JA, et al. NPAT links cyclin E-Cdk2 to the regulation of replication-dependent histone gene transcription. Genes Dev 2000;14(18):2283-2297.

61. Tokuyama Y, Horn HF, Kawamura K, Tarapore P, Fukasawa K. Specific phosphorylation of nucleophosmin on Thr199 by cyclin-dependent kinase 2-cyclin E and its role in centrosome duplication. J Biol Chem 2001;276(24):21529-21537.

62. Girard F, Strausfeld U, Fernandez A, Lamb NJC. Cyclin A is required for the onset of DNA replication in mammalian fibroblasts. Cell 1991;67(6):1169-1179.

63. Jinno S, Suto K, Nagata A, Igarashi M, Kanaoka Y, Nojima H, et al. Cdc25A is a novel phosphatase functioning early in the cell cycle. EMBO J 1994;13(7):1549-1556.

64. Hoffmann I, Karsenti E. The role of cdc25 in checkpoints and feedback controls in the eukaryotic cell cycle. J Cell Sci Suppl 1994;18:75-79.

65. Singer JD, Gurian-West M, Clurman B, Roberts JM. Cullin-3 targets cyclin E for ubiquitination and controls S phase in mammalian cells. Genes Dev 1999;13(18):2375-2387.

66. Minella AC, Clurman BE. Mechanisms of tumor suppression by the SCFFbw7. Cell Cycle 2005;4(10):1356-1359.

67. Koepp DM, Schaefer LK, Ye X, Keyomarsi K, Chu C, Harper JW, et al. Phosphorylation-dependent ubiquitination of cyclin E by the SCFFbw7 ubiquitin ligase. Science 2001;294(5540):173-177.

68. Russo AA, Jeffrey PD, Patten AK, Massagué J, Pavletich NP. Crystal structure of the p27Kip1 cyclin-dependent-kinase inhibitor bound to the cyclin A-Cdk2 complex. Nature 1996;382(6589):325-331.

69. Hengst L, Göpfert U, Lashuel HA, Reed SI. Complete inhibition of Cdk/cyclin by one molecule of p21Cip1. Genes Dev 1998;12(24):3882-3888.

70. Serrano M, Hannon GJ, Beach D. A new regulatory motif in cell-cycle control causing specific inhibition of cyclin D/CDK4. Nature 1993;366(6456):704-707.

71. Hannon GJ, Beach D. p15INK4B is a potential effector of TGF-beta-induced cell cycle arrest. Nature 1994;371(6494):257-261.

72. Guan K-L, Jenkins CW, Li Y, Nichols MA, Wu X, O'Keefe CL, et al. Growth suppression by p18, a p16INK4/MTS1-and p14INK4B/MTS2-related CDK6 inhibitor, correlates with wild-type pRb function. Genes Dev 1994;8(24):2939-2952.

73. Hirai H, Roussel MF, Kato JY, Ashmun RA, Sherr CJ. Novel INK4 proteins, p19 and p18, are specific inhibitors of the cyclin D-dependent kinases CDK4 and CDK6. Mol Cell Biol 1995;15(5):2672-2681.

74. Dong Y, Chi SL, Borowsky AD, Fan Y, Weiss RH. Cytosolic p21Waf1/Cip1 increases cell cycle transit in vascular smooth muscle cells. Cell Signal 2004;16(2):263-269.

75. Adkins JN, Lumb KJ. Intrinsic structural disorder and sequence features of the cell cycle inhibitor p57Kip2. Proteins 2002;46(1):1-7.

76. Affolter A, Helmbrecht S, Finger S, Hormann K, Gotte K. Altered expression of cell cycle regulators p21, p27, and p53 in tumors of salivary glands and paranasal sinuses. Oncol Rep 2005;13(6):1089-1094.

77. Coqueret O. New roles for p21 and p27 cell-cycle inhibitors: a function for each cell compartment? Trends Cell Biol 2003;13(2):65-70.

78. Sherr CJ, Weber JD. The ARF/p53 pathway. Curr Opin Genet Dev 2000;10(1):94-99.

79. Serrano M. The INK4a/ARF locus in murine tumorigenesis. Carcinogenesis 2000;21(5):865-869.

80. Quelle DE, Zindy F, Ashmun RA, Sherr CJ. Alternative reading frames of the INK4a tumor suppressor gene encode two unrelated proteins capable of inducing cell cycle arrest. Cell 1995;83(6):993-1000.

81. Zhang XP, Liu F, Wang W. Two-phase dynamics of p53 in the DNA damage response. Proc Natl Acad Sci U S A 2011;108(22):8990-8995.

82. Oliner JD, Pietenpol JA, Thiagalingam S, Gyuris J, Kinzler KW, Vogelstein B. Oncoprotein MDM2 conceals the activation domain of tumour suppressor p53. Nature 1993;362(6423):857-860.

83. Honda R, Tanaka H, Yasuda H. Oncoprotein MDM2 is a ubiquitin ligase E3 for tumor suppressor p53. FEBS Lett 1997;420(1):25-27.

84. Lee J-H, Paull TT. ATM activation by DNA double-strand breaks through the Mre11-Rad50-Nbs1 complex. Science 2005;308(5721):551-554.

85. Zou L, Elledge SJ. Sensing DNA damage through ATRIP recognition of RPA-ssDNA complexes. Science 2003;300(5625):1542-1548.

86. Falck J, Coates J, Jackson SP. Conserved modes of recruitment of ATM, ATR and DNA-PKcs to sites of DNA damage. Nature 2005;434(7033):605-611.

87. Smith J, Tho LM, Xu N, Gillespie DA. The ATM-Chk2 and ATR-Chk1 pathways in DNA damage signaling and cancer. Adv Cancer Res 2010;108:73-112.

88. Yang L, Zhang H-w, Hu R, Yang Y, Qi Q, Lu N, et al. Wogonin induces G1 phase arrest through inhibiting Cdk4 and cyclin D1 concomitant with an elevation in p21Cip1 in human cervical carcinoma HeLa cells. Biochem Cell Biol 2009;87(6):933-942.

89. Leman AR, Noguchi E. The Replication Fork: Understanding the Eukaryotic Replication Machinery and the Challenges to Genome Duplication. Genes (Basel) 2013;4(1):1-32.

90. Woo RA, Poon RY. Cyclin-dependent kinases and S phase control in mammalian cells. Cell Cycle 2003;2(4):316-324.

91. Masai H, Taniyama C, Ogino K, Matsui E, Kakusho N, Matsumoto S, et al. Phosphorylation of MCM4 by Cdc7 kinase facilitates its interaction with Cdc45 on the chromatin. J Biol Chem 2006;281(51):39249-39261.

92. Alani E, Thresher R, Griffith JD, Kolodner RD. Characterization of DNA-binding and strand-exchange stimulation properties of y-RPA, a yeast single-strand-DNA-binding protein. J Mol Biol 1992;227(1):54-71.

93. Squire CJ, Dickson JM, Ivanovic I, Baker EN. Structure and inhibition of the human cell cycle checkpoint kinase, Wee1A kinase: an atypical tyrosine kinase with a key role in CDK1 regulation. Structure 2005;13(4):541-550.

94. Lindqvist A, Rodriguez-Bravo V, Medema RH. The decision to enter mitosis: feedback and redundancy in the mitotic entry network. J Cell Biol 2009;185(2):193-202.

95. Lindqvist A, van Zon W, Karlsson Rosenthal C, Wolthuis RM. Cyclin B1-Cdk1 activation continues after centrosome separation to control mitotic progression. PLoS Biol 2007;5(5):e123.

96. Chow JP, Poon RY, Ma HT. Inhibitory phosphorylation of cyclin-dependent kinase 1 as a compensatory mechanism for mitosis exit. Mol Cell Biol 2011;31(7):1478-1491.

97. Takizawa CG, Morgan DO. Control of mitosis by changes in the subcellular location of cyclin-B1-Cdk1 and Cdc25C. Curr Opin Cell Biol 2000;12(6):658-665.

98. Yu M, Liu X, Cao S, Zhao Z, Zhang K, Xie Q, et al. Identification and characterization of three novel nuclear export signals in the influenza A virus nucleoprotein. J Virol 2012;86(9):4970-4980.

99. Timofeev O, Cizmecioglu O, Settele F, Kempf T, Hoffmann I. Cdc25 phosphatases are required for timely assembly of CDK1-cyclin B at the G2/M transition. J Biol Chem 2010;285(22):16978-16990.

100. Lammer C, Wagerer S, Saffrich R, Mertens D, Ansorge W, Hoffmann I. The cdc25B phosphatase is essential for the G2/M phase transition in human cells. J Cell Sci 1998;111(16):2445-2453.

101. Myer DL, El Mustapha Bahassi PJS. The Plk3-Cdc25 circuit. Oncogene 2005;24(2):299-305.

102. Nigg EA. Cyclin-dependent protein kinases: key regulators of the eukaryotic cell cycle. Bioessays 1995;17(6):471-480.

103. Branzei D, Foiani M. Regulation of DNA repair throughout the cell cycle. Nat Rev Mol Cell Biol 2008;9(4):297-308.

104. Xu B, Kim S-T, Lim D-S, Kastan MB. Two molecularly distinct G2/M checkpoints are induced by ionizing irradiation. Mol Cell Biol 2002;22(4):1049-1059.

105. Canman CE, Lim DS, Cimprich KA, Taya Y, Tamai K, Sakaguchi K, et al. Activation of the ATM kinase by ionizing radiation and phosphorylation of p53. Science 1998;281(5383):1677-1679.

106. Chin CF, Yeong FM. Safeguarding entry into mitosis: the antephase checkpoint. Molecular and cellular biology 2010;30(1):22-32.

107. Lampson MA, Cheeseman IM. Sensing centromere tension: Aurora B and the regulation of kinetochore function. Trends Cell Biol 2011;21(3):133-140.

108. Chan YW, Fava LL, Uldschmid A, Schmitz MH, Gerlich DW, Nigg EA, et al. Mitotic control of kinetochore-associated dynein and spindle orientation by human Spindly. J Cell Biol 2009;185(5):859-874.

109. Min M, Lindon C. Substrate targeting by the ubiquitin-proteasome system in mitosis. Semin Cell Dev Biol 2012;23(5):482-491.

110. Deshaies RJ. SCF and Cullin/Ring H2-based ubiquitin ligases. Annu Rev Cell Dev Biol 1999;15(1):435-467.

111. Morgan DO. Regulation of the APC and the exit from mitosis. Nat Cell Biol 1999;1(2):E47-53.

112. Visintin R, Prinz S, Amon A. CDC20 and CDH1: a family of substrate-specific activators of APC-dependent proteolysis. Science 1997;278(5337):460-463.

113. Kramer ER, Scheuringer N, Podtelejnikov AV, Mann M, Peters JM. Mitotic regulation of the APC activator proteins CDC20 and CDH1. Mol Biol Cell 2000;11(5):1555-1569.

114. Baker JC, Yan X, Peng T, Kasten S, Roche TE. Marked differences between two isoforms of human pyruvate dehydrogenase kinase. J Biol Chem 2000;275(21):15773-15781.

115. Kraft C, Herzog F, Gieffers C, Mechtler K, Hagting A, Pines J, et al. Mitotic regulation of the human anaphase-promoting complex by phosphorylation. EMBO J 2003;22(24):6598-6609.

116. Baker DJ, Dawlaty MM, Galardy P, van Deursen JM. Mitotic regulation of the anaphase-promoting complex. Cell Mol Life Sci 2007;64(5):589-600.

117. Musacchio A, Salmon ED. The spindle-assembly checkpoint in space and time. Nat Rev Mol Cell Biol 2007;8(5):379-393.

118. Lara-Gonzalez P, Westhorpe FG, Taylor SS. The spindle assembly checkpoint. Curr Biol 2012;22(22):R966-980.

119. Murray AW. A brief history of error. Nat Cell Biol 2011;13(10):1178-1182.

120. Stegmeier F, Rape M, Draviam VM, Nalepa G, Sowa ME, Ang XL, et al. Anaphase initiation is regulated by antagonistic ubiquitination and deubiquitination activities. Nature 2007;446(7138):876-881.

121. Hansen DV, Loktev AV, Ban KH, Jackson PK. Plk1 regulates activation of the anaphase promoting complex by phosphorylating and triggering SCFbetaTrCP-dependent destruction of the APC Inhibitor Emi1. Mol Biol Cell 2004;15(12):5623-5634.

122. Chang HY, Levasseur M, Jones KT. Degradation of APCcdc20 and APCcdh1 substrates during the second meiotic division in mouse eggs. J Cell Sci 2004;117(Pt 26):6289-6296.

123. Fulda S, Gorman AM, Hori O, Samali A. Cellular stress responses: cell survival and cell death. Int J Cell Biol 2010;2010:214074.

124. Hochwagen A, Amon A. Checking your breaks: surveillance mechanisms of meiotic recombination. Curr Biol 2006;16(6):R217-228.

125. Elmore S. Apoptosis: a review of programmed cell death. Toxicol Pathol 2007;35(4):495-516.

126. De Duve C, Baudhuin P. Peroxisomes (microbodies and related particles). Physiol Rev 1966;46(2):323-357.

127. De Duve C, Wattiaux R. Functions of lysosomes. Annu Rev Physiol 1966;28(1):435-492.

128. Lockshin RA, Zakeri Z. Programmed cell death and apoptosis: origins of the theory. Nat Rev Mol Cell Biol 2001;2(7):545-550.

129. Kerr JF, Wyllie AH, Currie AR. Apoptosis: a basic biological phenomenon with wide-ranging implications in tissue kinetics. Br J Cancer 1972;26(4):239-257.

130. Sulston JE, Horvitz HR. Post-embryonic cell lineages of the nematode, *Caenorhabditis elegans.* Dev Biol 1977;56(1):110-156.

131. Formigli L, Papucci L, Tani A, Schiavone N, Tempestini A, Orlandini GE, et al. Aponecrosis: morphological and biochemical exploration of a syncretic process of cell death sharing apoptosis and necrosis. J Cell Physiol 2000;182(1):41-49.

132. Sperandio S, de Belle I, Bredesen DE. An alternative, nonapoptotic form of programmed cell death. Proc Natl Acad Sci U S A 2000;97(26):14376-14381.

133. Dixon SJ, Lemberg KM, Lamprecht MR, Skouta R, Zaitsev EM, Gleason CE, et al. Ferroptosis: an iron-dependent form of nonapoptotic cell death. Cell 2012;149(5):1060-1072.

134. Saraste A, Pulkki K. Morphologic and biochemical hallmarks of apoptosis. Cardiovasc Res 2000;45(3):528-537.

135. Fischer A, Jacobson K, Rose J, Zeller R. Preparation of cells and tissues for fluorescence microscopy. In: Goldman Sa, editor. Basic Methods in Microscopy Cold Spring Harbor, NY, USA.: Cold Spring Harbor Laboratory Press; 2006.

136. Dinsdale D, Zhuang J, Cohen GM. Redistribution of Cytochrome< i> c</i> Precedes the Caspase-Dependent Formation of Ultracondensed Mitochondria, with a Reduced Inner Membrane Potential, in Apoptotic Monocytes. The American journal of pathology 1999;155(2):607-618.

137. Hengartner MO. The biochemistry of apoptosis. Nature 2000;407(6805):770-776.

138. Peter ME, Krammer PH. Mechanisms of CD95 (APO-1/Fas)-mediated apoptosis. Curr Opin Immunol 1998;10(5):545-551.

139. Bialik S, Zalckvar E, Ber Y, Rubinstein AD, Kimchi A. Systems biology analysis of programmed cell death. Trends Biochem Sci 2010;35(10):556-564.

140. Green DR, Reed JC. Mitochondria and apoptosis. Science 1998;281(5381):1309-1311.

141. Assuncao Guimaraes C, Linden R. Programmed cell deaths. Apoptosis and alternative deathstyles. Eur J Biochem 2004;271(9):1638-1650.

142. Terman A, Kurz T. Lysosomal iron, iron chelation, and cell death. Antioxid Redox Signal 2013;18(8):888-898.

143. Sakamaki K, Satou Y. Caspases: evolutionary aspects of their functions in vertebrates. J Fish Biol 2009;74(4):727-753.

144. Li J, Yuan J. Caspases in apoptosis and beyond. Oncogene 2008;27(48):6194-6206.

145. Zou H, Li Y, Liu X, Wang X. An APAF-1· cytochrome c multimeric complex is a functional apoptosome that activates procaspase-9. J Biol Chem 1999;274(17):11549-11556.

146. Chang HY, Yang X. Proteases for cell suicide: functions and regulation of caspases. Microbiol Mol Biol Rev 2000;64(4):821-846.

147. Huang Q, Li F, Liu X, Li W, Shi W, Liu FF, et al. Caspase 3-mediated stimulation of tumor cell repopulation during cancer radiotherapy. Nat Med 2011;17(7):860-866.

148. Hail Jr N, Carter B, Konopleva M. Apoptosis effector mechanisms: a requiem performed in different keys. Apoptosis 2006;11(6):889-904.

149. Bajt ML, Ramachandran A, Yan HM, Lebofsky M, Farhood A, Lemasters JJ, et al. Apoptosis-inducing factor modulates mitochondrial oxidant stress in acetaminophen hepatotoxicity. Toxicol Sci 2011;122(2):598-605.

150. Apostolov EO, Ray D, Alobuia WM, Mikhailova MV, Wang X, Basnakian AG, et al. Endonuclease G mediates endothelial cell death induced by carbamylated LDL. Am J Physiol Heart Circ Physiol 2011;300(6):H1997-2004.

151. Joza N, Susin SA, Daugas E, Stanford WL, Cho SK, Li CY, et al. Essential role of the mitochondrial apoptosis-inducing factor in programmed cell death. Nature 2001;410(6828):549-554.

152. Li LY, Luo X, Wang X. Endonuclease G is an apoptotic DNase when released from mitochondria. Nature 2001;412(6842):95-99.

153. Chwieralski CE, Welte T, Buhling F. Cathepsin-regulated apoptosis. Apoptosis 2006;11(2):143-149.

154. Sorimachi H, Ishiura S, Suzuki K. Structure and physiological function of calpains. Biochem J 1997;328 (Pt 3):721-732.

155. Nakagawa T, Yuan J. Cross-talk between two cysteine protease families activation of caspase-12 by calpain in apoptosis. J Cell Biol 2000;150(4):887-894.

156. Sharif-Askari E, Alam A, Rheaume E, Beresford PJ, Scotto C, Sharma K, et al. Direct cleavage of the human DNA fragmentation factor-45 by granzyme B induces caspase-activated DNase release and DNA fragmentation. EMBO J 2001;20(12):3101-3113.

157. Heibein JA, Goping S, Barry M, Pinkoski MJ, Shore GC, Green DR, et al. Granzyme B–mediated cytochrome c release is regulated by the Bcl-2 family members bid and Bax. J Exp Med 2000;192(10):1391-1402.

158. Rubio-Moscardo F, Blesa D, Mestre C, Siebert R, Balasas T, Benito A, et al. Characterization of 8p21.3 chromosomal deletions in B-cell lymphoma: TRAIL-R1 and TRAIL-R2 as candidate dosage-dependent tumor suppressor genes. Blood 2005;106(9):3214-3222.

159. Suliman A, Lam A, Datta R, Srivastava RK. Intracellular mechanisms of TRAIL: apoptosis through mitochondrial-dependent and -independent pathways. Oncogene 2001;20(17):2122-2133.

160. Lavrik I, Golks A, Krammer PH. Death receptor signaling. J Cell Sci 2005;118(Pt 2):265-267.

161. Sprick MR, Weigand MA, Rieser E, Rauch CT, Juo P, Blenis J, et al. FADD/MORT1 and caspase-8 are recruited to TRAIL receptors 1 and 2 and are essential for apoptosis mediated by TRAIL receptor 2. Immunity 2000;12(6):599-609.

162. Wajant H. The Fas signaling pathway: more than a paradigm. Science 2002;296(5573):1635-1636.

163. Rastogi RP, Sinha RP. Apoptosis: molecular mechanisms and pathogenicity. EXCIL Journal 2009;8:155-181.

164. Riedl SJ, Shi Y. Molecular mechanisms of caspase regulation during apoptosis. Nat Rev Mol Cell Biol 2004;5(11):897-907.

165. Safa AR. c-FLIP, a master anti-apoptotic regulator. Exp Oncol 2012;34(3):176-184.

166. Scaffidi C, Fulda S, Srinivasan A, Friesen C, Li F, Tomaselli KJ, et al. Two CD95 (APO-1/Fas) signaling pathways. EMBO J 1998;17(6):1675-1687.

167. Li H, Zhu H, Xu C-j, Yuan J. Cleavage of BID by caspase 8 mediates the mitochondrial damage in the Fas pathway of apoptosis. Cell 1998;94(4):491-501.

168. Kischkel FC, Hellbardt S, Behrmann I, Germer M, Pawlita M, Krammer PH, et al. Cytotoxicity-dependent APO-1 (Fas/CD95)-associated proteins form a death-inducing signaling complex (DISC) with the receptor. EMBO J 1995;14(22):5579-5588.

169. Tobiume K, Matsuzawa A, Takahashi T, Nishitoh H, Morita K, Takeda K, et al. ASK1 is required for sustained activations of JNK/p38 MAP kinases and apoptosis. EMBO Rep 2001;2(3):222-228.

170. Kavuri SM, Geserick P, Berg D, Dimitrova DP, Feoktistova M, Siegmund D, et al. Cellular FLICE-inhibitory protein (cFLIP) isoforms block CD95- and TRAIL death receptor-induced gene induction irrespective of processing of caspase-8 or cFLIP in the death-inducing signaling complex. J Biol Chem 2011;286(19):16631-16646.

171. Green DR, Kroemer G. The pathophysiology of mitochondrial cell death. Science 2004;305(5684):626-629.

172. Saelens X, Festjens N, Vande Walle L, van Gurp M, van Loo G, Vandenabeele P. Toxic proteins released from mitochondria in cell death. Oncogene 2004;23(16):2861-2874.

173. Riedl SJ, Salvesen GS. The apoptosome: signalling platform of cell death. Nat Rev Mol Cell Biol 2007;8(5):405-413.

174. Orrenius S, Gogvadze V, Zhivotovsky B. Mitochondrial oxidative stress: implications for cell death. Annu Rev Pharmacol Toxicol 2007;47:143-183.

175. Fletcher JI, Meusburger S, Hawkins CJ, Riglar DT, Lee EF, Fairlie WD, et al. Apoptosis is triggered when prosurvival Bcl-2 proteins cannot restrain Bax. Proc Natl Acad Sci U S A 2008;105(47):18081-18087.

176. Ito T, Deng X, Carr B, May WS. Bcl-2 phosphorylation required for anti-apoptosis function. J Biol Chem 1997;272(18):11671-11673.

177. Lewis A, Hayashi T, Su TP, Betenbaugh MJ. Bcl-2 family in inter-organelle modulation of calcium signaling; roles in bioenergetics and cell survival. J Bioenerg Biomembr 2013

178. Mendes CC, Gomes DA, Thompson M, Souto NC, Goes TS, Goes AM, et al. The type III inositol 1, 4, 5-trisphosphate receptor preferentially transmits apoptotic Ca2+ signals into mitochondria. J Biol Chem 2005;280(49):40892-40900.

179. Chen R, Valencia I, Zhong F, McColl KS, Roderick HL, Bootman MD, et al. Bcl-2 functionally interacts with inositol 1,4,5-trisphosphate receptors to regulate calcium release from the ER in response to inositol 1,4,5-trisphosphate. J Cell Biol 2004;166(2):193-203.

180. Vanden Abeele F, Skryma R, Shuba Y, Van Coppenolle F, Slomianny C, Roudbaraki M, et al. Bcl-2-dependent modulation of Ca(2+) homeostasis and store-operated channels in prostate cancer cells. Cancer Cell 2002;1(2):169-179.

181. Giorgio V, von Stockum S, Antoniel M, Fabbro A, Fogolari F, Forte M, et al. Dimers of mitochondrial ATP synthase form the permeability transition pore. Proc Natl Acad Sci U S A 2013;110(15):5887-5892.

182. Yen TC, Wey SP, Liao CH, Yeh CH, Shen DW, Achilefu S, et al. Measurement of the binding parameters of annexin derivative-erythrocyte membrane interactions. Anal Biochem 2010;406(1):70-79.

183. Martin SJ, Reutelingsperger CP, McGahon AJ, Rader JA, van Schie RC, LaFace DM, et al. Early redistribution of plasma membrane phosphatidylserine is a general feature of apoptosis regardless of the initiating stimulus: inhibition by overexpression of Bcl-2 and Abl. J Exp Med 1995;182(5):1545-1556.

184. Koopman G, Reutelingsperger CP, Kuijten GA, Keehnen RM, Pals ST, van Oers MH. Annexin V for flow cytometric detection of phosphatidylserine expression on B cells undergoing apoptosis. Blood 1994;84(5):1415-1420.

185. Tait JF, Gibson D. Phospholipid binding of annexin V: effects of calcium and membrane phosphatidylserine content. Arch Biochem Biophys 1992;298(1):187-191.

186. Wong JY, Huggins GS, Debidda M, Munshi NC, De Vivo I. Dichloroacetate induces apoptosis in endometrial cancer cells. Gynecol Oncol 2008;109(3):394-402.

187. Stander BA, Joubert F, Tu C, Sippel KH, McKenna R, Joubert AM. Signaling Pathways of ESE-16, an Antimitotic and Anticarbonic Anhydrase Estradiol Analog, in Breast Cancer Cells. PLoS One 2013;8(1):e53853.

188. Glick D, Barth S, Macleod KF. Autophagy: cellular and molecular mechanisms. J Pathol 2010;221(1):3-12.

189. Levine B, Kroemer G. Autophagy in aging, disease and death: the true identity of a cell death impostor. Cell Death Differ 2009;16(1):1-2.

190. Wang CW, Klionsky DJ. The molecular mechanism of autophagy. Mol Med 2003;9(3-4):65-76.

191. Jung CH, Ro SH, Cao J, Otto NM, Kim DH. mTOR regulation of autophagy. FEBS Lett 2010;584(7):1287-1295.

192. Pattingre S, Tassa A, Qu X, Garuti R, Liang XH, Mizushima N, et al. Bcl-2 antiapoptotic proteins inhibit Beclin 1-dependent autophagy. Cell 2005;122(6):927-939.

193. Clarke PG. Developmental cell death: morphological diversity and multiple mechanisms. Anat Embryol (Berl) 1990;181(3):195-213.

194. Eskelinen EL, Saftig P. Autophagy: a lysosomal degradation pathway with a central role in health and disease. Biochim Biophys Acta 2009;1793(4):664-673.

195. Zoncu R, Efeyan A, Sabatini DM. mTOR: from growth signal integration to cancer, diabetes and ageing. Nat Rev Mol Cell Biol 2011;12(1):21-35.

196. Hara K, Maruki Y, Long X, Yoshino K, Oshiro N, Hidayat S, et al. Raptor, a binding partner of target of rapamycin (TOR), mediates TOR action. Cell 2002;110(2):177-189.

197. Sarbassov DD, Guertin DA, Ali SM, Sabatini DM. Phosphorylation and regulation of Akt/PKB by the rictor-mTOR complex. Science 2005;307(5712):1098-1101.

198. Arsham AM, Neufeld TP. Thinking globally and acting locally with TOR. Curr Opin Cell Biol 2006;18(6):589-597.

199. Ma L, Chen Z, Erdjument-Bromage H, Tempst P, Pandolfi PP. Phosphorylation and functional inactivation of TSC2 by Erk implications for tuberous sclerosis and cancer pathogenesis. Cell 2005;121(2):179-193.

200. Cybulski N, Hall MN. TOR complex 2: a signaling pathway of its own. Trends Biochem Sci 2009;34(12):620-627.

201. Gozuacik D, Kimchi A. Autophagy and cell death. Curr Top Dev Biol 2007;78:217-245.

202. Shen X, Xi G, Radhakrishnan Y, Clemmons DR. PDK1 recruitment to the SHPS-1 signaling complex enhances insulin-like growth factor-i-stimulated AKT activation and vascular smooth muscle cell survival. J Biol Chem 2010;285(38):29416-29424.

203. Medina JsR. Selective 3-Phosphoinositide-Dependent Kinase 1 (PDK1) Inhibitors: Dissecting the Function and Pharmacology of PDK1: Miniperspective. J Med Chem 2013;56(7):2726-2737.

204. Yung HW, Charnock-Jones DS, Burton GJ. Regulation of AKT phosphorylation at Ser473 and Thr308 by endoplasmic reticulum stress modulates substrate specificity in a severity dependent manner. PloS One 2011;6(3):e17894.

205. Xiao L, Gong LL, Yuan D, Deng M, Zeng XM, Chen LL, et al. Protein phosphatase-1 regulates Akt1 signal transduction pathway to control gene expression, cell survival and differentiation. Cell Death Differ 2010;17(9):1448-1462.

206. Inoki K, Ouyang H, Zhu T, Lindvall C, Wang Y, Zhang X, et al. TSC2 integrates Wnt and energy signals via a coordinated phosphorylation by AMPK and GSK3 to regulate cell growth. Cell 2006;126(5):955-968.

207. Gwinn DM, Shackelford DB, Egan DF, Mihaylova MM, Mery A, Vasquez DS, et al. AMPK phosphorylation of raptor mediates a metabolic checkpoint. Mol Cell 2008;30(2):214-226.

208. Schwarzer R, Tondera D, Arnold W, Giese K, Klippel A, Kaufmann J. REDD1 integrates hypoxia-mediated survival signaling downstream of phosphatidylinositol 3-kinase. Oncogene 2005;24(7):1138-1149.

209. Efeyan A, Zoncu R, Sabatini DM. Amino acids and mTORC1: from lysosomes to disease. Trends Mol Med 2012;18(9):524-533.

210. Pous C, Codogno P. Lysosome positioning coordinates mTORC1 activity and autophagy. Nat Cell Biol 2011;13(4):342-344.

211. Alexander A, Cai SL, Kim J, Nanez A, Sahin M, MacLean KH, et al. ATM signals to TSC2 in the cytoplasm to regulate mTORC1 in response to ROS. Proc Natl Acad Sci U S A 2010;107(9):4153-4158.

212. Alexander A, Kim J, Walker CL. ATM engages the TSC2/mTORC1 signaling node to regulate autophagy. Autophagy 2010;6(5):672-673.

213. Zhang J, Kim J, Alexander A, Cai S, Tripathi DN, Dere R, et al. A tuberous sclerosis complex signalling node at the peroxisome regulates mTORC1 and autophagy in response to ROS. Nat Cell Biol 2013;15(10):1186-1196.

214. Coevoets R, Arican S, Hoogeveen-Westerveld M, Simons E, van den Ouweland A, Halley D, et al. A reliable cell-based assay for testing unclassified TSC2 gene variants. Eur J Hum Genet 2009;17(3):301-310.

215. Ma XM, Blenis J. Molecular mechanisms of mTOR-mediated translational control. Nat Rev Mol Cell Biol 2009;10(5):307-318.

216. Laplante M, Sabatini DM. An emerging role of mTOR in lipid biosynthesis. Curr Biol 2009;19(22):R1046-1052.

217. Jewell JL, Russell RC, Guan KL. Amino acid signalling upstream of mTOR. Nat Rev Mol Cell Biol 2013;14(3):133-139.

218. Hayashi-Nishino M, Fujita N, Noda T, Yamaguchi A, Yoshimori T, Yamamoto A. A subdomain of the endoplasmic reticulum forms a cradle for autophagosome formation. Nat Cell Biol 2009;11(12):1433-1437.

219. Hara T, Takamura A, Kishi C, Iemura S-i, Natsume T, Guan J-L, et al. FIP200, a ULK-interacting protein, is required for autophagosome formation in mammalian cells. J Cell Biol 2008;181(3):497-510.

220. Yang Z, Klionsky DJ. Mammalian autophagy: core molecular machinery and signaling regulation. Curr Opin Cell Biol 2010;22(2):124-131.

221. Matsunaga K, Saitoh T, Tabata K, Omori H, Satoh T, Kurotori N, et al. Two Beclin 1-binding proteins, Atg14L and Rubicon, reciprocally regulate autophagy at different stages. Nat Cell Biol 2009;11(4):385-396.

222. Russell RC, Tian Y, Yuan H, Park HW, Chang YY, Kim J, et al. ULK1 induces autophagy by phosphorylating Beclin-1 and activating VPS34 lipid kinase. Nat Cell Biol 2013;15(7):741-750.

223. Mizushima N, Komatsu M. Autophagy: renovation of cells and tissues. Cell 2011;147(4):728-741.

224. Mizushima N, Yoshimori T, Levine B. Methods in mammalian autophagy research. Cell 2010;140(3):313-326.

225. Li WW, Li J, Bao JK. Microautophagy: lesser-known self-eating. Cell Mol Life Sci 2012;69(7):1125-1136.

226. Mijaljica D, Prescott M, Devenish RJ. Microautophagy in mammalian cells: revisiting a 40-year-old conundrum. Autophagy 2011;7(7):673-682.

227. de Waal EJ, Vreeling-Sindelarova H, Schellens JP, Houtkooper JM, James J. Quantitative changes in the lysosomal vacuolar system of rat hepatocytes during short-term starvation. A morphometric analysis with special reference to macro- and microautophagy. Cell Tissue Res 1986;243(3):641-648.

228. Sakai M, Araki N, Ogawa K. Lysosomal movements during heterophagy and autophagy: with special reference to nematolysosome and wrapping lysosome. J Electron Microsc Tech 1989;12(2):101-131.

229. Todde V, Veenhuis M, van der Klei IJ. Autophagy: principles and significance in health and disease. Biochim Biophys Acta 2009;1792(1):3-13.

230. Uttenweiler A, Schwarz H, Mayer A. Microautophagic vacuole invagination requires calmodulin in a Ca2+-independent function. J Biol Chem 2005;280(39):33289-33297.

231. Muller O, Sattler T, Flotenmeyer M, Schwarz H, Plattner H, Mayer A. Autophagic tubes: vacuolar invaginations involved in lateral membrane sorting and inverse vesicle budding. J Cell Biol 2000;151(3):519-528.

232. Sattler T, Mayer A. Cell-free reconstitution of microautophagic vacuole invagination and vesicle formation. J Cell Biol 2000;151(3):529-538.

233. Neff NT, Bourret L, Miao P, Dice JF. Degradation of proteins microinjected into IMR-90 human diploid fibroblasts. J Cell Biol 1981;91(1):184-194.

234. Orenstein SJ, Cuervo AM. Chaperone-mediated autophagy: molecular mechanisms and physiological relevance. Semin Cell Dev Biol 2010;21(7):719-726.

235. Kaushik S, Bandyopadhyay U, Sridhar S, Kiffin R, Martinez-Vicente M, Kon M, et al. Chaperone-mediated autophagy at a glance. J Cell Sci 2011;124(4):495-499.

236. Majeski AE, Dice JF. Mechanisms of chaperone-mediated autophagy. Int J Biochem Cell Biol 2004;36(12):2435-2444.

237. Su M, Mei Y, Sinha S. Role of the Crosstalk between Autophagy and Apoptosis in Cancer. J Oncol 2013;2013:102735

238. Eisenberg-Lerner A, Bialik S, Simon H, Kimchi A. Life and death partners: apoptosis, autophagy and the cross-talk between them. Cell Death Differ 2009;16(7):966-975.

239. Platini F, Perez-Tomas R, Ambrosio S, Tessitore L. Understanding autophagy in cell death control. Curr Pharm Des 2010;16(1):101-113.

240. Yang ZJ, Chee CE, Huang S, Sinicrope FA. The role of autophagy in cancer: therapeutic implications. Mol Cancer Ther 2011;10(9):1533-1541.

241. Keller CW, Fokken C, Turville SG, Lunemann A, Schmidt J, Munz C, et al. TNF-alpha induces macroautophagy and regulates MHC class II expression in human skeletal muscle cells. J Biol Chem 2011;286(5):3970-3980.

242. He W, Wang Q, Xu J, Xu X, Padilla MT, Ren G, et al. Attenuation of TNFSF10/TRAIL-induced apoptosis by an autophagic survival pathway involving TRAF2- and RIPK1/RIP1-mediated MAPK8/JNK activation. Autophagy 2012;8(12):1811-1821.

243. Pyo J-O, Jang M-H, Kwon Y-K, Lee H-J, Jun J-I, Woo H-N, et al. Essential roles of Atg5 and FADD in autophagic cell death dissection of autophagic cell death into vacuole formation and cell death. J Biol Chem 2005;280(21):20722-20729.

244. Akar U, Chaves-Reyez A, Barria M, Tari A, Sanguino A, Kondo Y, et al. Silencing of Bcl-2 expression by small interfering RNA induces autophagic cell death in MCF-7 breast cancer cells. Autophagy 2008;4(5):669-679.

245. Sun Y, Liu JH, Jin L, Lin SM, Yang Y, Sui YX, et al. Over-expression of the Beclin1 gene upregulates chemosensitivity to anti-cancer drugs by enhancing

therapy-induced apoptosis in cervix squamous carcinoma CaSki cells. Cancer Lett 2010;294(2):204-210.

246. Oltersdorf T, Elmore SW, Shoemaker AR, Armstrong RC, Augeri DJ, Belli BA, et al. An inhibitor of Bcl-2 family proteins induces regression of solid tumours. Nature 2005;435(7042):677-681.

247. Maiuri MC, Le Toumelin G, Criollo A, Rain J-C, Gautier F, Juin P, et al. Functional and physical interaction between Bcl-XL and a BH3-like domain in Beclin-1. EMBO J 2007;26(10):2527-2539.

248. Wei Y, Sinha S, Levine B. Dual role of JNK1-mediated phosphorylation of Bcl-2 in autophagy and apoptosis regulation. Autophagy 2008;4(7):949-951.

249. Wei Y, Pattingre S, Sinha S, Bassik M, Levine B. JNK1-mediated phosphorylation of Bcl-2 regulates starvation-induced autophagy. Mol Cell 2008;30(6):678-688.

250. Ventura JJ, Hubner A, Zhang C, Flavell RA, Shokat KM, Davis RJ. Chemical genetic analysis of the time course of signal transduction by JNK. Mol Cell 2006;21(5):701-710.

251. Weston CR, Davis RJ. The JNK signal transduction pathway. Curr Opin Cell Biol 2007;19(2):142-149.

252. Haldar S, Chintapalli J, Croce CM. Taxol induces bcl-2 phosphorylation and death of prostate cancer cells. Cancer Res 1996;56(6):1253-1255.

253. He C, Bassik MC, Moresi V, Sun K, Wei Y, Zou Z, et al. Exercise-induced BCL2-regulated autophagy is required for muscle glucose homeostasis. Nature 2012;481(7382):511-515.

254. Davis RJ. Signal transduction by the JNK group of MAP kinases. In: Gordon L, Morgan D, editors. Inflammatory Processes: Molecular Mechanisms and Therapeutic Opportunities: Springer; 2000. p. 13-21.

255. Yujiri T, Sather S, Fanger GR, Johnson GL. Role of MEKK1 in cell survival and activation of JNK and ERK pathways defined by targeted gene disruption. Science 1998;282(5395):1911-1914.

256. Yujiri T, Ware M, Widmann C, Oyer R, Russell D, Chan E, et al. MEK kinase 1 gene disruption alters cell migration and c-Jun NH2-terminal kinase regulation but does not cause a measurable defect in NF-κB activation. Proc Natl Acad Sci U S A 2000;97(13):7272-7277.

257. Yeh W-C, Shahinian A, Speiser D, Kraunus J, Billia F, Wakeham A, et al. Early lethality, functional NF-κB activation, and increased sensitivity to TNF-induced cell death in TRAF2-deficient mice. Immunity 1997;7(5):715-725.

258. Baud V, Liu Z-G, Bennett B, Suzuki N, Xia Y, Karin M. Signaling by proinflammatory cytokines: oligomerization of TRAF2 and TRAF6 is sufficient for

JNK and IKK activation and target gene induction via an amino-terminal effector domain. Genes Dev 1999;13(10):1297-1308.

259. Nishitoh H, Matsuzawa A, Tobiume K, Saegusa K, Takeda K, Inoue K, et al. ASK1 is essential for endoplasmic reticulum stress-induced neuronal cell death triggered by expanded polyglutamine repeats. Genes Dev 2002;16(11):1345-1355.

260. Sakon S, Xue X, Takekawa M, Sasazuki T, Okazaki T, Kojima Y, et al. NF-κB inhibits TNF-induced accumulation of ROS that mediate prolonged MAPK activation and necrotic cell death. EMBO J 2003;22(15):3898-3909.

261. Lamb JA, Ventura JJ, Hess P, Flavell RA, Davis RJ. JunD mediates survival signaling by the JNK signal transduction pathway. Mol Cell 2003;11(6):1479-1489.

262. Ventura JJ, Cogswell P, Flavell RA, Baldwin AS, Jr., Davis RJ. JNK potentiates TNF-stimulated necrosis by increasing the production of cytotoxic reactive oxygen species. Genes Dev 2004;18(23):2905-2915.

263. Sui X, Jin L, Huang X, Geng S, He C, Hu X. p53 signaling and autophagy in cancer: a revolutionary strategy could be developed for cancer treatment. Autophagy 2011;7(6):565-571.

264. Crighton D, Wilkinson S, Ryan KM. DRAM links autophagy to p53 and programmed cell death. Autophagy 2007;3(1):72-74.

265. Feng Z. p53 regulation of the IGF-1/AKT/mTOR pathways and the endosomal compartment. Cold Spring Harb Perspect Biol 2010;2(2):a001057.

266. Lowe J, Shatz M, Resnick M, Menendez D. Modulation of immune responses by the tumor suppressor p53. BioDiscovery 2013;8(8)

267. Muller M, Wilder S, Bannasch D, Israeli D, Lehlbach K, Li-Weber M, et al. p53 activates the CD95 (APO-1/Fas) gene in response to DNA damage by anticancer drugs. J Exp Med 1998;188(11):2033-2045.

268. Wu GS, Burns TF, McDonald 3rd E, Meng RD, Kao G, Muschel R, et al. Induction of the TRAIL receptor KILLER/DR5 in p53-dependent apoptosis but not growth arrest. Oncogene 1999;18(47):6411-6418.

269. Reuter S, Eifes S, Dicato M, Aggarwal BB, Diederich M. Modulation of anti-apoptotic and survival pathways by curcumin as a strategy to induce apoptosis in cancer cells. Biochem Pharmacol 2008;76(11):1340-1351.

270. Moll UM, Wolff S, Speidel D, Deppert W. Transcription-independent pro-apoptotic functions of p53. Curr Opin Cell Biol 2005;17(6):631-636.

271. Jing L, Anning L. Role of JNK activation in apoptosis: a double-edged sword. Cell Res 2005;15(1):36-42.

272. Freinbichler W, Colivicchi MA, Stefanini C, Bianchi L, Ballini C, Misini B, et al. Highly reactive oxygen species: detection, formation, and possible functions. Cellular and Molecular Life Sciences 2011;68(12):2067-2079.

273. Culotta VC, Yang M, O'Halloran TV. Activation of superoxide dismutases: putting the metal to the pedal. Biochim Biophys Acta 2006;1763(7):747-758.

274. Galaris D, Pantopoulos K. Oxidative stress and iron homeostasis: mechanistic and health aspects. Crit Rev Clin Lab Sci 2008;45(1):1-23.

275. Adam-Vizi V, Chinopoulos C. Bioenergetics and the formation of mitochondrial reactive oxygen species. Trends Pharmacol Sci 2006;27(12):639-645.

276. St-Pierre J, Buckingham JA, Roebuck SJ, Brand MD. Topology of superoxide production from different sites in the mitochondrial electron transport chain. J Biol Chem 2002;277(47):44784-44790.

277. Giorgio M, Trinei M, Migliaccio E, Pelicci PG. Hydrogen peroxide: a metabolic by-product or a common mediator of ageing signals? Nature Reviews Molecular Cell Biology 2007;8(9):722-728.

278. Ray PD, Huang B-W, Tsuji Y. Reactive oxygen species (ROS) homeostasis and redox regulation in cellular signaling. Cellular signalling 2012;24(5):981-990.

279. Valko M, Leibfritz D, Moncol J, Cronin MT, Mazur M, Telser J. Free radicals and antioxidants in normal physiological functions and human disease. The international journal of biochemistry & cell biology 2007;39(1):44-84.

280. Katz M, Amit I, Yarden Y. Regulation of MAPKs by growth factors and receptor tyrosine kinases. Biochimica et Biophysica Acta 2007;1773(8):1161-1176.

281. McCubrey JA, Steelman LS, Chappell WH, Abrams SL, Wong EW, Chang F, et al. Roles of the Raf/MEK/ERK pathway in cell growth, malignant transformation and drug resistance. Biochimica et Biophysica Acta 2007;1773(8):1263-1284.

282. Fujino G, Noguchi T, Takeda K, Ichijo H. Thioredoxin and protein kinases in redox signaling. Semin Cancer Biol 2006;16(6):427-435.

283. Matsuzawa A, Ichijo H. Redox control of cell fate by MAP kinase: physiological roles of ASK1-MAP kinase pathway in stress signaling. Biochimica et Biophysica Acta 2008;1780(11):1325-1336.

284. Droge W. Free radicals in the physiological control of cell function. Physiol Rev 2002;82(1):47-95.

285. Valko M, Rhodes CJ, Moncol J, Izakovic M, Mazur M. Free radicals, metals and antioxidants in oxidative stress-induced cancer. Chem Biol Interact 2006;160(1):1-40.

286. Arner ES, Holmgren A. The thioredoxin system in cancer. Seminars in cancer biology 2006;16(6):420-426.

287. Lyakhovich VV, Vavilin VA, Zenkov NK, Menshchikova EB. Active defense under oxidative stress. The antioxidant responsive element. Biochemistry (Mosc) 2006;71(9):962-974.

288. Dickinson DA, Forman HJ. Cellular glutathione and thiols metabolism. Biochemical Pharmacology 2002;64(5-6):1019-1026.

289. Chiarugi P, Buricchi F. Protein tyrosine phosphorylation and reversible oxidation: two cross-talking posttranslation modifications. Antioxidants & Redox Signaling 2007;9(1):1-24.

290. Monteiro HP, Arai RJ, Travassos LR. Protein tyrosine phosphorylation and protein tyrosine nitration in redox signaling. Antioxidants & Redox Signaling 2008;10(5):843-889.

291. Wang X, Destrument A, Tournier C. Physiological roles of MKK4 and MKK7: insights from animal models. Biochim Biophys Acta 2007;1773(8):1349-1357.

292. Cuenda A, Rousseau S. p38 MAP-kinases pathway regulation, function and role in human diseases. Biochimica et Biophysica Acta 2007;1773(8):1358-1375.

293. Chatterjee A, Mambo E, Sidransky D. Mitochondrial DNA mutations in human cancer. Oncogene 2006;25(34):4663-4674.

294. Stander BA. In silico design, synthesis and in vitro evaluation of antimitotic agents. University of Pretoria; 2013.

295. van den Beucken T, Koritzinsky M, Wouters BG. Translational control of gene expression during hypoxia. Cancer Biol Ther 2006;5(7):749-755.

296. Kapp LD, Lorsch JR. The molecular mechanics of eukaryotic translation. Annu Rev Biochem 2004;73:657-704.

297. Jung SN, Yang WK, Kim J, Kim HS, Kim EJ, Yun H, et al. Reactive oxygen species stabilize hypoxia-inducible factor-1 alpha protein and stimulate transcriptional activity via AMP-activated protein kinase in DU145 human prostate cancer cells. Carcinogenesis 2008;29(4):713-721.

298. Lin L, Stringfield TM, Shi X, Chen Y. Arsenite induces a cell stress-response gene, RTP801, through reactive oxygen species and transcription factors Elk-1 and CCAAT/enhancer-binding protein. Biochem J 2005;392(Pt 1):93-102.

299. Koumenis C, Wouters BG. "Translating" tumor hypoxia: unfolded protein response (UPR)-dependent and UPR-independent pathways. Mol Cancer Res 2006;4(7):423-436.

300. Clarke R, Cook KL, Hu R, Facey CO, Tavassoly I, Schwartz JL, et al. Endoplasmic reticulum stress, the unfolded protein response, autophagy, and the integrated regulation of breast cancer cell fate. Cancer Res 2012;72(6):1321-1331.

301. Gorlach A, Klappa P, Kietzmann T. The endoplasmic reticulum: folding, calcium homeostasis, signaling, and redox control. Antioxid Redox Signal 2006;8(9-10):1391-1418.

302. Malhotra JD, Kaufman RJ. Endoplasmic reticulum stress and oxidative stress: a vicious cycle or a double-edged sword? Antioxid Redox Signal 2007;9(12):2277-2293.

303. Ke Q, Costa M. Hypoxia-inducible factor-1 (HIF-1). Mol Pharmacol 2006;70(5):1469-1480.

304. Bardos JI, Ashcroft M. Negative and positive regulation of HIF-1: a complex network. Biochim Biophys Acta 2005;1755(2):107-120.

305. Schofield CJ, Ratcliffe PJ. Signalling hypoxia by HIF hydroxylases. Biochem Biophys Res Commun 2005;338(1):617-626.

306. Bell EL, Klimova TA, Eisenbart J, Moraes CT, Murphy MP, Budinger GR, et al. The Qo site of the mitochondrial complex III is required for the transduction of hypoxic signaling via reactive oxygen species production. J Cell Biol 2007;177(6):1029-1036.

307. Jung S-N, Yang WK, Kim J, Kim HS, Kim EJ, Yun H, et al. Reactive oxygen species stabilize hypoxia-inducible factor-1 alpha protein and stimulate transcriptional activity via AMP-activated protein kinase in DU145 human prostate cancer cells. Carcinogenesis 2008;29(4):713-721.

308. Young RM, Wang SJ, Gordan JD, Ji X, Liebhaber SA, Simon MC. Hypoxia-mediated selective mRNA translation by an internal ribosome entry site-independent mechanism. J Biol Chem 2008;283(24):16309-16319.

309. Warburg O. On the origin of cancer cells. Science 1956;123(3191):309-314.

310. Gatenby RA, Gillies RJ. Why do cancers have high aerobic glycolysis? Nat Rev Cancer 2004;4(11):891-899.

311. Gillies RJ, Gatenby RA. Hypoxia and adaptive landscapes in the evolution of carcinogenesis. Cancer Metastasis Rev 2007;26(2):311-317.

312. Gatenby RA, Gillies RJ. A microenvironmental model of carcinogenesis. Nat Rev Cancer 2008;8(1):56-61.

313. Guzy RD, Schumacker PT. Oxygen sensing by mitochondria at complex III: the paradox of increased reactive oxygen species during hypoxia. Exp Physiol 2006;91(5):807-819.

314. Dang CV, Kim JW, Gao P, Yustein J. The interplay between MYC and HIF in cancer. Nat Rev Cancer 2008;8(1):51-56.

315. Heddleston JM, Li Z, Lathia JD, Bao S, Hjelmeland AB, Rich JN. Hypoxia inducible factors in cancer stem cells. Br J Cancer 2010;102(5):789-795.

316. Seth P, Grant A, Tang J, Vinogradov E, Wang X, Lenkinski R, et al. On-target inhibition of tumor fermentative glycolysis as visualized by hyperpolarized pyruvate. Neoplasia 2011;13(1):60-71.

317. Kim JW, Tchernyshyov I, Semenza GL, Dang CV. HIF-1-mediated expression of pyruvate dehydrogenase kinase: a metabolic switch required for cellular adaptation to hypoxia. Cell Metab 2006;3(3):177-185.

318. Knoechel TR, Tucker AD, Robinson CM, Phillips C, Taylor W, Bungay PJ, et al. Regulatory roles of the N-terminal domain based on crystal structures of human pyruvate dehydrogenase kinase 2 containing physiological and synthetic ligands. Biochemistry 2006;45(2):402-415.

319. Garber K. Energy deregulation: licensing tumors to grow. Science 2006;312(5777):1158-1159.

320. Ristow M. Oxidative metabolism in cancer growth. Curr Opin Clin Nutr Metab Care 2006;9(4):339-345.

321. Schulz TJ, Thierbach R, Voigt A, Drewes G, Mietzner B, Steinberg P, et al. Induction of oxidative metabolism by mitochondrial frataxin inhibits cancer growth: Otto Warburg revisited. J Biol Chem 2006;281(2):977-981.

322. Plas DR, Thompson CB. Cell metabolism in the regulation of programmed cell death. Trends Endocrinol Metab 2002;13(2):75-78.

323. Sun RC, Fadia M, Dahlstrom JE, Parish CR, Board PG, Blackburn AC. Reversal of the glycolytic phenotype by dichloroacetate inhibits metastatic breast cancer cell growth in vitro and in vivo. Breast Cancer Res Treat 2010;120(1):253-260.

324. Stander BA, Marais S, Vorster CJ, Joubert AM. In vitro effects of 2-methoxyestradiol on morphology, cell cycle progression, cell death and gene expression changes in the tumorigenic MCF-7 breast epithelial cell line. J Steroid Biochem Mol Biol 2010;119(3-5):149-160.

325. Bonnet S, Archer SL, Allalunis-Turner J, Haromy A, Beaulieu C, Thompson R, et al. A mitochondria-K^+ channel axis is suppressed in cancer and its normalization promotes apoptosis and inhibits cancer growth. Cancer Cell 2007;11(1):37-51.

326. Kozmar A, Greenlee-Wacker MC, Bohlson SS. Macrophage response to apoptotic cells varies with the apoptotic trigger and is not altered by a deficiency in LRP expression. J Innate Immun 2010;2(3):248-259.

327. Newman SP, Foster PA, Ho YT, Day JM, Raobaikady B, Kasprzyk PG, et al. The therapeutic potential of a series of orally bioavailable anti-angiogenic microtubule disruptors as therapy for hormone-independent prostate and breast cancers. Br J Cancer 2007;97(12):1673-1682.

328. Vander Heiden MG, Cantley LC, Thompson CB. Understanding the Warburg effect: the metabolic requirements of cell proliferation. Science 2009;324(5930):1029-1033.

329. Hanahan D, Weinberg RA. Hallmarks of cancer: the next generation. Cell 2011;144(5):646-674.

330. Attolini CS, Michor F. Evolutionary theory of cancer. Ann N Y Acad Sci 2009;1168(1):23-51.

331. Valko M, Leibfritz D, Moncol J, Cronin MT, Mazur M, Telser J. Free radicals and antioxidants in normal physiological functions and human disease. Int J Biochem Cell Biol 2007;39(1):44-84.

332. Arner ES, Holmgren A. The thioredoxin system in cancer. Semin Cancer Biol 2006;16(6):420-426.

333. Lopez-Lazaro M. Dual role of hydrogen peroxide in cancer: possible relevance to cancer chemoprevention and therapy. Cancer Lett 2007;252(1):1-8.

334. Tso SC, Qi X, Gui WJ, Wu CY, Chuang JL, Wernstedt-Asterholm I, et al. Structure-guided development of specific pyruvate dehydrogenase kinase inhibitors targeting the ATP-binding pocket. J Biol Chem 2014;289(7):4432-4443.

335. Michelakis E, Sutendra G, Dromparis P, Webster L, Haromy A, Niven E, et al. Metabolic modulation of glioblastoma with dichloroacetate. Sci Transl Med 2010;2(31):31ra34.

336. Sutendra G, Dromparis P, Kinnaird A, Stenson T, Haromy A, Parker J, et al. Mitochondrial activation by inhibition of PDKII suppresses HIF1a signaling and angiogenesis in cancer. Oncogene 2012

337. Xiao L, Li X, Niu N, Qian J, Xie G, Wang Y. Dichloroacetate (DCA) enhances tumor cell death in combination with oncolytic adenovirus armed with MDA-7/IL-24. Mol Cell Biochem 2010;340(1-2):31-40.

338. Pearson H. Cancer patients opt for unapproved drug. Nature 2007;446(7135):474-475.

339. Mori M, Yamagata T, Goto T, Saito S, Momoi MY. Dichloroacetate treatment for mitochondrial cytopathy: long-term effects in MELAS. Brain Dev 2004;26(7):453-458.

340. Zhou J, Giannakakou P. Targeting microtubules for cancer chemotherapy. Curr Med Chem Anticancer Agents 2005;5(1):65-71.

341. Islam MN, Iskander MN. Microtubulin binding sites as target for developing anticancer agents. Mini Rev Med Chem 2004;4(10):1077-1104.

342. Giannakakou P, Nakano M, Nicolaou KC, O'Brate A, Yu J, Blagosklonny MV, et al. Enhanced microtubule-dependent trafficking and p53 nuclear accumulation by suppression of microtubule dynamics. Proc Natl Acad Sci U S A 2002;99(16):10855-10860.

343. Jordan MA, Wilson L. Microtubules as a target for anticancer drugs. Nat Rev Cancer 2004;4(4):253-265.

344. Bunker JM, Wilson L, Jordan MA, Feinstein SC. Modulation of microtubule dynamics by tau in living cells: implications for development and neurodegeneration. Mol Biol Cell 2004;15(6):2720-2728.

345. Jordan MA, Wilson L. Microtubules as a target for anticancer drugs. Nature reviews. Cancer 2004;4(4):253-265.

346. Kamath K, Okouneva T, Larson G, Panda D, Wilson L, Jordan MA. 2-Methoxyestradiol suppresses microtubule dynamics and arrests mitosis without depolymerizing microtubules. Molecular Cancer Therapeutics 2006;5(9):2225-2233.

347. Cirla A, Mann J. Combretastatins: from natural products to drug discovery. Natural Product Reports 2003;20(6):558-564.

348. Kamath K, Okouneva T, Larson G, Panda D, Wilson L, Jordan MA. 2-Methoxyestradiol suppresses microtubule dynamics and arrests mitosis without depolymerizing microtubules. Mol Cancer Ther 2006;5(9):2225-2233.

349. Mueck AO, Seeger H. 2-Methoxyestradiol--biology and mechanism of action. Steroids 2010;75(10):625-631.

350. Joubert A, Marais S. In vitro effects of 2-methoxyestradiol on cell morphology and Cdc2 kinase activity in SNO oesophageal carcinoma cells. Cell Biochem Funct 2007;25(3):357-362.

351. LaVallee TM, Zhan XH, Johnson MS, Herbstritt CJ, Swartz G, Williams MS, et al. 2-Methoxyestradiol up-regulates death receptor 5 and induces apoptosis through activation of the extrinsic pathway. Cancer Res 2003;63(2):468-475.

352. Circu ML, Aw TY. Reactive oxygen species, cellular redox systems, and apoptosis. Free Radic Biol Med 2010;48(6):749-762.

353. Bhati R, Gokmen-Polar Y, Sledge GW, Jr., Fan C, Nakshatri H, Ketelsen D, et al. 2-methoxyestradiol inhibits the anaphase-promoting complex and protein translation in human breast cancer cells. Cancer Res 2007;67(2):702-708.

354. Dubey RK, Jackson EK. Potential vascular actions of 2-methoxyestradiol. Trends Endocrinol Metab 2009;20(8):374-379.

355. Mooberry SL. Mechanism of action of 2-methoxyestradiol: new developments. Drug Resist Updat 2003;6(6):355-361.

356. Sweeney C, Liu G, Yiannoutsos C, Kolesar J, Horvath D, Staab MJ, et al. A phase II multicenter, randomized, double-blind, safety trial assessing the pharmacokinetics, pharmacodynamics, and efficacy of oral 2-methoxyestradiol capsules in hormone-refractory prostate cancer. Clin Cancer Res 2005;11(18):6625-6633.

357. Lakhani NJ, Lepper ER, Sparreboom A, Dahut WL, Venitz J, Figg WD. Determination of 2-methoxyestradiol in human plasma, using liquid chromatography/tandem mass spectrometry. Rapid Communications in Mass Spectrometry 2005;19(9):1176-1182.

358. Bruce JY, Eickhoff J, Pili R, Logan T, Carducci M, Arnott J, et al. A phase II study of 2-methoxyestradiol nanocrystal colloidal dispersion alone and in combination with sunitinib malate in patients with metastatic renal cell carcinoma progressing on sunitinib malate. Investigational new drugs 2012;30(2):794-802.

359. Tevaarwerk AJ, Holen KD, Alberti DB, Sidor C, Arnott J, Quon C, et al. Phase I trial of 2-methoxyestradiol NanoCrystal dispersion in advanced solid malignancies. Clin Cancer Res 2009;15(4):1460-1465.

360. Newman SP, Ireson CR, Tutill HJ, Day JM, Parsons MF, Leese MP, et al. The role of 17beta-hydroxysteroid dehydrogenases in modulating the activity of 2-methoxyestradiol in breast cancer cells. Cancer Res 2006;66(1):324-330.

361. Liu ZJ, Lee WJ, Zhu BT. Selective insensitivity of ZR-75-1 human breast cancer cells to 2-methoxyestradiol: evidence for type II 17beta-hydroxysteroid dehydrogenase as the underlying cause. Cancer Res 2005;65(13):5802-5811.

362. Zhou Q, Gustafson D, Nallapareddy S, Diab S, Leong S, Lewis K, et al. A phase I dose-escalation, safety and pharmacokinetic study of the 2-methoxyestradiol analog ENMD-1198 administered orally to patients with advanced cancer. Invest New Drugs 2011;29(2):340-346.

363. Brueggemeier RW, Bhat AS, Lovely CJ, Coughenour HD, Joomprabutra S, Weitzel DH, et al. 2-Methoxymethylestradiol: a new 2-methoxy estrogen analog that exhibits antiproliferative activity and alters tubulin dynamics. J Steroid Biochem Mol Biol 2001;78(2):145-156.

364. Ho A, Kim YE, Lee H, Cyrus K, Baek SH, Kim KB. SAR studies of 2-methoxyestradiol and development of its analogs as probes of anti-tumor mechanisms. Bioorg Med Chem Lett 2006;16(13):3383-3387.

365. Elger W, Schwarz S, Hedden A, Reddersen G, Schneider B. Sulfamates of various estrogens are prodrugs with increased systemic and reduced hepatic estrogenicity at oral application. J Steroid Biochem Mol Biol 1995;55(3-4):395-403.

366. Stander A, Joubert F, Joubert A. Docking, synthesis, and in vitro evaluation of antimitotic estrone analogs. Chem Biol Drug Des 2011;77(3):173-181.

367. Visagie MH, Joubert AM. The in vitro effects of 2-methoxyestradiol-bis-sulphamate on cell numbers, membrane integrity and cell morphology, and the possible induction of apoptosis and autophagy in a non-tumorigenic breast epithelial cell line. Cell Mol Biol Lett 2010;15(4):564-581.

368. Foster PA, Ho YT, Newman SP, Kasprzyk PG, Leese MP, Potter BV, et al. 2-MeOE2bisMATE and 2-EtE2bisMATE induce cell cycle arrest and apoptosis in

breast cancer xenografts as shown by a novel ex vivo technique. Breast Cancer Res Treat 2008;111(2):251-260.

369. Parsons MF, Foster PA, Chander SK, Jhalli R, Newman SP, Leese MP, et al. The in vivo properties of STX243: a potent angiogenesis inhibitor in breast cancer. Br J Cancer 2008;99(9):1433-1441.

370. Chander SK, Foster PA, Leese MP, Newman SP, Potter BV, Purohit A, et al. In vivo inhibition of angiogenesis by sulphamoylated derivatives of 2-methoxyoestradiol. Br J Cancer 2007;96(9):1368-1376.

371. Leese MP, Leblond B, Smith A, Newman SP, Di Fiore A, De Simone G, et al. 2-substituted estradiol bis-sulfamates, multitargeted antitumor agents: synthesis, in vitro SAR, protein crystallography, and in vivo activity. J Med Chem 2006;49(26):7683-7696.

372. Ho YT, Purohit A, Vicker N, Newman SP, Robinson JJ, Leese MP, et al. Inhibition of carbonic anhydrase II by steroidal and non-steroidal sulphamates. Biochem Biophys Res Commun 2003;305(4):909-914.

373. Supuran CT, Scozzafava A. Carbonic anhydrases as targets for medicinal chemistry. Bioorg Med Chem 2007;15(13):4336-4350.

374. Pastorekova S, Ratcliffe PJ, Pastorek J. Molecular mechanisms of carbonic anhydrase IX-mediated pH regulation under hypoxia. BJU Int 2008;101 Suppl 4:8-15.

375. Leese MP, Hejaz HA, Mahon MF, Newman SP, Purohit A, Reed MJ, et al. A-ring-substituted estrogen-3-O-sulfamates: potent multitargeted anticancer agents. J Med Chem 2005;48(16):5243-5256.

376. Stander BA, Joubert F, Tu C, Sippel KH, McKenna R, Joubert AM. In Vitro Evaluation of ESE-15-ol, an Estradiol Analogue with Nanomolar Antimitotic and Carbonic Anhydrase Inhibitory Activity. PLoS One 2012;7(12):e52205.

377. Stander XX, Stander BA, Joubert AM. In vitro effects of an in silico-modelled 17beta-estradiol derivative in combination with dichloroacetic acid on MCF-7 and MCF-12A cells. Cell Prolif 2011;44(6):567-581.

378. Nkandeu DS, Mqoco TV, Visagie MH, Stander BA, Wolmarans E, Cronje MJ, et al. In vitro changes in mitochondrial potential, aggresome formation and caspase activity by a novel 17-beta-estradiol analogue in breast adenocarcinoma cells. Cell Biochem Funct 2013

379. Klionsky DJ, Emr SD. Autophagy as a regulated pathway of cellular degradation. Science 2000;290(5497):1717-1721.

380. Viola G, Bortolozzi R, Hamel E, Moro S, Brun P, Castagliuolo I, et al. MG-2477, a new tubulin inhibitor, induces autophagy through inhibition of the Akt/mTOR pathway and delayed apoptosis in A549 cells. Biochem Pharmacol 2012;83(1):16-26.

381. Mathew R, Karantza-Wadsworth V, White E. Role of autophagy in cancer. Nat Rev Cancer 2007;7(12):961-967.

382. Attolini CS, Michor F. Evolutionary theory of cancer. Annals of the New York Academy of Sciences 2009;1168:23-51.

383. Diaz LA, Jr., Williams RT, Wu J, Kinde I, Hecht JR, Berlin J, et al. The molecular evolution of acquired resistance to targeted EGFR blockade in colorectal cancers. Nature 2012;486(7404):537-540.

384. Hanahan D, Weinberg RA. The hallmarks of cancer. Cell 2000;100(1):57-70.

385. Liu H, Hu YP, Savaraj N, Priebe W, Lampidis TJ. Hypersensitization of tumor cells to glycolytic inhibitors. Biochemistry 2001;40(18):5542-5547.

386. Tagg SL, Foster PA, Leese MP, Potter BV, Reed MJ, Purohit A, et al. 2-Methoxyoestradiol-3,17-O,O-bis-sulphamate and 2-deoxy-D-glucose in combination: a potential treatment for breast and prostate cancer. Br J Cancer 2008;99(11):1842-1848.

387. Phelan MC. Basic Techniques in Mammalian Cell Tissue Culture. In: Current Protocols in Cell Biology: John Wiley & Sons, Inc.; 2001.

388. Xiao L, Li X, Niu N, Qian J, Xie G, Wang Y. Dichloroacetate (DCA) enhances tumor cell death in combination with oncolytic adenovirus armed with MDA-7/IL-24. Mol Cell Biochem 2010

389. Xiong S, Pang HD, Fan J, Ge F, Yang XX, Liu QY, et al. In vitro and in vivo antineoplastic activity of a novel bromopyrrole and its potential mechanism of action. Br J Pharmacol 2010;159(4):909-918.

390. Olberding KE, Wang X, Zhu Y, Pan J, Rai SN, Li C. Actinomycin D synergistically enhances the efficacy of the BH3 mimetic ABT-737 by downregulating Mcl-1 expression. Cancer Biol Ther 2010;10(9):918-929.

391. Xing JZ, Zhu L, Jackson JA, Gabos S, Sun XJ, Wang XB, et al. Dynamic monitoring of cytotoxicity on microelectronic sensors. Chem Res Toxicol 2005;18(2):154-161.

392. Kirstein SL, Atienza JM, Xi B, Zhu J, Yu N, Wang X, et al. Live cell quality control and utility of real-time cell electronic sensing for assay development. Assay Drug Dev Technol 2006;4(5):545-553.

393. Limame R, Wouters A, Pauwels B, Fransen E, Peeters M, Lardon F, et al. Comparative analysis of dynamic cell viability, migration and invasion assessments by novel real-time technology and classic endpoint assays. PLoS One 2012;7(10):e46536.

394. Vega-Avila E, Pugsley MK. An overview of colorimetric assay methods used to assess survival or proliferation of mammalian cells. Proc West Pharmacol Soc 2011;54:10-14.

395. Wakelin LP, Adams A, Hunter C, Waring MJ. Interaction of crystal violet with nucleic acids. Biochemistry 1981;20(20):5779-5787.

396. Gillies RJ, Didier N, Denton M. Determination of cell number in monolayer cultures. Anal Biochem 1986;159(1):109-113.

397. Kueng W, Silber E, Eppenberger U. Quantification of cells cultured on 96-well plates. Anal Biochem 1989;182(1):16-19.

398. Sun RC, Fadia M, Dahlstrom JE, Parish CR, Board PG, Blackburn AC. Reversal of the glycolytic phenotype by dichloroacetate inhibits metastatic breast cancer cell growth in vitro and in vivo. Breast Cancer Res Treat 2009

399. Allen M, Millett P, Dawes E, Rushton N. Lactate dehydrogenase activity as a rapid and sensitive test for the quantification of cell numbers in vitro. Clin Mater 1994;16(4):189-194.

400. Joubert A, Marais S, Maritz C. Influence of 2-methoxyestradiol on MCF-7 cells: an improved differential interference contrasting technique and Bcl-2 and Bax protein expression levels. Biocell 2009;33(1):67-70.

401. Danz R, Vogelgsang A, Käthner R. PlasDIC - a useful modification of the differential interference contrast according to Smith/Nomarski in transmitted light arrangement Carl Zeiss Inc., Germany; 2004; Available from: http://www.zeiss.com/C12567BE00472A5C/EmbedTitelIntern/Article-PlasDic_Photonic_e/$File/PlasDIC_Photonik_2004March_e.pdf.

402. Visagie M, Mqoco T, Joubert A. Sulphamoylated estradiol analogue induces antiproliferative activity and apoptosis in breast cell lines. Cell Mol Biol Lett 2012;17(4):549-558.

403. Klionsky DJ, Cuervo AM, Seglen PO. Methods for monitoring autophagy from yeast to human. Autophagy 2007;3(3):181-206.

404. Ono K, Kim SO, Han J. Susceptibility of lysosomes to rupture is a determinant for plasma membrane disruption in tumor necrosis factor alpha-induced cell death. Mol Cell Biol 2003;23(2):665-676.

405. Brunk UT, Dalen H, Roberg K, Hellquist HB. Photo-oxidative disruption of lysosomal membranes causes apoptosis of cultured human fibroblasts. Free Radic Biol Med 1997;23(4):616-626.

406. Vorster CJ, Joubert AM. In vitro effects of 2-methoxyestradiol-bis-sulphamate on the non-tumorigenic MCF-12A cell line. Cell Biochem Funct 2010;28(5):412-419.

407. Pozarowski P, Darzynkiewicz Z. Analysis of cell cycle by flow cytometry. Methods Mol Biol 2004;281:301-311.

408. Vermes I, Haanen C, Steffens-Nakken H, Reutelingsperger C. A novel assay for apoptosis. Flow cytometric detection of phosphatidylserine expression on early

apoptotic cells using fluorescein labelled Annexin V. J Immunol Methods 1995;184(1):39-51.

409. Yang S, Wang X, Contino G, Liesa M, Sahin E, Ying H, et al. Pancreatic cancers require autophagy for tumor growth. Genes Dev 2011;25(7):717-729.

410. Klionsky DJ, Abeliovich H, Agostinis P, Agrawal DK, Aliev G, Askew DS, et al. Guidelines for the use and interpretation of assays for monitoring autophagy in higher eukaryotes. Autophagy 2008;4(2):151-175.

411. Karlsson M, Kurz T, Brunk UT, Nilsson SE, Frennesson CI. What does the commonly used DCF test for oxidative stress really show? Biochem J 2010;428(2):183-190.

412. Zhang Y, Guo J, Zeng L, Zhang J, Hui Y, Liu J, et al. Tert-butyl-2(4,5-dihydrogen-4,4,5,5-tetramethyl-3-O-1H-imidazole-3-cationic-1-oxy l-2-pyrrolidine-1-carboxylic ester displays novel cytotoxicity through reactive oxygen species-mediated oxidative damage in MCF-7 and MDA-MB-231 cells. Chem Biol Interact 2011;192(3):287-297.

413. Spencer JP. The interactions of flavonoids within neuronal signalling pathways. Genes Nutr 2007;2(3):257-273.

414. Passiatore G, Gentilella A, Rom S, Pacifici M, Bergonzini V, Peruzzi F. Induction of Id-1 by FGF-2 involves activity of EGR-1 and sensitizes neuroblastoma cells to cell death. J Cell Physiol 2011;226(7):1763-1770.

415. Letai AG. Diagnosing and exploiting cancer's addiction to blocks in apoptosis. Nat Rev Cancer 2008;8(2):121-132.

416. Letai A, Kutuk O. Regulation of Bcl-2 family proteins by posttranslational modifications. Curr Mol Med 2008;8(2):102-118.

417. Zimmermann KC, Bonzon C, Green DR. The machinery of programmed cell death. Pharmacol Ther 2001;92(1):57-70.

418. Stander BA. Differential effects of Sutherlandia frutescens subs. microphylla on cell numbers, morphology, gene and protein expression in a breast adenocarcinoma and a normal breast epithelial cell line. University of Pretoria; 2007.

419. Wettenhall JM, Smyth GK. limmaGUI: a graphical user interface for linear modeling of microarray data. Bioinformatics 2004;20(18):3705-3706.

420. Smyth G. Limma: linear models for microarray data. Bioinformatics and computational biology solutions using R and bioconductor. Springer; 2005. p. 397-420.

421. Smyth GK, Speed T. Normalization of cDNA microarray data. Methods 2003;31(4):265-273.

422. Benjamini Y, Hochberg Y. Controlling the false discovery rate: a practical and powerful approach to multiple testing. J R Stat Soc Series B Stat Methodol 1995:289-300.

423. Nogales-Cadenas R, Carmona-Saez P, Vazquez M, Vicente C, Yang X, Tirado F, et al. GeneCodis: interpreting gene lists through enrichment analysis and integration of diverse biological information. Nucleic Acids Res 2009;37(suppl 2):W317.

424. Pirooznia M, Nagarajan V, Deng Y. GeneVenn—a web application for comparing gene lists using Venn diagrams. Bioinformation 2007;1(10):420-422.

425. Agniswamy J, Fang B, Weber IT. Plasticity of S2-S4 specificity pockets of executioner caspase-7 revealed by structural and kinetic analysis. FEBS J 2007;274(18):4752-4765.

426. Tabas-Madrid D, Nogales-Cadenas R, Pascual-Montano A. GeneCodis3: a non-redundant and modular enrichment analysis tool for functional genomics. Nucleic Acids Res 2012;40(Web Server issue):W478-483.

427. Roy G, De Crescenzo G, Khaleghpour K, Kahvejian A, O'Connor-McCourt M, Sonenberg N. Paip1 interacts with poly(A) binding protein through two independent binding motifs. Mol Cell Biol 2002;22(11):3769-3782.

428. Imataka H, Sonenberg N. Human eukaryotic translation initiation factor 4G (eIF4G) possesses two separate and independent binding sites for eIF4A. Mol Cell Biol 1997;17(12):6940-6947.

429. Cao Y, Karin M. NF-kappaB in mammary gland development and breast cancer. J Mammary Gland Biol Neoplasia 2003;8(2):215-223.

430. Karin M, Lin A. NF-kappaB at the crossroads of life and death. Nat Immunol 2002;3(3):221-227.

431. Murata K, Hattori M, Hirai N, Shinozuka Y, Hirata H, Kageyama R, et al. Hes1 directly controls cell proliferation through the transcriptional repression of p27Kip1. Mol Cell Biol 2005;25(10):4262-4271.

432. Fu T-J, Peng J, Lee G, Price DH, Flores O. Cyclin K functions as a CDK9 regulatory subunit and participates in RNA polymerase II transcription. J Biol Chem 1999;274(49):34527-34530.

433. Luo Y, Kong F, Wang Z, Chen D, Liu Q, Wang T, et al. Loss of ASAP3 destabilizes cytoskeletal protein ACTG1 to suppress cancer cell migration. Mol Med Rep 2014;9(2):387-394.

434. Goswami C, Hucho T. Submembraneous microtubule cytoskeleton: biochemical and functional interplay of TRP channels with the cytoskeleton. FEBS J 2008;275(19):4684-4699.

435. Heng JI, Chariot A, Nguyen L. Molecular layers underlying cytoskeletal remodelling during cortical development. Trends Neurosci 2010;33(1):38-47.

436. Dean M, Fojo T, Bates S. Tumour stem cells and drug resistance. Nat Rev Cancer 2005;5(4):275-284.

437. Jaeger W. Classical resistance mechanisms. Int J Clin Pharmacol Ther 2009;47:46-48.

438. Imamichi Y, Mizutani T, Ju Y, Matsumura T, Kawabe S, Kanno M, et al. Transcriptional regulation of human ferredoxin reductase through an intronic enhancer in steroidogenic cells. Biochim Biophys Acta 2014;1839(1):33-42.

439. Liu G, Chen X. The ferredoxin reductase gene is regulated by the p53 family and sensitizes cells to oxidative stress-induced apoptosis. Oncogene 2002;21(47):7195-7204.

440. Pegg AE. Spermidine/spermine-N(1)-acetyltransferase: a key metabolic regulator. Am J Physiol Endocrinol Metab 2008;294(6):E995-1010.

441. Mandal S, Mandal A, Johansson HE, Orjalo AV, Park MH. Depletion of cellular polyamines, spermidine and spermine, causes a total arrest in translation and growth in mammalian cells. Proc Natl Acad Sci U S A 2013;110(6):2169-2174.

442. Xie J, Guo Q. Apoptosis antagonizing transcription factor protects renal tubule cells against oxidative damage and apoptosis induced by ischemia-reperfusion. J Am Soc Nephrol 2006;17(12):3336-3346.

443. Seegers JC, Aveling ML, Van Aswegen CH, Cross M, Koch F, Joubert WS. The cytotoxic effects of estradiol-17 beta, catecholestradiols and methoxyestradiols on dividing MCF-7 and HeLa cells. J Steroid Biochem 1989;32(6):797-809.

444. Lottering ML, Haag M, Seegers JC. Effects of 17 beta-estradiol metabolites on cell cycle events in MCF-7 cells. Cancer Res 1992;52(21):5926-5932.

445. Lottering ML, de Kock M, Viljoen TC, Grobler CJ, Seegers JC. 17beta-Estradiol metabolites affect some regulators of the MCF-7 cell cycle. Cancer Lett 1996;110(1-2):181-186.

446. Amant F, Lottering ML, Joubert A, Thaver V, Vergote I, Lindeque BG. 2-methoxyestradiol strongly inhibits human uterine sarcomatous cell growth. Gynecol Oncol 2003;91(2):299-308.

447. Van Zijl C, Lottering ML, Steffens F, Joubert A. In vitro effects of 2-methoxyestradiol on MCF-12A and MCF-7 cell growth, morphology and mitotic spindle formation. Cell Biochem Funct 2008;26(5):632-642.

448. Purohit A, Williams GJ, Howarth NM, Potter BV, Reed MJ. Inactivation of steroid sulfatase by an active site-directed inhibitor, estrone-3-O-sulfamate. Biochemistry 1995;34(36):11508-11514.

449. Purohit A, Vernon KA, Hummelinck AE, Woo LW, Hejaz HA, Potter BV, et al. The development of A-ring modified analogues of oestrone-3-O-sulphamate as potent steroid sulphatase inhibitors with reduced oestrogenicity. J Steroid Biochem Mol Biol 1998;64(5-6):269-275.

450. Howarth NM, Purohit A, Reed MJ, Potter BV. Estrone sulfamates: potent inhibitors of estrone sulfatase with therapeutic potential. J Med Chem 1994;37(2):219-221.

451. MacCarthy-Morrogh L, Townsend PA, Purohit A, Hejaz HAM, Potter BVL, Reed MJ, et al. Differential effects of estrone and estrone-3-O-sulfamate derivatives on mitotic arrest, apoptosis, and microtubule assembly in human breast cancer cells. Cancer Res 2000;60(19):5441-5450.

452. Vicker N, Ho Y, Robinson J, Woo LL, Purohit A, Reed MJ, et al. Docking studies of sulphamate inhibitors of estrone sulphatase in human carbonic anhydrase II. Bioorg Med Chem Lett 2003;13(5):863-865.

453. Utsumi T, Leese MP, Chander SK, Gaukroger K, Purohit A, Newman SP, et al. The effects of 2-methoxyoestrogen sulphamates on the in vitro and in vivo proliferation of breast cancer cells. J Steroid Biochem Mol Biol 2005;94(1-3):219-227.

454. Foster PA, Ho YT, Newman SP, Leese MP, Potter BV, Reed MJ, et al. STX140 and STX641 cause apoptosis via the intrinsic mitochondrial pathway and down-regulate survivin and XIAP expression in ovarian and prostate cancer cells. Anticancer Res 2009;29(10):3751-3757.

455. Verenich S, Gerk PM. Therapeutic promises of 2-methoxyestradiol and its drug disposition challenges. Mol Pharm 2010;7(6):2030-2039.

456. Newman SP, Foster PA, Stengel C, Day JM, Ho YT, Judde J-G, et al. STX140 is efficacious in vitro and in vivo in taxane-resistant breast carcinoma cells. Clin Cancer Res 2008;14(2):597-606.

457. Casini A, Abbate F, Scozzafava A, Supuran CT. Carbonic anhydrase inhibitors: X-ray crystallographic structure of the adduct of human isozyme II with a bis-sulfonamide-two heads are better than one? Bioorganic & Medicinal Chemistry Letters 2003;13(16):2759-2763.

458. Supuran CT, Scozzafava A. Carbonic anhydrases as targets for medicinal chemistry. Bioorg Med Chem 2007;15(13):4336-4350.

459. Cushman M, He HM, Katzenellenbogen JA, Lin CM, Hamel E. Synthesis, antitubulin and antimitotic activity, and cytotoxicity of analogs of 2-methoxyestradiol, an endogenous mammalian metabolite of estradiol that inhibits tubulin polymerization by binding to the colchicine binding site. J Med Chem 1995;38(12):2041-2049.

460. Tinley TL, Leal RM, Randall-Hlubek DA, Cessac JW, Wilkens LR, Rao PN, et al. Novel 2-methoxyestradiol analogues with antitumor activity. Cancer Research 2003;63(7):1538-1549.

461. Supuran CT. Inhibition of carbonic anhydrase IX as a novel anticancer mechanism. World journal of clinical oncology 2012;3(7):98.

462. Raez LE, Papadopoulos K, Ricart AD, Chiorean EG, Dipaola RS, Stein MN, et al. A phase I dose-escalation trial of 2-deoxy-D-glucose alone or combined with docetaxel in patients with advanced solid tumors. Cancer Chemother Pharmacol 2013;71(2):523-530.

463. Cao W, Yacoub S, Shiverick KT, Namiki K, Sakai Y, Porvasnik S, et al. Dichloroacetate (DCA) sensitizes both wild‐type and over expressing Bcl‐2 prostate cancer cells in vitro to radiation. The Prostate 2008;68(11):1223-1231.

464. Sanchez WY, McGee SL, Connor T, Mottram B, Wilkinson A, Whitehead JP, et al. Dichloroacetate inhibits aerobic glycolysis in multiple myeloma cells and increases sensitivity to bortezomib. Br J Cancer 2013;108(8):1624-1633.

465. Shen Y, Ou D, Hsu C, Lin K, Chang C, Lin C, et al. Activating oxidative phosphorylation by a pyruvate dehydrogenase kinase inhibitor overcomes sorafenib resistance of hepatocellular carcinoma. British journal of cancer 2013;108(1):72-81.

466. Xie J, Wang BS, Yu DH, Lu Q, Ma J, Qi H, et al. Dichloroacetate shifts the metabolism from glycolysis to glucose oxidation and exhibits synergistic growth inhibition with cisplatin in HeLa cells. Int J Oncol 2011;38(2):409-417.

467. Tavares-Valente D, Baltazar F, Moreira R, Queirós O. Cancer cell bioenergetics and pH regulation influence breast cancer cell resistance to paclitaxel and doxorubicin. J Bioenerg Biomembr 2013;45(5):467-475.

468. Olszewski U, Poulsen TT, Ulsperger E, Poulsen HS, Geissler K, Hamilton G. In vitro cytotoxicity of combinations of dichloroacetate with anticancer platinum compounds. Clin Pharmacol 2010;2:177-183.

469. Fiebiger W, Olszewski U, Ulsperger E, Geissler K, Hamilton G. In vitro cytotoxicity of novel platinum-based drugs and dichloroacetate against lung carcinoid cell lines. Clin Transl Oncol 2011;13(1):43-49.

470. Dhar S, Lippard SJ. Mitaplatin, a potent fusion of cisplatin and the orphan drug dichloroacetate. Proc Natl Acad Sci U S A 2009;106(52):22199-22204.

471. Graziano MJ, Spoon TA, Cockrell EA, Rowse PE, Gonzales AJ. Induction of Apoptosis in Rat Peripheral Blood Lymphocytes by the Anticancer Drug CI-994 (Acetyldinaline)(*). J Biomed Biotechnol 2001;1(2):52-61.

472. Parhamifar L, Andersen H, Moghimi SM. Lactate dehydrogenase assay for assessment of polycation cytotoxicity. In: Nanotechnology for Nucleic Acid Delivery: Springer; 2013. p. 13-22.

473. Nettles JH, Li H, Cornett B, Krahn JM, Snyder JP, Downing KH. The binding mode of epothilone A on α, ß-tubulin by electron crystallography. Science 2004;305(5685):866-869.

474. Wolmarans E, Mqoco TV, Stander A, Nkandeu SD, Sippel K, McKenna R, et al. Novel estradiol analogue induces apoptosis and autophagy in esophageal carcinoma cells. Cell Mol Biol Lett 2014;19(1):98-115.

475. Visagie MH, Birkholtz LM, Joubert AM. 17-beta-estradiol analog inhibits cell proliferation by induction of apoptosis in breast cell lines. Microsc Res Tech 2014;77(3):236-242.

476. Fukui M, Zhu BT. Mechanism of 2-methoxyestradiol-induced apoptosis and growth arrest in human breast cancer cells. Mol Carcinog 2009;48(1):66-78.

477. Voigt O, Poggeler S. Self-eating to grow and kill: autophagy in filamentous ascomycetes. Appl Microbiol Biotechnol 2013;97(21):9277-9290.

478. Madeo F, Eisenberg T, Buttner S, Ruckenstuhl C, Kroemer G. Spermidine: a novel autophagy inducer and longevity elixir. Autophagy 2010;6(1):160-162.

479. Sun RC, Board PG, Blackburn AC. Targeting metabolism with arsenic trioxide and dichloroacetate in breast cancer cells. Mol Cancer 2011;10:142.

480. Shen YC, Ou DL, Hsu C, Lin KL, Chang CY, Lin CY, et al. Activating oxidative phosphorylation by a pyruvate dehydrogenase kinase inhibitor overcomes sorafenib resistance of hepatocellular carcinoma. Br J Cancer 2013;108(1):72-81.

481. Carter WO, Narayanan PK, Robinson JP. Intracellular hydrogen peroxide and superoxide anion detection in endothelial cells. J Leukoc Biol 1994;55(2):253-258.

482. Halliwell B, Whiteman M. Measuring reactive species and oxidative damage in vivo and in cell culture: how should you do it and what do the results mean? Br J Pharmacol 2004;142(2):231-255.

483. Kurz T, Eaton JW, Brunk UT. The role of lysosomes in iron metabolism and recycling. Int J Biochem Cell Biol 2011;43(12):1686-1697.

484. Hasan MR, Koikawa S, Kotani S, Miyamoto S, Nakagawa H. Ferritin forms dynamic oligomers to associate with microtubules in vivo: implication for the role of microtubules in iron metabolism. Exp Cell Res 2006;312(11):1950-1960.

485. Zhang Y, Luo M, Zu Y, Fu Y, Gu C, Wang W, et al. Dryofragin, a phloroglucinol derivative, induces apoptosis in human breast cancer MCF-7 cells through ROS-mediated mitochondrial pathway. Chem Biol Interact 2012;199(2):129-136.

486. Lee J-J, Lee J-H, Ko Y-G, Hong S, Lee J-S. Prevention of premature senescence requires JNK regulation of Bcl-2 and reactive oxygen species. Oncogene 2009;29(4):561-575.

487. van der Luit AH, Vink SR, Klarenbeek JB, Perrissoud D, Solary E, Verheij M, et al. A new class of anticancer alkylphospholipids uses lipid rafts as membrane gateways to induce apoptosis in lymphoma cells. Mol Cancer Ther 2007;6(8):2337-2345.

488. Bock J, Gulbins E. The transmembranous domain of CD40 determines CD40 partitioning into lipid rafts. FEBS Lett 2003;534(1):169-174.

489. Wu Z, Tandon R, Ziembicki J, Nagano J, Hujer KM, Miller RT, et al. Role of ceramide in Ca2+-sensing receptor-induced apoptosis. J Lipid Res 2005;46(7):1396-1404.

490. Chalfant CE, Szulc Z, Roddy P, Bielawska A, Hannun YA. The structural requirements for ceramide activation of serine-threonine protein phosphatases. J Lipid Res 2004;45(3):496-506.

491. Yu C, Minemoto Y, Zhang J, Liu J, Tang F, Bui TN, et al. JNK suppresses apoptosis via phosphorylation of the proapoptotic Bcl-2 family protein BAD. Mol Cell 2004;13(3):329-340.

492. Ruvolo PP, Deng X, May WS. Phosphorylation of Bcl2 and regulation of apoptosis. Leukemia 2001;15(4):515-522.

493. Haldar S, Basu A, Croce CM. Bcl2 is the guardian of microtubule integrity. Cancer Res 1997;57(2):229-233.

494. Li D, Ueta E, Kimura T, Yamamoto T, Osaki T. Reactive oxygen species (ROS) control the expression of Bcl‐2 family proteins by regulating their phosphorylation and ubiquitination. Cancer Sci 2004;95(8):644-650.

495. Miliani de Marval PL, Zhang Y. The RP-Mdm2-p53 pathway and tumorigenesis. Oncotarget 2011;2(3):234-238.

496. Wakai T, Shirai Y, Sakata J, Korita PV, Matsuda Y, Takamura M, et al. Alteration of p53-binding protein 1 expression as a risk factor for local recurrence in patients undergoing resection for extrahepatic cholangiocarcinoma. Int J Oncol 2011;38(5):1227-1236.

497. Reaper PM, Griffiths MR, Long JM, Charrier JD, Maccormick S, Charlton PA, et al. Selective killing of ATM- or p53-deficient cancer cells through inhibition of ATR. Nat Chem Biol 2011;7(7):428-430.

498. Puthalakath H, O'Reilly LA, Gunn P, Lee L, Kelly PN, Huntington ND, et al. ER stress triggers apoptosis by activating BH3-only protein Bim. Cell 2007;129(7):1337-1349.

499. Nahta R, Yuan LX, Fiterman DJ, Zhang L, Symmans WF, Ueno NT, et al. B cell translocation gene 1 contributes to antisense Bcl-2-mediated apoptosis in breast cancer cells. Mol Cancer Ther 2006;5(6):1593-1601.

500. Hofer-Warbinek R, Schmid JA, Mayer H, Winsauer G, Orel L, Mueller B, et al. A highly conserved proapoptotic gene, IKIP, located next to the APAF1 gene locus, is regulated by p53. Cell Death Differ 2004;11(12):1317-1325.

501. Park JE, Park BC, Kim HA, Song M, Park SG, Lee do H, et al. Positive regulation of apoptosis signal-regulating kinase 1 by dual-specificity phosphatase 13A. Cell Mol Life Sci 2010;67(15):2619-2629.

502. Katagiri C, Masuda K, Nomura M, Tanoue K, Fujita S, Yamashita Y, et al. DUSP13B/TMDP inhibits stress-activated MAPKs and suppresses AP-1-dependent gene expression. Mol Cell Biochem 2011;352(1-2):155-162.

503. Nagai H, Noguchi T, Takeda K, Ichijo H. Pathophysiological roles of ASK1-MAP kinase signaling pathways. J Biochem Mol Biol 2007;40(1):1-6.

504. Mazurek S, Michel A, Eigenbrodt E. Effect of extracellular AMP on cell proliferation and metabolism of breast cancer cell lines with high and low glycolytic rates. J Biol Chem 1997;272(8):4941-4952.

505. Scherz-Shouval R, Elazar Z. Regulation of autophagy by ROS: physiology and pathology. Trends Biochem Sci 2011;36(1):30-38.